Fracture Toughness and Fatigue Crack Propagation Testing and Evaluation of Additive Manufactured Titanium Alloy Metals at Different Orientations by Electron Beam Melting

Peter Addess

A thesis

submitted in partial fulfillment of the

requirements for the degree of

Master of Science in Engineering

University of Washington

2021

Committee:

Ramulu Mamidala

John Kramlich

Dan Sanders

Program Authorized to Offer Degree:

Mechanical Engineering

University of Washington

Abstract

Fracture Toughness and Fatigue Crack Propagation Testing and Evaluation of Additive Manufactured Titanium Alloy Metals at Different Orientations by Electron Beam Melting

Peter Addess

Chair of Supervisory Committee:
Dr. Ramulu Mamidala
Department of Mechanical Engineering

Certain Naval applications use titanium based components which offer outstanding structural benefit. While risk to mission capability can be reduced by having a wide assortment of spare parts available, one small material item can place a unit in a mission hold status. The next step for the U.S. Military is to consider additive manufacturing for quality controlled use. Two experiments were conducted to further understand the materials produced by an ARCAM A2X machine with Ti-6Al-4V powder. The first experiment tested fracture toughness of specimens made from brand new powder. The second experiment tested the fatigue crack growth rate of specimens made from powder that had been reused. These two experiments also studied the effects build orientation has on material properties by conducting the first two tests with specimens at four different orientations; 0°, 30°, 60°, and 90° relative to the XY build plane.

Table of Contents

Table of Figures

List of Tables

Acknowledgements

This research would not have happened without the assistance of the following individuals and organizations. Firstly, this research could not have been done without the support from my wife. In the academic realm, thanks goes out to William Kuykendall and Sean Ghods for rapid procurement of resources and production of the 3D printed parts for this project. Thanks to Eamon McQuaide, the Lab Engineer in the machine shop for preparing my specimens prior to testing. Thanks are also given to the University of Washington's Mechanical Engineering Department for funding necessary to complete this project. Lastly, I sincerely appreciate all of the mentorship and knowledge that Dr. Ramulu Mamidala has given to assist with the successful completion of this project.

Dedication

To my wife Rebecca, and my late father, Stanley.

Chapter 1: Introduction

1.1 Overview

The Additive Manufacturing (AM) process has been revised and developed significantly since its invention in the 1980's. First having been developed for plastics, the AM process now can make parts out of metals. Certain processes such as wire arc, selective laser melting (SLM), and electron beam melting (EBM) are just a few examples [1].

Titanium material is used by manufacturers in many industries based on its high resistivity to corrosion, high strength to weight ratio, biocompatibility, and excellent mechanical properties. However, high costs are associated with titanium milling [1]. Milling also requires special tools to machine parts based on approximately 80% of the heat generated being transferred into the tool. Titanium material properties have low thermal conductivity, so the fast flow of the chips when separated during traditional milling cannot escape in comparison to materials with higher thermal conductivity. And lastly milling generates a significant amount of wastage which is economically cumbersome [14].

A cost effective alternative of milling is to AM titanium. Comparatively, titanium AM produces a significantly reduced amount of material waste which makes it economically attractive. Furthermore, some AM processes such as EBM allow for material to be reused in subsequent processes [1]. Unfortunately the EBM process produces specimens with significant surface defects which result in mechanical properties quantitatively poorer than those of milled titanium. Limitations to AM of titanium also exist. For example, as technology currently allows, AM machines have only a finite space to make parts and as such size is limited [1]. Additionally, companies would prefer that the machine can operate without significant maintenance down time, and that the machine can produce parts without defects, which may fail inspection requirements [12, 18]. As AM technologies develop larger build volumes, engineering companies now need to start assessment as to the mechanical properties associated with builds to legally base factor of safety to meet industrial implementation guidelines. In a mechanical approach, certainty requires assuredness that a certain product functions over its lifetime in its intended design usage. One such consideration of EBM builds specifically is that machined specimens contain significantly higher surface roughness. Significant research into how these surface defects will affect the final product will give better understanding of lifetime and fatigue properties [1].

In 2014, the U.S. Navy announced intentions to utilize AM for components on naval vessels as a potential solution for material issues while ships are underway and unable to access resources for viable solutions. The initiative “Print the Fleet” at the time of the announcement experimented with polymer-based products in a harsh environment laboratory in Dam Neck, Virginia [15]. Since then, the Office of Naval Research Workforce Development program trains active duty sailors who, while deployed without access to vital resources, can rapidly produce parts, including metallic, which may not be in the supply chain [16-18].

This study will characterize and compare the fracture toughness (FT) of virgin titanium powder by following the ASTM E399-20 standard. Specimens will undergo a fatigue precracking to a specific length prior to being subjected to a constantly increasing ramping force until fracture. Outputs of the test frame will produce measured data by a displacement gauge and applied force. Data acquired will be converted in MATLAB and validated before informing the user of the value for FT [31].

This study will also characterize and compare the effects recycled powder has on AM EBM Ti-6Al-4V by performing Fatigue Crack Growth Rate (FCGR) calculations in accordance with ASTM E647-15. Specimens will be placed in testing fixtures rigidly mounted to a cyclic loading machine which will maintain a constant amplitude sinusoidal wave for the duration of the test until failure. Outputs of the test frame will produce evenly measured data representing the number of cycles, measured displacement, and loading. Data acquired for each test will be reduced by means of MATLAB code to output graphical representations of the change in crack length divided by the change in number of cycles (da/dN) versus the stress intensity factor (ΔK) [33].

Each test will also study the effects build orientation dependence has on material performance in non-orthogonal directions. Specimens built for both tests will be built in four angles. The first orientation is in the XY plane, or how a cutting board would rest on a table. Imagine only one edge of the cutting board were to be lifted such that the angle between the table and the cutting board were 30 degrees; this concept is congruent with what this research will study. Similarly, this angle will be tested at 60 and 90 degrees to study the effect anisotropy.

1.2 Objectives

The objectives of this research are to:

- Experimentally test the FT and Fatigue Crack Propagation of four differently oriented titanium components built by the EBM process with no post-processing techniques.
- Assess the effects of recycled powder on fatigue crack growth behavior.

Chapter 2: Background and Literature Review

2.1 Additive Manufacturing

Traditional manufacturing of materials is generally subtractive in nature by a machining process or additive by forming or casting process. Subtractive machining requires significant production time, high energy cutting forces, specialty and replacement tools, and adequate cooling for generated heat. This process is an especially wasteful process at material waste values between approximately 40-80% [4, 5]. Even though metal recycling can repurpose waste, added cost to the manufacturing process is incurred [13].

Although AM has been developed for decades, only in the past ten years or so has AM technology advanced to a level of serious inquiry for design. AM utilizes a layer-by-layer technique to form a final component from a computer assisted three-dimensional model. Computer-aided design (CAD) files store a digital blueprint from which a machine can generate any desired shape from simple to complex geometries [13]. AM offers a unique method to manufacture designs compared to traditional manufacturing processes, while reducing the carbon footprint. The AM process also allows for unique construction and complex shapes which would have otherwise been too difficult or impossible to create by conventional manufacturing methods. Lastly, AM creates a more efficient business opportunity based on relatively negligible material wastage less than 10% [4]. Traditionally, AM is recognized as fusing plastics, however industry has recognized that this process can feasibly use metal alloys such as Ti-6Al-4V [3]. This research studies materials generated EBM powder bed fusion (PBF) where electrons melt a metal powder bed in a vacuum by means of imparting energy through electrons to selectively sinter and melt the material [3]. AM of titanium could provide industry a viable option to reduce costs of machined components that last longer than steel or aluminum [10]. Manufacturers can also design additively manufactured parts to optimize load paths in a part that otherwise would have been difficult or expensive to manufacture [11]. Titanium specifically offers a significantly higher strength to weight ratio which benefits nearly all industries based on reducing the amount of fuel consumption [14]. Because of the mechanical properties of titanium, its industrial applications range from Department of Defense assets such as aircraft, naval ships, and armor plating, to consumer applications such as sporting goods [13]. Typical mechanical properties between orientation builds and material characteristics which are listed in Table 1 for EBM and wrought milled titanium [41].

Table 1: Mechanical property comparison of titanium built materials [41]

	Young's Modulus (GPa)	Yield Strength (MPa)	Ultimate Tensile Strength (MPa)	Ref
Arcam A2X	120	950	1040	[10]
Wrought Titanium	120	860	930	[21]

2.2 Electron Beam Melting Process

An EBM machine uses three main subsystems to generate a solid three-dimensional component: an electron beam gun, powder magazine/canvas, and a build chamber as can be seen in Figure 1. At the start of the build, powder hoppers on both sides of the build chamber introduce incoming powder which is smoothly raked to provide a canvas to be sintered. This canvas is bombarded with directed electrons, via an electron gun to melt or sinter the loose powder into the desired shape layer by layer until the build is complete. Between each layer, the formed piece retracts downward before new powder from the hoppers are raked in preparation for the new layer to be formed. At the end of the build process, the entire part is completely surrounded by excess powder in the form of a rectangular cake. After the user opens the machine and removes the heat shield, this cake filler matrix is transferred to a Powder Recovery System (PRS) where excess powder is blasted with pressurized air. This excess powder is then collected and sieved in order to recycle powder for the next build [42].

Prior to a build taking place, the user will generate a three dimensional (3D) CAD by utilizing software, most commonly Materialise Magics, to upload a build file to the machine. The build process requires supports for reasons which will be explained later. Prior to the CAD file making its way to the build machine, these supports will be inserted just after the design process. This EBM system is advantageous due to the ability to introduce high resolution features such as internal passages as well as maintaining dimensional control, however improperly arranged parts during the design process may lead to build failures [4, 32, 42].

Prior to a build commencing, the operator must ensure that a completely sterile environment exists; therefore, meticulous cleaning is required before and after builds. Requisite powder is added for the entire build since access to the build chamber is not possible. Then, careful leveling of the build plate, which rests on a bed of powder, is performed by gently tapping corners and reassessing distance measurements until satisfied. Lastly, a calibration of the thermocouple attached to the build plate is performed. Variability in these steps means that initial machine setup can take anywhere from 2-4 hours [42].

During a build, the amount of energy deposited relates to the physical properties directly. Equation 1 represents a basic starting point for comparing AM processes. E is energy density, α is absorptivity of the powder bed, P is the power, ν is the scanning speed, h is the hatch spacing, and t is the layer thickness [19]. This fundamental concept is introduced to illustrate firstly that all parameters here are variable, and secondly that the energy required for EBM AM is less than that of traditional machining [4].

$$E = \frac{\alpha P}{vht} \qquad \text{Eq. 1}$$

During an EBM build, the chamber is sealed off, a turbo vacuum pump is turned on, and the chamber preheats to a specified value around 700°C prior to the build cycle initiating. Supports are required in the design to offset the beginning of the build to physically distance the actual part from the build plate. This precludes conduction from occurring which will very likely execute a build failure due to warping. A secondary reason for these supports is to facilitate easier removal of parts. After the build is complete, a slow cooldown occurs until around 80°C at which point vacuum pumps are turned off and the part can be extracted. Depending on the amount of material to be sintered, the time between which vacuum pumps are turned on and off can range from 10-15 hours [42].

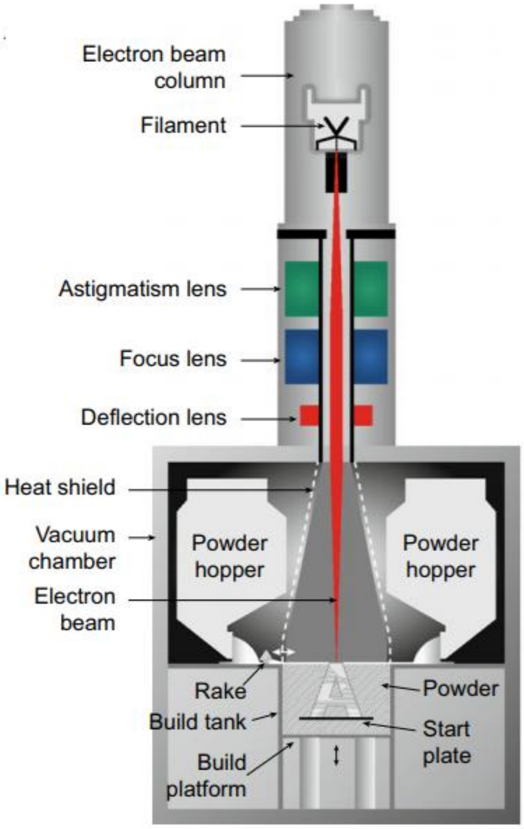

Figure 1: Schematic drawing of an ARCAM EBM machine [20]

Energy deposition into air impurities contained in the environment results in less than ideal energy deposition into the powder bed. Therefore, a vacuum sealed chamber should reduce air impurities to a negligible level [9]. Most EBM builds are conducted in a vacuum of 10^{-4} bar or greater to reduce energy deposition to these impurities [19]. Additionally, high ambient temperature and slow cooling rate of powder bed serve to reduce residual stresses [9]. During the EBM process heat is conducted from the metal through the unmelted powders to the environment to dissipate heat slowly [19]. Finally, a theoretical phenomenon called raking exists in EBM machines where an electron beam while melting, pushes other unmelted powder in the direction it moves. This has the potential to cause incomplete melting and the formation of voids which ultimately contribute to a decrease in fatigue strength. Most machines have strict procedures for ensuring variables such as hatching, powder cleanliniess requirements, and rake inspections are followed [9].

2.3 Material Defects and Variability

EBM PBF Ti-6Al-4V typically contains microstructures generally characterized as acicular alpha in prior beta grains, very fine lamellar, alpha laths in prior beta, or prior beta grains that grow across build layers [19]. The inhomogeneity of the microstructure due to the build direction can lead to the location and orientation dependence of mechanical performance of the part. Post process heat treatment can reduce residual stresses at the expense of largening the lamellar alpha structure, ultimately lowering strength slightly and allowing for ductility to be relied upon prior to yielding. In the EBM process, however, post-processing heat treatment normally is not necessarily required based on elevated build chamber temperature and build duration [7]. Several studies have already been conducted on the performance of AM Ti-6Al-4V materials. In general, regardless of the observations pointed out in these future subsections, previous research indicates material performance of EBM PBF underperforming in comparison to traditional casting processes of Ti-6Al-4V. Lewandowski et. al studied the material performance of EBM Ti-6Al-4V materials and showed that the performance of wrought material was better than EBM built components. Table 2 lists differing models which AM 3D parts by EBM. As a preview to a followon research discussed later, this research also shows the mechanical properties of EBM built at differing angles [10].

Table 2: Summary of mechanical properties of AM Ti-6Al-4V [10]

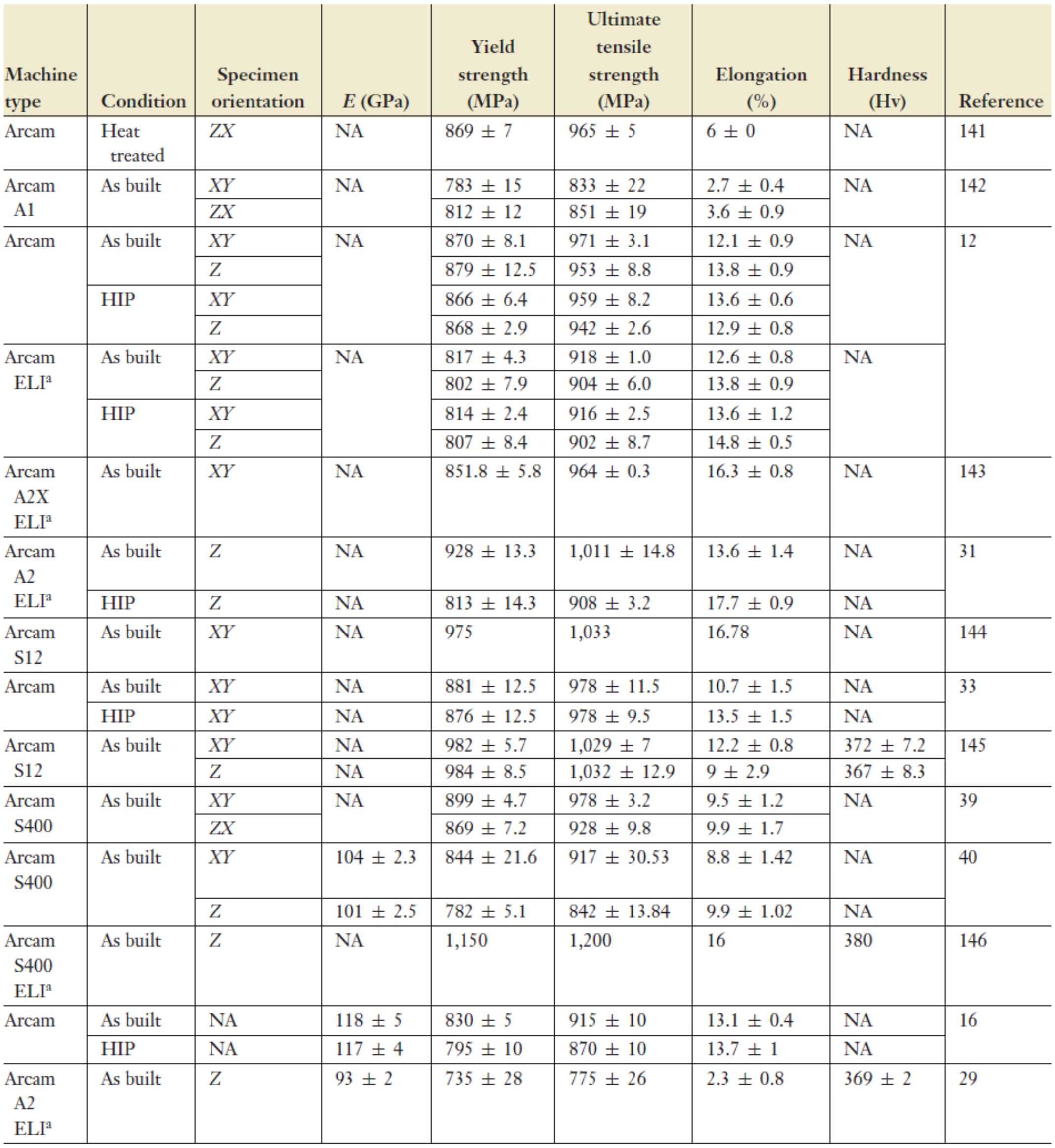

Machine type	Condition	Specimen orientation	*E* (GPa)	Yield strength (MPa)	Ultimate tensile strength (MPa)	Elongation (%)	Hardness (Hv)	Reference
Arcam	Heat treated	*ZX*	NA	869 ± 7	965 ± 5	6 ± 0	NA	141
Arcam A1	As built	*XY*	NA	783 ± 15	833 ± 22	2.7 ± 0.4	NA	142
		ZX		812 ± 12	851 ± 19	3.6 ± 0.9		
Arcam	As built	*XY*	NA	870 ± 8.1	971 ± 3.1	12.1 ± 0.9	NA	12
		Z		879 ± 12.5	953 ± 8.8	13.8 ± 0.9		
	HIP	*XY*		866 ± 6.4	959 ± 8.2	13.6 ± 0.6		
		Z		868 ± 2.9	942 ± 2.6	12.9 ± 0.8		
Arcam ELI^{a}	As built	*XY*	NA	817 ± 4.3	918 ± 1.0	12.6 ± 0.8	NA	
		Z		802 ± 7.9	904 ± 6.0	13.8 ± 0.9		
	HIP	*XY*		814 ± 2.4	916 ± 2.5	13.6 ± 1.2		
		Z		807 ± 8.4	902 ± 8.7	14.8 ± 0.5		
Arcam A2X ELI^{a}	As built	*XY*	NA	851.8 ± 5.8	964 ± 0.3	16.3 ± 0.8	NA	143
Arcam A2 ELI^{a}	As built	*Z*	NA	928 ± 13.3	1,011 ± 14.8	13.6 ± 1.4	NA	31
	HIP	*Z*	NA	813 ± 14.3	908 ± 3.2	17.7 ± 0.9	NA	
Arcam S12	As built	*XY*	NA	975	1,033	16.78	NA	144
Arcam	As built	*XY*	NA	881 ± 12.5	978 ± 11.5	10.7 ± 1.5	NA	33
	HIP	*XY*	NA	876 ± 12.5	978 ± 9.5	13.5 ± 1.5	NA	
Arcam S12	As built	*XY*	NA	982 ± 5.7	1,029 ± 7	12.2 ± 0.8	372 ± 7.2	145
		Z	NA	984 ± 8.5	1,032 ± 12.9	9 ± 2.9	367 ± 8.3	
Arcam S400	As built	*XY*	NA	899 ± 4.7	978 ± 3.2	9.5 ± 1.2	NA	39
		ZX		869 ± 7.2	928 ± 9.8	9.9 ± 1.7		
Arcam S400	As built	*XY*	104 ± 2.3	844 ± 21.6	917 ± 30.53	8.8 ± 1.42	NA	40
		Z	101 ± 2.5	782 ± 5.1	842 ± 13.84	9.9 ± 1.02	NA	
Arcam S400 ELI^{a}	As built	*Z*	NA	1,150	1,200	16	380	146
Arcam	As built	NA	118 ± 5	830 ± 5	915 ± 10	13.1 ± 0.4	NA	16
	HIP	NA	117 ± 4	795 ± 10	870 ± 10	13.7 ± 1	NA	
Arcam A2 ELI^{a}	As built	*Z*	93 ± 2	735 ± 28	775 ± 26	2.3 ± 0.8	369 ± 2	29

2.3.1 Porosity

Impurities trapped in an EBM build environment can cause increased porosity which can affect mechanical properties. Porosity in EBM prevails from either gas pores or lack-of-fusion pores as depicted in Figure 2. Gas pores take either a spherical or elliptic shape and have random distribution with average diameter ranging from 1-100 micrometers. During the melting process, gas trapped in the molten pool that does not escape create gas pores. Slowing down scanning speed while simultaneously increasing beam power has a very minor but non-negligible effect of eliminating gas pores. Lack-of-fusion pores feature irregular-wedge or band shapes with sharp tips at both ends. Typical locations for these pores are near the boundaries of two adjacent layers. Lack-of-fusion pores mainly form due to a deviation from optimal melting conditions. Specifically, when energy is reduced on an excessive layer of powders, insufficient melting creates weak bonds between the two formed layers. Lack-of-fusion pores can fatally affect the performance of a final product under loading conditions. Lack-of-fusion pores can be avoidable by increasing the input energy density and optimized machine parameters [19].

Specifically, Biswas et. al. and Li et. al. showed that pores act as nucleation sites for adiabatic shear bands which have a high tendency to create microcracks [38, 39]. Ackelid and Svensson characterized as-built EBM materials via X-ray tomography to a porosity of approximately 0.17% with pore sizes ranging from 50 micrometers to 300 micrometers [19].

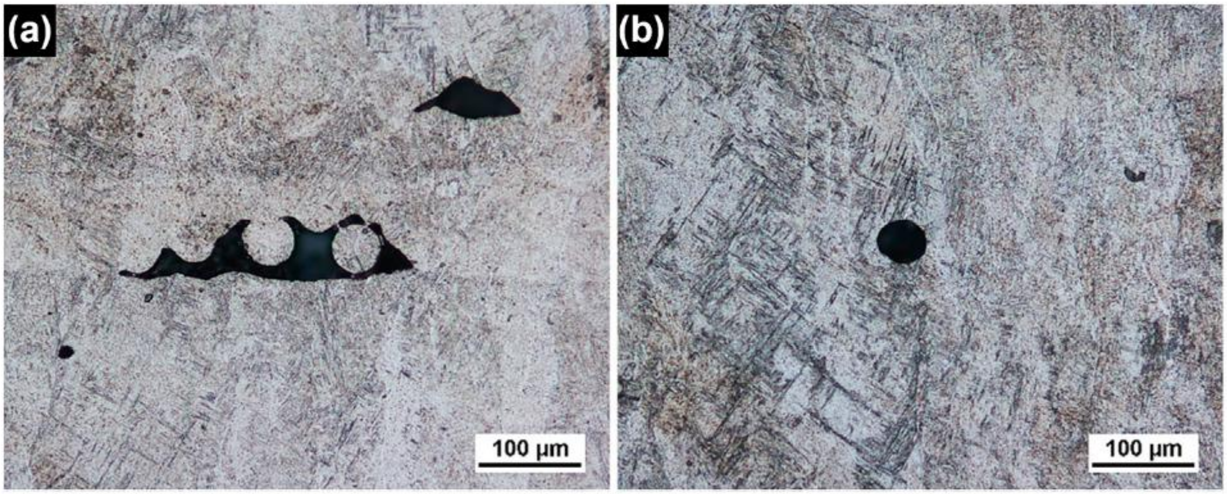

Figure 2: Porosity in EBM of Ti-6Al-4V: (a) lack-of-fusion pore and (b) gas pore [19]

2.3.2 Surface Finish

Bannantine et. al. assessed steel to have a certain surface factor which could be utilized in calculations to determine a high confidence fatigue limit. This surface factor is driven mainly from an assessment of the root mean square or the arithmetic average via ASTM D7127-17 which can characterize a materials susceptibility to crack formation. [22]. Fundamentally, most crack initiations originate from rough surface features [10]. This concept holds true for all materials. Vayssette et. al conducted a fatigue experiment utilizing EBM and SLM as-built and hot isostatically processed (HIP) components. As expected, the EBM samples with larger surface roughness demonstrated a lower fatigue strength compared to those which had post-processing. Fractography results indicated that crack initiation sites were located on the surface. For comparison, Figure 3 shows that regardless of post-processing techniques, crack initiation occurs at the surface [23].

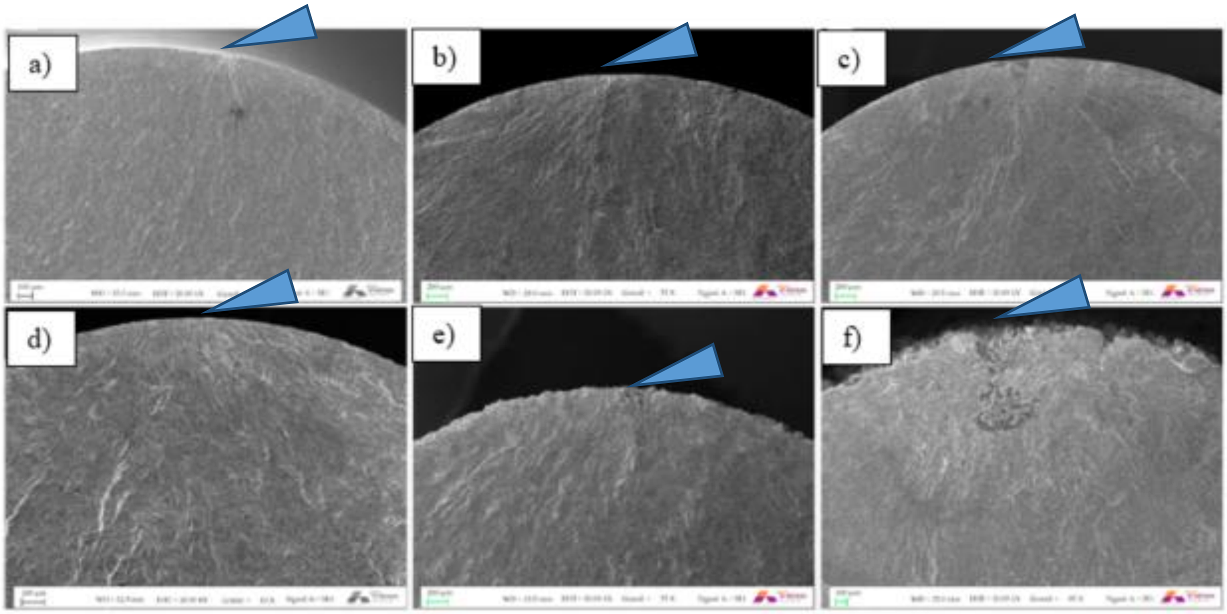

Figure 3: Typical initiation site for a) hot rolled, b) EBM HIP machined with no defect c) EBM machined with remaining defect d) SLM HIP machined e) SLM as-built f) EBM as-built [23]

An alternative method to reduce the surface roughness of titanium alloys not discussed yet is a process called rotary ultrasonic machining (RUM). In this process, an ultrasonic wave of a high frequency and low amplitude induces brittle work and only removes from the contact surface metal particles which are swept away in a slurry. Ahmed et. al. demonstrated that on EBM made materials of Ti-6Al-4V, a surface roughness of less than 0.1 microns could be achieved with RUM [21].

2.3.3 Build Orientation

With the emergence of EBM technology, industry can take advantage of building uniquely designed shapes which otherwise would be difficult to manufacture from wrought material. One such example of this is structures resembling lattices. Some applications explicitly desire lattice structures for their material efficiency, however a reduction of material will incur an increase in stress loading for particular branches of the lattice [12]. T. Persenot et. al. studied an EBM made titanium lattice structure shown in Figure 4 [8].

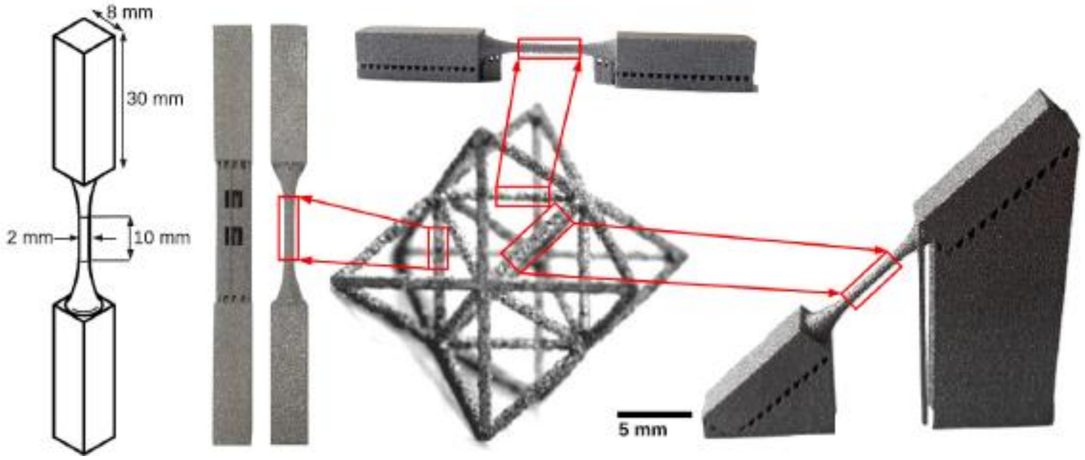

Figure 4: 3D isometric view of titanium lattice structure with orientation depiction of fatigue specimens for 90 degrees (vertical orientation), 0 degrees (horizontal orientation), and 45 degrees [8]

Persenot studied uniaxial fatigue test specimens created by an ARCAM A1 EBM machine to determine the effect of build orientation on fatigue lifetime for various stress levels. Results from this uniaxial fatigue test experiment resulted in a determination that highest to lowest fatigue resistant orientations in order were 0 degrees, 45 degrees, and 90 degrees. A visual representation of the path crack propagation will take with respect to the build layer is illustrated in Figure 5. In all cases, crack initiation were all assessed at locations defined with notch like defects, as summarized in Figure 6 [8].

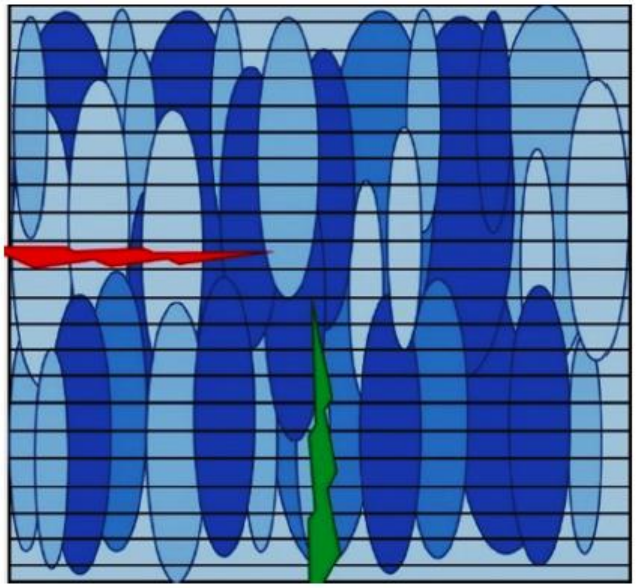

Figure 5: Example schematic of crack propagation in horizontally built (green) and vertically built (red) specimens [6]

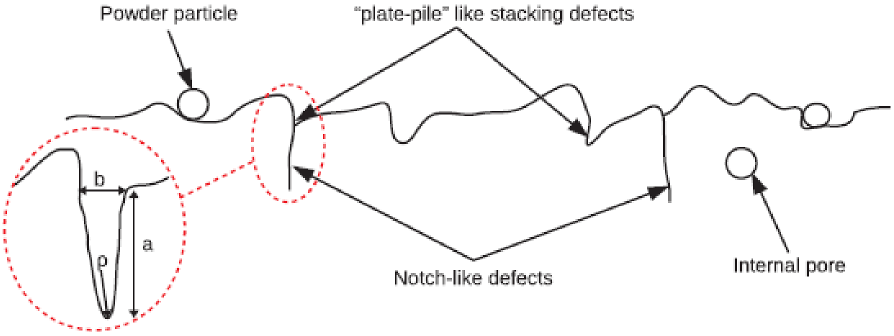

Figure 6: Illustration of common defects found in EBM built samples [8]

Furthermore, Debroy et. al. reported that fracture surfaces of vertically generated specimens showed a significant increase in lack-of-fusion pores attributed to metallization falling onto the powder bed resulting in unmelted powder underneath each layer. Secondly, microstructure characterization of columnar beta grains laid parallel to the build direction would cause dislocation pinning in specimens built in the horizontal direction, a phenomenon which would be largely absent in vertically built specimens [40].

2.3.4 Powder Reuse

EBM boasts the ability to recycle powder used in previous builds, resulting in cost savings when compared to subtractive manufacturing methods. Ti-6Al-4V stock powder is atomized powder generated by spraying high pressure argon gas into a stream of molten metal which separates into small droplets and cools to solidify into metal powder [32]. Figure 7 shows a high magnification image of Ti-6Al-4V powder, representative of that used in this study. Ghods et. al. discovered that reused powder in over 30 build cycles introduced performance and characteristic deviations including surface deformation, partial melting, partial fusion and fracture, and tightening of the particle size distribution. Ghods also reported via ASTM F2429-14 an increase in the allowable oxygen content above the limit of 0.2% after 11 reuse cycles. Tables 3 and 4 show the percentages by weight of chemical composition for virgin and reused powder. Introduction of oxygen into titanium typically shows embrittlement of the alpha phase which may or may not impact directional dependence from inherent anisotropy [30].

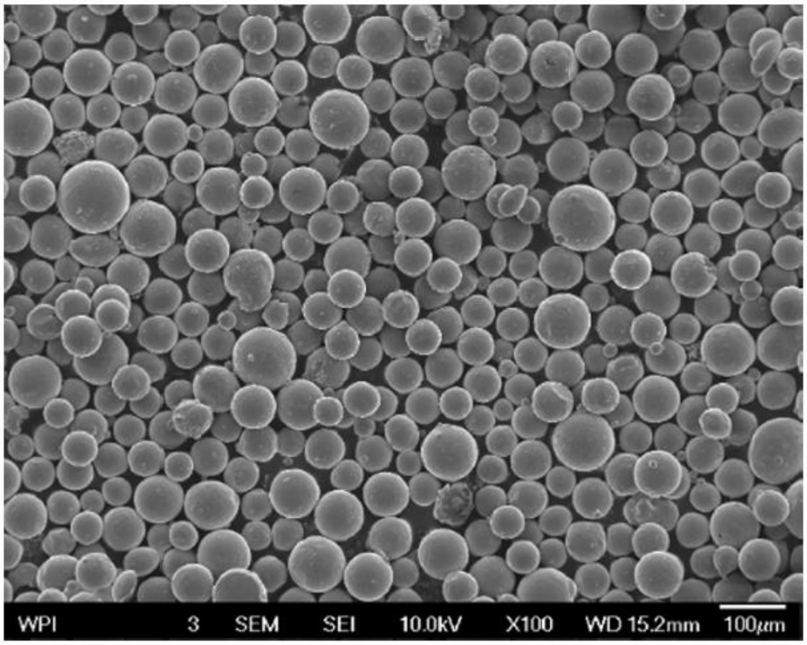

Figure 7: High magnification of example Ti-6Al-4V powder used in this study [6]

Table 3: Composition of EBM powders according to specifications by powder producers [32]

AM Technology	Weight					
	O (wt%)	N (wt%)	H (wt%)	Al (wt%)	V (wt%)	Fe (wt%)
EBM	0.07	0.02	0.001	6.49	4.01	0.18

Table 4: Concentration of key elements of powder during reuse cycles [30]

Build	O (wt%)	N (wt%)	H (wt%)	Al (wt%)	V (wt%)	Fe (wt%)
1 (virgin)	0.142	0.024	0.0014	5.41	3.43	0.21
10	0.189	0.026	0.0010	5.50	3.26	0.25
20	0.269	0.027	0.0012	5.54	3.40	0.26
30	0.356	0.030	0.0009	5.58	3.36	0.29

2.4 Fracture Mechanics

Fracture mechanics is the field of mechanics concerned with the study of the propagation of cracks in materials. In materials science, fracture mechanics is an important tool used to assess the performance by quantifying when structural failure will occur given crack size and shape, loading conditions, and material properties [22].

2.4.1 Fracture Toughness

Linear Elastic Fracture Mechanics (LEFM) is used to relate the amount of stress at a crack tip to three key elements of a tested material: the remote stresses applied, crack size and shape, and the material properties [22]. Three loading modes of fracture are shown in Figure 8. The theory assumes that crack propagation will occur so long as ΔK at the crack tip reaches a critical value [22].

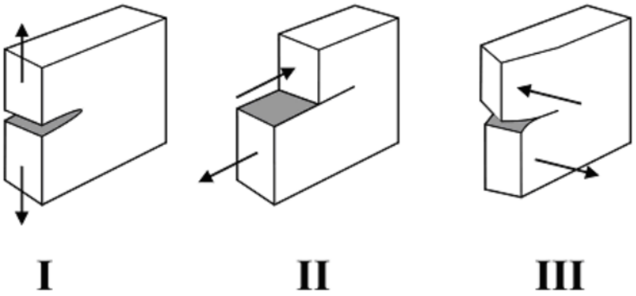

Figure 8: Modes of shear: I (Opening), II (Shearing), III (Tearing) [22]

FT, or K_{IC}, represents a materials ability to withstand failure in the presence of a small crack. FT can be represented by Equation 2 where σ is applied stress, Y is a correction factor for the shape of the defect, a is the crack size, and K_{IC} is reported in units of $MPa\sqrt{m}$ [22].

$$K_{IC} = \sigma Y \sqrt{\pi a} \qquad \text{Eq. 2}$$

2.4.2 Fatigue Crack Growth

FCGR provides a means of characterizing resistance to fatigue failure. FCGR also assists with understanding fatigue life. Typical constant amplitude crack propagation data are shown in Figure 9, as a background to ASTM E647-15 for expected crack size plotted against cycles. To acquire tangible comparison for FCGR propagation rates, the derivative of the crack growth rate (change in crack length divided by the change in cycles, or da/dN) is plotted against calculated ΔK at that crack length; a typical example of the sigmoidal curve is shown in Figure 10 [22].

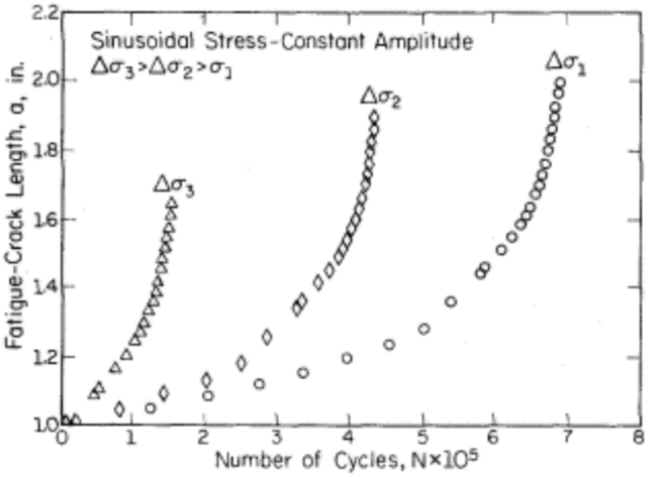

Figure 9: Typical constant amplitude crack size vs. cycles during FCGR testing [22]

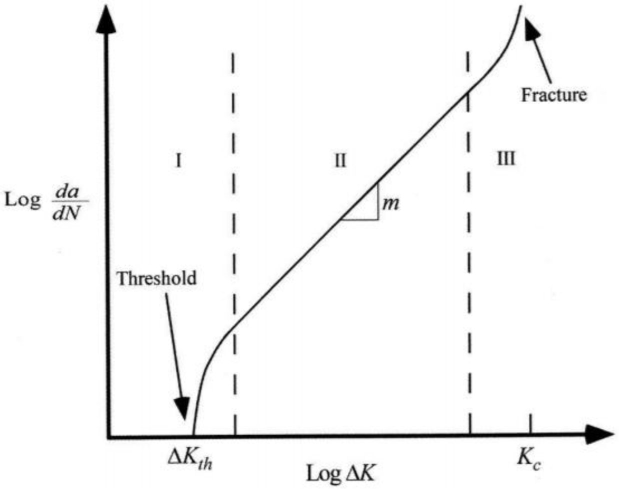

Figure 10: Crack growth behavior through regions 1-3 [22]

Fatigue is characterized by three distinguishable regions. In Region I, lower stress intensities at threshold value are associated with the initiation of sharp cracks from a blunt notch. In this region, fatigue crack growth is relatively indistinguishable or occurs at a rate too slow for measurement. For this reason, understanding of Region I behavior would require testing environment and/or loading conditions which simulate actual service conditions. From a design perspective, loading of a component under threshold intensities is desirable, however, may be impractical based on real world applications. Region II is distinguished by a progressive crack growth at an approximately linear rate for which the Paris' law has been widely accepted after being first proposed in 1963. Constants C and m are derived from material characterization, m is simply the rate at which a maximum regression curve fit is found, and ΔK is the stress intensity range, K_{max}-K_{min}. In Region III, unstable crack growth occurs. In 1967, Forman proposed the point at which Region II transitions to Region III in Equation 4 [22].

$$\frac{da}{dN} = C\Delta K^{m} \text{……………………………………….Eq. 3}$$

$$\frac{da}{dN} = \frac{C\Delta K^{m}}{(1-R)K_{IC}-\Delta K} \text{……………………………………….Eq. 4}$$

While understanding the FCGR of a material, important concepts of testing specifications, environmental effects, and metallurgy must be considered. Altering stress ratios have a significant impact on FCGR. In general, the more positive the stress ratio the higher the crack growth rate. Additionally, crack closure can possibly adversely affect crack growth rates. Crack closure is the phenomenon where the opposing faces of a crack could interfere with themselves by creating a temporary fulcrum and extend the crack even further as ΔK is lowered during a particular cycle. Possible sources of crack closure extend from plastic deformation during crack propagation, corrosion of crack surfaces, presence of fluids in the crack, or roughness at cracked surfaces. In the overall FCGR testing sequence, positive comparison of relative specimens can be made when stress ratios, environmental factors, and metallurgy are consistently sustained [22].

Chapter 3: Materials, Methods, and Procedures

The components in this study were fabricated by the University of Washington’s Mechanical Engineering Laboratory ARCAM EBM A2X system utilizing Ti-6Al-4V powdered alloy. The EBM components made for this research were manufactured utilizing the procedure the manufacturer of ARCAM distributed to ensure consistency. The only post-processing conducted for this experiment was completed using the PRS along with removal of supports to conduct testing. All specimens were measured on a Keyence VR-3000, provided by University of Washington’s MSTL Laboratory. Some specimens were analyzed by utilizing University of Washington’s Scanning Electron Microscope (SEM).

3.1 Materials

Ti-6Al-4V powder was acquired from the machine manufacturer (ARCAM: Batch P1303, Part #430944) for this investigation. A certificate was provided with the powder material that specified its chemistry and was used as a reference in assessing changes resulting from the accumulation of build and reuse cycles. A total of 50 kg of powder was used.

As mentioned in the previous chapter, EBM PBF creates parts with large surface roughness values which contribute to lower static mechanical properties compared to wrought. However, since the build chamber temperature is elevated during the entirety of the build, significant martensite is present contributing to higher values indicating brittle material. [10, 24]

Table 5 indicates that vertical builds demonstrate slightly better material properties than horizontally built specimens. To explain this, consideration of how the crack is related to the crack tip geometry. If the load axis is parallel to the lamellae long axes, then the crack with cut straight through the structure; this orientation is to be understood as the horizontal orientation. If the load axis is perpendicular to the lamellae, then the crack with grow along the lamellae boundaries; conversely this is to be understood as the vertical direction. Crack propagation in the horizontal orientation progresses along a constant the columnar grain structure control the crack branching where multiple crack tips progress. Crack propagation in vertically oriented specimens travel parallel to grain boundaries and perpendicular to the scan layers. This promotes crack deflection resulting in a more torturous crack path resulting in higher static values than horizontally oriented specimens. Keeping the same line of thinking for cyclic testing, as built EBM threshold ΔK (K_{th}) for the vertical specimen has been observed to be higher than the horizontal specimen. Additionally, Figure 11 shows FCGR testing for virgin powder specimens showing K_{th} values of around 3-4 MPa*$m^{0.5}$ depending on either a horizontal or vertical build orientation [6].

Table 5: Tensile properties of as-built AM Ti-6Al-4V at different orientations

Orientation	UTS (MPa)	0.2% YS (MPa)	% Elongation	Ref
Horizontal	833/850	783/890	2.7	[25]/[32]
Vertical	851/900	812/930	3.6	[25]/[32]

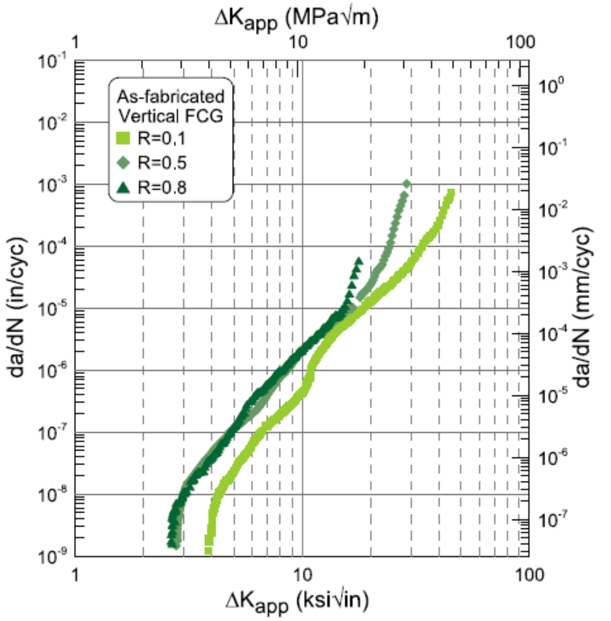

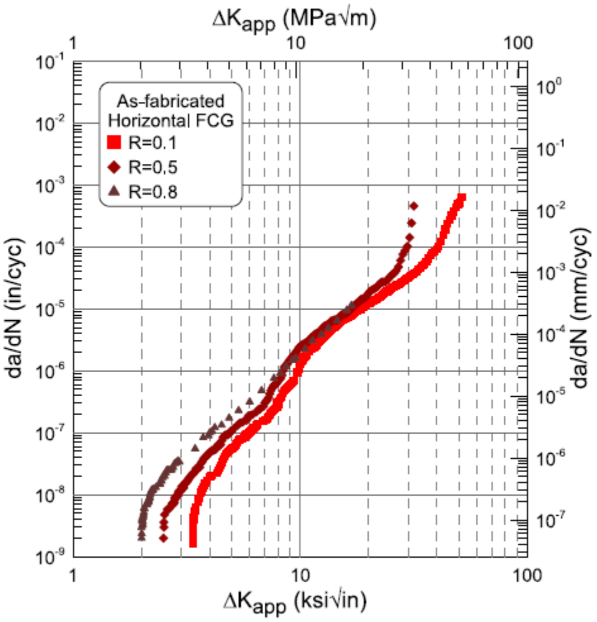

Figure 11: FCGR behavior for as built EBM Ti-6Al-4V at differing stress levels for vertically (left) and horizontally oriented (right) specimens [6]

Although FT testing of AM EBM Ti-6Al-4V remains scarce, Lewandowski reported FT ranges between 65-110 MPa*m$^{0.5}$ for as built EBM Ti-6Al-4V specimens made of virgin powder. Of these specimens, FT values in the vertical direction were reported higher than those built in the horizontal direction by approximately 14% [10].

3.2 Experimental Setup and Procedure

All materials in this research were fabricated using an ARCAM A2X EBM PBF AM machine. The machine has the ability to melt layers to a minimum of 130 micrometers in thickness of titanium powder using an electron beam whose power ranges from 50 to 3000 Watts with a spot size of 0.2-1.0 mm and a beam speed of 8000 m/s inside a chamber at approximately 3x10^{-4} bar at approximately 730 °C [20]. The machine itself features user interface on the left and the build cabinet on the right. Behind the machine are all of its support systems including vacuum pump and electronic cooling units. Observation during the build process can be seen through a shielded window.

Two experiments were conducted for this work and can be reviewed in the following chapters. The first experiment consisted of printing a batch of Compact Tension (C(T)) specimens solely from virgin powder. C(T) specimens were then tested in accordance with ASTM E399-20 in order to quantify FT values in their as built condition. Four separate orientations were built, beginning with what this research will call 0 degrees, or in the XY plane. The next orientation was at 30 degrees; imagine one edge was pinned and the opposite edge was raised to make a 30 degree angle between the XY plane and the specimen. The same concept is also applied to a 60 degree specimen and a 90 degree specimen. It should be noted that these specimens were all built from the same batch of virgin powder. The idea behind this experiment is to confirm past research and quantify the mechanical behavior of anisotropies when considering non-orthogonal directional stresses.

The second experiment consisted of printing another batch of C(T) specimens this time from heavily recycled powder. C(T) specimens were then tested in accordance with ASTM E647-15 in order to quantify FCGR values in their as built condition. Specimen builds in this experiment mirrored the same orientation setup as the first experiment. The thought with this experiment is to quantify values generated by FCGR testing, compare to past-research, and determine the effects of utilizing heavily recycled powder.

3.3 ARCAM Build Process

The first precaution is always safety. Ti-6Al-4V powder handling requirements dictate non-vented goggles, a high efficiency particulate filter respirator, and gloves. As stated before, the first experiment utilized C(T) specimens generated solely from brand new powder. The second experiment used C(T) specimens generated from recycled powder that had been used in 31 previous builds. No chemical analysis was performed on this powder but it likely follows data reported by S. Ghods et. al. [30]. Preparation for the build included generating CAD drawings of specimens and arranging them to fit in the build chamber. Although this specific CAD file was not used, Figure 12 shows a generalized setup of the specimens in the build without supports. Setup of the ARCAM A2X, shown in Figure 13, consisted of calibrating and leveling the build pate, installing the heat shield, cleaning the door and seals and starting the vacuum. After ideal vacuum was reached and preheating was finished, the build was performed. After the build was complete, the cake filler matrix was blasted in the PRS shown in Figure 14 where loose powder was vacuumed. At this point, the supports for all specimens were manually removed and the holes through which clevis pins passed through were bored to specification.

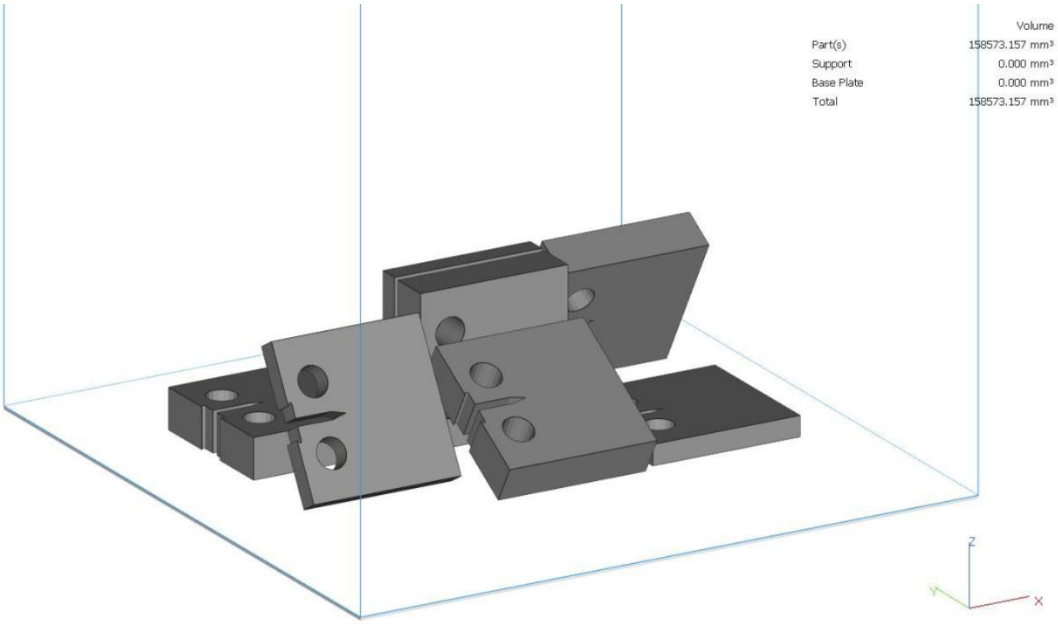

Figure 12: Build layout of respective 0°, 30°, 60°, and 90° specimens

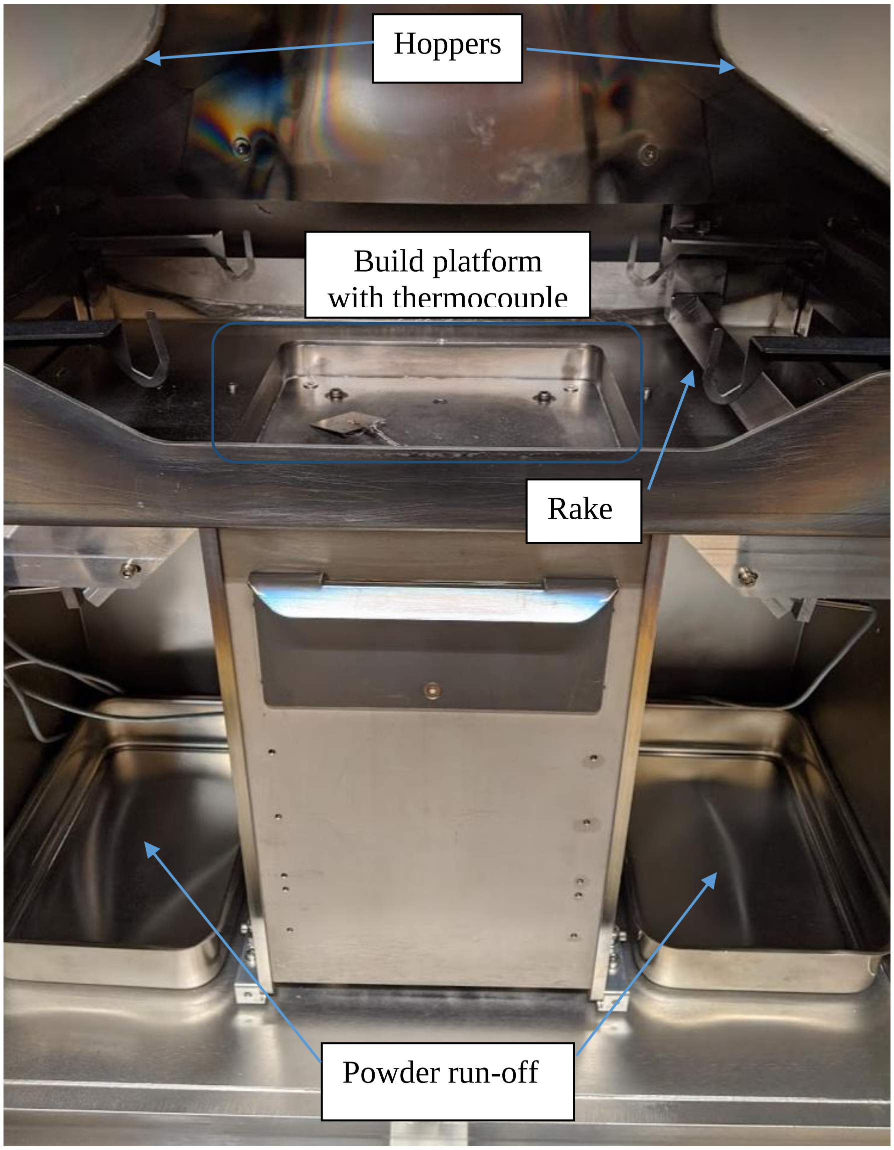

Figure 13: Inside ARCAM build chamber showing hoppers, powder run-off catches, rake, and build platform

Figure 14: PRS chamber in which produced specimens were air blasted

3.4 Testing Fixture

Preparation for testing required manufacturing a set of fixtures that would attach each side of the specimens to the cyclic loading machine. Shown in Figure 15, two sets of fixtures, constructed from AISI 1018 carbon steel, were made for each size specimen Each pair of fixtures were fabricated to accommodate the width for the clip on displacement (COD) gauge. A side view experiment setup is shown in Figure 16.

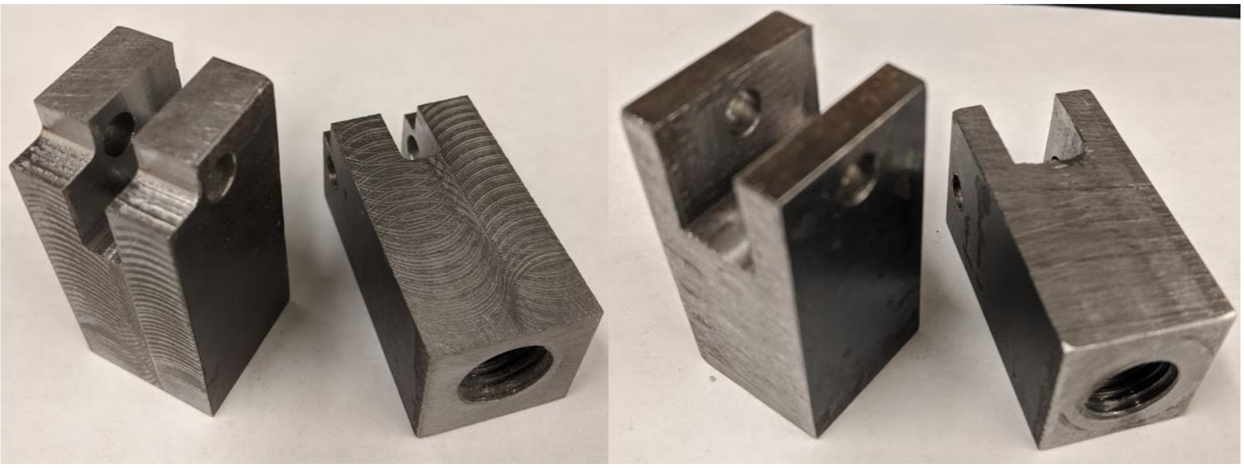

Figure 15: Test fixtures for the 6 mm specimens (left) and the 12 mm specimens (right)

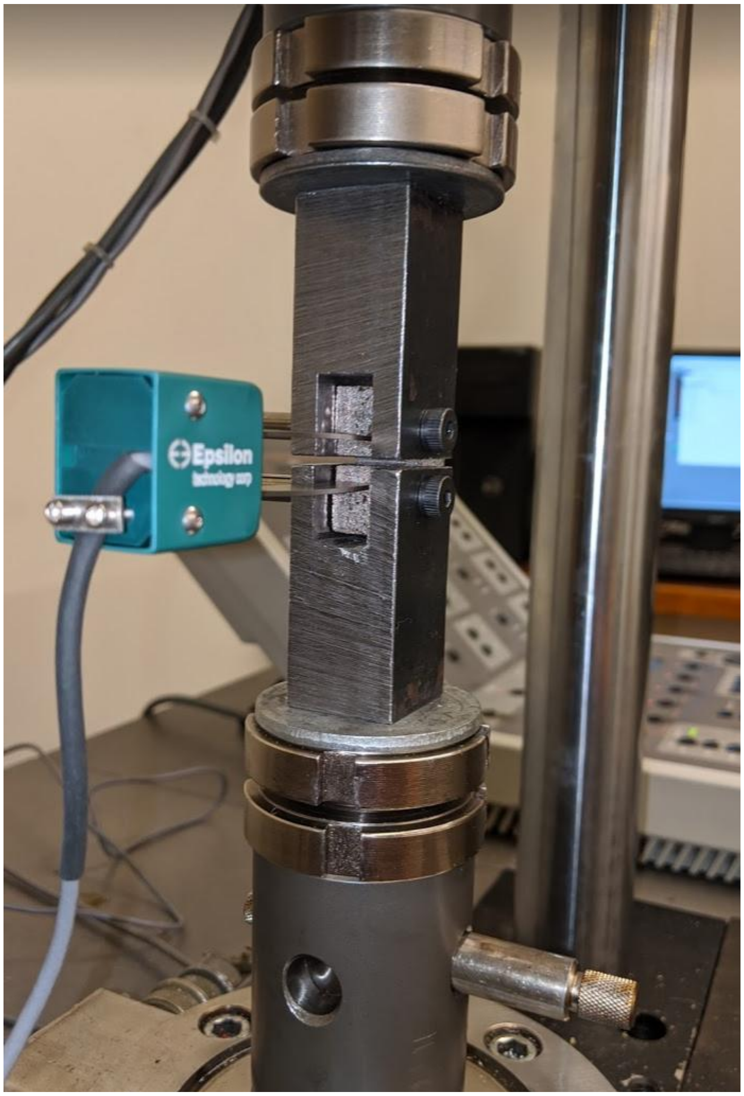

Figure 16: Side view of specimen in test fixture with COD gauge installed

3.5 Mechanical Test System

An Instron 8511 servo hydraulic materials test frame, shown in Figure 17, of 20 kN capacity supplied by the University of Washington's Mechanical Engineering Laboratory was utilized to induce both incremental and cyclic loading which was generated by means of a hydraulic pump and high-speed actuator. Preparation for testing involved twisting the fixtures onto the test frame and locking them in place with collar friction locks tightened by means of a spanner wrench. Then specimens were attached to the testing fixture using clevis pins. It should be noted that during the test, the lower collar is rigidly fixed to the test frame. This machine outputs three channels which for purposes of these experiments are time elapsed, load, and displacement. These data values are imported by a LabView program which allows the user to observe real time data and record for analyzation. Prior to each specimen test, calibration of displacement was conducted at zero load by altering an offset Voltage determined by the user to achieve a zero displacement.

This research conducts two separate types of testing: FT and FCGR. After calibration of the displacement gauge, machine preparation for FT testing starts by setting a waveform of step-ramp by a predetermined value. A position event in excess of 8 mm as seen by the machine was activated to automatically terminate the actuator and stop the testing. 8 mm was chosen such that by that position, the C(T) specimen would have fractured by that time and the machine wouldn't damage itself by travelling to its hard stop. In load control, after having induced a zero load, "Record" in LabView is pushed to record data and the command start button on the test machine is pushed to start the ramping force.

FCGR testing operations were similar in nature to setup for FT testing. However, the waveform selected is sinusoidal instead of ramping. In this step the user also inputs the amplitude and frequency of testing. The same termination event is inserted to protect the machine; FCGR testing takes significant time so this step was important if the user had to leave the machine for some reason. The calibration gauge is calibrated and a “Go To” command is given to load the specimen to its mid-load value. Say, for example, stress ratio is 0.1 and maximum load is 10kN.Waveform amplitude input should be 4.5 kN and current load 5.5 kN. At this point, “Record” in Labview is started along with the waveform until termination of the test. This general machine setup for FCGR testing is congruent with precracking for FT specimens. The only difference is when the user recognizes testing should be terminated “Stop” is pushed on the machine.

Figure 17: Instron 8511 with C(T) specimen setup

Specifications for the displacement gauge are listed in Table 6. Based on the features of the C(T) specimens, this gauge can be left on the specimen through failure. Test certificate of the displacement gauge indicates that independent calibration and verification test was completed in June of 2020. It is assumed that the temperature of the environment in which testing was completed remained constant through the duration of each independent test. Data acquired was converted to crack lengths according to the values and equations directed by ASTM E399-20 and ASTM E647-15 for the location of the displacement gauge shown in Figure 18.

Table 6: Specifications of Model 3541 Epsilon Tech displacement gauge

Excitation	5-10 Volts DC
Output	2-4 mV/V
Linearity	≤0.15% of full scale range
Temperature Range	-40°F-210°F
Operating Force	9-15 N
Maximum Operating Frequency	5-200 Hz

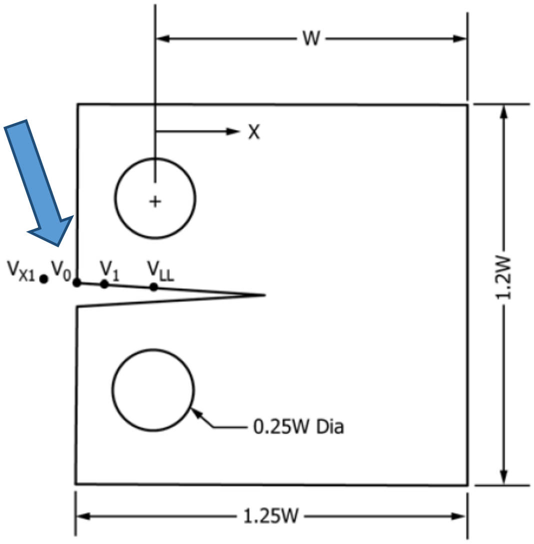

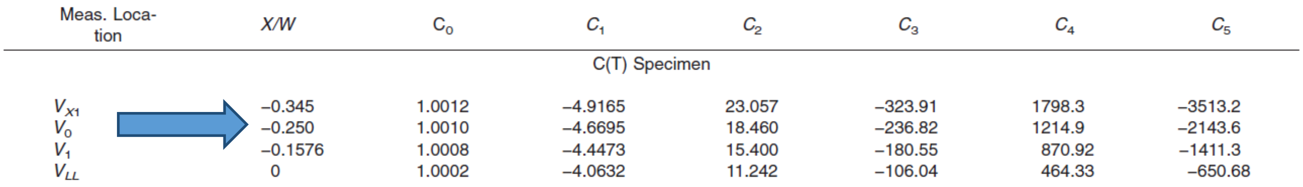

Meas. Location	X/W	C_0	C_1	C_2	C_3	C_4	C_5
			C(T) Specimen				
V_{X1}	−0.345	1.0012	−4.9165	23.057	−323.91	1798.3	−3513.2
V_0	−0.250	1.0010	−4.6695	18.460	−236.82	1214.9	−2143.6
V_1	−0.1576	1.0008	−4.4473	15.400	−180.55	870.92	−1411.3
V_{LL}	0	1.0002	−4.0632	11.242	−106.04	464.33	−650.68

Figure 18: Clip gauge locations and associated coefficients for calculating crack length

3.6 Optical/SEM Inspection

Both experiments in this research were evaluated by using non-contact profilometry (Keyence VR-3100) to determine surface roughness and topological profiles. The machine uses a high-intensity LED and a 4 megapixel monochrome CMOS to obtain a projection image of up to 160x magnification. Through software the data acquired can give high resolution analysis. However higher magnifications are desired to observe microstructures and perform fractographic evaluation. SEM images were acquired with a Phillips Model XL which features 20-800,000x magnification by imparting electrons to generate a high resolution image.

Chapter 4 Fracture Toughness Testing

The goal of this research was to characterize the FT for AM EBM Ti-6Al-4V made from powder that had never been used before. The purpose of this experiment was to gain a broader understanding of the relative strength between differing build orientations and the relative material properties between virgin powder and heavily recycled powder. The goal of this testing is to further understand the anisotropic behavior which aids in fabricating fail safe designs.

4.1 Specimen Build and Design

A total of 12 FT specimens were fabricated from virgin Ti-6Al-4V powder. Of these 12 generated specimens, three were built at each angle with their notched pointed in the same direction to provide triplicate testing.

The C(T) specimens were not subjected to any post-processing methods. Supports were inserted using ARCAM A2X's Magics software in the design phase in order to ensure the specimens do not warp. After completion of the build process, the chamber was cooled down and depressurized and the specimens were inserted into a PRS where pressurized air was used to remove any excess titanium powder which may have been stuck to the sides. After cleanup, supports were removed to obtain specimens. It should be noted that 90 degree specimens have supports generated inside the holes through which clevis pins will be inserted. To ensure compliance, all loading holes were bored to specifications outlined in ASTM E399-20.

4.2 Specimen Shape and Dimensions

C(T) specimens were built in accordance with ASTM E399-20 shown in Figure 19. To minimize material wastage, a minimum dimension specimen was chosen for W = 25 mm. All specimens for this experiment were built at a B=6 mm as shown in Figure 20 to satisfy thickness tolerances. One authorized modification to the specimens which were generated was the introduction of knife edges at the edge-to-support attachment of a Fracture Mechanics Clip-On Displacement (COD) Gauge Model 3541 which directly measured displacement and output to connected data acquisition boards and chart recorders.

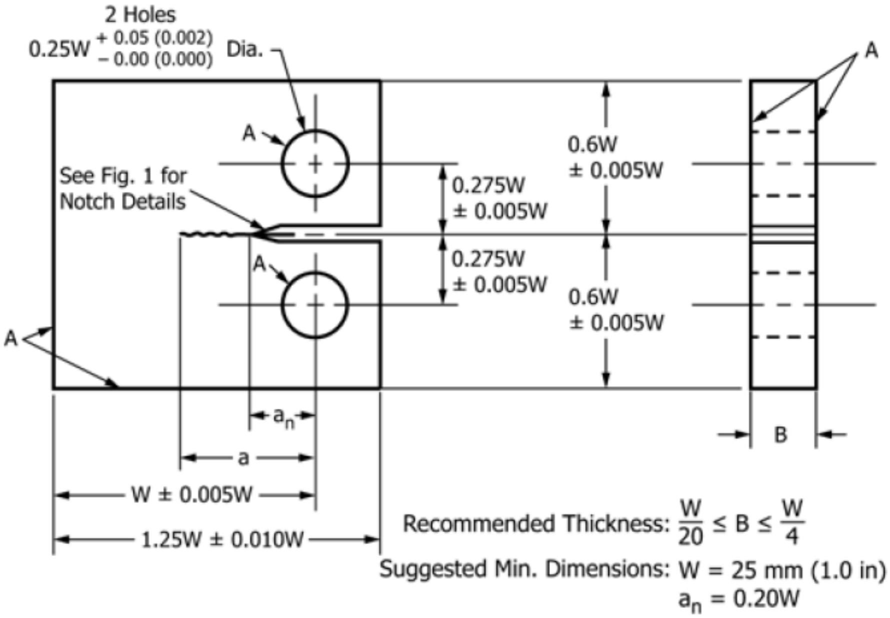

Figure 19: Standard Compact C(T) Specimen for FCGR and FT Testing [31, 33]

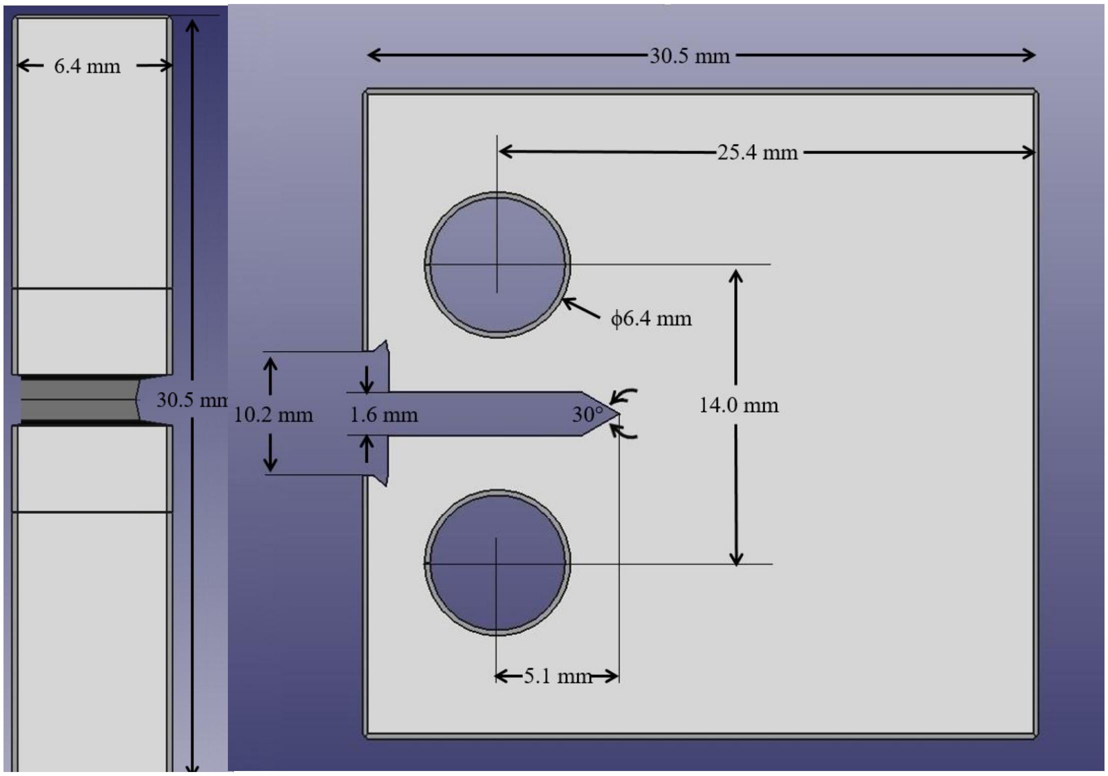

Figure 20: ASTM E647-15 Annex A1 and ASTM E399-20 Annex A4 compliant CAD drawing [31, 33]

4.3 Fracture Toughness Testing

FT testing was completed using the procedure outlined in ASTM E399-20 for the C(T) specimens fabricated during this experiment. The procedure requires two steps: first precracking was completed to a pre-determined value, then the specimens were loaded at a constantly increasing stress rate until failure. Two indications were marked on both sides of the specimens to indicate 1 mm and 1.3 mm from the start of the premade notch. This was done with a sharpie which has a 0.3mm felt tip such that careful placement of the line satisfied the two required precracking indications. Precracking at a maximum load of 5.6 kN was conducted at a stress ratio of R=0.1 at a frequency of 10 Hz in a sinusoidal waveform until the first crack on either side reached the first marking. Then precracking continued at the same stress ratio and frequency at a maximum load of 3.55 kN until the crack on both sides visibly reached the second marking at 1.3 mm. Stress values chosen during precracking are related to 80% and 60% of the conditional FT value. Based on the frequency of the machine, a camera was setup with a different frequency setting to allow the operator to better visualize the position of the precrack extension. After precracking was completed, the specimen was loaded and the displacement gauge was installed and calibrated. Starting at zero load, load was incrementally applied at a rate of 0.15 kN/sec until fracture while load-displacement data were recorded [31].

4.4 Fracture Toughness Calculations

Data recordings of the machine were outputted in time, displacement, and load. Based on research, calculations are expected to process Type I fracture behavior shown in Figure 21. After a discretionary value of P_u is determined by the user to represent the maximum amount of experienced linearity, a MATLAB code calculates a 95% slope value secant line is drawn until intersection of the rest of the data in the non-linear region where P_Q is determined, which represents the force which will be associated with K_{IC}. As long as crack length, a, and specimen width, W satisfy the relation in Equation 5, the calculation for ΔK is considered to be within 0.5%. As directed by ASTM E399-20, two validity tests are to be performed to validate final ΔK to be FT. The first test determines the validity of LEFM in Equation 6 is where P_{max} is the maximum force recorded and P_Q is the discretionary force for Type I fracture behavior. If the conditional statement is false, then K_{IC} generated is not valid and the user is directed to ASTM E1820-20a as J_{IC} is to be used to determine FT. The second test again determines if a valid K_{IC} was generated by comparing values determined by Equation 7, where σ_{YS} is yield strength. Should either or both of the validity tests fail to meet their requirements, a larger specimen will be needed to determine K_{IC}. Calculation of crack size using crack mouth opening, v, specimen thickness, B, force P, and modulus of elasticity, E, are fed from Equation 8 into Equation 9. ΔK is calculated using Equations 10 and 11 [31].

$0.2 \leq a/W \leq 0.8$……………………………………Eq. 5

${P_{max}}/{P_Q} < 1.1$…………………..…………………Eq. 6

$2.5 * ({K_{IC}}/{\sigma_{YS}})^2 < W - a$……………………..……….Eq. 7

$u_x = \left(\left[\frac{EvB}{P}\right]^{.5} + 1\right)^{-1}$…………………………………Eq. 8

$\frac{a}{W} = 1.001 - 4.6695 * u_x + 18.46 * u_x^2 - 236.82 * u_x^3 + 1214.9 * u_x^4 - 2143.6 * u_x^5$….Eq. 9

$\alpha = \frac{a}{W}$…………………………………...…….Eq. 10

$\Delta K = \frac{P}{B\sqrt{W}} \frac{(2+\alpha)}{(1-\alpha)^{3/2}} (0.886 + 4.64\alpha - 13.32\alpha^2 + 14.72\alpha^3 - 5.6\alpha^4)$… ..…..Eq. 11

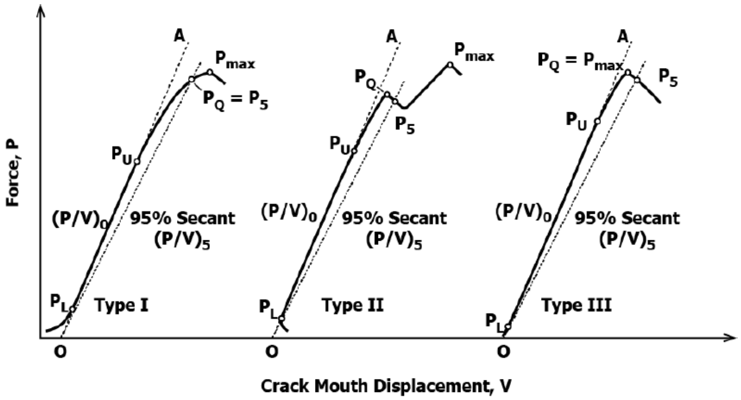

Figure 21: Principal types of force-displacement records [31]

4.5 Fracture Toughness Results

Table 7 shows data obtained from this experiment which can be compared to data in Table 8, which is listed for comparative purposes. FT values acquired during this experiment clearly show their slight competitive edge only with annealed titanium. Data collected from specimens oriented at 90 degrees failed to meet criteria for the first test described, thus invalidating the K_{IC}. Average FT values for each angle are comparatively close to one another as can be seen in Figure 22, which supports their validity. Vertically oriented specimens showed a 7% increase when compared to horizontally oriented specimens. Although this may not be as high as research, the trend does suggest accuracy of these values. Calculated final crack lengths and final crack extensions were visually examined using a Keyence VR-3000 Profilometer. Figure 23 shows selected load displacement curves which indicate that as orientation angle is increased, the more to Elastic Plastic behavior the specimen becomes. This is evident on the progressive flatness of the shape of the curve. Figure 24 shows a selected specimen from each angle showing where the estimated precrack extension stopped. These values can be compared to final crack length in Table 7 (after converting out W) to a high degree of accuracy. Figure 24 also shows a fair amount of shear lipping especially at higher angles. As can be seen in Figure 25, a 3D representation of select specimens from all angles illustrates the progressive amount of shear lipping that is induced when the build orientation angle is increased. Lastly, surface roughness values were obtained of the fracture surface only to be able to compare to the fracture surfaces in the next experiment. Figure 26 shows an increasingly large amount of surface roughness as build orientation is increased, but is relatively precise at 0 degrees. Overall, however, fracture area surface roughness is very high.

Table 7: FT testing results

Specimen	Orientation	a_0/W	Final Crack Length (mm)	a_f/W	FT MPa*m^0.5	Average FT MPa*m^0.5
1	0	0.2979	8.24	0.3433	64.2254	62.7214
2	0	0.2958	9.34	0.3890	62.1903	
3	0	0.2917	10.06	0.4190	61.7487	
4	30	0.3000	8.14	0.3392	71.5484	72.2261
5	30	0.2979	8.24	0.3433	70.5629	
6	30	0.3000	6.53	0.2721	74.5669	
7	60	0.3979	8.24	0.3567	67.5758	67.5126
8	60	0.3000	8.17	0.3403	66.1202	
9	60	0.2958	7.84	0.3267	68.8418	
10	90	0.3979	8.96	0.3735	67.2988	67.5493
11	90	0.3042	7.08	0.2949	66.5427	
12	90	0.3402	7.26	0.3025	68.8065	

Table 8: FT ranges for cast/wrought Ti-6Al-4V

	FT (MPa*m$^{0.5}$)	Ref
Forged	90-110	[34] [35]
Cast HIP AMS 4962	100-110	[36]
Annealed	65-90	[37]

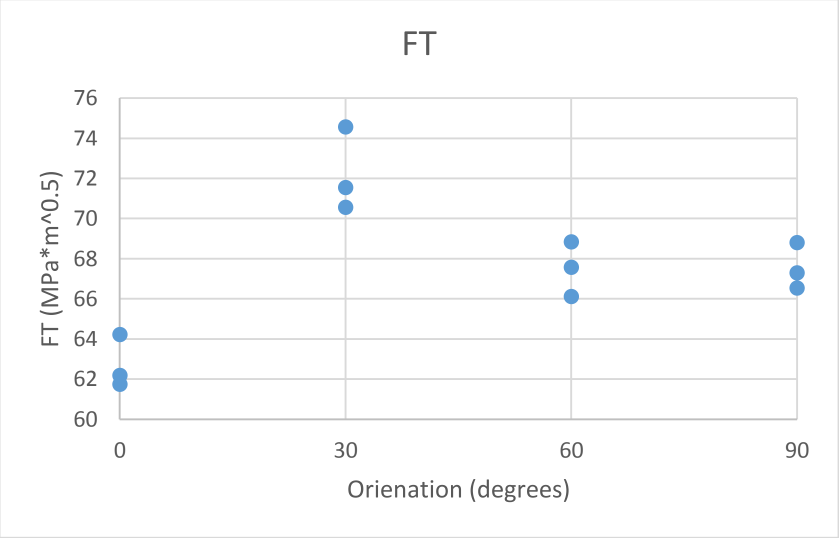

Figure 22: FT results from FT testing

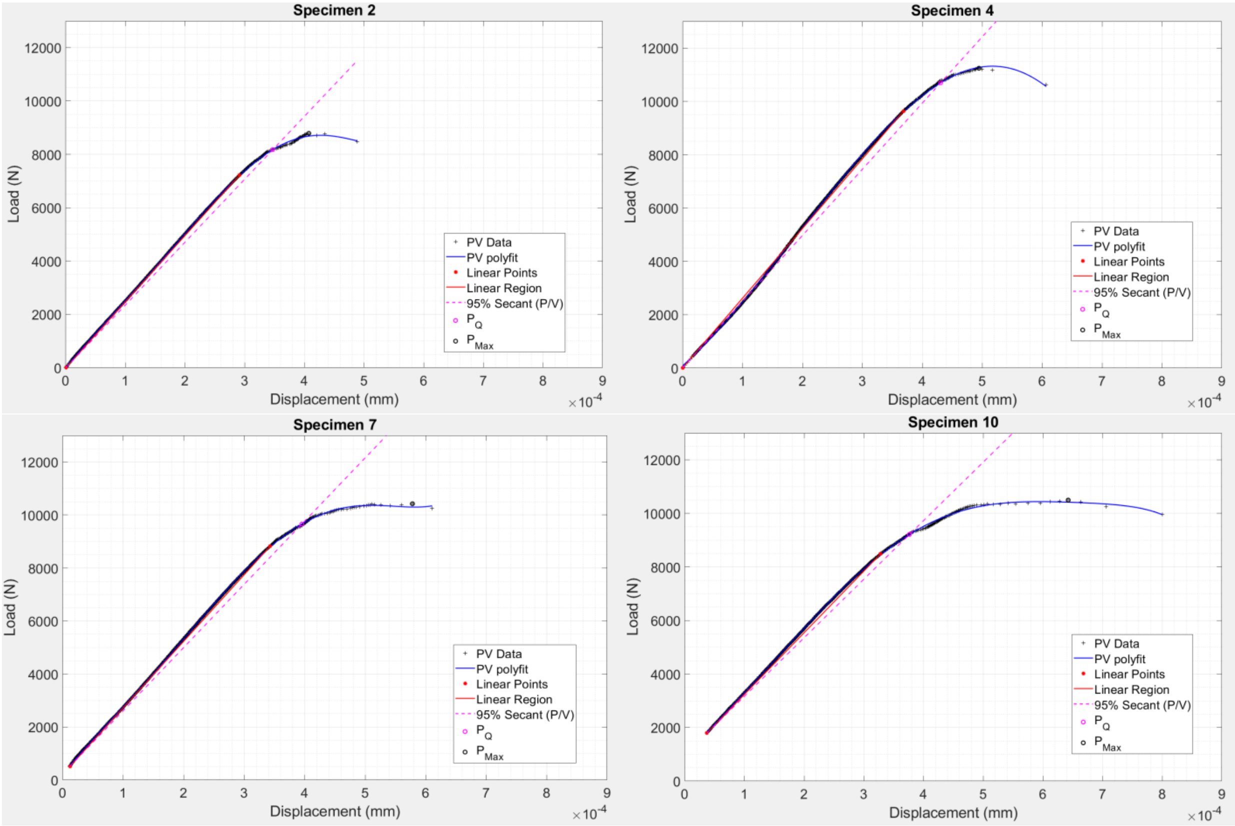

Figure 23: Load-Displacement curves generated from four selected specimens at 0 (top left), 30 (top right), 60 (bottom left), and 90 (bottom right) degrees

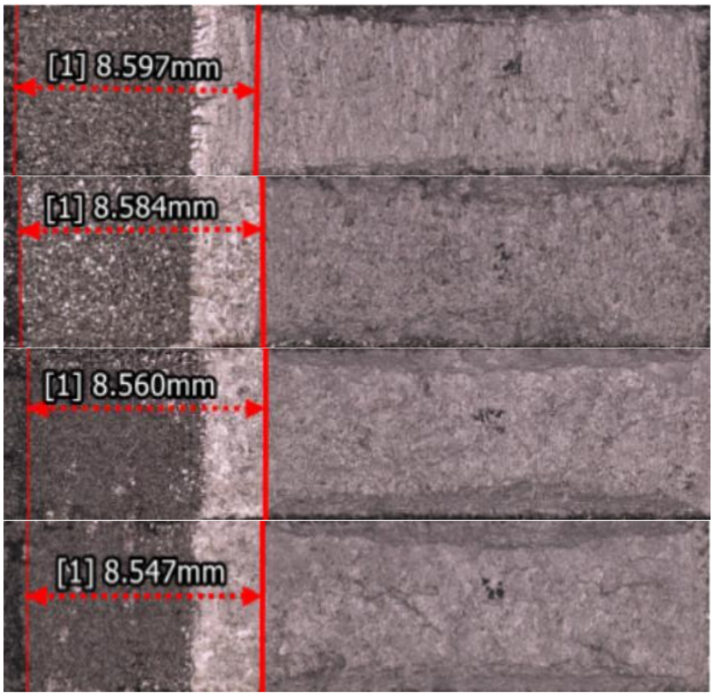

Figure 24: Measured precracking fatigue crack length of four selected specimens at 0, 30, 60, and 90 degrees (top to bottom)

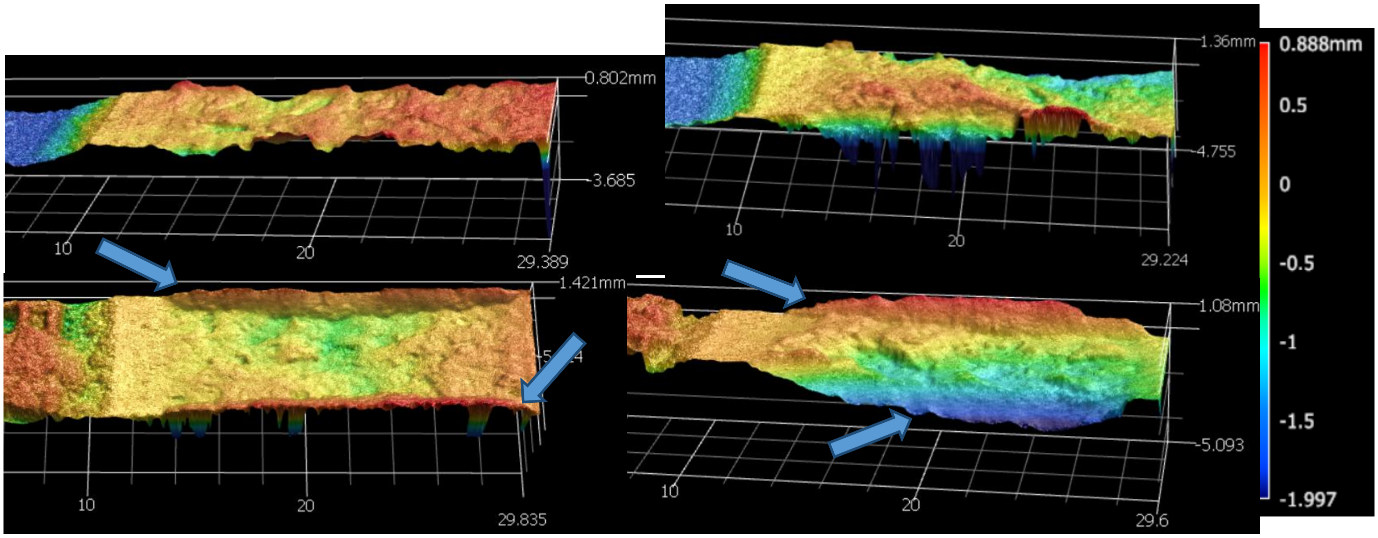

Figure 25: Selected 3D profile renderings of fracture surfaces of 0 (top left), 30 (top right), 60 (bottom left), and 90 (bottom right) degree oriented specimens demonstrating shear lipping at higher orientations

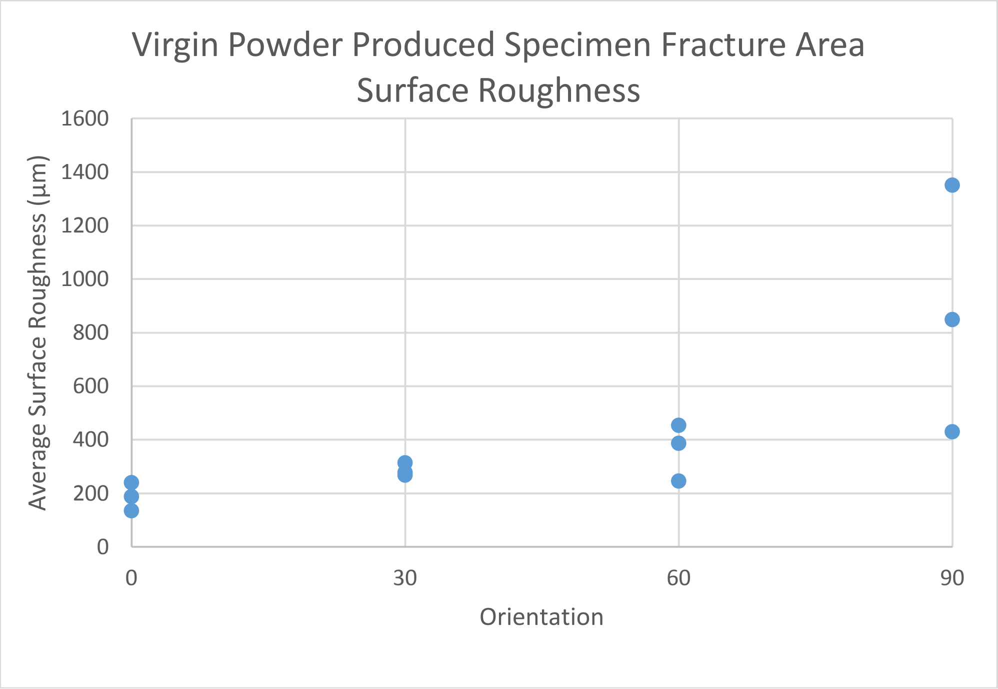

Figure 26: FT surface roughness values by orientation (specimens built by virgin powder)

4.6 Fracture Toughness SEM Images

High resolution SEM were acquired of various surfaces of tested specimens to gain further visual understanding of the fractography. Since selected images were used in data presentation, the reader is directed towards Appendix C for follow-on observation.

Figures 27-30 are images of the fracture surfaces from FT testing (virgin powder) at all tested angles. Of these images the following observations can be made about the microstructure. Micro-void coalescence is evident in the fracture surfaces of all specimens regardless of build direction. Dimpling is scarce throughout all analyzed regions and exhibited grain boundaries which are more peeled out. Additionally, a few of the fracture surfaces exhibited small colonies of fracture flutes which appeared to be no more than 100 μm in length and much smaller in width. Orientation of fluting appeared to be independent of build direction. Finally, clear evidence of gas pores and lack-of-fusion voids measured at approximately 20 μm and 150 μm respectively. Gas pores appeared to exist in all specimens regardless of degree orientation, where lack-of-fusion voids appeared in specimens with higher angles (60° and 90°). Among all specimens a significant amount of shear lipping occurred especially at higher angles.

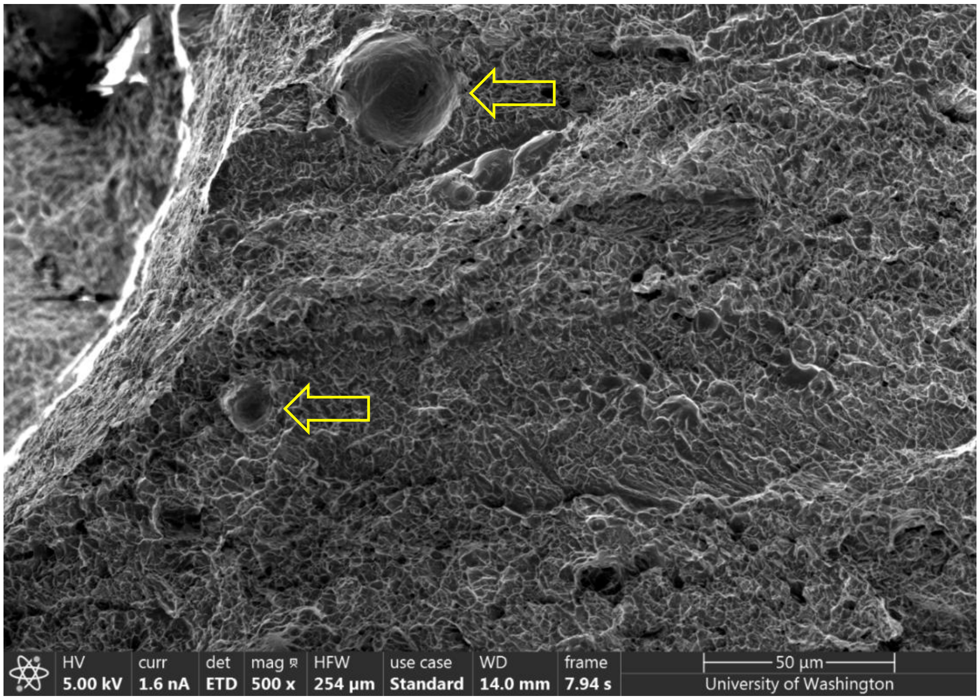

Figure 27: Selected SEM image from virgin powder specimen 2 (0 degrees) showing gas pores

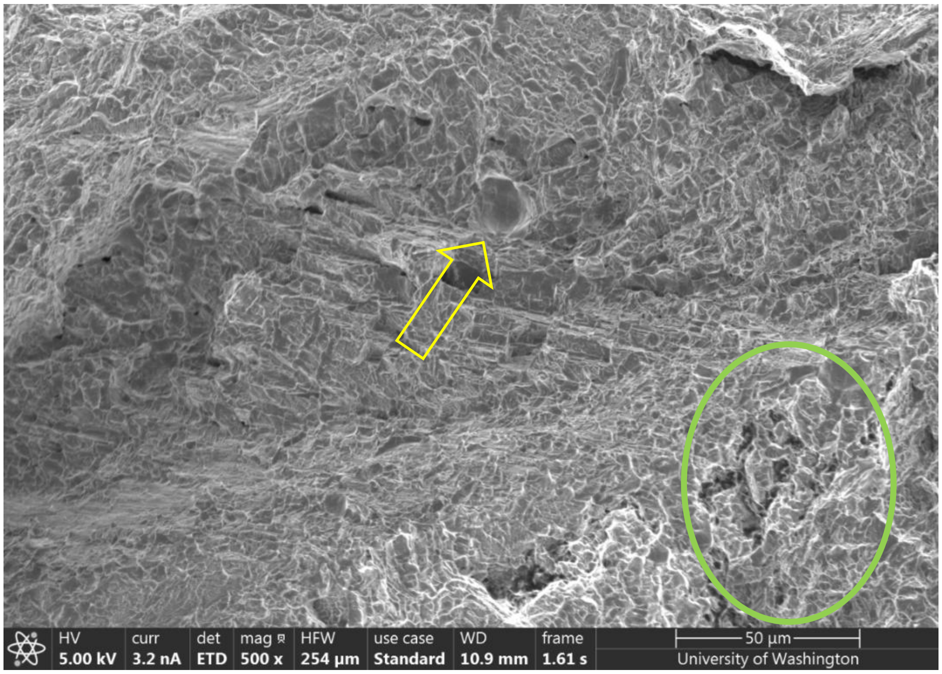

Figure 28: Selected SEM image from virgin powder specimen 5 (30 degrees) identifying a gas pore (yellow) and microvoid coalescence (green)

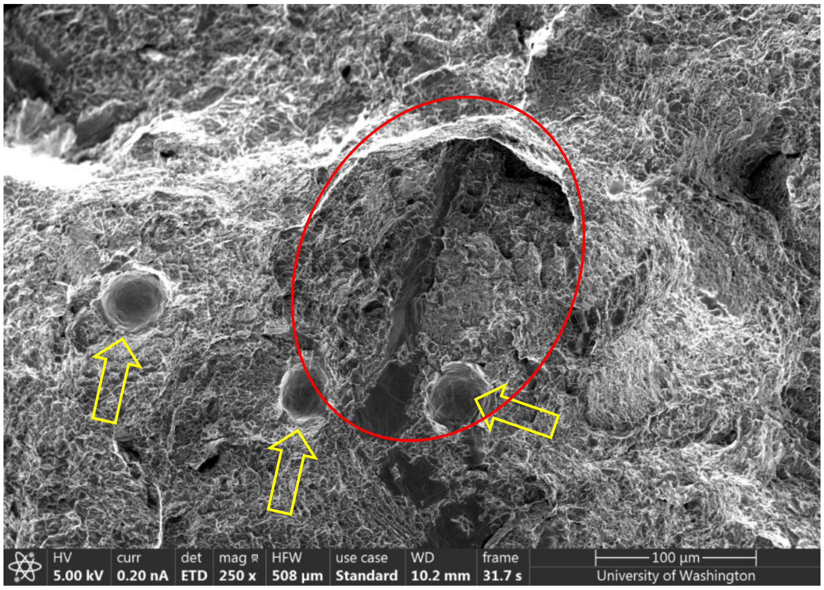

Figure 29: Selected SEM image from virgin powder specimen 7 (60 degrees) showing lack-of-fusion void (red) and gas pores (yellow)

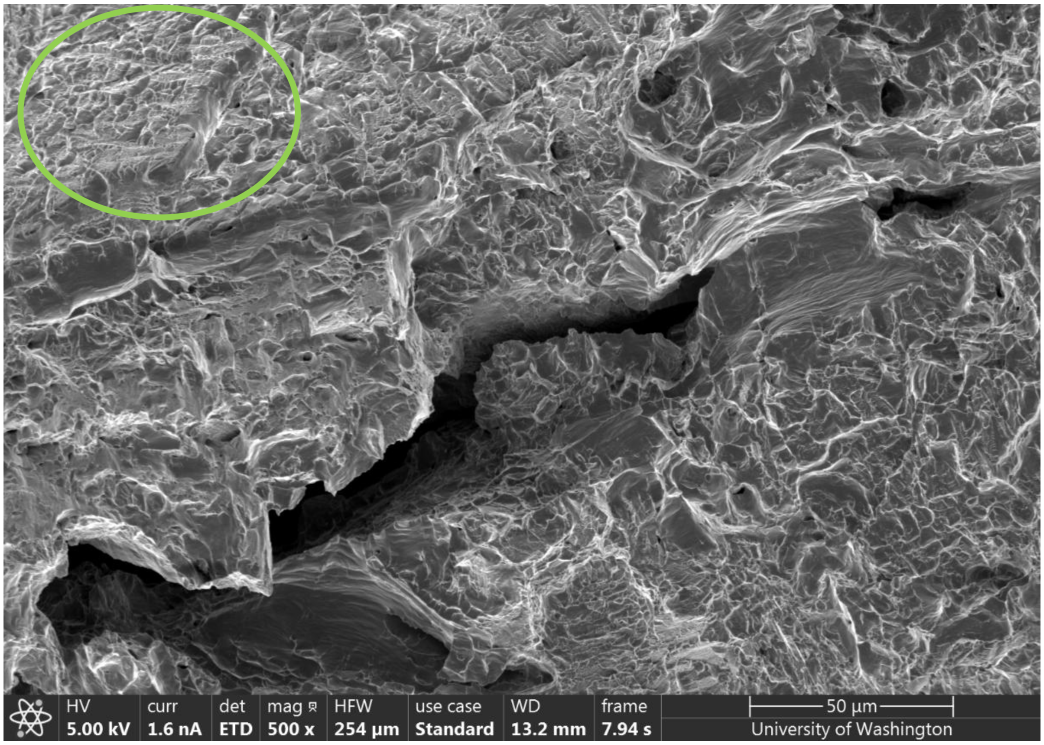

Figure 30: Selected SEM image from virgin powder specimen 10 (90 degrees) identifying microvoid coalescence

4.7 Discussion

This research performed FT testing on virgin powder specimens to aid in fail safe designs. FT testing results indicate that vertically oriented specimens exhibit a higher FT than horizontally oriented specimens which is backed by literature. Lewandowski et. al. studied performance of EBM Ti-6Al-4V orientation dependence and reported that XYZ oriented specimens (comparable to specimens oriented vertically in this research) outperformed XZY specimens (comparable to specimens oriented horizontally in this research) in terms of Offset Yield Strength and Ultimate Yield Strength [32]. Assessment is given towards validity of the vertically oriented specimens outperforming the horizontally oriented specimens due to crack propagation parallel to the build plane vice through the build plane. Beta grain boundaries oriented parallel to the build direction in horizontal specimens could be contributing to pinning dislocations while horizontal loading is perpendicular to the grain boundary. Changing the build direction to 30 degrees demonstrated an increase of FT to the highest averaged value of the four orientations. Specimens built at 60 degrees showed a reduction of overall FT values comparable, but slightly higher than, values obtained from vertically oriented specimens. Based on anisotropic materials posing local differences throughout the material combined with understanding of vertically oriented specimens outperforming horizontally oriented specimens, 30 degree specimens show the maximum amount of FT based on crack propagation both through and along the build layer. This effect poses the highest resistivity to fracture among the four build orientations tested most likely due to stress concentration at the crack tip meeting the grain boundary requiring more energy input to pin dislocations and cause further crack propagation. Data acquired from the 60 degree specimens suggest that resistivity to fracture is more heavily based on crack propagation along the build layer and less though the build layer, resulting in data much closer to the vertically oriented specimens.

Especially at higher angles, FT specimens (built with virgin powder) experienced a significant amount of shear lipping which is indicative of the mechanism for ductile failure. A significant reduction in shear lipping was observed in recycled powder specimens which were nearly flat, as illustrated by longitudinal and transverse surface profiles. Fracture surface roughness exhibited in virgin powder specimens were overall significantly higher than recycled powder specimens. Specimens exhibited values consistently low in no discernable pattern. Although fracture surface roughness from this research may not trend to any particular build orientation, the ductility and shear lipping of FT specimens indicate that higher surface roughness values can confirm the amount of powder reuse. An increase in oxygen content during every reuse is clearly evident in the material behavior for reduction in shear lip area as shown by transverse profile comparison.

Chapter 5 FCGR Testing

The goal of this research was to characterize the FCGR for AM EBM Ti-6Al-4V made from powder that had been heavily recycled. The purpose of this experiment was to gain a broader understanding of the relative strength between differing build orientations and the relative material properties between virgin powder and heavily recycled powder. The goal of this testing is to further understand the anisotropic behavior and how that can affect crack growth prior to fracture.

5.1 Specimen Build and Design

A total of 14 C(T) specimens were fabricated from recycled Ti-6Al-4V powder. Of these 14 generated specimens, a variation of sizes and orientation were built. Half of the build consisted of 12 mm and the other half of the build was 6 mm thickness specimens as shown in Table 9. Specimens for FCGR testing were fabricated from powdered Ti-6Al-4V built from their 32nd reuse build cycle. Figures 31 and 32 show that the notch location for the build varied by being rotated 90 degrees.

The C(T) specimens were not subjected to any post-processing methods. Supports were inserted using ARCAM A2X's Magics software in the generation phase in order to ensure the specimens do not warp. After completion of the build process, the chamber was cooled down and depressurized and the specimens were inserted into a powder recover system (PRS) chamber where pressurized air was used to remove any excess titanium powder which may have been stuck to the sides. After cleanup, supports were removed to obtain specimens. It should be noted that 90 degree specimens have supports generated inside the holes through which clevis pins will be inserted. To ensure compliance, all loading holes were bored to specifications outlined in ASTM E647-15.

Table 9: Number of FCGR specimens built at their associated angles and thicknesses

		Build Orientation			
		0°	30°	60°	90°
Build Thickness	6 mm	1	2	1	3
	12 mm	1	2	2	2
Total Specimens		2	4	3	5

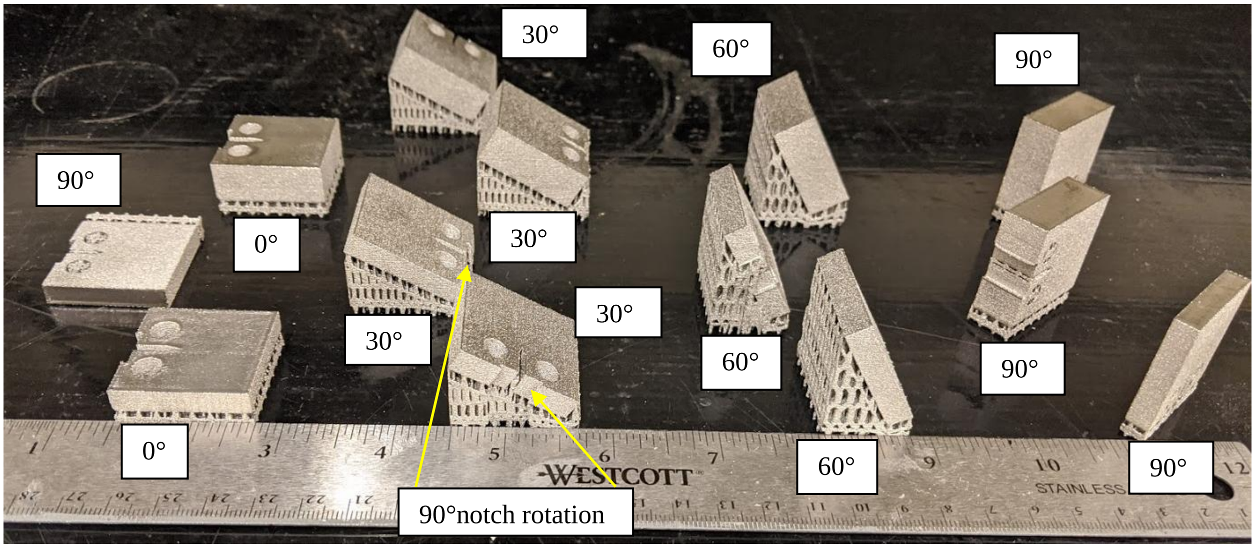

Figure 31: Batch of recycled specimens (for FCGR testing) built at four different angles and widths (6 mm widths near bottom of their division and 12 mm near the top)

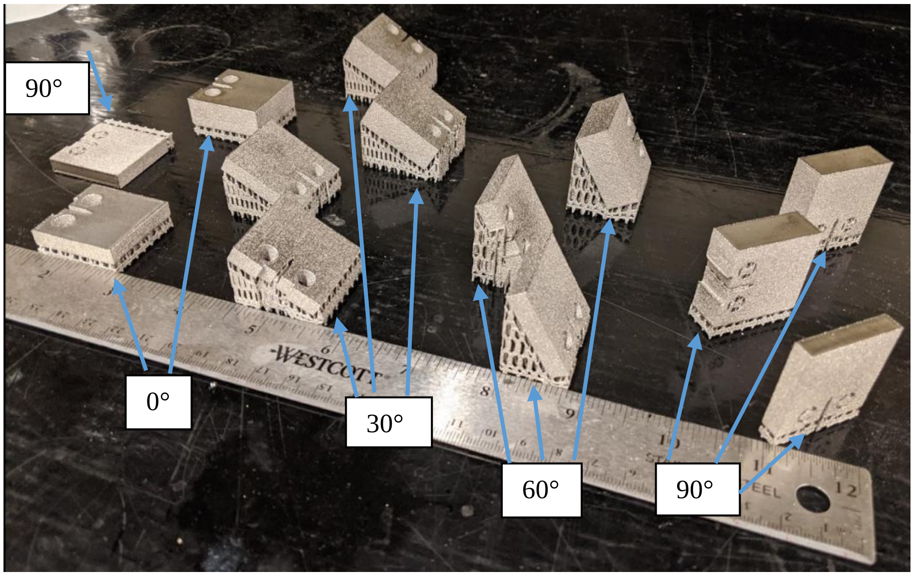

Figure 32: FCGR specimens (recycled powder) organized in 0°, 30°, 60°, and 90° layout prior to support removal

5.2 Specimen Shape and Dimensions

C(T) specimens were built in accordance with the ASTM E647-15 shown in Figure 33. To minimize material wastage, the minimum dimension for all specimens was chosen as W = 25 mm. Procedure recommends thickness of $W/20 \leq B \leq W/4$. 6 mm thick specimens fall within this range, however 12 mm thickness specimens fall outside of this range. Figures 34 and 35 show CAD drawings illustrating the specimen dimensions. One authorized modification to the specimens which were generated was the introduction of knife edges at the edge-to-support attachment of a Fracture Mechanics Clip-On Displacement (COD) Gauge Model 3541 which directly measured displacement and output to connected data acquisition boards and chart recorders.

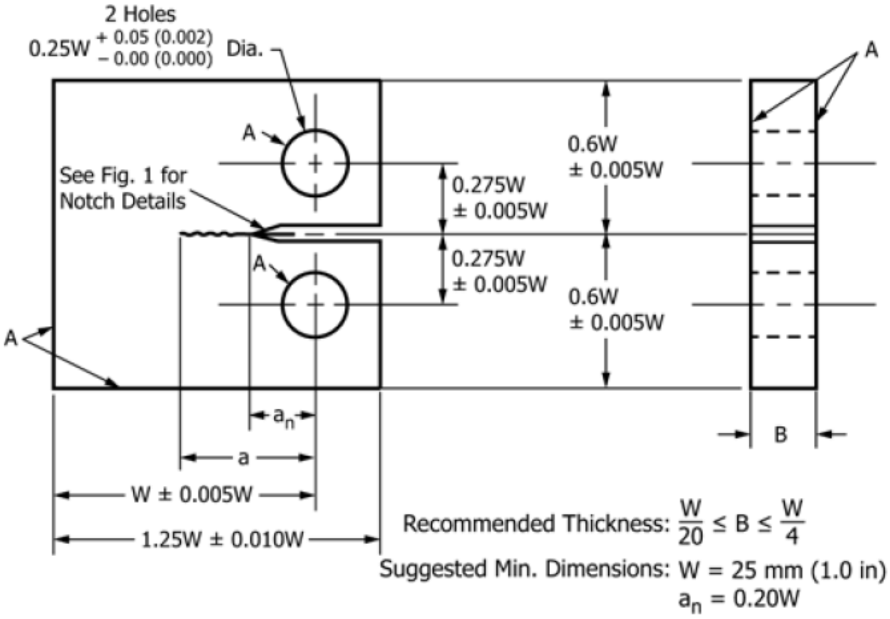

Figure 33: Standard Compact C(T) Specimen for FCGR and FT Testing [31, 33]

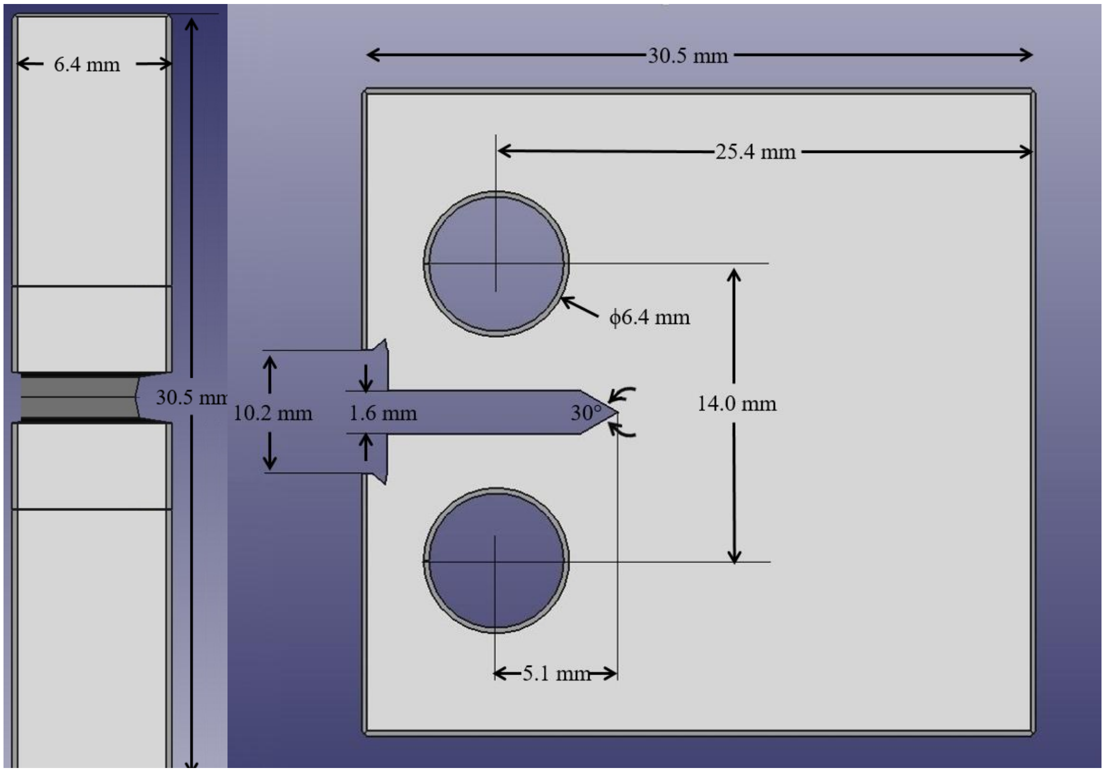

Figure 34: ASTM E647-15 Annex A1 and ASTM E399-20 Annex A4 compliant CAD drawing for 6 mm thick specimens [31, 33]

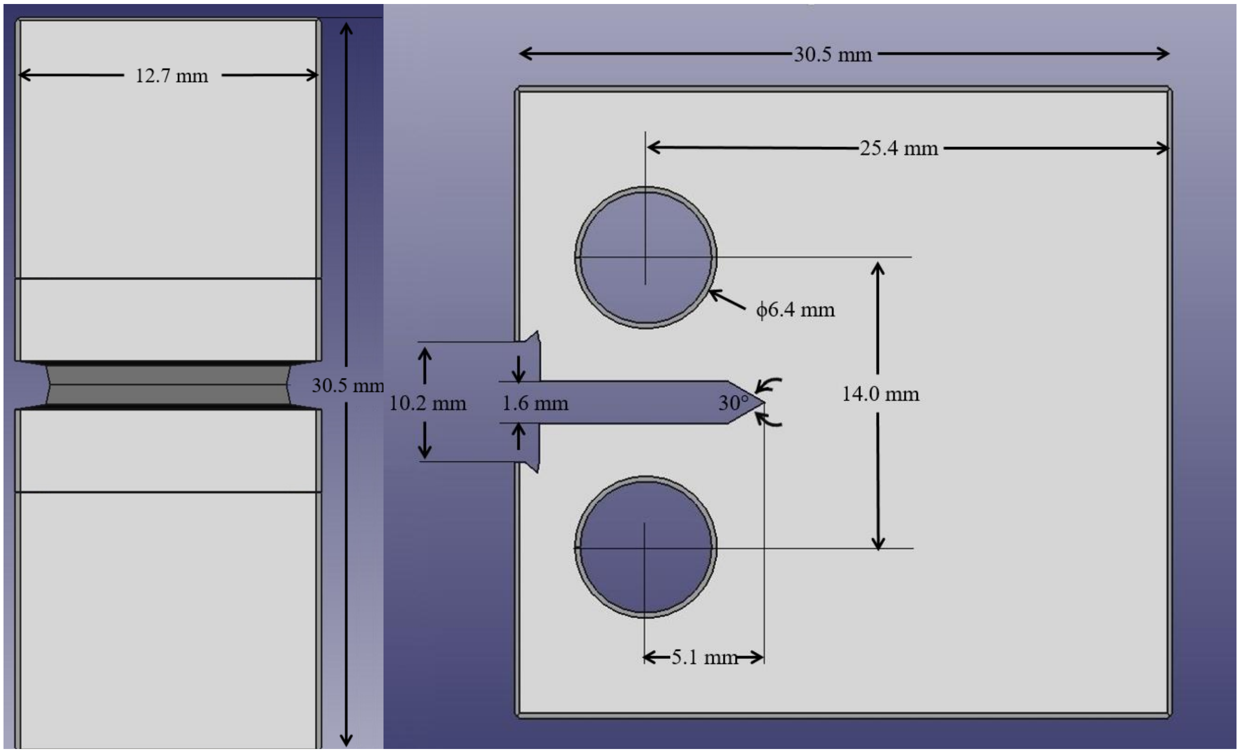

Figure 35: ASTM E647-15 Annex A1 and ASTM E399-20 Annex A4 non-compliant CAD drawing for 12 mm thick specimens [31, 33]

5.3 Fatigue Crack Growth Rate Testing

FCGR testing was completed using the procedure outlined in ASTM E647-15 for recycled powder built C(T) specimens at various widths and thicknesses discussed earlier in this section. The procedure requires two steps: first precracking shall be completed to a pre-determined value, then the specimen shall be loaded at a constant amplitude sinusoidal load until failure. Precracking was conducted at a stress ratio 0.1 at a frequency of 10 Hz to a sinusoidal waveform at a maximum load of 5 and 3 kN respectively for 12 and 6 mm. Precrack was observed visually until it reached a preset line on the side off the specimen at 1 mm. After precracking was completed, the specimen was loaded and the displacement gauge was installed and calibrated before each data run. FCGR testing was conducted at stress ratio 0.1 and set to maximum and minimum load values indicated in Table 10 [31]. Unfortunately, no easy method exists to determine the correct amount of load desired for FCGR testing to obtain accurate data within a reasonable time frame. Too high a load could result in inconclusive data, yet to low of a load may unnecessarily take too long. For this reason, loading was altered between specimens to gain a good middle ground. It should be noted that loading amplitude remained the same for all specimens during their respective test.

Table 10: Applied cyclic loads during fatigue testing

Specimen	Thickness (mm)	Build Orientation	Minimum Force (kN)	Maximum Force (kN)
1	12	60°	1.00	10.0
2	12	30°	0.50	5.0
3	12	60°	0.80	8.0
4	12	90°	0.80	8.0
5	6	90°	0.36	3.6
6	6	30°	0.36	3.6
7	6	60°	0.36	3.6
8	6	90°	0.36	3.6
9	6	0°	0.36	3.6
10	6	30°	0.36	3.6
11	6	90°	0.36	3.6
12	12	0°	0.80	8.0
13	12	30°	0.80	8.0
14	12	90°	0.80	8.0

5.4 Fatigue Crack Growth Calculations

The number of cycles, displacement from the COD gauge, and force were recorded and used to calculate the crack length and ΔK factor. The crack length was determined by measuring displacement, v, and calculating crack to width ratio a/W by using modulus of elasticity, E, specimen thickness, B, force, P in Equations 12 and 13, where u_x is simply a precursor calculation. Test results are valid for those α's calculated in Equation 14, known as the crack-to-width ratio, that satisfy Equation 15. Then ΔK is calculated using Equation 16 [33].

$u_x = \left(\left[\frac{EvB}{P}\right]^{.5} + 1\right)^{-1}$ ……………………………………Eq. 12

$\frac{a}{W} = 1.001 - 4.6695 * u_x + 18.46 * u_x^2 - 236.82 * u_x^3 + 1214.9 * u_x^4 - 2143.6 * u_x^5$…..Eq. 13

$\alpha = \frac{a}{W}$………………………………………..…….Eq. 14

$\alpha \geq 0.2$…………………………..…………..…….Eq. 15

$\Delta K = \frac{\Delta P}{B\sqrt{W}} \frac{(2+\alpha)}{(1-\alpha)^{3/2}} (0.886 + 4.64\alpha - 13.32\alpha^2 + 14.72\alpha^3 - 5.6\alpha^4)$……..…..Eq. 16

For each of the 14 specimens tested, a power law fit was computed to represent Region 2 behavior. This was accomplished for ΔK between the assessed ranges of ΔK factors for Region 2. These power law fits take the form of that described in Equation 4 developed by Paris. This power law can be used to compute a fatigue crack growth life (N_f), given an applied stress range (Δσ), initial crack length (a_0), and finial crack length (a_f). The experimentally derived values of C and m corresponding to the Paris equation (Eq. 3) were determined to 95% accuracy using MATLAB code.

5.5 Fatigue Crack Growth Rate Results

FCGR testing was conducted to determine the effects of specimen build orientation on anisotropic fatigue crack growth behavior. Figures 36 and 37 show calculated crack length versus number of cycles and illustrate that testing was consistent with the background literature that Bannantine laid out. Specifically, Figure 36 shows an exaggerated amount of cycles based on such a relatively low loading value chosen. Interestingly, a semi-wave action occurs in the data which may be representative of crack front meeting new boundaries and easily travelling prior to slowing down again when meeting another build layer. Table 11 shows critical data attributes which are compared later. For example, data for a_f/W was required to remain above a value of 0.2 which ensures that acquired data is valid. Figures 38 through 42 show relative comparisons between certain orientations to illustrate their relative performance. As expected from FCGR data results in Table 11, 12 mm specimens overall showed better performance data than 6 mm specimens. Also as expected from data results, 90° specimens perform better than 0° specimens overall as referenced to earlier by literature. To a reasonable degree, all build orientations have relatively similar trends with few exceptions. Specimen 2 represents the most sidmoidal behavior due to the lower load chosen for its test. While other specimens show a more linear behavior (on a log-log scale), their relative performance suggests valid data results. K_{th} can be estimated by continuing the left side of the da/dN vs ΔK curves to the x-axis in a sigmoidal fashion and are estimated to between 12-18 MPa*m$^{0.5}$.

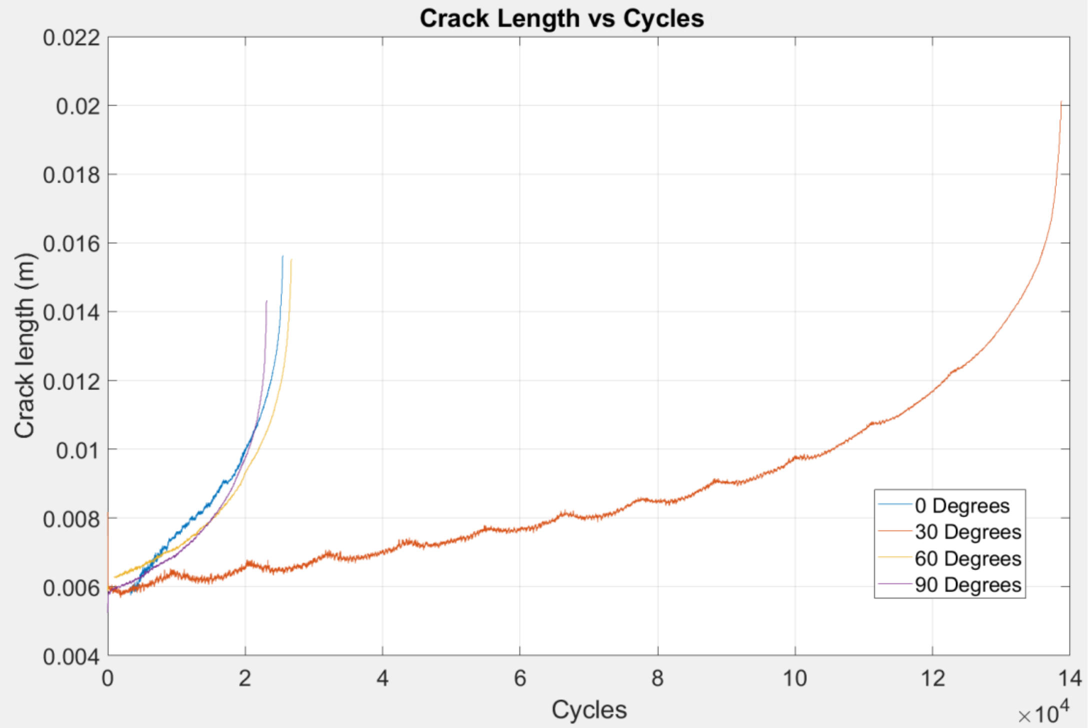

Figure 36: Calculated crack length vs number of cycles for 12 mm specimens in FCGR testing

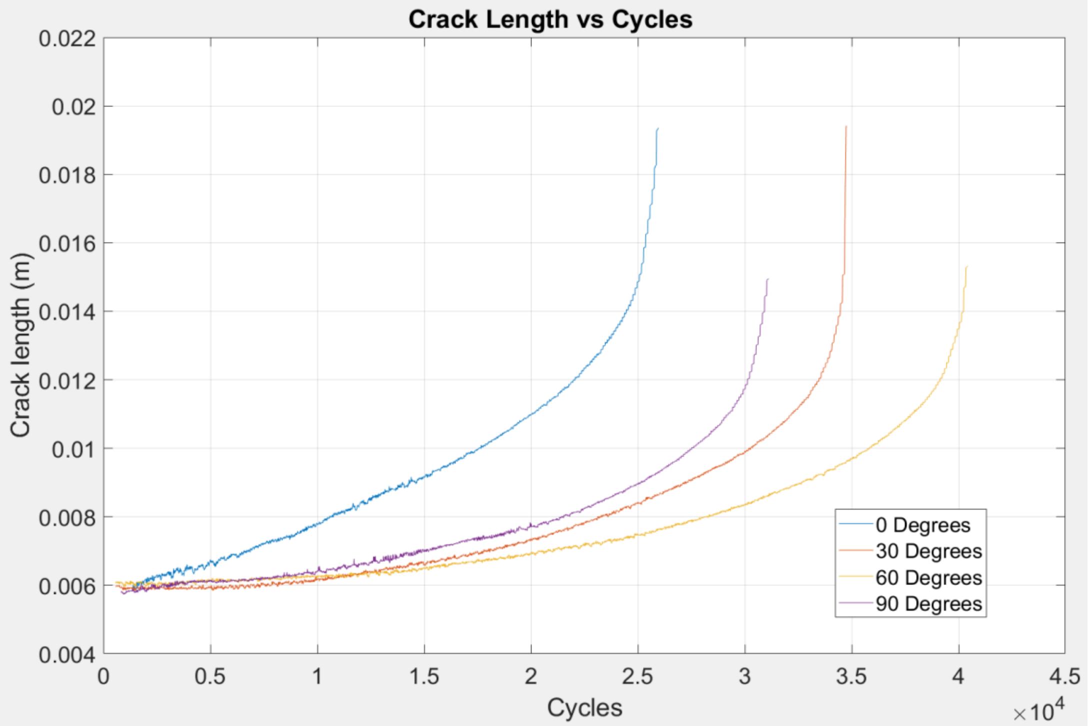

Figure 37: Calculated crack length vs number of cycles for 6 mm specimens in FCGR testing

Table 11: FCGR Results of recycled Ti-6Al-4V Powder

Specimen	Width (mm)	Orientation	Max Load (kN)	Stress Intensity at Failure (MPa $m^{0.5}$)	a_f/W	Cycles to Failure	Calculated Final Crack Length (mm)	Visual Final Crack Length (mm)
1	12	60	10	40.864	0.4740	19600	11.4	11.387
2	12	30	5	59.430	0.7555	138742	18.1	18.930
3	12	60	8	59.390	0.6470	26771	15.5	15.595
4	12	90	8	54.808	0.6228	33399	14.9	14.100
5	6	0	4	43.473	0.5627	15899	13.5	12.850
6	6	30	3.6	54.486	0.6458	31982	15.5	15.551
7	6	60	3.6	50.841	0.6300	40458	15.1	15.161
8	6	90	3.6	50.844	0.6481	40000	15.6	15.392
9	6	0	3.6	47.793	0.6605	25970	15.9	15.987
10	6	30	3.6	54.630	0.7966	34751	15.5	16.506
11	6	90	3.6	50.735	0.6500	31149	15.6	15.562
12	12	0	8	51.926	0.6097	25533	14.6	14.290
13	12	30	8	43.717	0.5643	29499	13.5	13.068
14	12	90	8	54.259	0.6344	23169	15.2	15.121

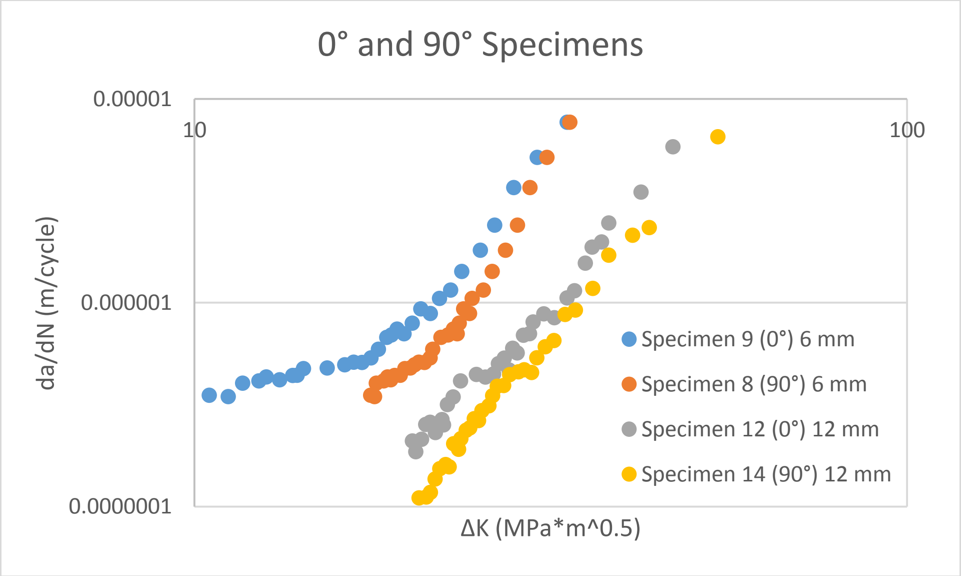

Figure 38: da/dN vs. ΔK comparison between 0° and 90° specimens

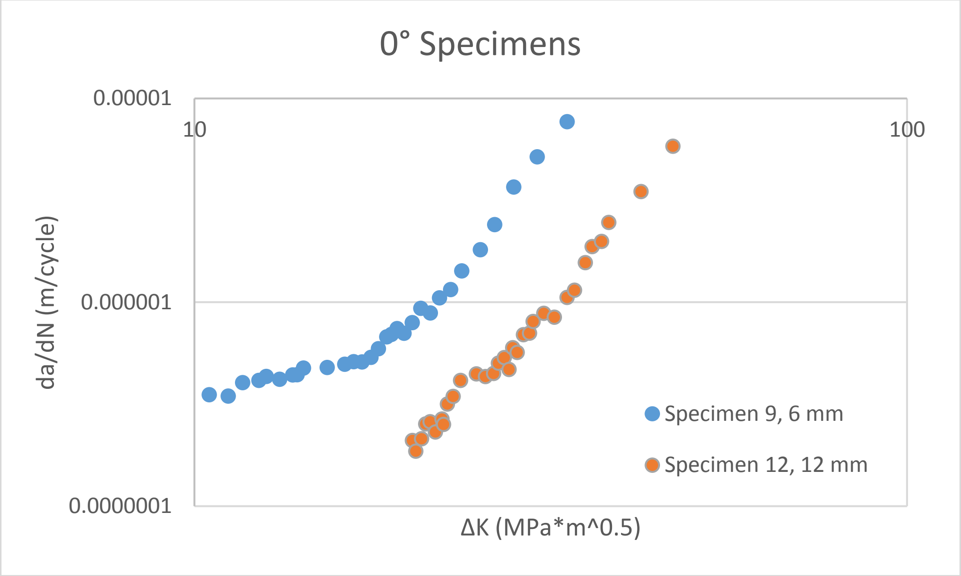

Figure 39: da/dN vs. ΔK for 0° specimens

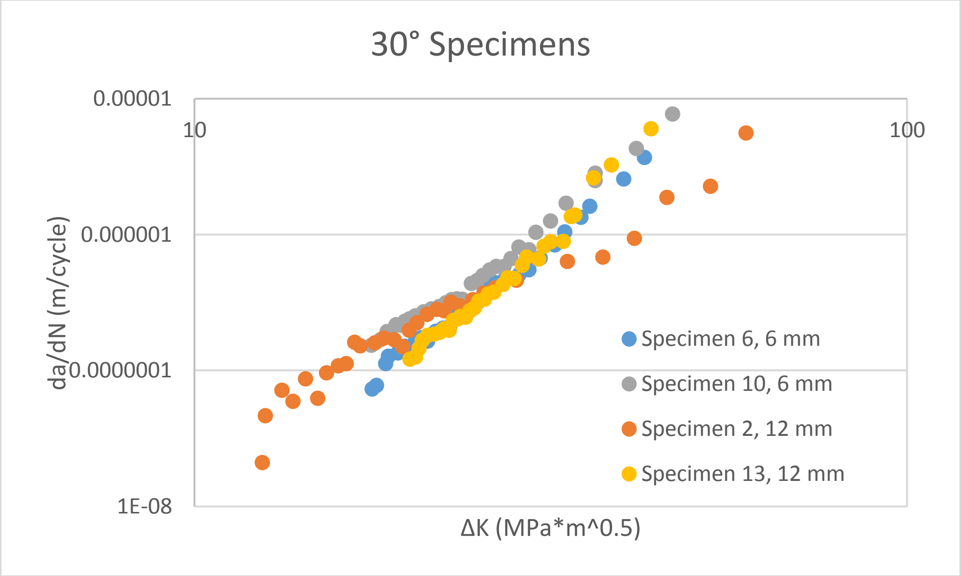

Figure 40: da/dN vs. ΔK for all 30° specimens

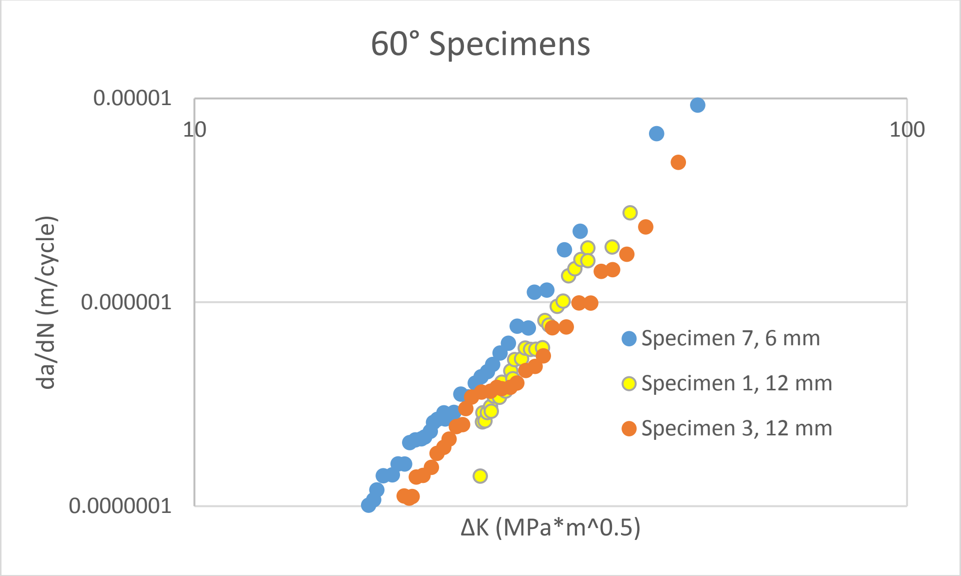

Figure 41: da/dN vs. ΔK for all 60° specimens

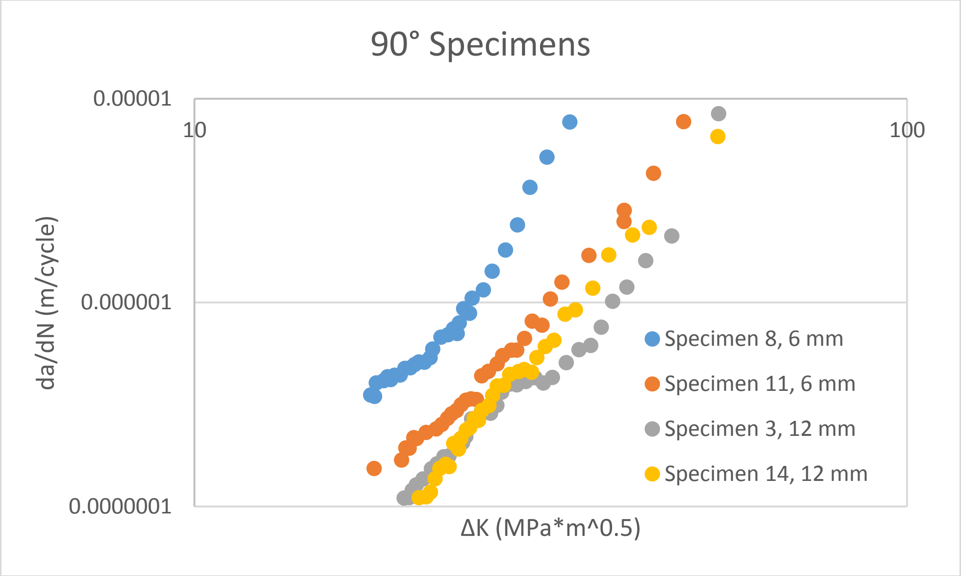

Figure 42: da/dN vs. ΔK for all 90° specimens

In order to confirm final calculated crack length generated by MATLAB, each specimen was observed using Keyence VR-3000 Profilometer to visually assess validity of final crack length. In general, edge placement of the measurement tool rests at the transition point between fatigue cracking and fracture. Selected specimens from both thicknesses and orientations are illustrated in Figures 43 and 43 whose sub-figures are oriented with the crack front moving from left to right. Critical transition points are clear based on roughness transitions points, introduction of valleys/plateaus (evident in 90 degree samples), and edge fracture. Comparison of visual crack length and computed crack length resulted in error of less than 5% for all specimens. ΔK calculated is graphically shown in Figure 45 by specimen width which shows similar behavior to that of those FT values in the first experiment. Figure 46 and Table 12 show the m values calculated from Region II behavior and their degree of precision. Data here supports the 30 degree behavior shown elsewhere as the lower m value represents a higher degree of resistivity to crack propagation.

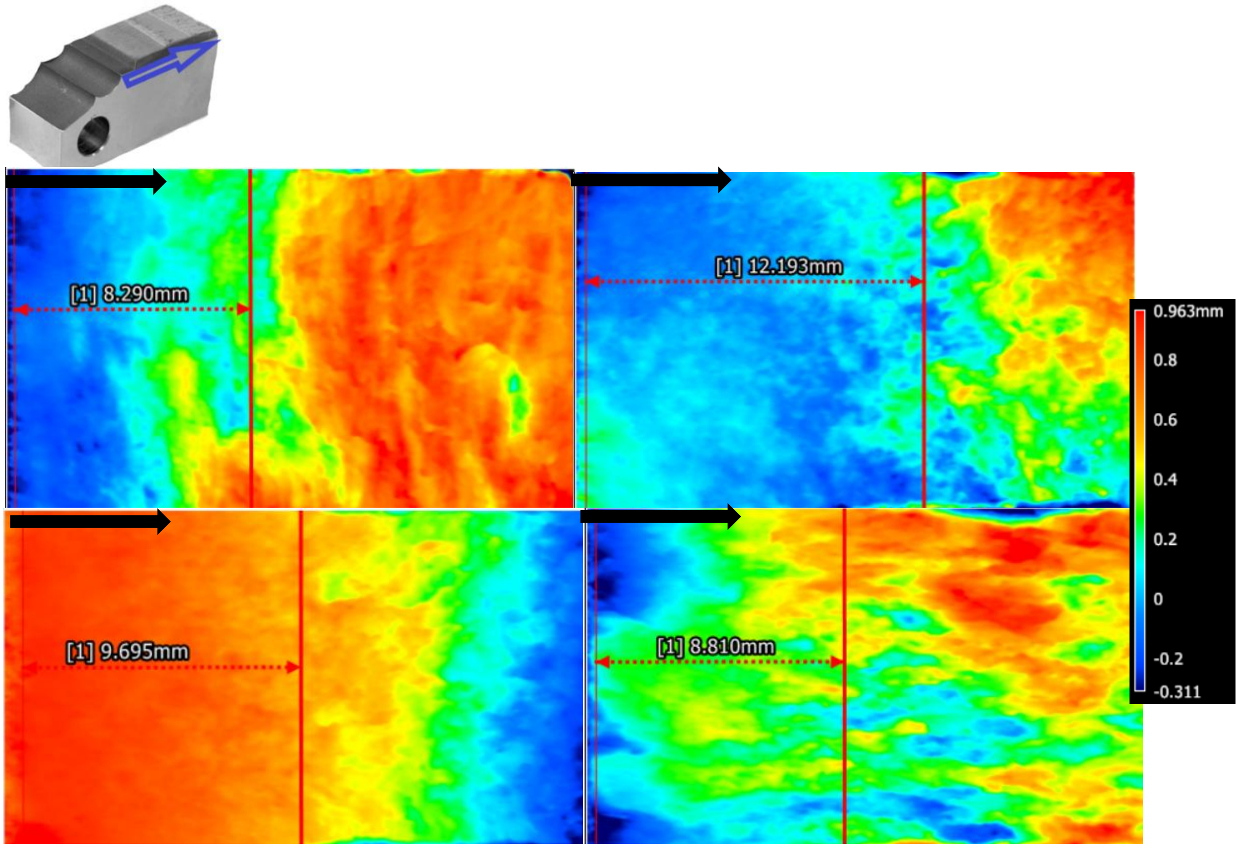

Figure 43: Surface profile and final crack length measurements of 12 mm specimens at 0 (top left), 30 (top right), 60 (bottom left), and 90 (bottom right) degrees

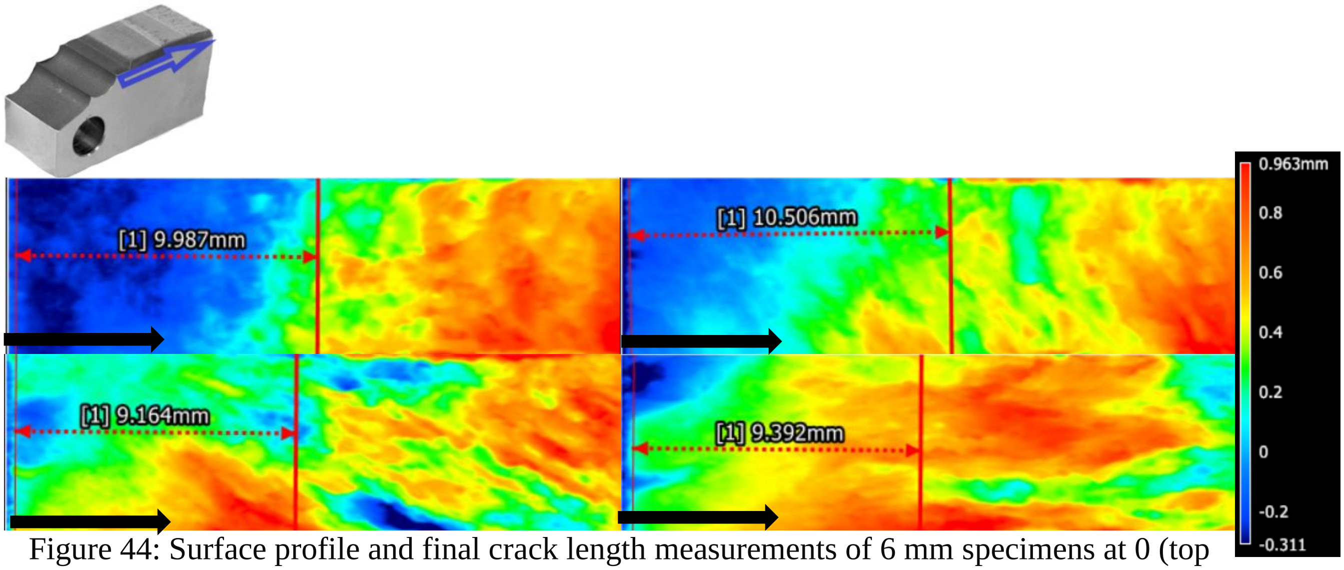

Figure 44: Surface profile and final crack length measurements of 6 mm specimens at 0 (top left), 30 (top right), 60 (bottom left), and 90 (bottom right) degrees

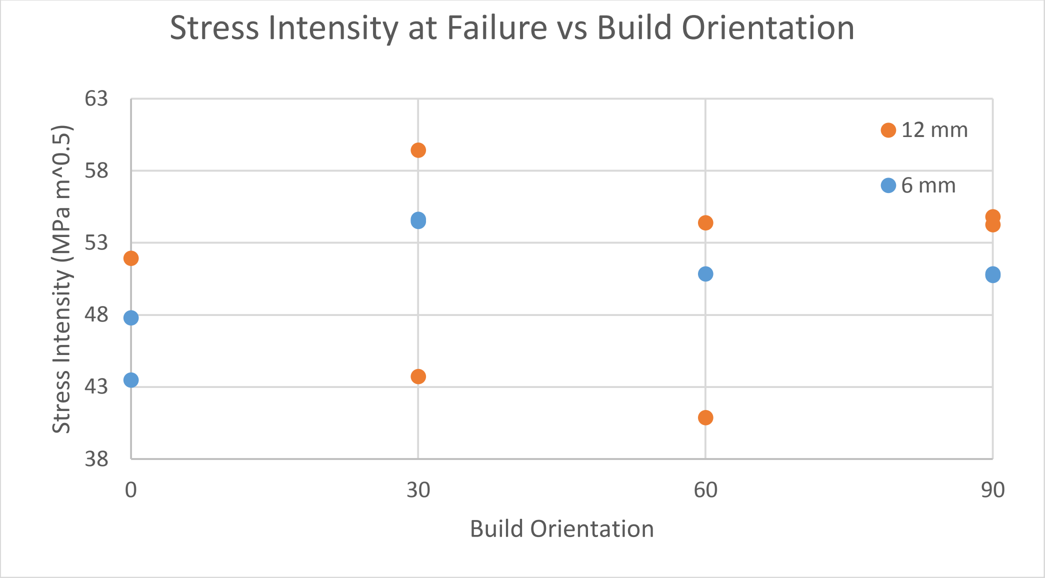

Figure 45: ΔK calculated from FCGR testing

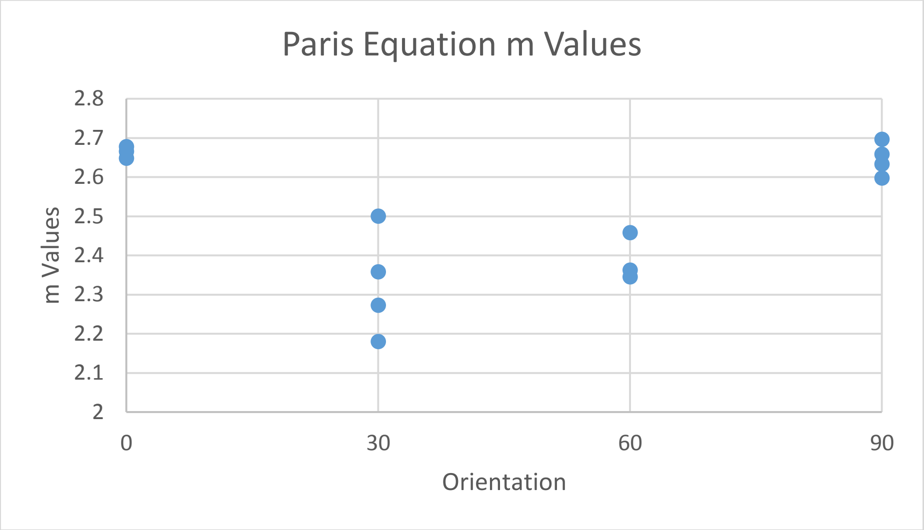

Figure 46: Paris equation m values generated from Region II behavior for all specimens

Table 12: Average and Standard Deviation values for Paris equation constants

	C		m	
Orientation	Average	STDEV	Average	STDEV
0	2.67E-07	4.71E-08	2.664	0.012
30	3.50E-07	2.18E-07	2.328	0.118
60	2.33E-07	1.89E-07	2.388	0.050
90	3.25E-07	3.34E-07	2.646	0.036

Figures 47 and 48 show a side view of selected specimens for the 6 mm and 12 mm specimens respectively where the left side of the figure starts at the machined notch. Triangles in these figures show select locations where crack path on the side of the specimen has taken significant turns, indicative of mode II failure based on the tortuous crack path. Overall, 30 degree specimens show the highest degree of qualitative and quantitative stacking like defects. In comparison, 60 and 90 degree specimens show less and 0 degree specimens show the least indications of the crack taking a tortuous path.

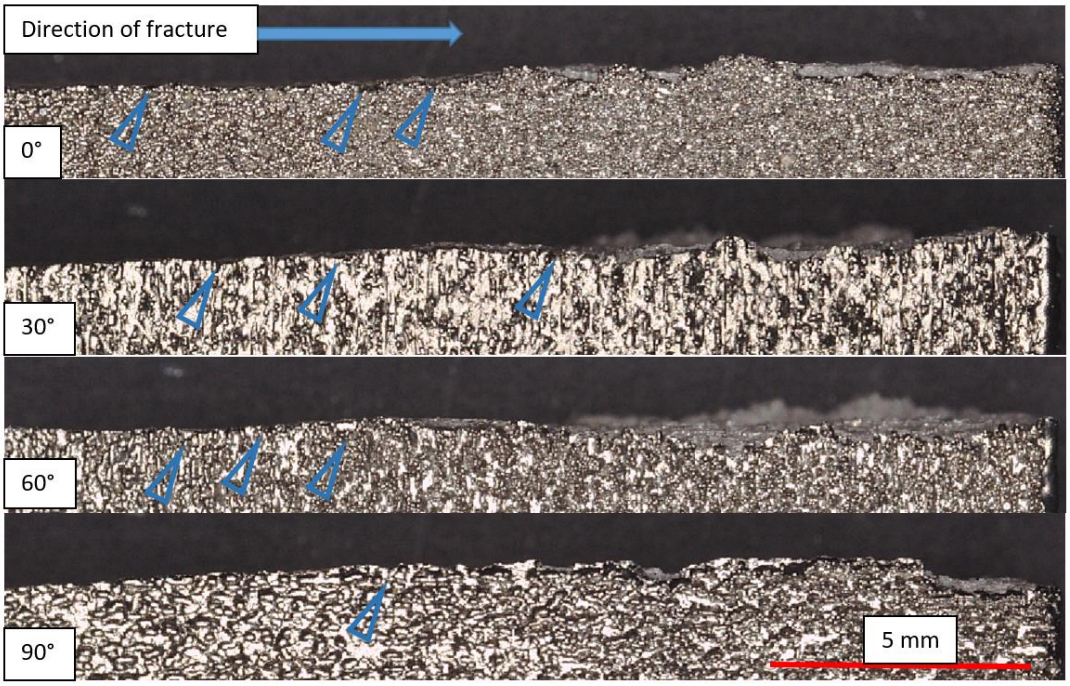

Figure 47: Side view of select 6 mm specimens denoting crack path

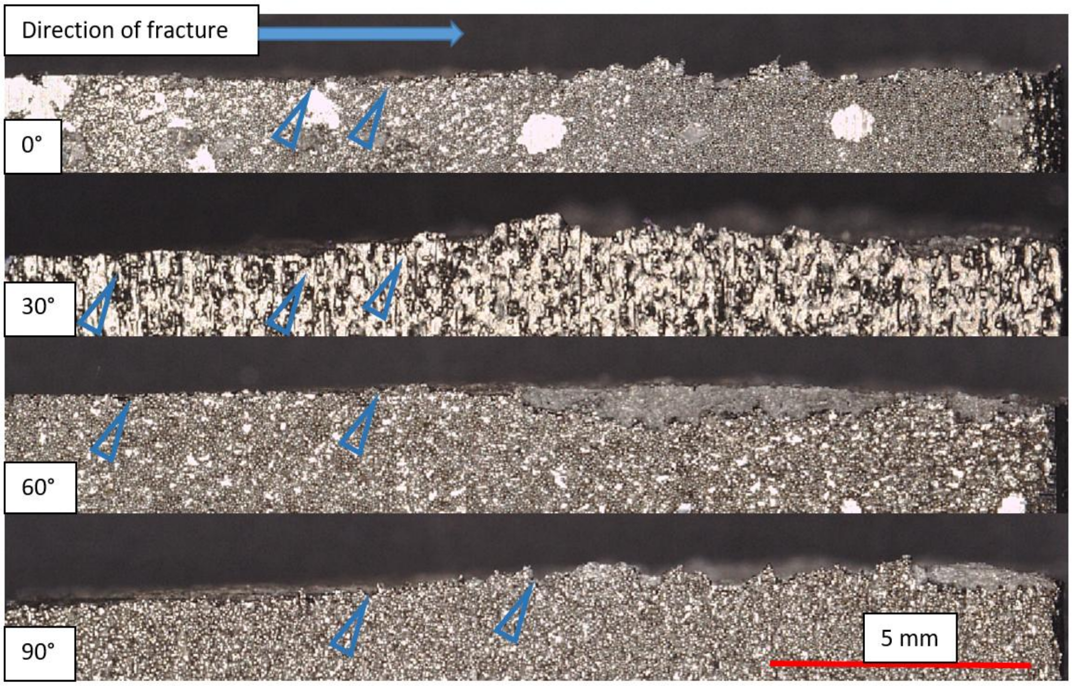

Figure 48: Side view of select 12 mm specimens denoting crack path

Selected specimens from all angles were plotted against values associated with the Forman Equation. General trends show a subtle transition from Region II to Region III behavior in Figures 49 and 50 which show only minor differences between theoretical curve fits and actual data. To additionally compare acquired data, Forman’s equation was used to calculate da/dN at the final ΔK. Recall, that FT is required, which is not available for recycled powder specimens. FT was acquired for virgin powder specimens was instead used in calculations. Table 13 shows a comparison of the Forman equation and final calculated da/dN.

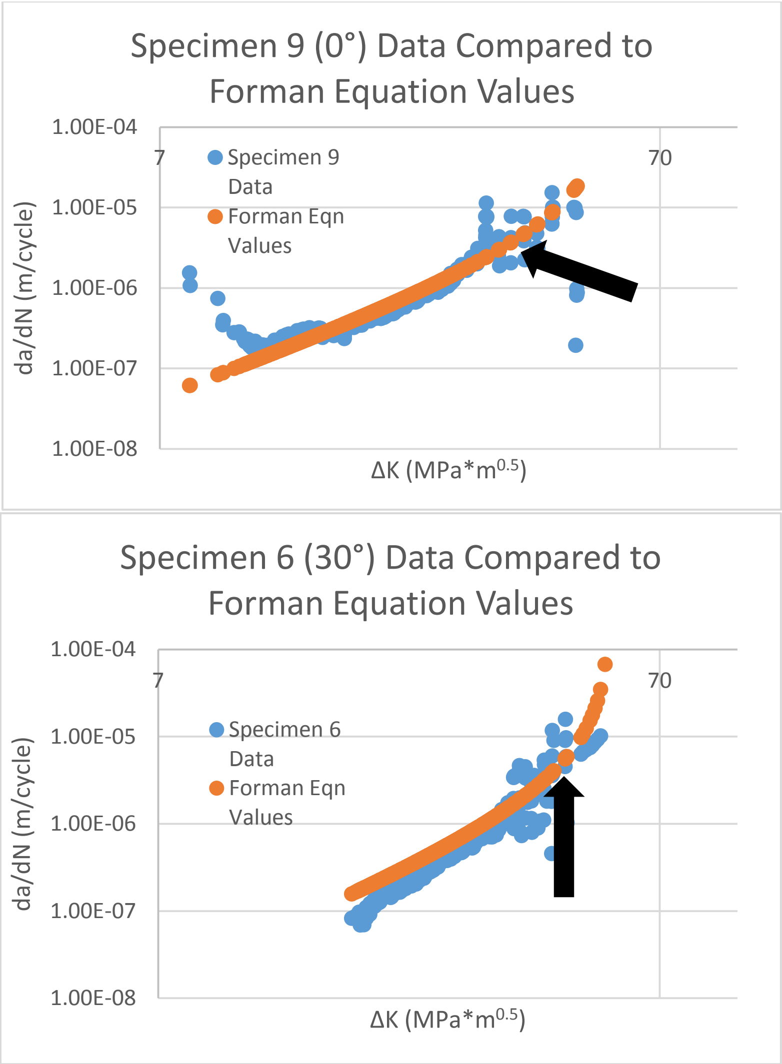

Figure 49: Specimens 9 and 6 showing Forman Equation transition to Region III

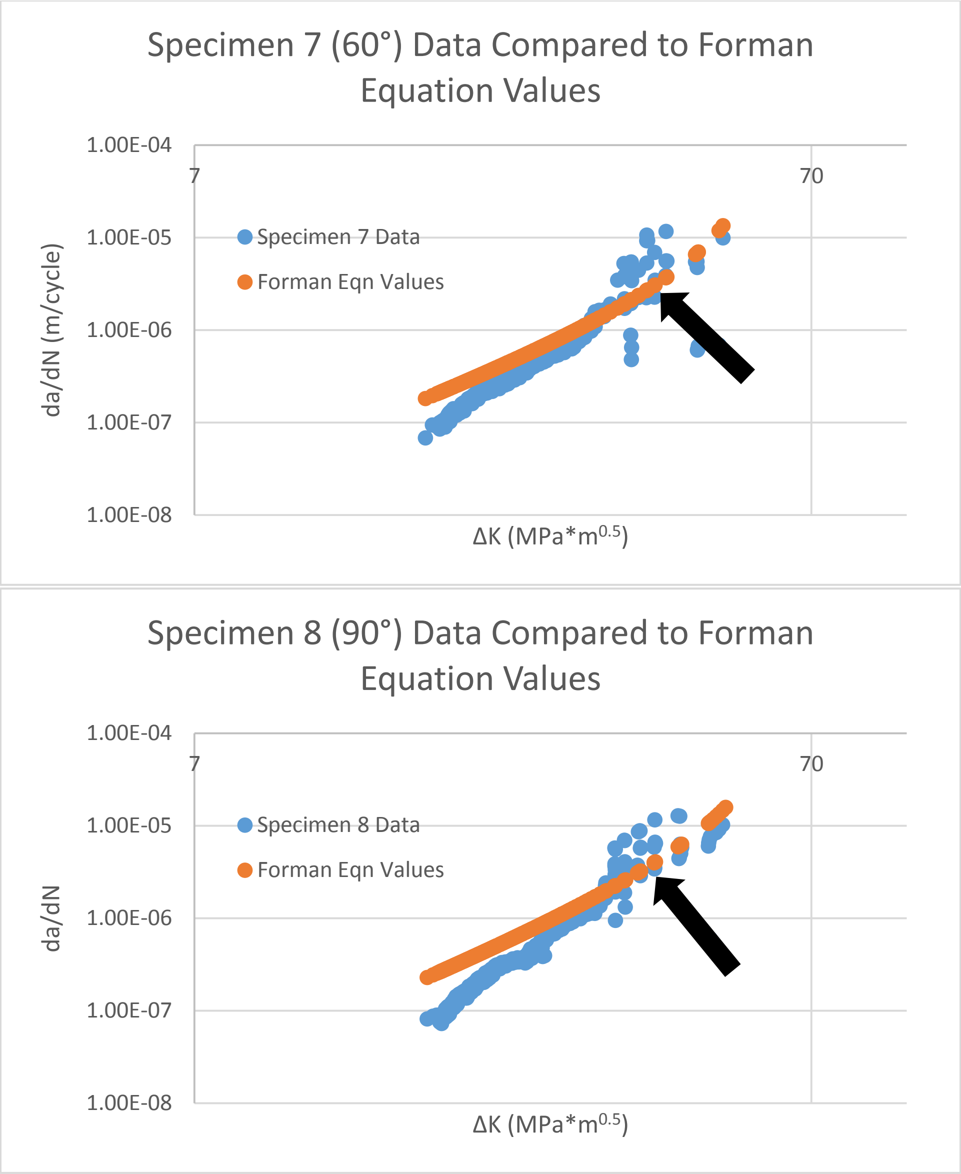

Figure 50: Specimens 7 and 8 showing Forman Equation transition to Region III

Table 13: da/dN calculations by Forman equation and MATLAB

FCGR Specimens	Forman Eqn. Ccalculated da/dN (m/cycle)	Calculated da/dN (m/cycle)
1	1.51E-04	3.79E-06
2	2.74E-04	1.37E-05
3	1.13E-03	1.03E-05
4	7.00E-04	8.45E-06
5	5.38E-04	1.04E-05
6	6.25E-04	1.67E-05
7	1.58E-04	9.28E-06
8	6.24E-04	9.98E-06
9	7.25E-04	8.92E-05
10	4.14E-04	1.53E-05
11	2.67E-04	1.47E-05
12	2.31E-03	1.26E-05
13	2.01E-04	6.02E-06
14	6.54E-03	6.53E-06

Galarraga et. al. studied FCGR in virgin powder specimens made from Ti-6Al-4V powder by EBM at a stress ratio of 0.1 reporting ΔK values of 45 and 52 MPa*m$^{0.5}$ for horizontally and vertically built specimens [6]. FCGR data results from this research are similar for the 0 degree specimens. However results from this research are lower in comparison by approximately 5 MPa*m$^{0.5}$ for vertically oriented specimens. While these values do loosely compare to one another, oxygen embrittlement is assumed to have a factor in the differences between the two tests.

In a macroscopic observation of specimens conducted by FCGR testing, layer lines on the fracture surface can easily be easily identified with the naked eye. Topographic maps of each fracture surface can be seen in Figures 51 and 52. These images illustrate evidence of the layered building process. In general, all specimens not oriented in the 0 degree direction showed evidence of valleys indicating their specimen build orientation. Consequently, those specimens built in the 0 degree orientation showed relatively less indications of valleys. Table 14 gives a quantitative representation of surface roughness as determined by profilometery. For data reading purposes, FCGR fracture surface roughness values are graphically shown in Figure 53. As observed from the first experiment in this research, the only notable pattern identified for FT specimens (virgin powder) was that fracture surface roughness increases with the angle of build orientation. Two notable observations are observed from the FGCR specimens (recycled powder) fracture surface roughness. First, all values surface roughnesses are much lower than FT specimens, which is indicative of the oxygen embrittlement caused by powder reuse. Secondly, all FCGR fracture surface roughness values illustrate no notable pattern with respect to build orientation except for 30 degree specimens. While build orientation may suggest a conclusion about surface roughness in this case, further testing is needed to capture this effect.

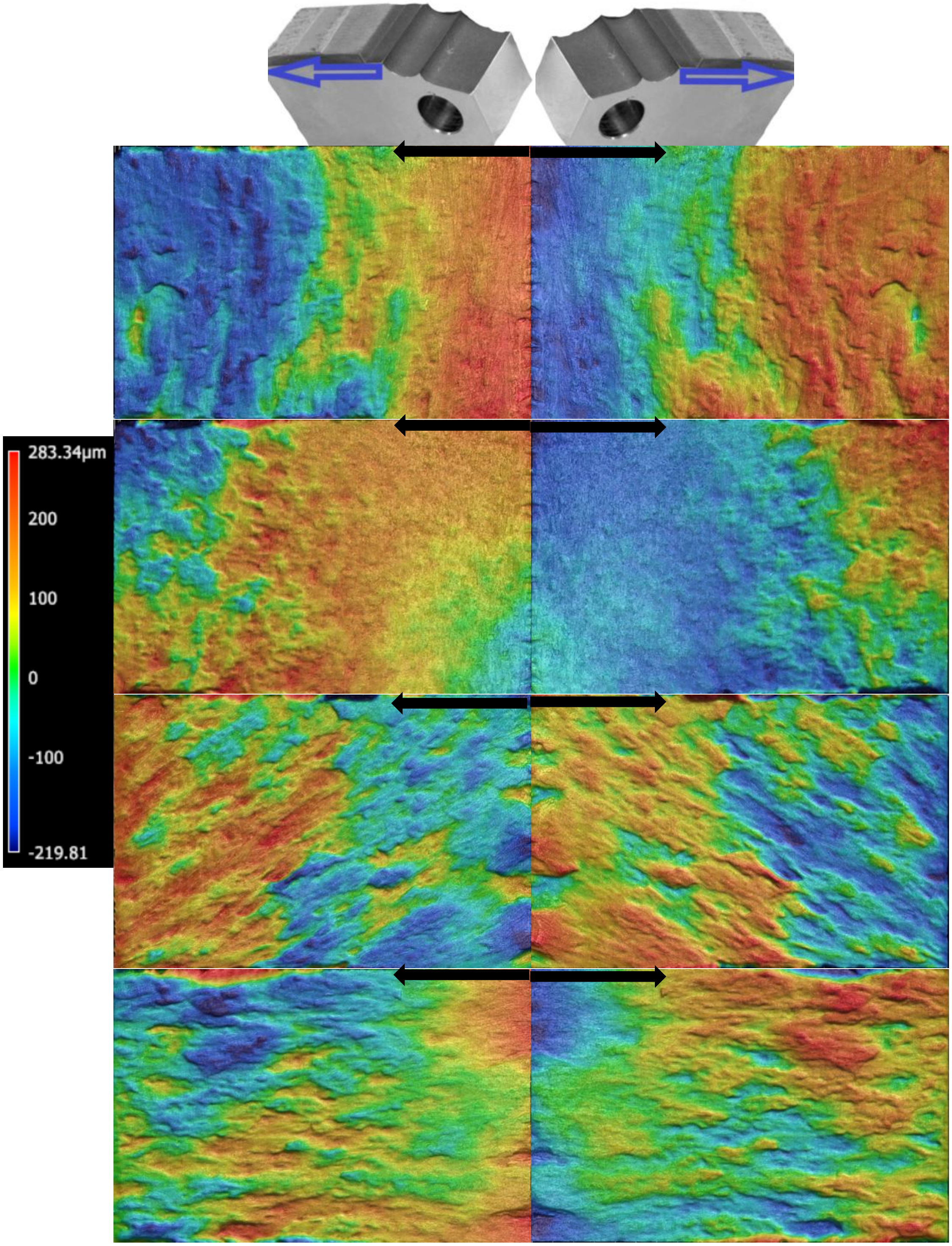

Figure 51: 12 mm specimen facture surfaces (complementary halves side by side) with build orientations (top to bottom) 0, 30, 60, and 90 degrees from FCGR testing

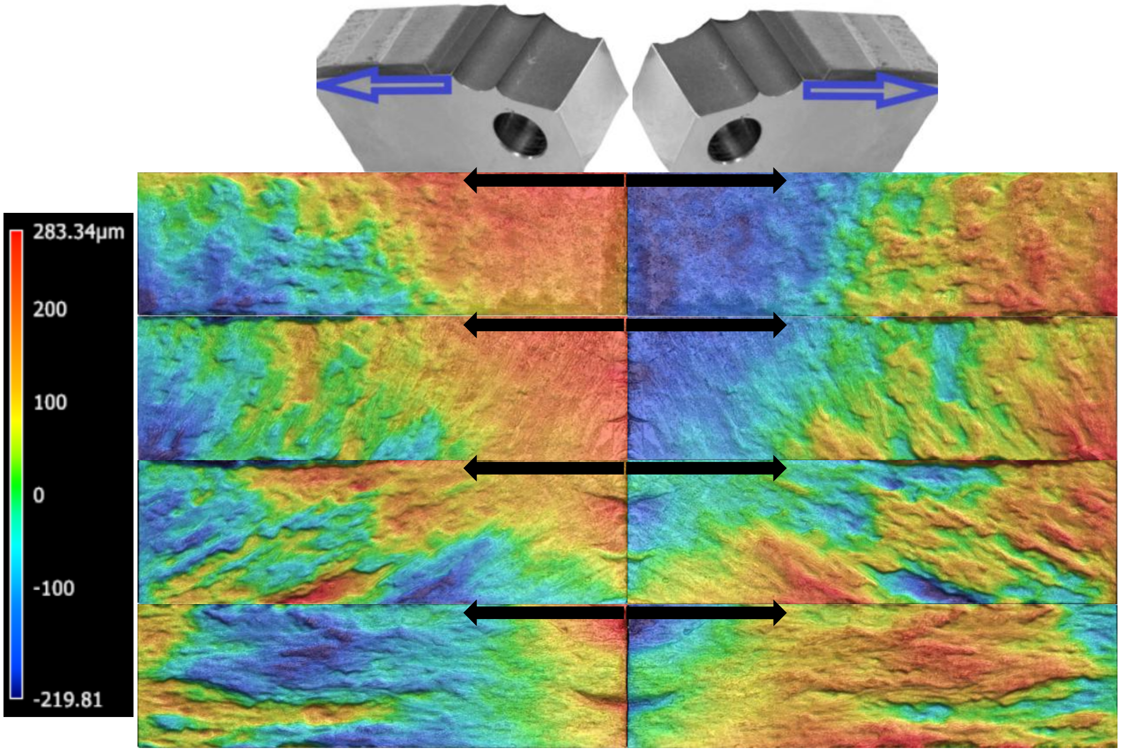

Figure 52: 6 mm specimen facture surfaces (complementary halves side by side) with build orientations (top to bottom) 0, 30, 60, and 90 degrees from FCGR testing

Table 14: Surface roughness values on the fracture surface for batch built from virgin powder in FT testing (left) and recycled powder used in FCGR testing (right)

FT			FCGR		
Specimen	Orientation	Surface Roughness	Specimen	Orientation	Surface Roughness
1	0	188	1	60	91
2	0	135	2	30	85
3	0	240	3	60	120
4	30	314	4	90	110
5	30	278	5	0	57
6	30	268	6	30	75
7	60	246	7	60	94
8	60	387	8	90	127
9	60	454	9	0	206
10	90	430	10	30	156
11	90	1351	11	90	123
12	90	849	12	0	171
-	-	-	13	30	94
-	-	-	14	90	197

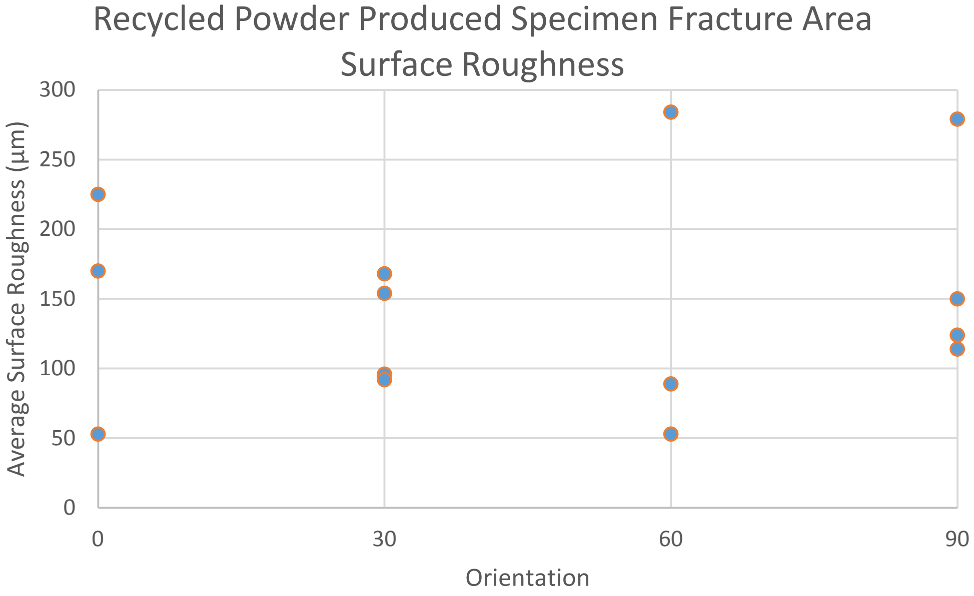

Figure 53: FCGR surface roughness values by orientation (specimens built by heavily recycled powder)

5.6 Fatigue Crack Growth Rate SEM Images

High resolution SEM were acquired of various surfaces of tested specimens to gain further visual understanding of the fracture and fatigue mechanics results. Since selected images were used in data presentation, the reader is directed towards Appendix C for follow-on observation. For all stitched figures in this section, direction of fracture is oriented from left to right.

Figures 54-61 in this section show select images of recycled powder specimens. Stitched images of the entire fracture surface area and zoomed in locations where fatigue behavior was observed are illustrated. Overall, clear micro-void coalescence is evident among all specimens and is comparable in size to those found in FT specimens however there are many more dimples in recycled powder specimens than virgin powder specimens. Of note, micro-void coalescence location and quantity does not appear to follow any orientation pattern. Interestingly, fracture flutes are extremely common among all specimens and can be seen below in all subfigures for this section. Much like the surface roughness images shown, fracture flutes appear to follow the angle of build orientation and exhibit the size characteristics of those described in the FT specimens earlier. All low magnification figures in this section show a green arrow pointing to the fracture line. Additionally, a red arrow showing some of the many pore voids evident among all recycled powder specimens. In general pore quantities increase as the build orientation angle was increased.

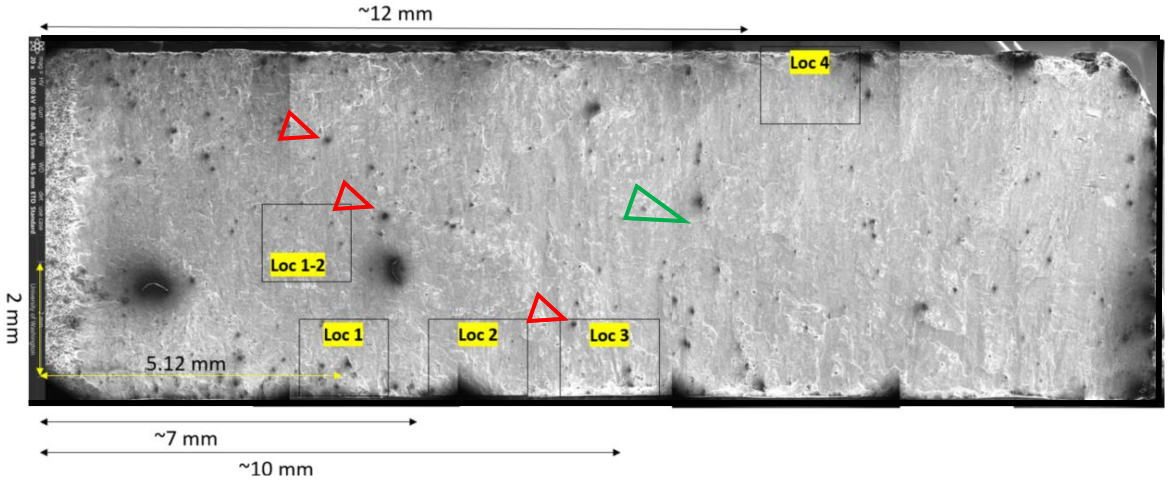

Figure 54: FCGR specimen 5 (0 degrees) with fatigue locations magnified in Figure 55

Table 15: Locations and striation widths of FCGR testing for 0 degrees

0 degrees (Sample 5)			
Location	Distance from notch (mm)	Observed da/dN (*10^-6)	Calculated da/dN (*10^-6)
1	5.1	0.664	0.612
1-2	4.5	0.66	0.478
2	7.0	1.38	0.812
3	10.0	*0.60	-
4	12.0	*0.769	-

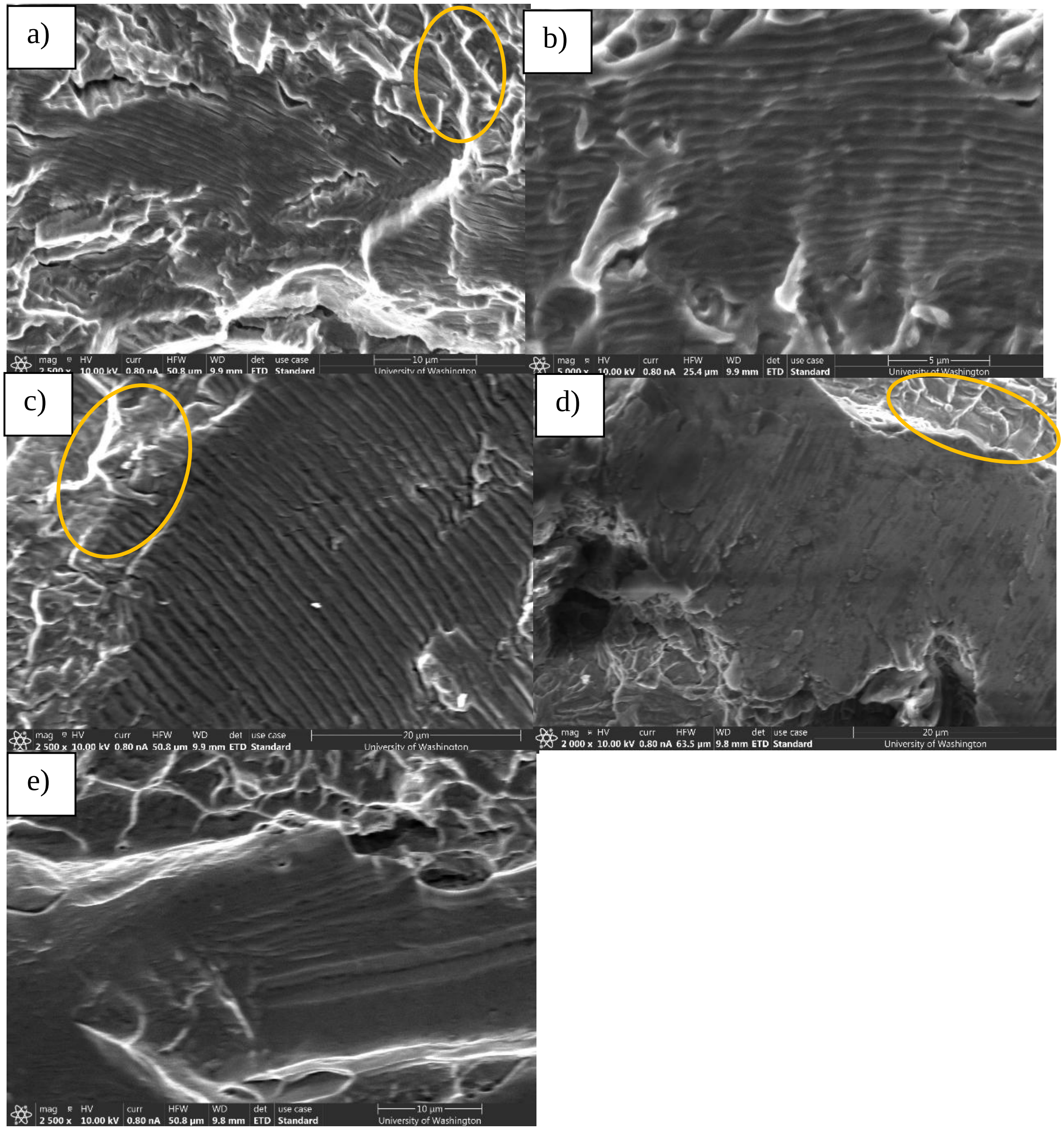

Figure 55: FCGR specimen 5 with locations a) 1, b) 1-2, c) 2, d) 3, and e) 5 from Figure 54 showing microvoid coalescence

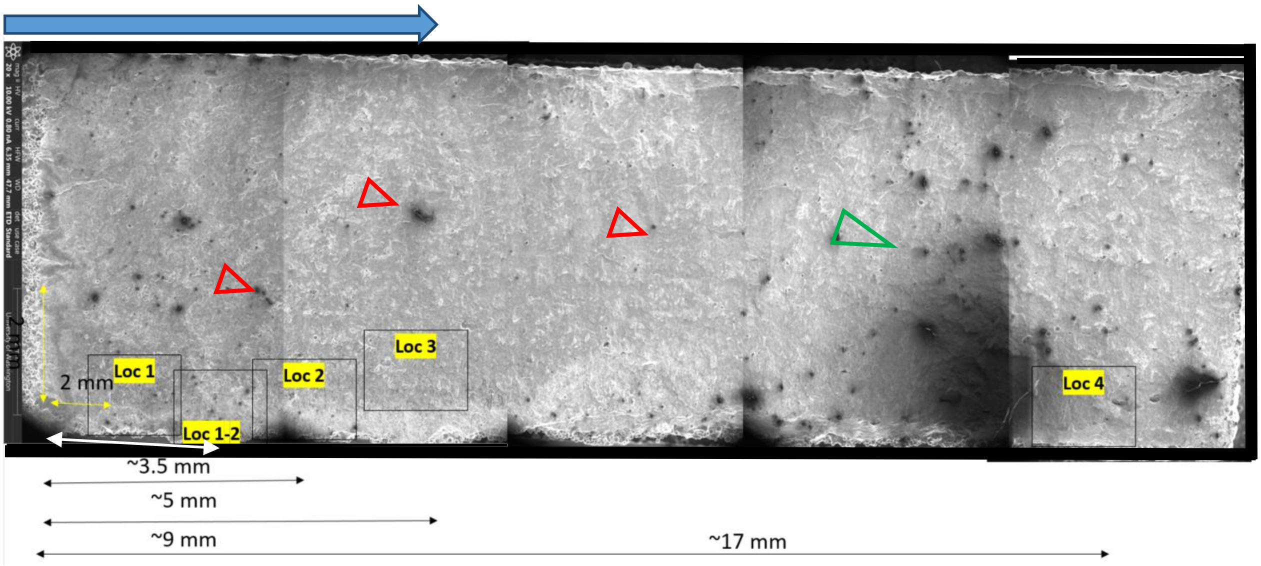

Figure 56: FCGR specimen 6 (30 degrees) with fatigue locations magnified in Figure 57

Table 16: Locations and striation widths of FCGR testing for 30 degrees

30 degree (Sample 6)			
Location	Distance from notch (mm)	Observed da/dN (*10^-6)	Calculated da/dN (*10^-6)
1	1	0.42	0.14
1-2	3.5	*0.23	0.33
2	5	0.29	0.39
3	9	1.11	1.03
4	17	*0.91	-

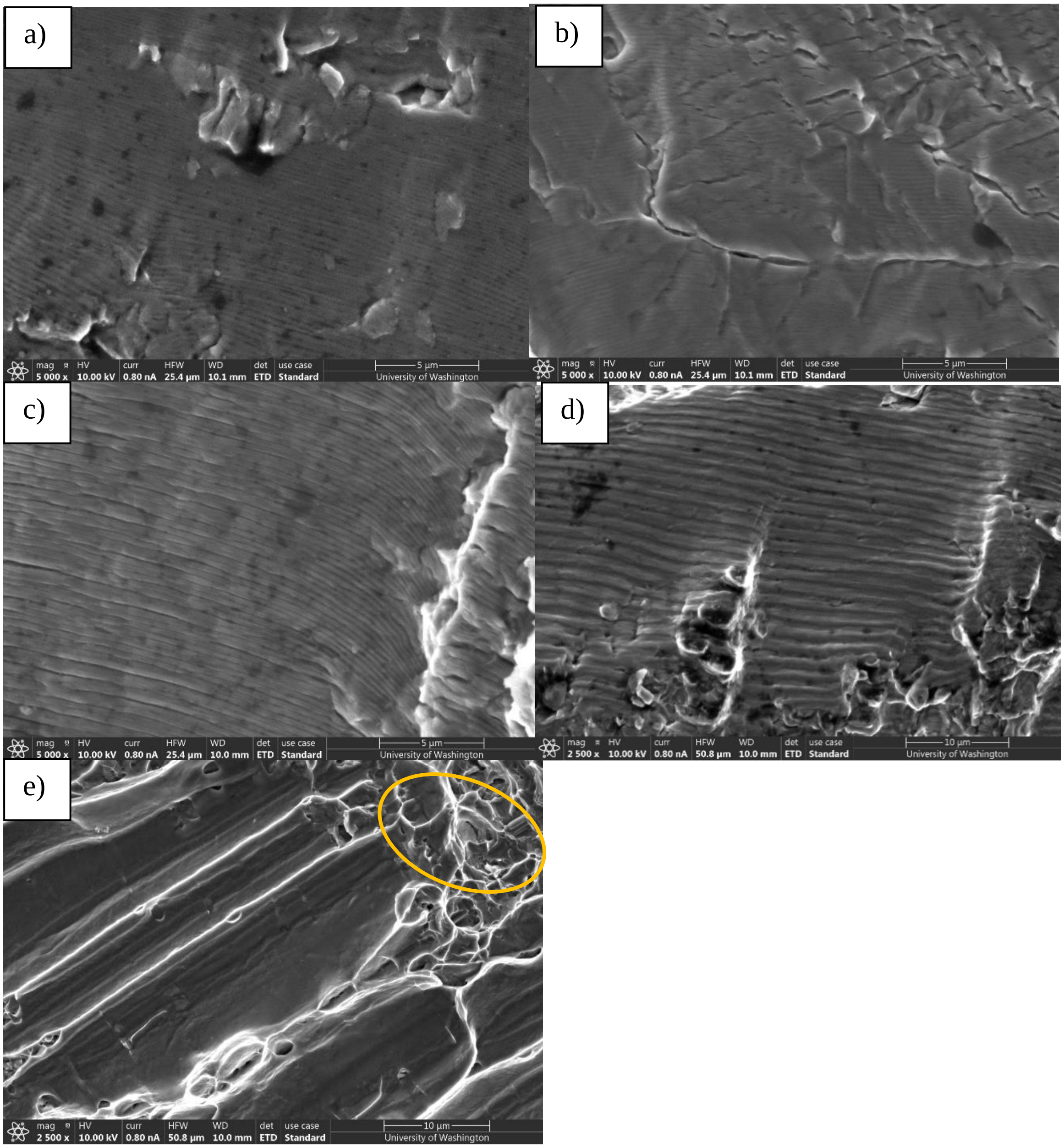

Figure 57: FCGR specimen 6 with locations a) 1, b) 1-2, c) 2, d) 3, and e) 4 from Figure 56 showing microvoid coalescence

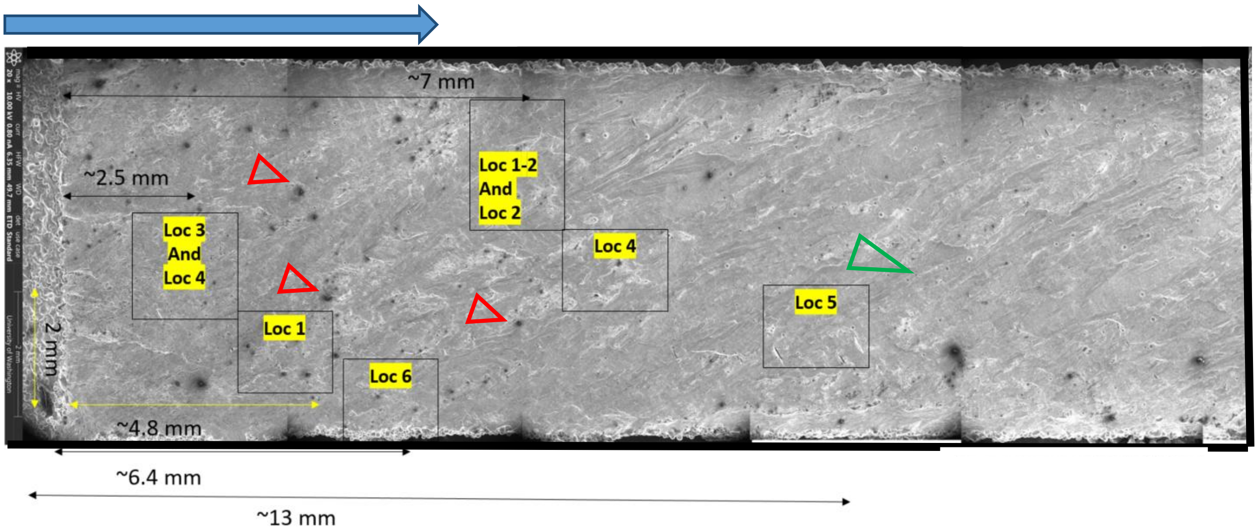

Figure 58: FCGR specimen 7 (60 degrees) with fatigue locations magnified in Figure 59

Table 17: Locations and striation widths of FCGR testing for 60 degrees

60 degree (Sample 7)			
Location	Distance from notch (mm)	Observed da/dN (*10^-6)	Calculated da/dN (*10^-6)
1	4.8	0.83	0.64
1-2	7.0	1.11	0.72
2	7.0	1.25	0.72
3	2.5	0.19	0.026
4	2.5	*0.55	0.026

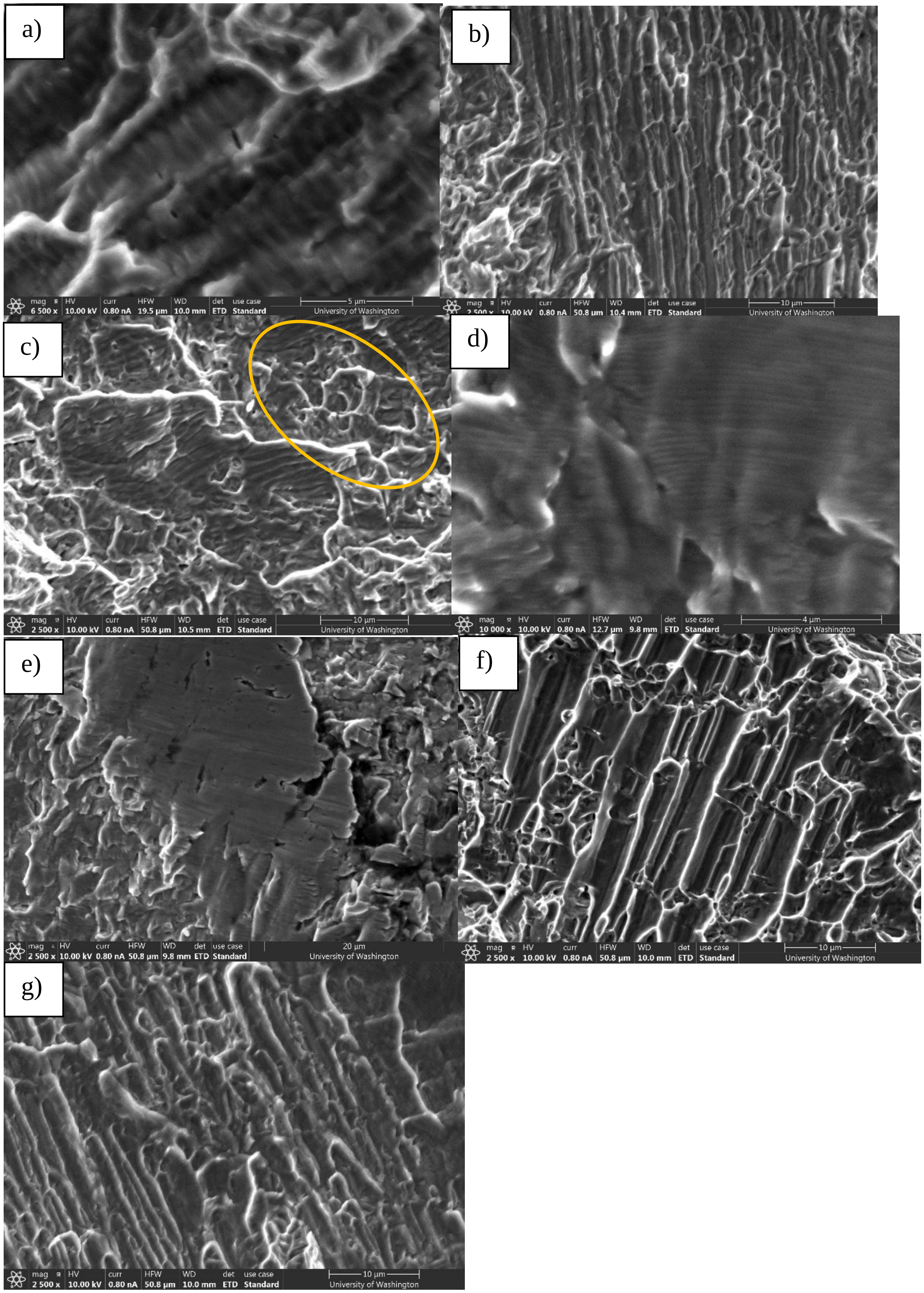

Figure 59: FCGR specimen 7 with locations a) 1, b) 1-2, c) 2, d) 3, e) 4, f) 5, and g) 6 from Figure 58 showing microvoid coalescence

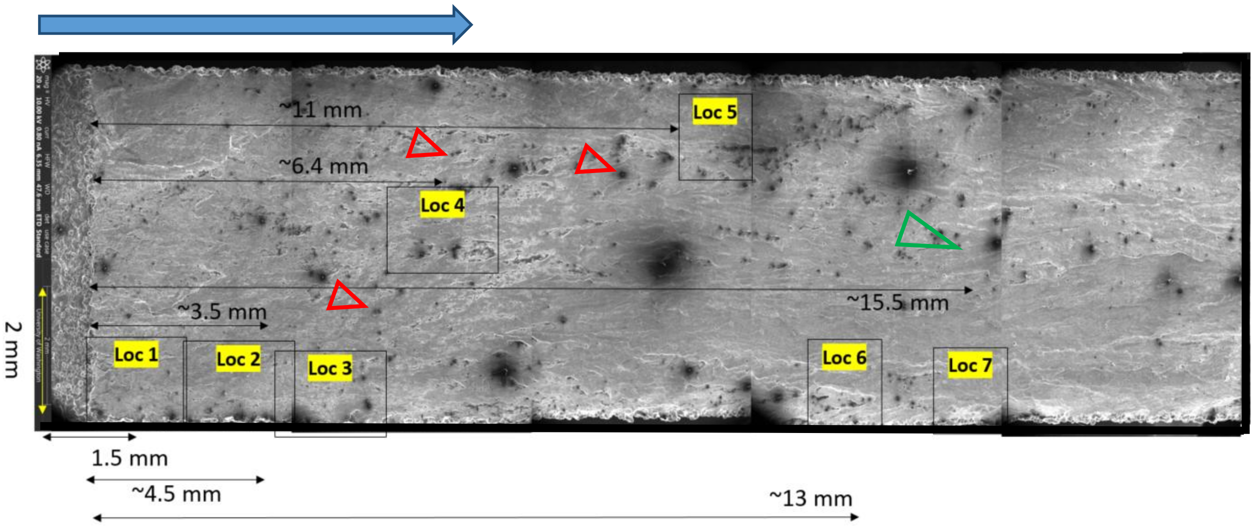

Figure 60: FCGR specimen 8 (90 degrees) with fatigue locations magnified in Figure 61

Table 18: Locations and striation widths of FCGR testing for 90 degrees

90 degree (Sample 8)			
Location	Distance from notch (mm)	Observed da/dN (*10^-6)	Calculated da/dN (*10^-6)
1	1.5	0.438	0.022
2	3.5	*1.43	0.043
3	4.5	*0.38	0.11
4	6.4	0.71	0.57
5	11	0.83	-

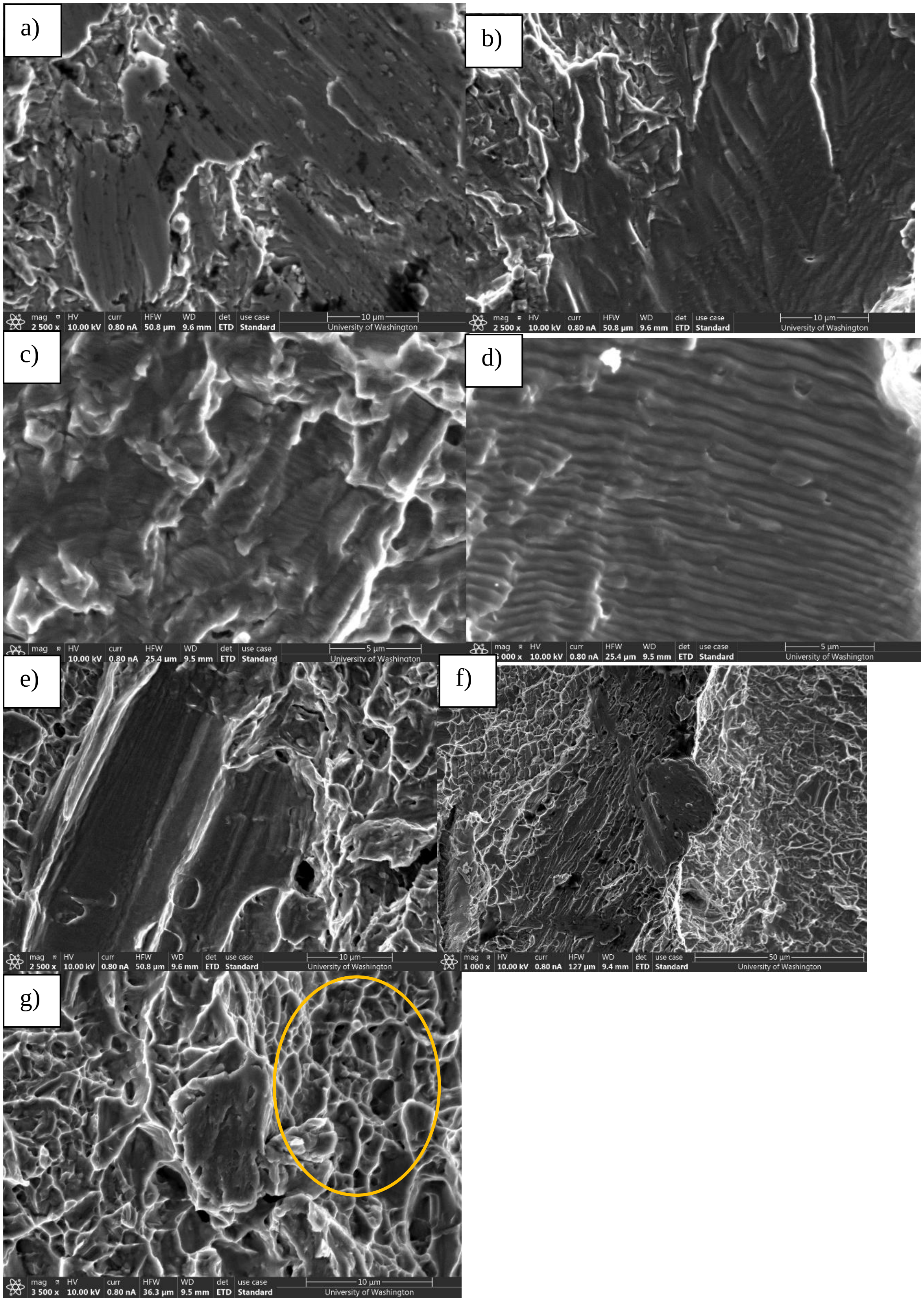

Figure 61: FCGR specimen 8 with locations a) 1, b) 2, c) 3, d) 4, e) 5, f) 6, and g) 7 from Figure 60 showing microvoid coalescence

Calculations were performed on SEM imagery to compare da/dN calculations during testing. Tables 15-18 show visually calculated da/dN values which pair to their associated in process testing values. All asterisked values denote either mixed results or evidence of shear lipping that lead to numerical deviations from calculated values. To further assess the validity of the values calculated in Tables 15-18, a simple comparison was made using an empirical relationship proposed by Bates and Clark in Equation 17, where E is Young's Modulus and ΔK at that location. Most average striation widths satisfied within reasonable tolerance Bates' and Clark's relationship for ΔK further confirming data findings.

$$\Delta K \approx E\sqrt{\frac{Avg\ striation\ width}{6}} \quad \text{Eq. 17}$$

5.7 Discussion

This research performed FCGR testing on recycled powder specimens to aid with understanding how long crack growth can occur prior to failure for use in high integrity systems. FCGR testing resulted in the same general performance as FT testing among most specimen orientations with few outliers. Paris equation m values in horizontal and vertical testing from this research compare reasonably in trend from Edwards et. al. XY and XZ testing respectively [29]. A comparison of Paris equation m values generated from this testing demonstrated that 30 degrees and 60 degrees show a higher resistivity to FCGR based on reasons explained by FT testing. Notably, the same trend in calculated FT was loosely seen between two different sized specimens. Paired data with Forman Equation overlay gave visual recognition of the proposed transition point between Region II and Region III behavior around 40-45 MPa*m$^{0.5}$. This also confirms the validity of obtained data and curve fits. Trend outliers include Specimen 5 whose cycles to failure resulted suspiciously low indicative of significant lack-of-fusion voids degrading its material performance. While SEM pictures shown in Appendix C for this specimen do indicate lack-of-fusion voids, imagery of other build orientations indicate similar characteristics in quantity which warrants further investigation. Other outliers include Specimen 1 whose resultant lower than averaged ΔK is more than likely due to high cyclic loading. Confirmation of this result requires SEM imagery which was not taken of this specimen and requires further investigation.

The general trend between both tests complement each other. However observation should be given to the relative performance between these two tests. As calculated earlier, K_{th} was indirectly calculated between 8-23 MPa*m$^{0.5}$. Visual inspections of da/dN vs. ΔK curves shown in Appendix B confirm these calculations. Region I behavior at the tail of data expressing a sigmoidal shape trends downward at an infinite slope to cross the x-axis, the value at which K_{th} is taken. Since research suggests an average threshold of approximately 4 MPa*m$^{0.5}$ for virgin powder specimens, indirect comparison suggests an increase of K_{th} anywhere between 2-6 times for materials built from heavily recycled powder [8]. However, differences between the two batches indicate non-negligible quantities of lack-of-fusion voids, spherical voids, and cracks. Therefore the calculation of Kth in future research requires investigation of anticipated changes in material properties between the two types of powders used. Lastly, powder reuse is demonstrating a fair quantity of interstitial oxides which could be contributing to a wider variation in ΔK values based on higher oxygen content leading to embrittlement [30]. Calculation of da/dN using Forman's equation resulted in values calculated for the end of each test differing from those calculated in this research. Although these values calculated are difficult to compare based on their very low values, general trending of da/dN values are less than those calculated using Forman's equation. Mathematically determining FT values for heavily recycled powder specimens was not conducted in this research. However, assuming FT values for virgin powder specimens used in this comparison are to be correct, these values are then only affected by the final ΔK for the test. Conversely, assuming ΔK are to be correct, final FT values would be affecting da/dN. In either case, a concrete argument can be made for the differences calculated during this comparison. Another reason for which these values can be affected is the distance from the build plate. As build orientation is increased, so is the pre-built notch from the build plate. A non-negligible temperature gradient from the build plate could be affecting the final product in the vicinity of the notch and its material properties, which can yield higher strength values. As such, a plausible argument for 60° and 90° build orientations having similar values can be made, however further investigation should be conducted.

Higher magnification features showed a dominant feature of micro-void coalescence regardless of build orientation or powder reuse. Dimple size varied within the individual fracture surfaces possibly due to the observed range of grain sizes. Because dimples can form at grain boundaries, a wide array of dimple sizes can exist within a single specimen. Also observed at higher magnification were flutes which were characteristic only to recycled powder specimens. Flutes are elongated dimples, common to hexagonal close packed structures, which appear in colonies in recycled powder specimens due to oxygen embrittlement. Flutes generally followed a pattern of laying parallel to the build orientation.

Visual inspections of fatigue striations on SEM images for FCGR specimens (recycled powder) mostly matched (within 30% accuracy) data calculated during testing especially when regions of calculations were near the middle of the specimen. Visual inspections disagreeing with calculated da/dN vales were most likely due to a result of either crack front curvature or shear lipping causing a few mismatched calculations. The same general accuracy described for da/dN values was valid for Bates’ and Clark’s equation confirming validity of their work. While these beach marks further confirm the brittle nature of the recycled powder specimens, follow-on research involving FCGR testing on virgin powder specimens should be considered to exhaustively capture the material properties fabricated by the EBM process.

Chapter 6: Summary and Additional Work

The goals of this research were to characterize the orientation dependence of FT and FCGR by AM Ti-6Al-4V EBM and test the material performance of virgin powder versus heavily reused powder. Testing methodology was derived from ASTM E399-20 and E647-15. C(T) specimens were subjected to a constant ramping force in tension until fracture for FT testing and to constant amplitude fatigue stress in tension until fracture for FCGR testing and. Both tests required measurement of a growing crack length and the amplitude of force applied. Crack length was measured by means of a crack opening displacement gauge and the force applied was measured by means of a load cell on the testing frame. Hypothesized questions for this research were as follows: What effect does build orientation in non-orthogonal directions have on material performance? How much effect does recycled powder have on material performance?

1. FT testing reported values primarily within the lower end of the rage of previous research for as built EBM Ti-6Al-4V and well below the ranges for other cast and wrought ranges. FCGR testing reported calculated Paris Law values congruent of those also from previous research. While AM poses unique opportunities to generate Ti-6Al-4V materials of a complex nature, careful consideration must be given towards its intended use. Recommendation for future testing includes conducting FT testing on recycled powder specimens.
2. Orientation dependence effects were examined to determine the effect anisotropy has on material performance. Use of AM Ti-6Al-4V for quality controlled testing comes with careful understanding of applied force. In this research build orientation affects Kth at the crack tip due to energy dispersion differences at dislocations. This dependence leads to a comparatively reduced performance when built in the horizontal direction. Consequently,

performance capitalization can be achieved simply by changing the direction at which a specimen is built. While this research identified 30 degrees to ultimately serve as the best angle, future work should be conducted to assess the orientation dependence of more finely chosen angles to more thoroughly understand the effects of material characteristics.

3. Effects of powder reuse were examined in this study such that powder reuse decreases performance mainly due to oxidization of powder from an increase of Oxygen concentration. An increase in dislocations microstructurally create small defects leading to the ultimate degradation of material performance. Since powder reused in this study was heavily reused, future work should characterize powder content and examine FT to exhaustively examine the effects of recycled powder on material performance.

References

1 Charkaluk, E. & Chastand, V. (2018). Fatigue of Additive Manufacturing Specimens: A Comparison with Casting Processes. *The 18th International Conference on Experimental Mechanics*, 2(8), 474. https://doi.org/10.3390/ICEM18-05352

2 Babu, S. S. & Godridge,R. (2015). Additive Manufacturing. *Materials Science and Technology*, 31(8), 881-883. https://doi.org/10.1179/0267083615Z.000000000929

3 Blackwell, P. L. & Wisbey, A. (2005). Laser-aided manufacturing technologies; their application to the near-net shape forming of a high strength titanium alloy. *Journal of Materials Processing Technology*, 170, 268-276. https://doi.org/10.1016/j.jmatprotec.2005.05.014

4 Frazier, W. (2014). Metal Additive Manufacturing: A Review. *Journal of Materials Engineering and Performance*, 23, 1917-1928. https://doi.org/10.1007/s11665-014-0958-z

5 Khidhir, B. (2016). Comprehensive Study on Machinability of Titanium Composite. *Journal of Materials Science and Chemical Engineering*, 4(2), 1-7. http://dx.doi.org/10.4236/msce.2016.42001

6 Galarraga, H., Warren, R., Lados, D., Dehoff, R., & Kirka, M. (2017). Fatigue crack growth mechanisms at the microstructure scale in as-fabricated and heat treated Ti-6Al-4V ELI manufactured by electron beam melting (EBM). *Engineering Fracture Mechanics, 176*, 263-280. https://doi.org/10.1016/j.engfracmech.2017.03.024

7 Edwards, P. & Mamidala, R. (2014). Fatigue performance evaluation of selective laser melted Ti-6Al-4V. *Materials Science & Engineering A*, 598, 327-337. https://doi.org/10.1016/j.msea.2014.01.041

8 Persenot, T., Burr, A., Martin, G., Buffiere, J., Dendievel, R., & Maire, E. (2018). Effect of build orientation on the fatigue properties of as-built Electron Beam Melted Ti-6Al-4V alloy. *International Journal of Fatigue*, 118, 65-76. https://doi.org/10.1016/j.ijfatigue.2018.08.006

9 Hrabe, N. & Quinn, T. (2013). Effects of processing on microstructure and mechanical properties of a titanium alloy (Ti-6Al-4V) fabricated using electron beam melting (EBM), Part 2: Energy input, orientation, and location. *Materials Science & Engineering A*, 573, 271-277. https://doi.org/10.1016/j.msea.2013.02.065

10 Lewandowski, J. & Seifi, M. (2016). Metal Additive Manufacturing: A Review of Mechanical Properties. *Annual Review of Materials Research*, 46, 151-186. https://doi.org/10.1146/annurev-matsci-070115-032024

11 Edwards, P., O’Conner, A., & Mamidala, R. (2013). Electron Beam Additive manufacturing of Titanium Components: Properties and Performance. *Journal of Manufacturing Science and Engineering*, 135(6), 061016. https://doi.org/10.1115/1.4025773

12 Pereira, T., Kennedy, J., Potgieter, J. (2019). A comparison of traditional manufacturing vs additive manufacturing, the best method for the job. *Procedia Manufacturing*, 30, 11-18. https://doi.org/10.1016/j.promfg.2019.02.003

13 Kumar, K., Zindani, D., & Davim, J. (2019). *Additive manufacturing technologies from an optimization perspective.* https://doi.org/10.4018/978-1-5225-9167-2

14 Carou, D. & Davim, J. (2018). *Machining of Light Alloy*s: Aluminum, Titanium, and Magnesium (1st ed.). Routledge. https://doi.org/10.1201/b22153

15 Tadjedeh, Y. (2014). Navy Beefs Up 3D Printing Efforts with New 'Print the Fleet' Program. *National Defense*, 99(731), 24-26. Retrieved from: https://www.military.com/daily-news/2014/10/17/navy-beefs-up-3dprinting-efforts-with-new-print-the-fleet-pro.html

16 Jovanovic, V., Bilgen, O., Arcaute., & Audette, M. (2017). Active Duty Training for Support of Navy's Additive Manufacturing Strategy. *American Society for Engineering Education,* 17844. https://doi.org/10.18260/1-2--27534

17 Bevan, M, (2018). Navy Awards Potential $6.4 Million Quality Metal Additive Manufacturing (Quality MADE) Contract to Concurrent Technologies Corporation. *GlobeNewsire.* Retrieved from: https://www.globenewswire.com/news-release/2018/03/27/1453836/0/en/Navy-Awards-Potential-6-4-Million-Quality-Metal-Additive-Manufacturing-Quality-MADE-Contract-to-Concurrent-Technologies-Corporation.html

18 Kosowatz, J. (2019). U.S. Navy Lays The Keel for 3-D Printing. *Mechanical Engineering,* 141(03), 42-45. https://doi.org/10.1115/1.2019-MAR-3

19 Lin, S. & Shin, Y. (2019). Additive manufacturing of Ti6Al4V alloy: A review. *Materials and Design,* 164, 107552. https://doi.org/10.1016/j.matdes.2018.107552

20 Seifi, M., Dahar, M., Aman, R., Harrysson, O., Beuth, J., & Lewandowski, J. (2015). Evaluation of Orientation Dependence of Fracture Toughness and Fatigue Crack Propagation Behavior of As-Deposited ARCAM EBM Ti-6Al-4V. *Journal of Minerals, Metals & Materials Society,* 67(3), 597-607. https://doi.org/10.1007/s11837-015-1298-7

21 Ahmed, N., Basem, A., Saied, D., Moiduddin, K., Pervaiz, S., Alahmari, A., & Naveed, M. (2017). Electron beam melting of titanium alloy and surface finish improvement trough rotary ultrasonic machining. *International Journal of Advanced Manufacturing Technology,* 92(1), 3349-3361. http://doi.org/10.1007/s00170-017-0365-3

22 Bannantine, J., Comer, J., & Handrock, J. (1990). Fundamentals of Metal Fatigue Analysis. Englewood Cliffs, New Jersey: Prentice Hall.

23 Vayssette, B., Saintier, N., Brugger, C., Elmay, M. (2018). Surface roughness for Ti-6Al-4V parts obtained by SLM and EBM: Effect on the High Cycle Fatigue life. *Procedia Engineering,* 213, 89-97. http://doi.org/10.1016/j.proeng.2018.02.010

24 Greitemeier, D., Palm, F., Syassen, F., & Melz, T. (2017). Fatigue performencae of additive manufactured TiAl6V4 using electron and laser beam melting. *International Journal of Fatigue,* 94, 211-217. https://doi.org/10.1016/j.ijfatigue.2016.05.001

25 Liu, S. & Shin, Y. (2019). Additive manufacturing of Ti6Al4V alloy: a review. *Materials and Design,* 164, 107552. https://doi.org/10.1016/j.matdes.2018.107552

26 Anderson T. (2017). *Fracture Mechanics - Fundamentals and Applications (3^{rd} ed.).* CRC Press. https://doi.org/10.1201/9781315370293

27 Rice, J. (1968). *Mathematical Analysis in the Mechanics of Fracture*. Chapter 3 of Fracture: An Advanced Treatise (Vol. 2, Mathematical Fundamentals) (ed. H. Liebowitz). Academic Press, N.Y. 191-311.

28 ASTM E1820-20a, "Standard Test Method for Measurement of Fracture Toughness," ASTM International, West Conshohocken, PA, 2020. https://doi.org/10.1520/E1820-20A

29 Edwards, P. & Mamidala, R. (2015). Effect of build direction on the fracture toughness and fatigue crack growth in selective laser melted Ti-6Al-4V. *Fatigue & Fracture of Engineering Materials & Structures,* 38(10), 1228-1236. https://doi.org/10.1111/ffe.12303

30 Ghods, S., Schultz, E., Wisdom, C., Schur, R., Pahuja, R., Montelione, A., Arola, D., & Mamidala, R. (2020). Electron beam additive manufacturing of Ti6Al4V: Evolution of powder morphology and part microstructure with powder reuse. *Materialia*, 9(6), 100631. https://doi.org/10.1016/j.mtla.2020.100631

31 ASTM E399-20, "Standard Test Method for Linear-Elastic Plane-Strain Fracture Toughness of Metallic Materials," ASTM International, West Conshohocken, PA, 2020. https://doi.org/10.1520/E0399-20

32 Mertova, K., Dzugan, J., Roudnicka, M., Daniel, M., Vojtech, D., Seifi, M., & Lewandowski, J. (2020). Build Size and Orientation Influence on Mechanical Properties of Powder Bed Fusion Deposited Titanium Parts. *Metals,* 10(10), 1340. https://doi.org/10.3390/met10101340

33 ASTM E647-15, "Standard Test Method for Measurement of Fatigue Crack Growth Rates," ASTM International, West Conshohocken, PA, 2016. https://doi.org/10.1520/E0647-15

34 Boyce, B. & Ritchie, R. (2001). Effect of load ratio and maximum stress intensity on the fatigue threshold in Ti-6Al-4V. *Engineering Fracture Mechanics,* 68(2), 129-147. https://doi.org/10.1016/S0013-7944(00)00099-0

35 Ding, J., Hall, R., & Byrne, J. (2005). Effects of stress ratio and temperature on fatigue crack growth in a Ti-6Al-4V alloy. *International Journal of Fatigue,* 27(10), 1551-1558. https://doi.org/10.1016/j.ijfatigue.2005.06.007

36 AMS 4962, "Titanium Alloy, Investment Castings 6Al 4V Hot Isostatically Pressed," SAE International, Warrendale, PA, 2016. https://doi.org/10.4271/AMS4962

37 Froes, F. & Caplan, I. (1993). Titanium '92. *Titanium Committee of the Minerals, Metals & Materials Structural Metals Division,* 1, 311-318.

38 Biswas, N, Ding, J., Balla, V., Field, D., & Bandyoadhyay, A. (2012). Deformation and fracture behavior of laser processed dense and porous Ti6Al4V alloy under static and dynamic loading. *Materials Science and Engineering A,* 549, 213-221. https://doi.org/10.1016/j.msea.2012.04.036

39 Li, P., Guo, W., Huang, W., Su, Y., Lin, X., & Yuan, K. (2015). Thermomechanical response of 3D laser-deposited Ti–6Al–4V alloy over a wide range of strain rates and temperatures.

Materials Science and Engineering A, 647, 34-42. https://doi.org/10.1016/j.msea.2015.08.043

40 Debroy, T., Wei, H., Zuback, J., Mukherjee, T., Elmer, J., Milewski, J., Beese, A., Wilson-Heid, A., De, A., & Zhang, W. (2018). Additive manufacturing of metallic components – Process, structure and properties. *Progress in Materials Science*, 92, 112-224. https://doi.org/10.1016/j.pmatsci.2017.10.001

41 Tiferet, E., Ganor, M., Zolotaryov, D., & Garkun, A. (2019). Mapping the Tray of Electron Beam Melting of Ti-6Al-4V: Properties and Microstructure. *Materials,* 12(9), 1470. https://doi.org/10.3390/ma12091470

42 Körner, C. (2016). Additive manufacturing of metallic components by selective electron beam melting - A review. *International Materials Reviews*, 61(5), 361–377. https://doi.org/10.1080/09506608.2016.1176289

Appendix A: Fracture Toughness Data

A.1 MATLAB Code

```
clear all, close all, clc
```

Import Data

```
PV = load('12.txt');
title_ = PV(1,1);
a = PV(1,2); % final crack length m
PV(1,:) = [];
E = 120*10^9;%(Pa) Modulus of Elasticity
W = 0.024; % specimen width, m (in)
B = 0.006; % specimen thickness, m (in), standard is W/2
B_N = B; % unless side grooves are used, then B_N is the tickness
%between the roots
Sig_YS = 900000000; % 0.2% offset yield strength in tension, Pa
P = PV(:,3); %Given in N
V = PV(:,2); %Displacement in mm
P = -1.*P; % Flip the force vector due to machine output
V = V./1000; % Convert mm to m
% create a polynomial fit of the data for follow-on calcuations
[p,~,mu] = polyfit(V,P,6);
V1 = linspace(min(V),max(V),1000);
PVcurve = polyval(p,V1,[],mu);
```

Find Slope between Lower (P_l) and Upper (P_u) bound Force points

```
linpts = [450 477 433 631 581 761 565 490 484 445 413 462]; %Discretionary
%points identifying termination of linearity
% Identify P_l point as the start of linear region
P1_P = P(1); % P lower y coordinate
P1_V = V(1); % P lower x coordinate
% Identify P_u point as the upper end of linear region
P2_P = P(linpts(title_));
% P upper y coordinate
P2_V = V(linpts(title_));
% P upper x coordinate
P_V = [P1_V P2_V];
P_P = [P1_P P2_P];
SlopePV = (P_P(2)-P_P(1))/(P_V(2)-P_V(1)); % slope of test data
SlopeP_Q = .95*SlopePV; % slope of P_Q
y = SlopeP_Q*(V1-P1_V)+P1_P; % equation of 95% secant line for P_Q
```

Find P_Q point at the intersection of PV data and 95% Secant line

```
f1 = @(x) SlopeP_Q.*(x-V(1))+P(1);
i = 1;
y1 = 0;
while V1(i) < 0.0002
    y1 = PVcurve(i);
    xc = V1(i);
    i = i+1;
end

while f1(V1(i)) < PVcurve(i)
    y1 = PVcurve(i);
    xc = V1(i);
    i = i+1;
    if f1(V1(i)) > PVcurve(i)
        break
    end
end

P_Q = y1;
```

Identify P_max and corresponding index in V vector

```
[P_max,V_Index] = max(P);
figure(1)
plot(V,P,'+','LineWidth',0.75,'MarkerEdgeColor','k')
hold on
plot(V1,PVcurve,'b','LineWidth',1.5)
hold on
plot(P_V,P_P,'*r','LineWidth',1.5)
hold on
plot(P_V,P_P,'-r','LineWidth',1.5)
hold on
plot(V1,y,'--m','LineWidth',1.5)
hold on
plot(xc,P_Q,'om','LineWidth',1.5)
hold on
plot(V(V_Index),P_max,'ok','LineWidth',1.5)
grid on
grid minor
legend('PV Data','PV polyfit','Linear Points','Linear Region',...
    '95% Secant (P/V)','P_Q','P_M_a_x','location','best')
xlabel('Displacement (mm)')
ylabel('Load (N)')
specimen = "Specimen";
title_ = sprintf('%d',title_);
title(specimen + ' ' + title_);
ylim([0 inf])
```

Test 1 for data validity

```
test1 = P_max/P_Q;
if test1 > 1.10
 test1text = ['P_max/P_Q = ', num2str(test1),...
 ', P_max/P_Q > 1.10, test is not valid, must use elastic plastic fracture toughness'];
 disp(test1text)
else
 disp('Test 1 is valid')
end
```

Calculation of K_Q

```
aW = a/W;
W_minus_a = W-a;
F_aW = (2+aW)*(0.886+(4.64*aW)-(13.32*aW^2)+(14.72*aW^3)-...
(5.6*aW^4))/((1-aW)^(3/2));
K_Q = (P_Q/(sqrt(B*B_N)*sqrt(W)))*F_aW;

% Test 2 for data validity
test2 = 2.5*(K_Q/Sig_YS)^2;
if test2 < W_minus_a
 K_Ic = K_Q;
 test2text1 = ['K_Ic = ', num2str(K_Ic/1000000),' MPa*sqrt(m)'];
 disp('Test 2 is valid')
 disp(test2text1)
else
 test2text2 = ('Test 2 is invalid');
 disp(test2text2)
end
```

Published with MATLAB® R2019a

A.2 Load Displacement Curves

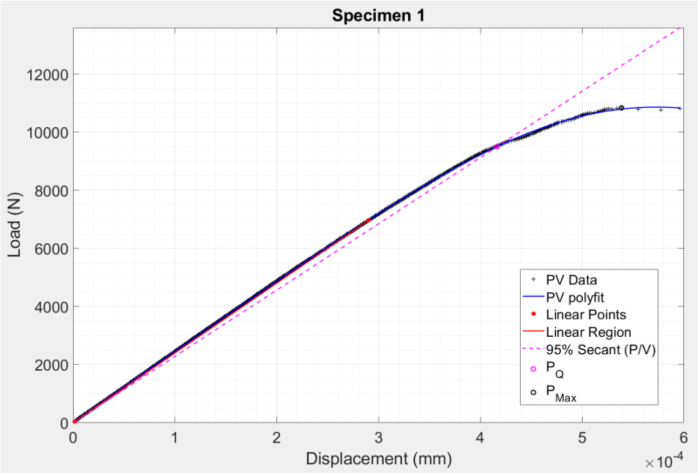

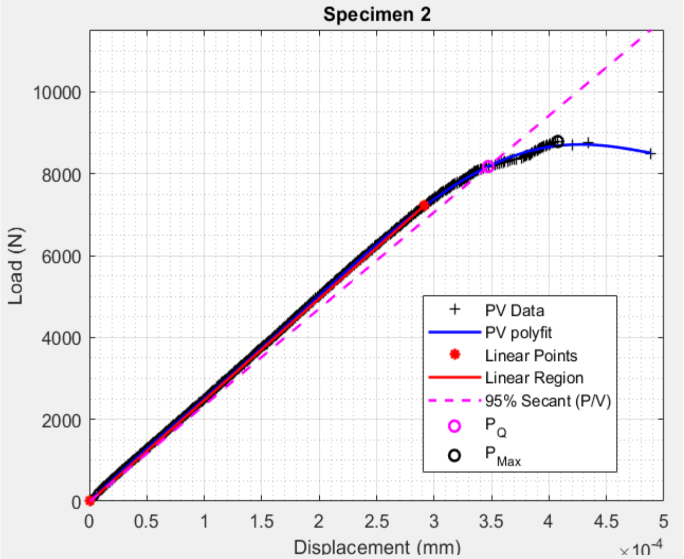

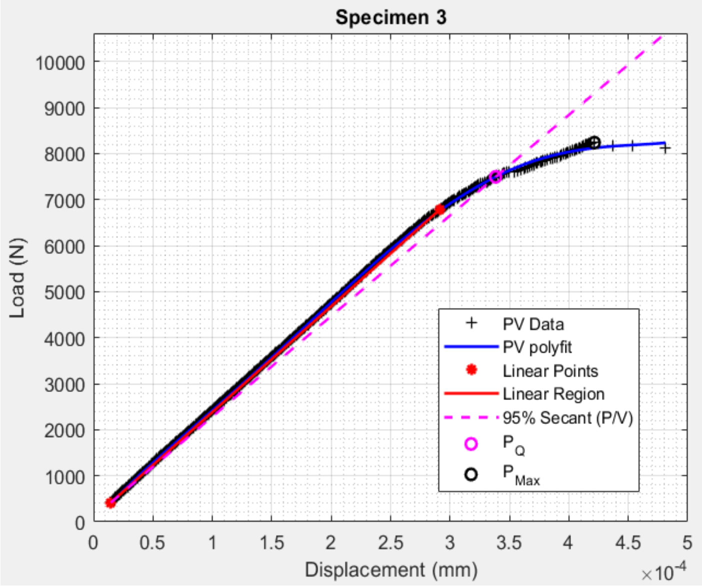

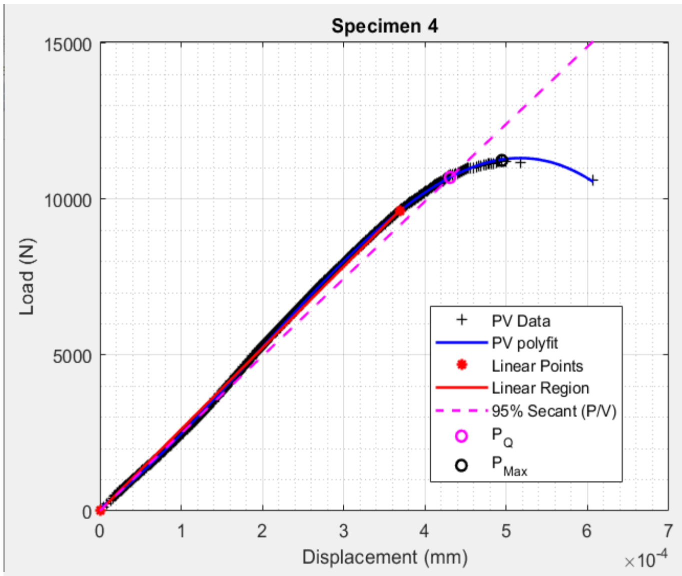
Specimen 4
Load (N)
15000
10000
5000
0
Displacement (mm)
0
1
2
3
4
5
6
7
×10⁻⁴
+ PV Data
PV polyfit
Linear Points
Linear Region
95% Secant (P/V)
P_Q
P_Max

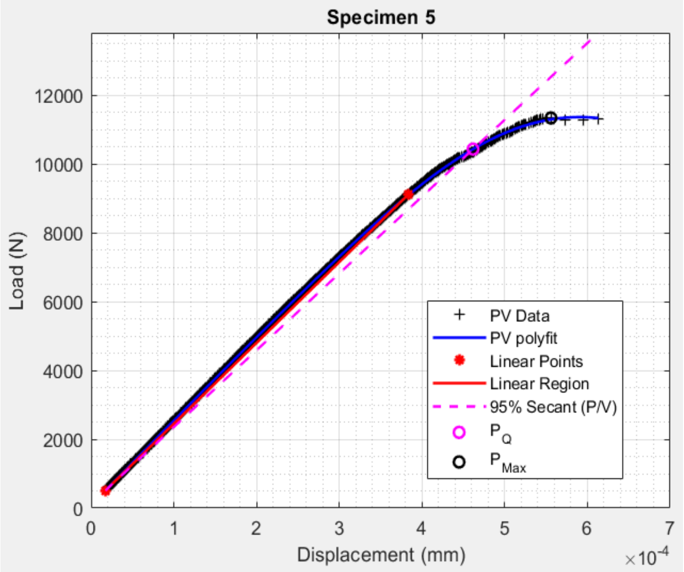
Specimen 5
Load (N)
12000
10000
8000
6000
4000
2000
0
Displacement (mm)
0
1
2
3
4
5
6
7
×10⁻⁴
+ PV Data
PV polyfit
Linear Points
Linear Region
95% Secant (P/V)
P_Q
P_Max

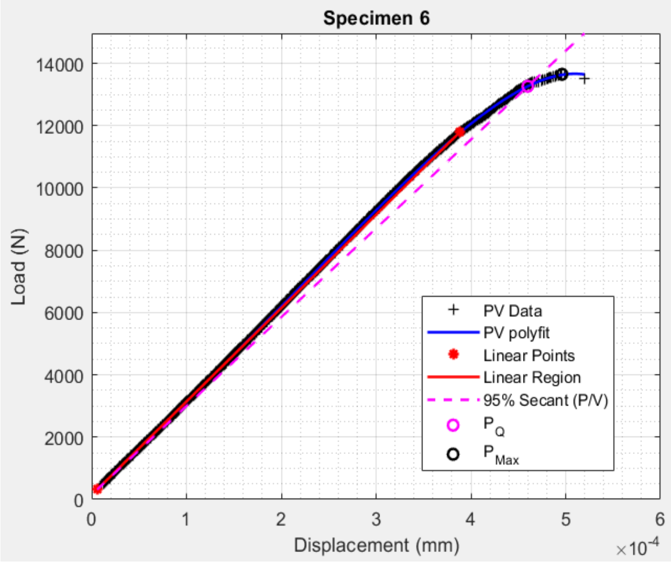
Specimen 6
Load (N)
14000
12000
10000
8000
6000
4000
2000
0
Displacement (mm)
0
1
2
3
4
5
6
×10⁻⁴
+ PV Data
PV polyfit
Linear Points
Linear Region
95% Secant (P/V)
P_Q
P_Max

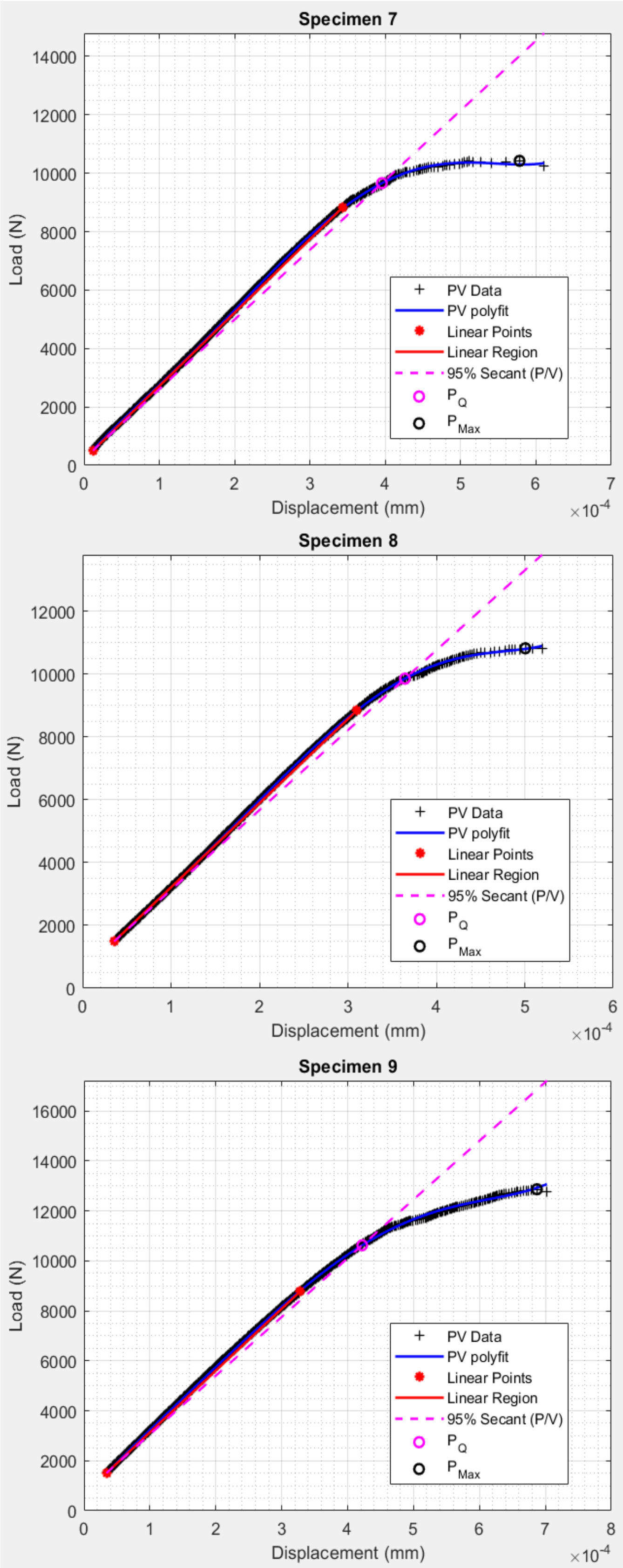
Specimen 7
Load (N)
Displacement (mm)
$\times 10^{-4}$
0
2000
4000
6000
8000
10000
12000
14000
0
1
2
3
4
5
6
7
PV Data
PV polyfit
Linear Points
Linear Region
95% Secant (P/V)
P_Q
P_{Max}
Specimen 8
Load (N)
Displacement (mm)
$\times 10^{-4}$
0
2000
4000
6000
8000
10000
12000
0
1
2
3
4
5
6
PV Data
PV polyfit
Linear Points
Linear Region
95% Secant (P/V)
P_Q
P_{Max}
Specimen 9
Load (N)
Displacement (mm)
$\times 10^{-4}$
0
2000
4000
6000
8000
10000
12000
14000
16000
0
1
2
3
4
5
6
7
8
PV Data
PV polyfit
Linear Points
Linear Region
95% Secant (P/V)
P_Q
P_{Max}

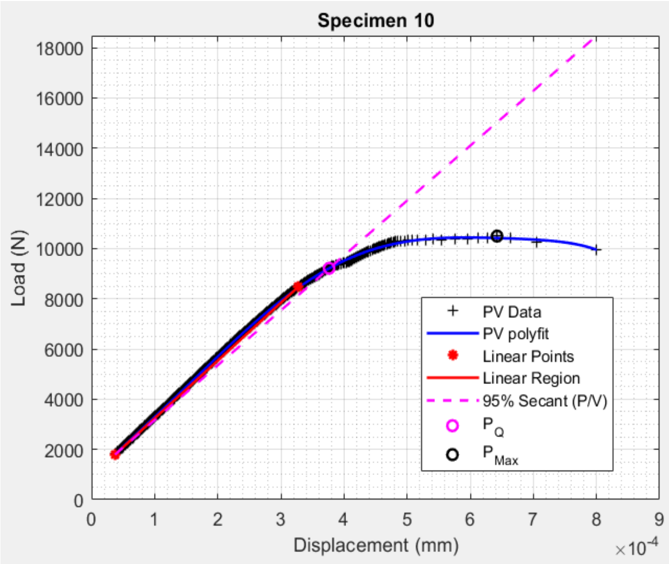
Specimen 10
Load (N)
18000
16000
14000
12000
10000
8000
6000
4000
2000
0
0
1
2
3
4
5
6
7
8
9
Displacement (mm)
×10^-4
PV Data
PV polyfit
Linear Points
Linear Region
95% Secant (P/V)
P_Q
P_Max

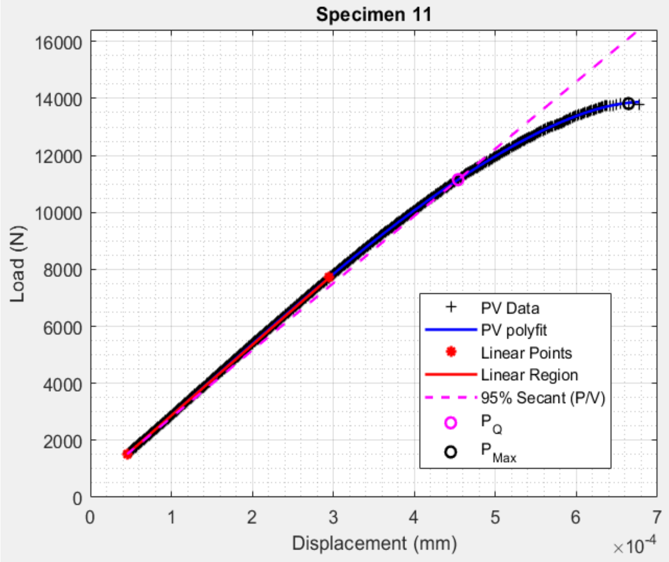
Specimen 11
Load (N)
16000
14000
12000
10000
8000
6000
4000
2000
0
0
1
2
3
4
5
6
7
Displacement (mm)
×10^-4
PV Data
PV polyfit
Linear Points
Linear Region
95% Secant (P/V)
P_Q
P_Max

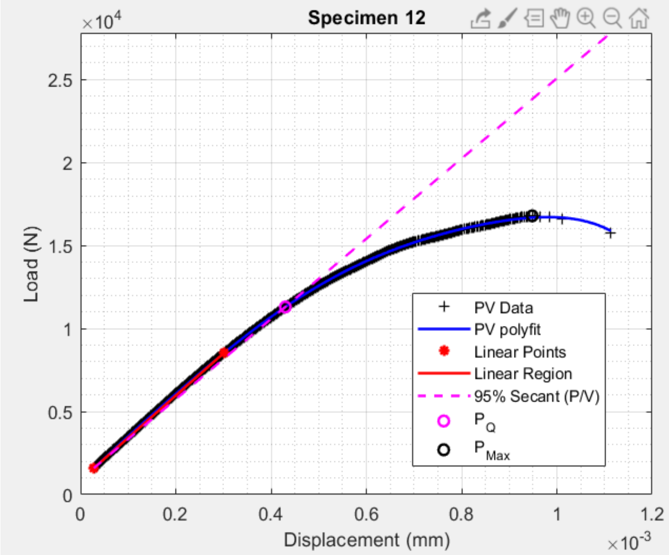
Specimen 12
×10^4
Load (N)
2.5
2
1.5
1
0.5
0
0
0.2
0.4
0.6
0.8
1
1.2
Displacement (mm)
×10^-3
PV Data
PV polyfit
Linear Points
Linear Region
95% Secant (P/V)
P_Q
P_Max

A.3 Critical FT Data

Specimen	a_0 (mm)	a_0/W	a_f (mm)	a_f/W
1	7.15	0.2979	8.24	0.3433
2	7.1	0.2958	9.34	0.3890
3	7.0	0.2917	10.06	0.4190
4	7.2	0.3000	8.14	0.3392
5	7.25	0.2979	8.24	0.3433
6	7.2	0.3000	6.53	0.2721
7	7.25	0.3979	8.24	0.3567
8	7.2	0.3000	8.17	0.3403
9	7.1	0.2958	7.8	0.3267
10	7.25	0.3979	8.96	0.3735
11	7.3	0.3042	7.08	0.2949
12	7.3	0.3402	7.26	0.3025

A.4 Longitudinal and Transverse Profiles

A.4.2 Specimen 4, 6 mm width, 30 degrees

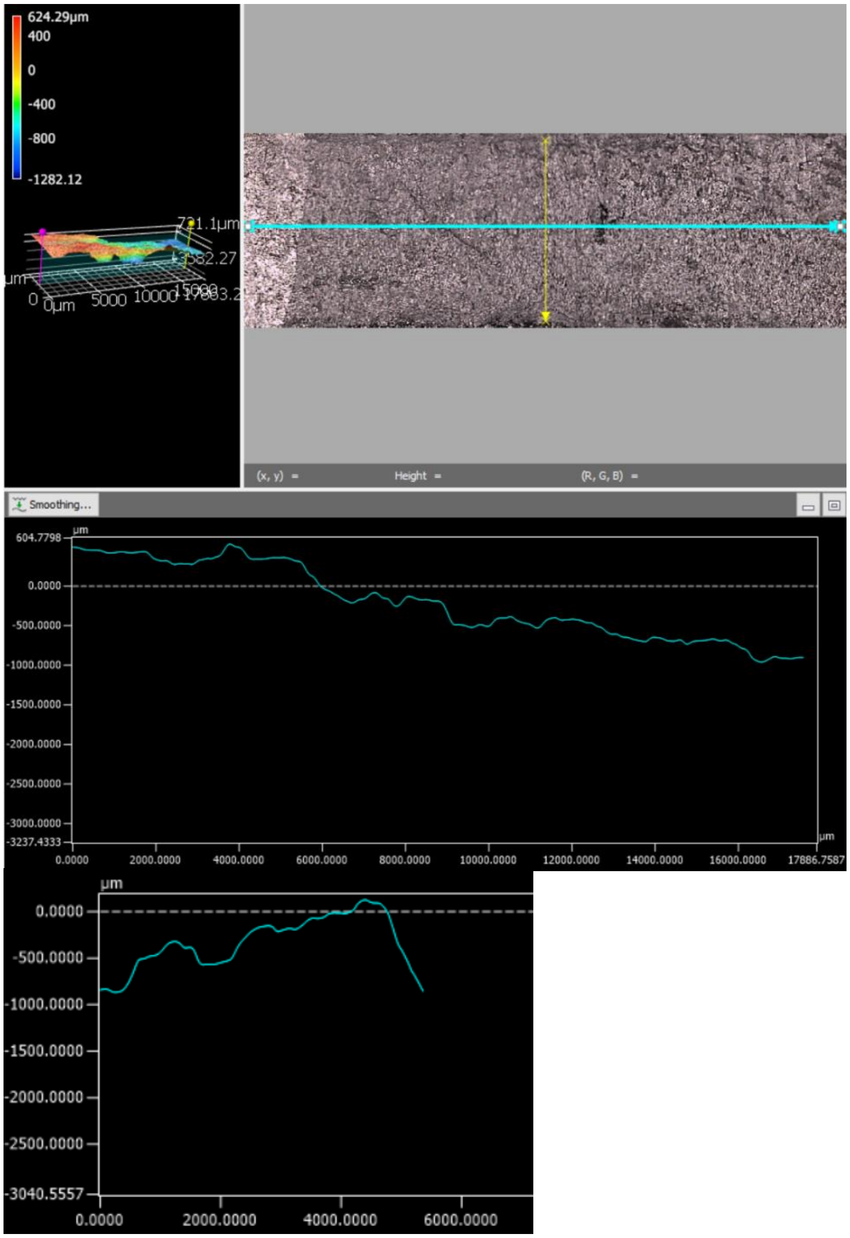

A.4.3 Specimen 8, 6 mm width, 60 degrees

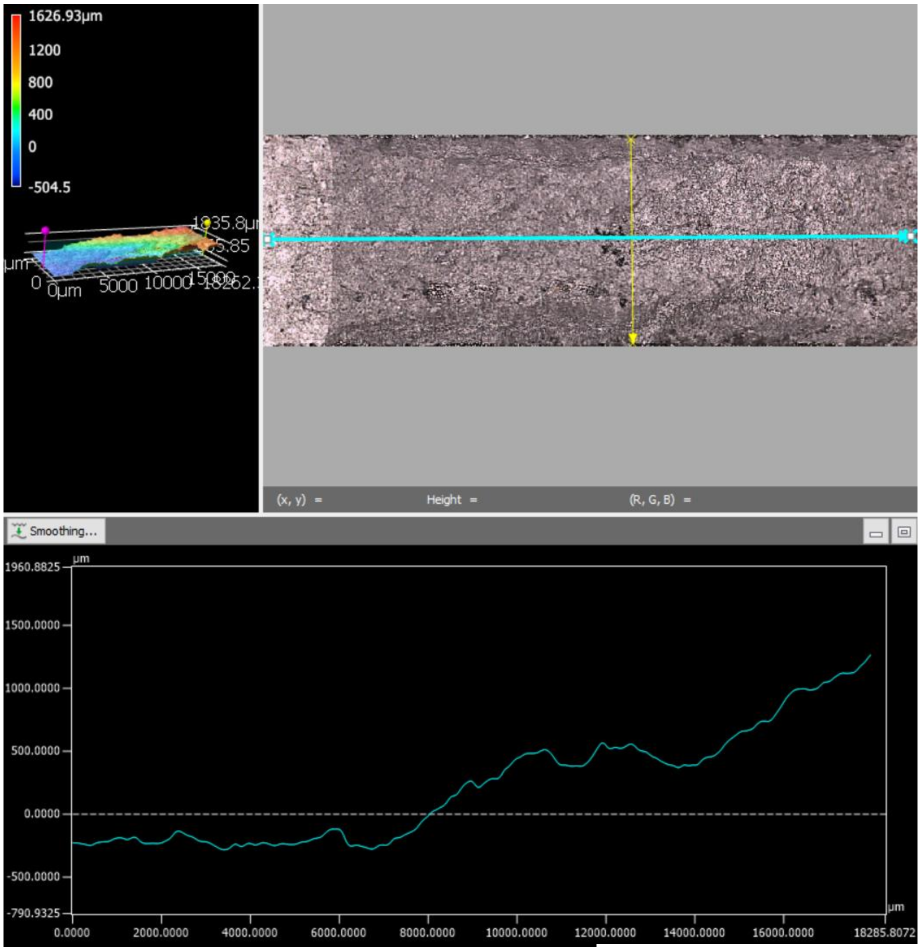

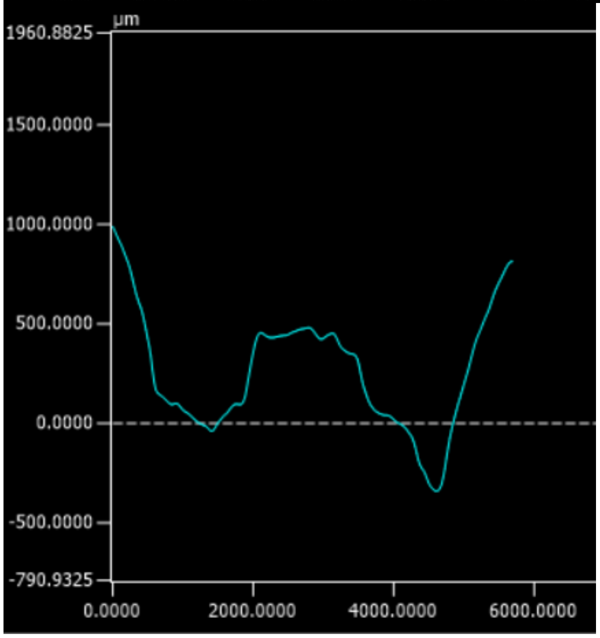

Appendix B: Fatigue Crack Growth Rate Data

B.1 MATLAB Code

```
clc,clear,close all
```

Batch process of values consistent across all specimens

```
W = 0.024; %m
E = 120*10^9;%(Pa) Modulus of Elasticity
```

User imports data

```
data = importdata('1.txt');
title_ = data(1,1);
offset = data(2,1);
P = data(1,2); %Value preloaded in .txt file
dP = 0.9*P;
B = data(1,3); %Value preloaded in .txt file
data(1,:) = []; %Clear preload values
data(1,:) = []; %Clear preload values
```

Condense and Assign Data

```
j = 1;
for i = 1:length(data)/10
    cycles(i) = j;
    j = j+10;
end

for i = 1:length(data)
    time(i) = data(i,1); % s
    cmod(i) = data(i,2)/1E3; %displacement at mouth in m
    force(i) = data(i,3); % N
end

[cmodMax,cmodMaxIdx] = findpeaks(cmod);
[cmodMin,cmodMinIdx] = findpeaks(-cmod);
Dcmod = (cmodMax - cmodMin)./(force(cmodMaxIdx)-force(cmodMinIdx));
Dcmod(Dcmod==-inf)=[];%Deletes any irrational values
```

Crack Length Calculation

```
ux = ((E.*Dcmod.*B).^.5 + 1).^-1;
ux = ux(ux==real(ux));
a = W*(1.0010 - 4.6695*ux + 18.460*ux.^2 - 236.82*ux.^3 + ...
1214.9*ux.^4 - 2143.6*ux.^5);
```

Delta K calculations

```
for i = 1:length(a)
    alpha(i) = a(i)/W;
end

cyclesdK = cycles;
cyclesdK(length(cycles)+1) = cycles(end)+1;

dK = dP.*(2+alpha).*(0.886+4.64.*alpha-13.32.*alpha.^2+...
        14.72.*alpha.^3-5.6.*alpha.^4)./(B.*sqrt(W).*((1-alpha).^(1.5)));
```

Calculate da/dN

```
adadn(1) = a(1); %Initiate starting point

%This loop results in a vector that only steps up crack size
j = 2;
for i = 2:length(a)
    if a(i) > adadn(j-1)
        adadn(j) = a(i);
        cyclesdn(j) = cyclesdK(i);
        j = j+1;
    end
end

aadadn(1) = adadn(1); %Initiate starting point
tol = 0.0005;

%This loop takes increasing crack size and generates a new vector for crack
%size based on tolerance averaging the batch crack size to cycles resulting
%in sensitive but accurate data up to Region III behavior.
j = 1;
for i = 1:0.9*length(adadn)
    r = i;
    while adadn(i) < aadadn(j) + tol
        i = i+1;
    end
        j = j+1;
    aadadn(j) = mean(adadn(r:i));
    ccyclesdn(j) = mean(cyclesdn(r:i));
end
```

```
%The next couple of iterative series performs the same function as previous
%loop but with predefined steps. This is necessary based on increasing rate
%of Region III da/dN behavior.
j = j+1;

for j = j:length(adadn)-10
    aadadn(j)=mean(adadn(j:j+10));
    ccyclesdn(j) = cyclesdn(j);
end

for j = j:length(adadn)-5
    aadadn(j)=mean(adadn(j:j+5));
    ccyclesdn(j) = cyclesdn(j);
end

for j = j:length(adadn)-3
    aadadn(j)=mean(adadn(j:j+5));
    ccyclesdn(j) = cyclesdn(j);
end

%Perform da/dN calculations and assign all negative values value of 0
for i = 1:length(aadadn)-1
    dadn(i) = (aadadn(i+1)-aadadn(i))/(ccyclesdn(i+1)-ccyclesdn(i));
    if dadn(i) < 0
        dadn(i) = 0;
    end
end

%Filter all calculated negative da/dN values
dadn(dadn==0)=[];

%Assigns values of dK for all calculated values of da/dN
i = 2;
while i < length(dadn)
    f = round(ccyclesdn(i)/10);
    dKnew(i) = dK(f);
    i = i+1;
end
```

Plot and label

```
%Over the course of the code, cycles have been divided by 10 (otherwise
%considered as 10*m/cycle)therefore dadn must be multiplied by 100 to
%achieve desired mm/cycle. Likewise dK must be divided by 1E6 to achieve
%desired MPa*m^0.5.

loglog(dKnew/1E6,dadn*100, 's')
xlabel('\DeltaK (MPa m^{(1/2)})')
ylabel('da/dN (mm/cycle)')
hold on
```

```
grid on
xlabel('\DeltaK (MPa m^{(1/2)})')
ylabel('da/dN (mm/cycle)')
hold on
set(gca, 'YScale', 'log')
set(gca, 'XScale', 'log')
specimen = "Specimen";
title_ = sprintf('%d',title_);
title(specimen + ' ' + title_);
```

Published with MATLAB® R2019a

B.2 da/dN vs. ΔK Curves

Specimen 1 (60°) B=12 mm

a	N	ΔK	da/dN
0.006109	1181	24.93438	1.40E-07
0.006119	1771	25.17725	2.59E-07
0.006126	2361	25.35529	2.87E-07
0.00614	2951	25.39073	2.62E-07
0.00615	3541	25.56559	2.88E-07
0.006166	4131	25.76154	3.08E-07
0.006176	4721	26.02994	2.92E-07
0.006183	5311	26.09275	3.47E-07
0.006188	5901	26.31907	3.59E-07
0.006206	6491	26.62916	3.42E-07
0.006211	7081	26.789	4.05E-07
0.006217	7671	26.99566	3.67E-07
0.006239	8261	27.32573	4.61E-07
0.006248	8851	27.78592	4.21E-07
0.006251	9441	27.97526	5.23E-07
0.006262	10031	28.13734	5.28E-07
0.006272	10621	28.7728	5.96E-07
0.006274	11211	29.11852	5.87E-07
0.006309	11801	29.6227	5.88E-07
0.0064	12391	30.12925	5.98E-07
0.006451	12981	30.78746	8.14E-07
0.006569	13571	31.02791	7.73E-07
0.006725	14161	31.43384	9.55E-07
0.006906	14751	32.28689	1.01E-06
0.007071	15341	32.90808	1.35E-06
0.007209	15931	33.49376	1.46E-06
0.007441	16521	34.1808	1.62E-06
0.007669	17111	34.85625	1.85E-06
0.008004	17701	35.6488	1.60E-06
0.090236	18291	35.6488	1.87E-06
0.010757	18881	38.563	2.75E-06
0.0114	19471	40.864	3.79E-06

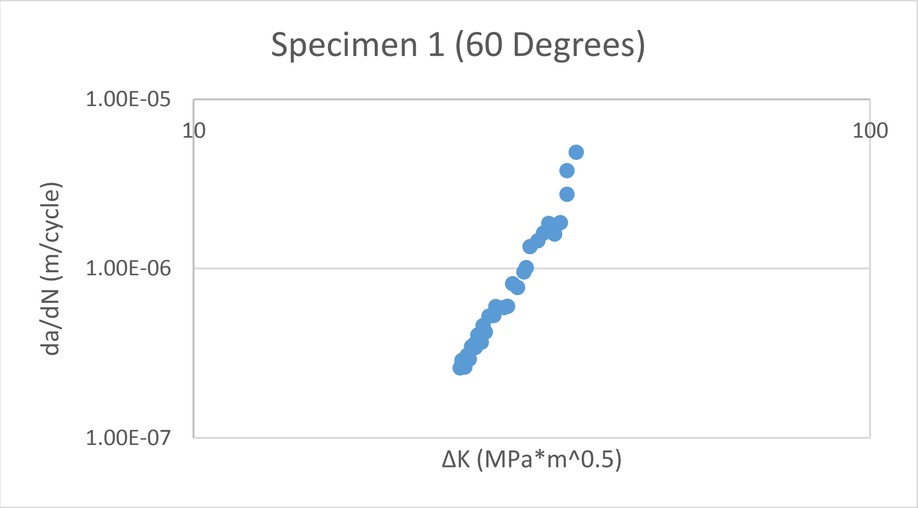

Specimen 2 (30°) B=12 mm

a	N	ΔK	da/dN
0.006106	1	0	2.10E-08
0.006126	4201	12.45009	4.65E-08
0.006139	8401	12.57016	7.15E-08
0.006168	12601	13.2636	5.93E-08
0.006172	16801	13.74584	8.68E-08
0.00619	21001	14.31595	6.24E-08
0.006205	25201	14.88954	9.61E-08
0.006224	29401	15.32134	1.08E-07
0.006245	33601	15.91551	1.12E-07
0.006259	37801	16.32832	1.61E-07
0.006288	42001	16.7792	1.52E-07
0.006296	46201	17.08043	1.60E-07
0.006308	50401	17.91798	1.73E-07
0.006339	54601	18.44203	1.68E-07
0.006358	58801	19.06435	1.50E-07
0.006364	63001	19.60133	1.98E-07
0.006374	67201	20.01298	2.24E-07
0.006394	71401	20.50907	2.59E-07
0.006412	75601	21.19847	2.82E-07
0.006461	79801	21.89771	2.75E-07
0.006646	84001	22.42345	3.18E-07
0.007077	88201	22.90181	3.00E-07
0.007053	92401	23.53537	3.32E-07
0.007381	96601	24.57869	3.72E-07
0.007753	100801	25.48295	4.06E-07
0.007935	105001	26.41528	4.62E-07
0.008476	109201	28.29562	6.35E-07
0.008837	113401	33.36925	6.83E-07
0.009315	117601	37.42003	9.40E-07
0.010015	121801	41.43149	1.88E-06
0.010672	126001	46.01622	2.27E-06
0.011622	130201	52.9866	5.60E-06
0.011814	134401	59.43	1.37E-05

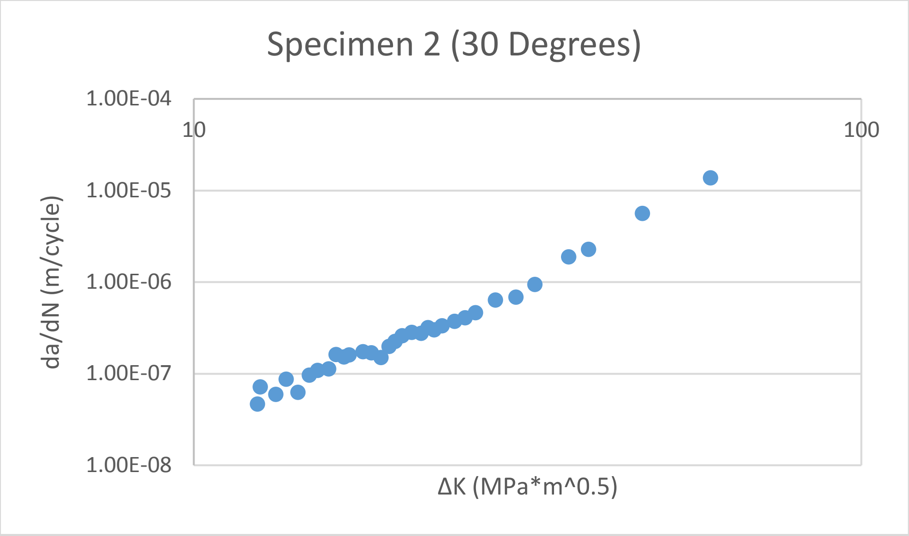

Specimen 3 (60°) B=12 mm

a	N	ΔK	da/dN
0.006107	1	0	1.10E-07
0.006303	811	19.68823	1.12E-07
0.00633	1621	20.01268	1.09E-07
0.006371	2431	20.20474	1.11E-07
0.006537	3241	20.47671	1.39E-07
0.006526	4051	20.92687	1.41E-07
0.006582	4861	21.50176	1.55E-07
0.006671	5671	21.89515	1.81E-07
0.006754	6481	22.37986	1.94E-07
0.006896	7291	22.76484	2.13E-07
0.006978	8101	23.30801	2.45E-07
0.007017	8911	23.78465	2.51E-07
0.007078	9721	24.03111	3.01E-07
0.007191	10531	24.48266	3.43E-07
0.007321	11341	25.28092	3.63E-07
0.007457	12151	26.02928	3.66E-07
0.007544	12961	26.56821	3.82E-07
0.007724	13771	26.98688	3.77E-07
0.007801	14581	27.74251	3.83E-07
0.00802	15391	28.33713	4.02E-07
0.008192	16201	29.17272	4.63E-07
0.008379	17011	30.06422	4.85E-07
0.008565	17821	30.87308	5.46E-07
0.008805	18631	31.78397	7.50E-07
0.009007	19441	33.24633	7.57E-07
0.00939	20251	34.63876	9.93E-07
0.009677	21061	35.98115	9.91E-07
0.009969	21871	37.22497	1.42E-06
0.01031	22681	38.62056	1.45E-06
0.010701	23491	40.4338	1.72E-06
0.012514	24301	42.9779	2.34E-06
0.013833	25111	47.75369	4.86E-06
0.0155	25921	54.3902	1.03E-05

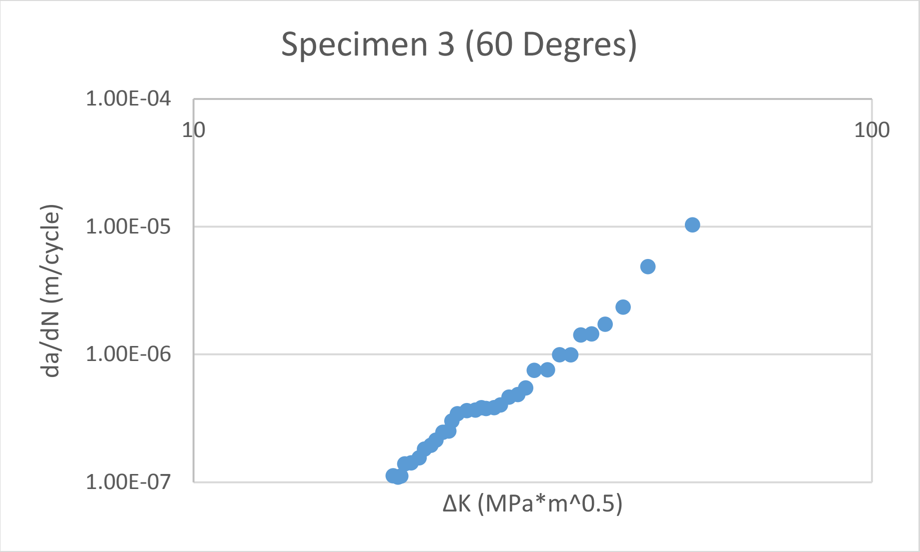

Specimen 4 (90°) B=12 mm

a	N	ΔK	da/dN
0.006147	1	0	7.77E-08
0.006184	1011	19.62978	1.10E-07
0.006177	2021	19.88946	1.10E-07
0.006183	3031	20.16545	1.20E-07
0.006196	4041	20.5751	1.27E-07
0.006241	5051	20.88874	1.36E-07
0.0063	6061	21.21558	1.53E-07
0.00637	7071	21.55046	1.62E-07
0.006407	8081	21.85635	1.75E-07
0.006462	9091	22.28294	1.77E-07
0.006486	10101	22.5729	2.05E-07
0.006559	11111	22.95245	2.06E-07
0.006632	12121	23.52901	2.20E-07
0.00674	13131	23.9224	2.69E-07
0.0068	14141	24.36068	2.93E-07
0.006913	15151	24.72124	2.86E-07
0.007028	16161	25.10169	3.13E-07
0.00714	17171	25.55767	3.63E-07
0.007283	18181	26.05134	3.98E-07
0.007377	19191	26.64931	3.95E-07
0.007565	20201	27.30715	4.10E-07
0.007706	21211	27.84626	4.28E-07
0.007894	22221	28.27907	4.03E-07
0.008085	23231	28.76015	4.29E-07
0.008268	24241	29.29289	5.07E-07
0.008528	25251	30.1228	5.88E-07
0.008812	26261	30.82598	6.16E-07
0.009102	27271	31.95241	7.57E-07
0.009493	28281	33.20971	1.01E-06
0.0099	29291	34.51465	1.19E-06
0.010871	30301	43.09087	1.61E-06
0.012858	31311	47.50063	2.12E-06
0.01489	32321	54.808	8.45E-06

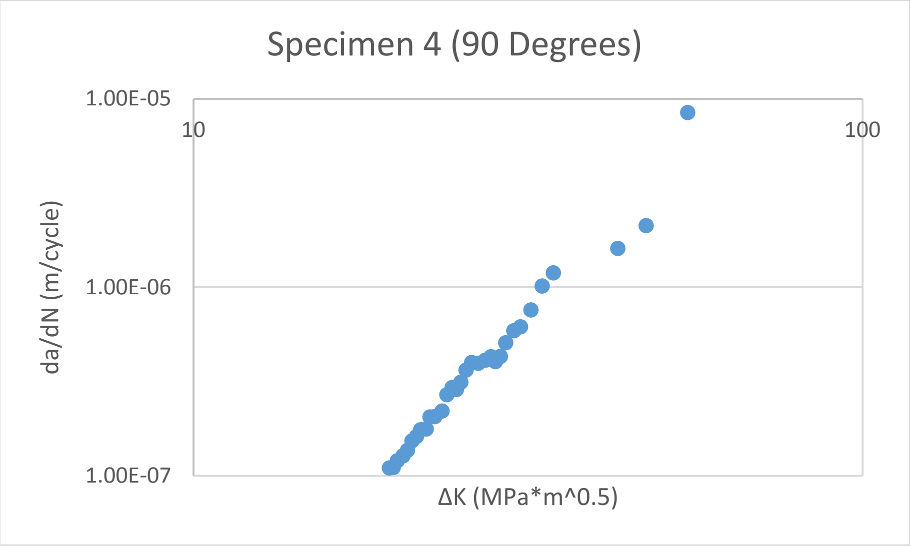

Specimen 5 (0°) B=6 mm

a	N	ΔK	da/dN
0.006027	1	0	1.23E-06
0.006151	481	21.12057	1.22E-06
0.006205	961	21.92109	1.29E-06
0.006393	1441	21.98508	1.23E-06
0.00656	1921	22.34346	1.26E-06
0.006678	2401	22.65049	1.28E-06
0.006787	2881	22.67003	1.28E-06
0.006956	3361	22.8685	1.24E-06
0.007053	3841	22.82355	1.25E-06
7.20E-03	4321	23.25495	1.22E-06
0.007313	4801	23.24549	1.21E-06
0.007448	5281	23.63959	1.32E-06
0.007592	5761	24.07829	1.27E-06
0.007793	6241	24.41177	1.42E-06
0.007948	6721	24.95207	1.52E-06
0.008083	7201	24.92483	1.51E-06
0.0082	7681	25.3063	1.37E-06
0.008345	8161	25.41459	1.51E-06
0.008484	8641	25.79776	1.57E-06
0.008669	9121	26.08505	1.53E-06
0.008858	9601	26.15088	1.52E-06
0.009013	10081	26.6662	1.52E-06
0.009167	10561	26.63306	1.60E-06
0.009409	11041	27.18741	1.71E-06
0.00962	11521	27.75946	1.63E-06
0.009783	12001	28.58794	1.82E-06
0.009996	12481	28.62985	2.30E-06
0.010234	12961	29.50033	2.66E-06
0.01052	13441	29.54005	2.42E-06
0.01084	13921	29.53404	2.30E-06
0.011284	14401	30.34836	3.72E-06
0.011703	14881	30.60249	2.97E-06
0.012402	15361	34.473	5.24E-06
0.013547	15841	43.473	1.04E-05

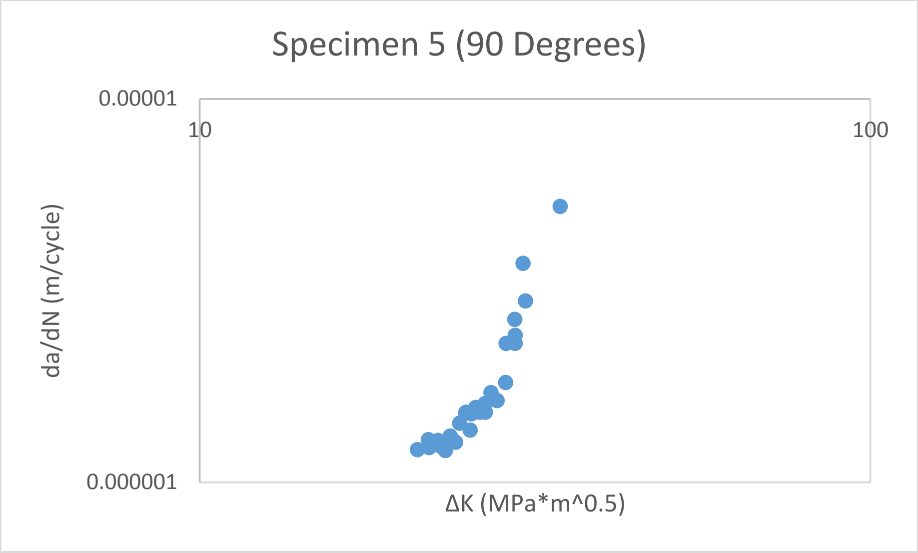

Specimen 6 (30°) B=6 mm

a	N	ΔK	da/dN
0.006107	1	0	7.51E-08
0.006366	961	17.75433	7.31E-08
0.006517	1921	18.00589	7.77E-08
0.00658	2881	18.54496	1.12E-07
0.006588	3841	18.70973	1.27E-07
0.006664	4801	19.28719	1.35E-07
0.006681	5761	19.71444	1.51E-07
0.006778	6721	20.13871	1.49E-07
0.006821	7681	20.41233	1.64E-07
0.00694	8641	20.79433	1.74E-07
0.006994	9601	21.23677	1.65E-07
0.007102	10561	21.79719	1.94E-07
0.007221	11521	22.32584	2.05E-07
0.007304	12481	22.81185	2.11E-07
0.007457	13441	23.19701	2.48E-07
0.007649	14401	23.75924	2.53E-07
0.007768	15361	24.19037	3.02E-07
0.007945	16321	24.61956	2.92E-07
0.008052	17281	25.02122	3.20E-07
0.008226	18241	25.49295	3.80E-07
0.008365	19201	25.98764	4.17E-07
0.008594	20161	26.40383	4.44E-07
0.008725	21121	27.28112	4.72E-07
0.008911	22081	28.53979	5.07E-07
0.00914	23041	29.46899	5.52E-07
0.009371	24001	30.55951	6.72E-07
0.009642	24961	32.04688	8.40E-07
0.009936	25921	33.08461	1.05E-06
0.01023	26881	34.86136	1.34E-06
0.010679	27841	35.87608	1.62E-06
0.012154	28801	40.02847	2.57E-06
0.013693	29761	47.79939	3.70E-06
0.0155	30721	54.486	1.67E-05

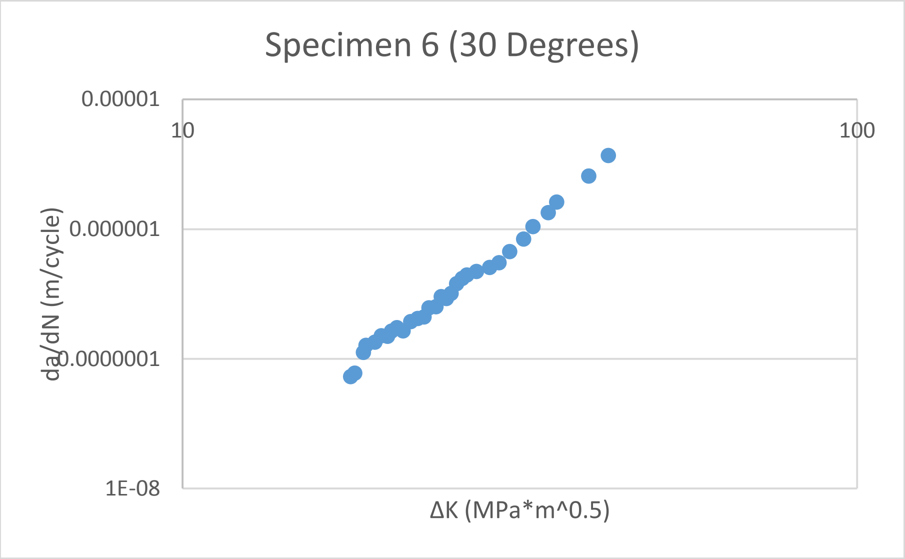

Specimen 7 (60°) B=6 mm

a	N	ΔK	da/dN
0.006112	1	0	7.31E-08
0.006128	1221	17.55368	1.01E-07
0.006155	2441	17.84325	1.07E-07
0.006188	3661	18.02538	1.20E-07
0.006203	4881	18.40461	1.41E-07
0.006225	6101	18.95207	1.42E-07
0.006243	7321	19.30623	1.61E-07
0.006271	8541	19.71906	1.61E-07
0.006296	9761	20.04518	2.05E-07
0.006321	10981	20.41451	2.11E-07
0.006338	12201	20.81537	2.14E-07
0.00636	13421	21.03899	2.18E-07
0.006396	14641	21.42464	2.33E-07
0.006423	15861	21.64536	2.57E-07
0.006479	17081	21.92672	2.66E-07
0.006565	18301	22.38677	2.87E-07
0.006663	19521	22.48469	2.68E-07
0.006796	20741	23.12607	2.88E-07
0.006932	21961	23.64482	3.54E-07
0.007042	23181	24.19895	3.43E-07
0.007216	24401	24.77286	4.01E-07
0.007367	25621	25.24481	4.31E-07
0.00757	26841	25.77183	4.57E-07
0.007782	28061	26.20681	4.95E-07
0.007997	29281	26.84092	5.64E-07
0.008284	30501	27.57684	6.29E-07
0.008586	31721	28.37083	7.63E-07
0.008907	32941	29.41398	7.48E-07
0.009192	34161	29.99233	1.12E-06
0.009641	35381	31.22282	1.15E-06
0.010169	36601	33.05068	1.81E-06
0.010834	37821	34.77756	2.23E-06
0.013883	39041	44.51898	6.72E-06
0.015104	40261	50.841	9.28E-06

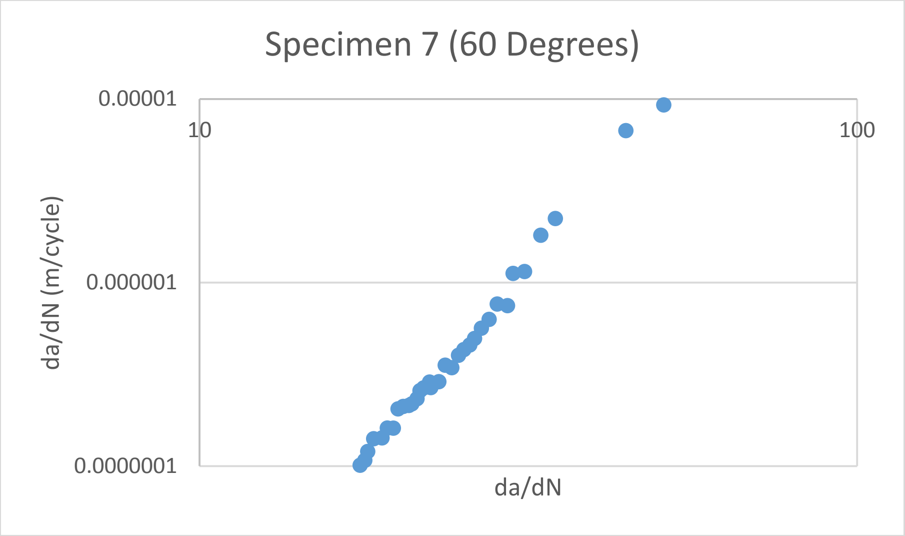

Specimen 8 (90°) B=6 mm

a	N	ΔK	da/dN
0.006101	1	0	7.74E-08
0.006136	1211	17.66889	7.86E-08
0.006154	2421	17.89233	9.97E-08
0.00617	3631	17.99324	1.09E-07
0.006174	4841	18.42718	1.19E-07
0.006195	6051	18.66196	1.16E-07
0.006215	7261	18.85273	1.50E-07
0.00624	8471	19.09326	1.60E-07
0.006247	9681	19.44009	1.64E-07
0.006276	10891	19.73388	1.82E-07
0.006282	12101	20.08533	2.10E-07
0.006311	13311	20.36651	2.07E-07
0.006326	14521	20.64609	2.39E-07
0.00635	15731	21.02371	2.31E-07
0.006474	16941	21.41329	2.78E-07
0.006528	18151	21.59236	3.10E-07
0.00661	19361	22.17276	3.25E-07
0.00673	20571	22.68698	3.29E-07
0.006826	21781	23.08595	3.46E-07
0.006961	22991	23.37211	3.62E-07
0.007097	24201	23.52552	3.45E-07
0.00713	25411	23.86152	3.66E-07
0.007386	26621	24.32191	3.61E-07
0.007582	27831	24.52804	4.63E-07
0.007807	29041	25.43229	4.42E-07
0.008018	30251	26.17031	6.32E-07
0.008277	31461	27.31752	8.51E-07
0.008611	32671	28.39795	9.64E-07
0.008966	33881	29.56627	1.14E-06
0.009431	35091	31.23351	1.59E-06
0.009796	36301	33.63157	2.15E-06
0.010444	37511	33.62859	2.85E-06
0.012823	38721	43.89215	5.33E-06
0.015664	39931	50.844	9.98E-06

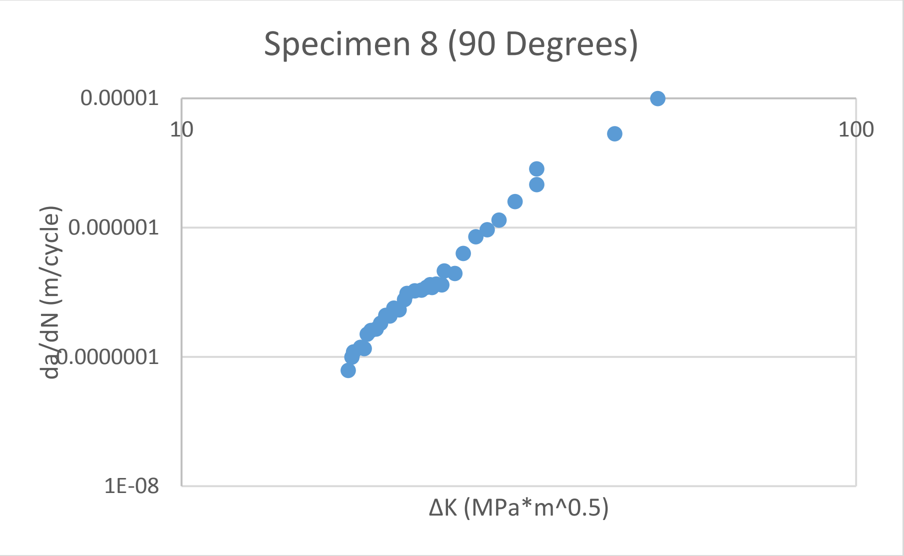

Specimen 9 (0°) B=6 mm

a	N	ΔK	da/dN
0.006069	1	0	3.50E-07
0.006119	781	10.4877	3.52E-07
0.006214	1561	11.15086	3.46E-07
0.006353	2341	11.68235	4.03E-07
0.00644	3121	12.31329	4.14E-07
0.006561	3901	12.60998	4.33E-07
0.006637	4681	13.16721	4.19E-07
0.00678	5461	13.73483	4.40E-07
0.006876	6241	13.93232	4.41E-07
0.007013	7021	14.22115	4.75E-07
0.007069	7801	15.3539	4.79E-07
0.00724	8581	16.24969	4.96E-07
0.007373	9361	16.72572	5.11E-07
0.00749	10141	17.18358	5.10E-07
0.007605	10921	17.68717	5.37E-07
0.007788	11701	18.11815	5.92E-07
0.007908	12481	18.61197	6.77E-07
0.008013	13261	18.89397	6.95E-07
0.008224	14041	19.24352	7.43E-07
0.008295	14821	19.68142	7.05E-07
0.008496	15601	20.20899	7.95E-07
0.008681	16381	20.77626	9.34E-07
0.008914	17161	21.42693	8.86E-07
0.009099	17941	22.07245	1.05E-06
0.009283	18721	22.87983	1.15E-06
0.009581	19501	23.71624	1.43E-06
0.00984	20281	25.18715	1.81E-06
0.010112	21061	26.38096	2.41E-06
0.010448	21841	28.05558	3.68E-06
0.01068	22621	30.26686	5.17E-06
0.011191	23401	33.34037	7.69E-06
0.012692	24181	39.65887	1.95E-05
0.013659	24961	43.8723	6.13E-05
0.0159	25741	47.793	8.92E-05

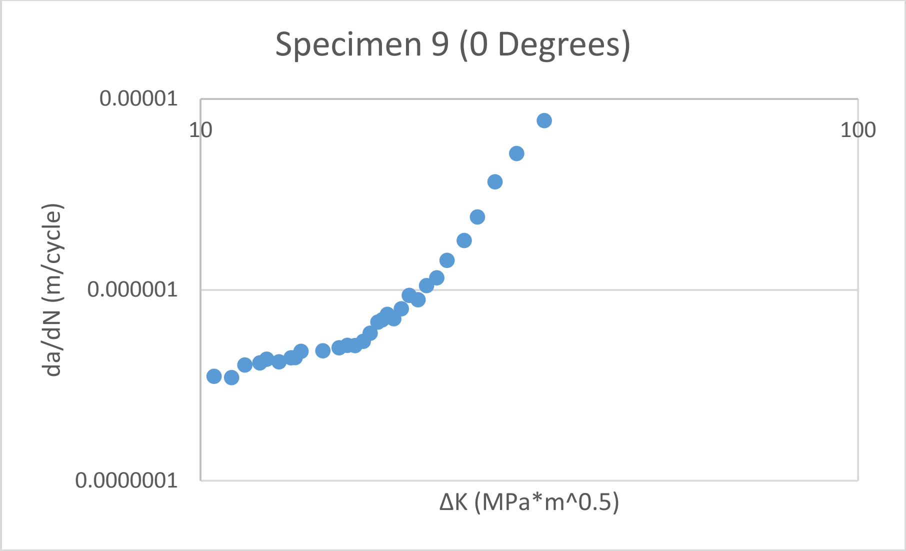

Specimen 10 (30°) B=6 mm

a	N	ΔK	da/dN
0.006114	1	0	7.99E-08
0.006134	1051	17.70837	1.53E-07
0.00615	2101	18.24791	1.69E-07
0.006155	3151	18.63364	1.94E-07
0.006178	4201	18.82555	1.93E-07
0.006184	5251	19.18281	2.17E-07
0.006197	6301	19.50097	2.15E-07
0.006227	7351	19.73577	2.31E-07
0.006238	8401	20.03146	2.40E-07
0.006254	9451	20.41937	2.52E-07
0.006278	10501	20.96946	2.71E-07
0.006288	11551	21.50896	2.84E-07
0.006304	12601	22.04727	2.95E-07
0.006325	13651	22.52872	3.15E-07
0.00634	14701	22.94155	3.32E-07
0.006422	15751	23.33039	3.37E-07
0.006582	16801	23.75265	3.34E-07
0.00672	17851	24.46305	4.37E-07
0.006866	18901	24.9399	4.60E-07
0.006985	19951	25.38425	5.01E-07
0.007218	21001	25.96048	5.50E-07
0.007426	22051	26.52264	5.84E-07
0.007661	23101	27.19397	5.84E-07
0.007875	24151	27.80746	6.67E-07
0.008143	25201	28.52511	8.11E-07
0.008424	26251	29.47444	7.74E-07
0.008718	27301	30.13614	1.04E-06
0.009039	28351	31.59799	1.26E-06
0.009373	29401	33.22762	1.70E-06
0.009781	30451	36.4978	2.50E-06
0.01032	31501	36.50931	2.84E-06
0.012916	32551	41.69393	4.31E-06
0.015392	33601	46.8736	7.72E-06
0.0191	34651	54.63	1.53E-05

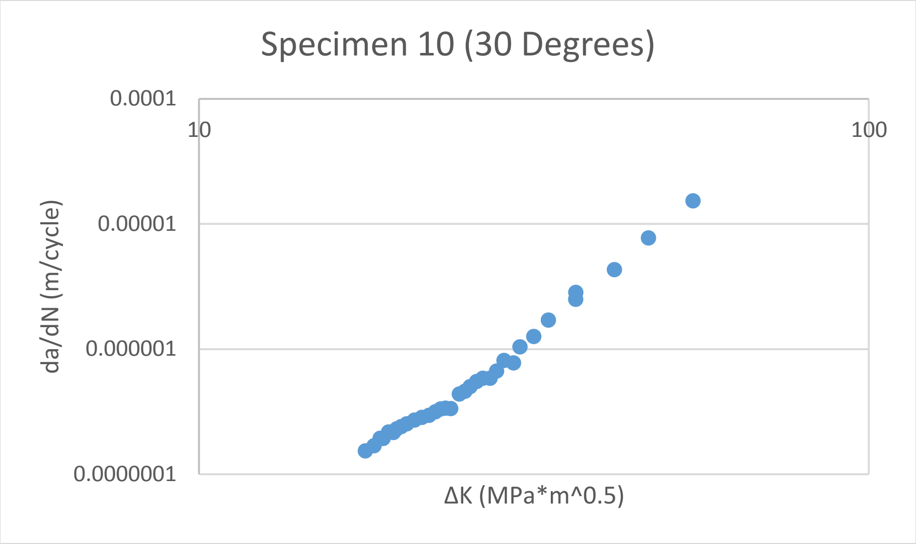

Specimen 11 (90°) B=6 mm

a	N	ΔK	da/dN
0.006193	1	0	7.42E-08
0.006412	941	17.86877	1.11E-07
0.006537	1881	19.52452	1.22E-07
0.006594	2821	19.79342	1.04E-07
0.006709	3761	20.01043	1.29E-07
0.006761	4701	20.31269	1.46E-07
0.00679	5641	20.49564	1.66E-07
0.006844	6581	21.13563	1.62E-07
0.006843	7521	21.83488	2.15E-07
0.007027	8461	22.23725	2.58E-07
0.006994	9401	22.65681	2.56E-07
0.007029	10341	22.94692	2.94E-07
0.00717	11281	23.3226	2.92E-07
0.007276	12221	23.67165	2.94E-07
0.007461	13161	24.0504	3.49E-07
0.007584	14101	24.43873	3.66E-07
0.007635	15041	24.87188	3.73E-07
0.007821	15981	25.29605	3.99E-07
0.007903	16921	25.85047	4.18E-07
0.008052	17861	26.59768	4.73E-07
0.008138	18801	27.06861	5.07E-07
0.008261	19741	27.85078	5.44E-07
0.008499	20681	28.32815	5.46E-07
0.008688	21621	29.05187	6.21E-07
0.008903	22561	29.78436	7.17E-07
0.009178	23501	30.7389	8.76E-07
0.00946	24441	31.58683	1.12E-06
0.009745	25381	32.78485	1.32E-06
0.010083	26321	35.77114	2.12E-06
0.010523	27261	40.06984	3.14E-06
0.010966	28201	40.09837	3.37E-06
0.011607	29141	44.07237	4.98E-06
0.013403	30081	48.5782	8.34E-06
0.015639	31021	54.808	1.47E-05

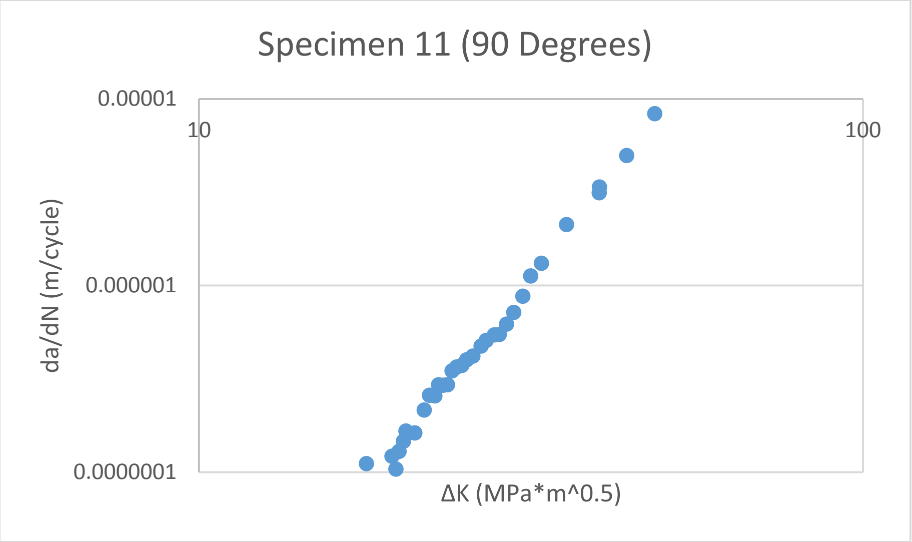

Specimen 12 (0°) B=12 mm

a	N	ΔK	da/dN
0.006027	1	0	1.22E-07
0.006151	771	20.21963	2.10E-07
0.006205	1541	20.44228	1.86E-07
0.006393	2311	20.82767	2.14E-07
0.00656	3081	21.1085	2.53E-07
0.006678	3851	21.41094	2.59E-07
0.006787	4621	21.7815	2.31E-07
0.006956	5391	22.25007	2.67E-07
0.007053	6161	22.3606	2.52E-07
0.007202	6931	22.64136	3.17E-07
0.007313	7701	23.06773	3.45E-07
0.007448	8471	23.62472	4.14E-07
0.007592	9241	24.86581	4.45E-07
0.007793	10011	25.6019	4.32E-07
0.007948	10781	26.28638	4.47E-07
0.008083	11551	26.69706	5.03E-07
0.0082	12321	27.21103	5.35E-07
0.008345	13091	27.6326	4.68E-07
0.008484	13861	27.96041	5.98E-07
0.008669	14631	28.37053	5.68E-07
0.008858	15401	28.94689	6.93E-07
0.009013	16171	29.52392	7.05E-07
0.009167	16941	29.86696	8.05E-07
0.009409	17711	30.91524	8.83E-07
0.00962	18481	31.98878	8.45E-07
0.009783	19251	33.33195	1.06E-06
0.009996	20021	34.14319	1.15E-06
0.010234	20791	35.35588	1.57E-06
0.01052	21561	36.14242	1.88E-06
0.01084	22331	37.2626	1.99E-06
0.011284	23101	38.1405	2.46E-06
0.012303	23871	42.33251	3.49E-06
0.013489	24641	46.9252	5.83E-06
0.01455	25411	54.3902	1.26E-05

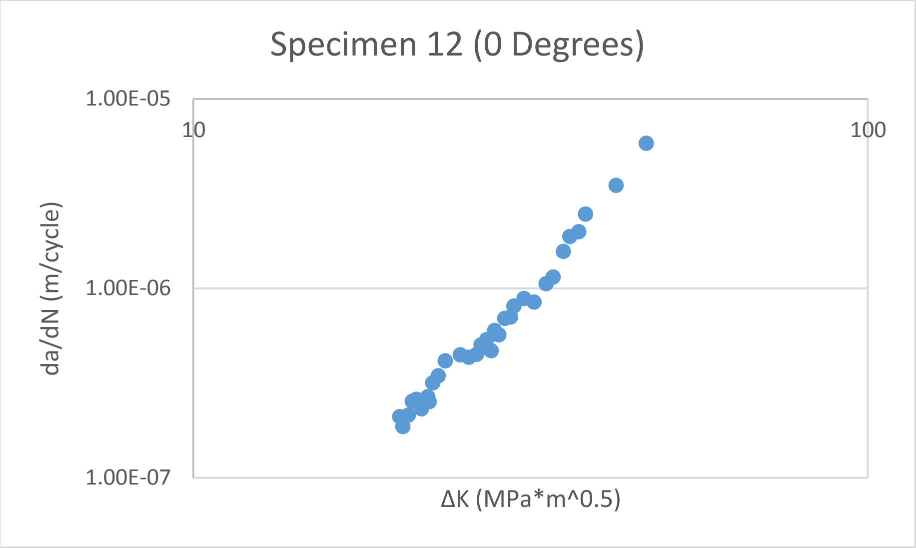

Specimen 13 (30°) B=12 mm

a	N	ΔK	da/dN
0.006116	1	0	9.84E-08
0.006141	891	20.06187	1.21E-07
0.006199	1781	20.42584	1.26E-07
0.006235	2671	20.65454	1.45E-07
0.00627	3561	20.87062	1.67E-07
0.006308	4451	21.25034	1.82E-07
0.006364	5341	21.71151	1.85E-07
0.006351	6231	22.09362	1.91E-07
0.006368	7121	22.41748	2.03E-07
0.006461	8011	22.77552	1.98E-07
0.006459	8901	23.07366	2.33E-07
0.006542	9791	23.39583	2.39E-07
0.006646	10681	23.63196	2.50E-07
0.006787	11571	24.01579	2.47E-07
0.006822	12461	24.33986	2.75E-07
0.006935	13351	24.69853	2.88E-07
0.007053	14241	25.06104	3.24E-07
0.007206	15131	25.52153	3.34E-07
0.007377	16021	25.84211	3.66E-07
0.007482	16911	26.32068	3.78E-07
0.007617	17801	27.10577	4.29E-07
0.007824	18691	27.5002	4.81E-07
0.007995	19581	28.08313	4.76E-07
0.008151	20471	28.83775	5.94E-07
0.008349	21361	29.25018	6.84E-07
0.008559	22251	30.40562	6.62E-07
0.008798	23141	30.94431	8.22E-07
0.009062	24031	31.6144	8.88E-07
0.009385	24921	32.92721	8.93E-07
0.009758	25811	33.7848	1.36E-06
0.010179	26701	34.17982	1.39E-06
0.01121	27591	36.30583	2.62E-06
0.012484	28481	38.4629	3.26E-06
0.013497	29371	43.717	6.02E-06

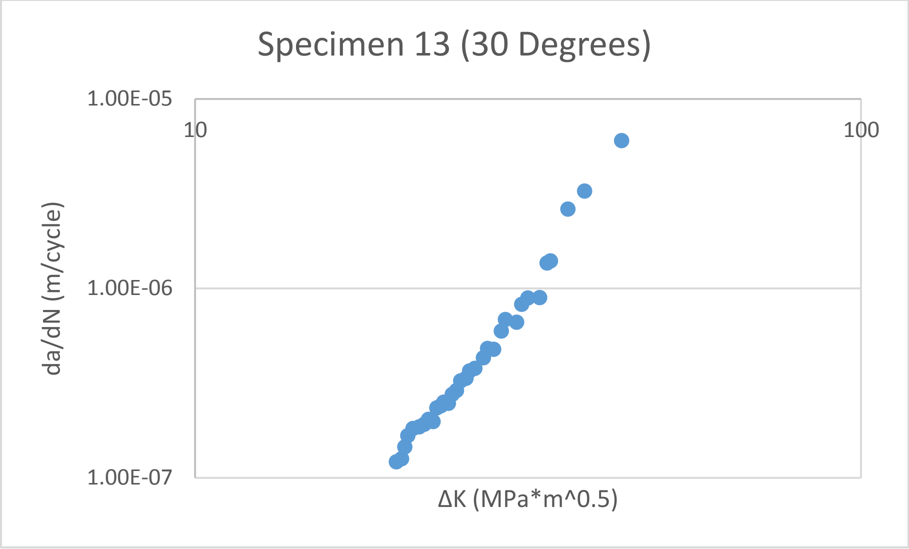

Specimen 14 (90°) B=12 mm

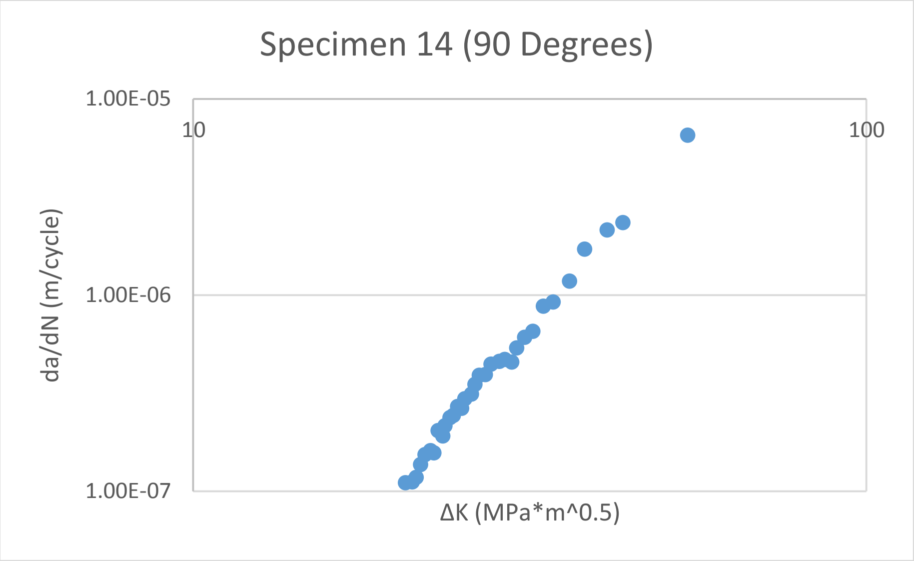

a	N	ΔK	da/dN
0.006147	1	0	1.19E-07
0.006836	701	20.66049	1.10E-07
0.0069	1401	21.14681	1.11E-07
0.006951	2101	21.43273	1.17E-07
0.006982	2801	21.758	1.37E-07
0.00704	3501	22.09126	1.53E-07
0.007122	4201	22.51113	1.61E-07
0.007188	4901	22.77215	1.57E-07
0.007314	5601	23.10268	2.03E-07
0.007397	6301	23.47562	1.91E-07
0.007487	7001	23.64999	2.15E-07
0.00761	7701	24.06277	2.37E-07
0.007674	8401	24.33788	2.43E-07
0.007736	9101	24.69715	2.70E-07
0.007793	9801	25.0403	2.64E-07
0.007939	10501	25.31298	2.96E-07
0.008011	11201	25.89337	3.12E-07
0.008159	11901	26.20446	3.50E-07
0.00831	12601	26.59799	3.90E-07
0.008433	13301	27.15766	3.93E-07
0.008601	14001	27.68608	4.44E-07
0.008779	14701	28.48811	4.59E-07
0.008924	15401	29.0198	4.69E-07
0.009129	16101	29.72189	4.55E-07
0.00935	16801	30.22764	5.37E-07
0.009563	17501	31.06113	6.08E-07
0.00981	18201	31.94766	6.53E-07
0.01015	18901	33.11622	8.77E-07
0.01045	19601	34.24172	9.21E-07
0.010768	20301	36.21775	1.18E-06
0.011193	21001	38.13613	1.71E-06
0.011736	21701	41.19191	2.15E-06
0.012782	22401	43.473	2.34E-06
0.015204	23101	54.259	6.53E-06

B.3 Critical Data Attributes

Specimen	a_0 (m)	a_0/W	a_f (m)	a_f/W	Cycles to Failure	Paris Eqn C value	Paris Eqn m value
1	0.0062	0.2569	0.0114	0.4740	19600	5.00E-07	2.3451
2	0.0061	0.2526	0.0181	0.7555	138742	1.00E-07	2.358
3	0.0061	0.2459	0.0155	0.6470	26771	1.00E-07	2.3623
4	0.0062	0.2601	0.1489	0.6228	33399	1.00E-07	2.6581
5	0.0071	0.2939	0.0135	0.5627	15899	3.00E-07	2.6654
6	0.0061	0.2545	0.0155	0.6458	31982	3.00E-07	2.5001
7	0.0060	0.2490	0.0151	0.6300	40458	1.00E-07	2.458
8	0.0060	0.2520	0.0156	0.6481	40000	2.00E-07	2.6328
9	0.0063	0.2620	0.0159	0.6605	25970	2.00E-07	2.6775
10	0.0061	0.2545	0.0191	0.7966	34751	7.00E-07	2.18
11	0.0062	0.2581	0.0156	0.6500	31149	1.00E-07	2.5973
12	0.0064	0.2675	0.0146	0.6097	25533	3.00E-07	2.6479
13	0.0065	0.2688	0.0135	0.5643	29499	3.00E-07	2.2727
14	0.0061	0.2561	0.0152	0.6344	23169	9.00E-07	2.6962

B.4 Longitudinal and Transverse Fracture Surface Profiles

B.4.1 Specimen 2, B = 12 mm, 30 degrees

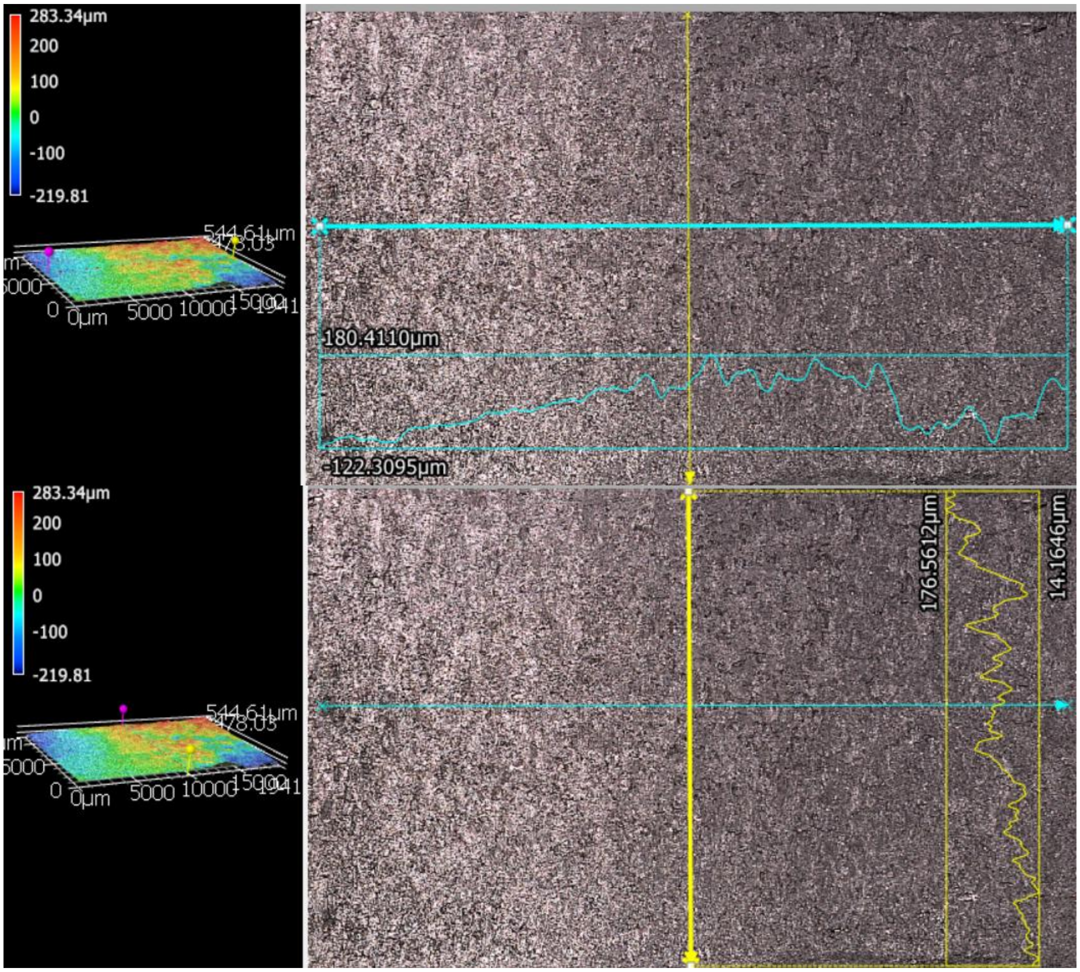

B.4.2 Specimen 3, B = 12 mm, 60 degrees

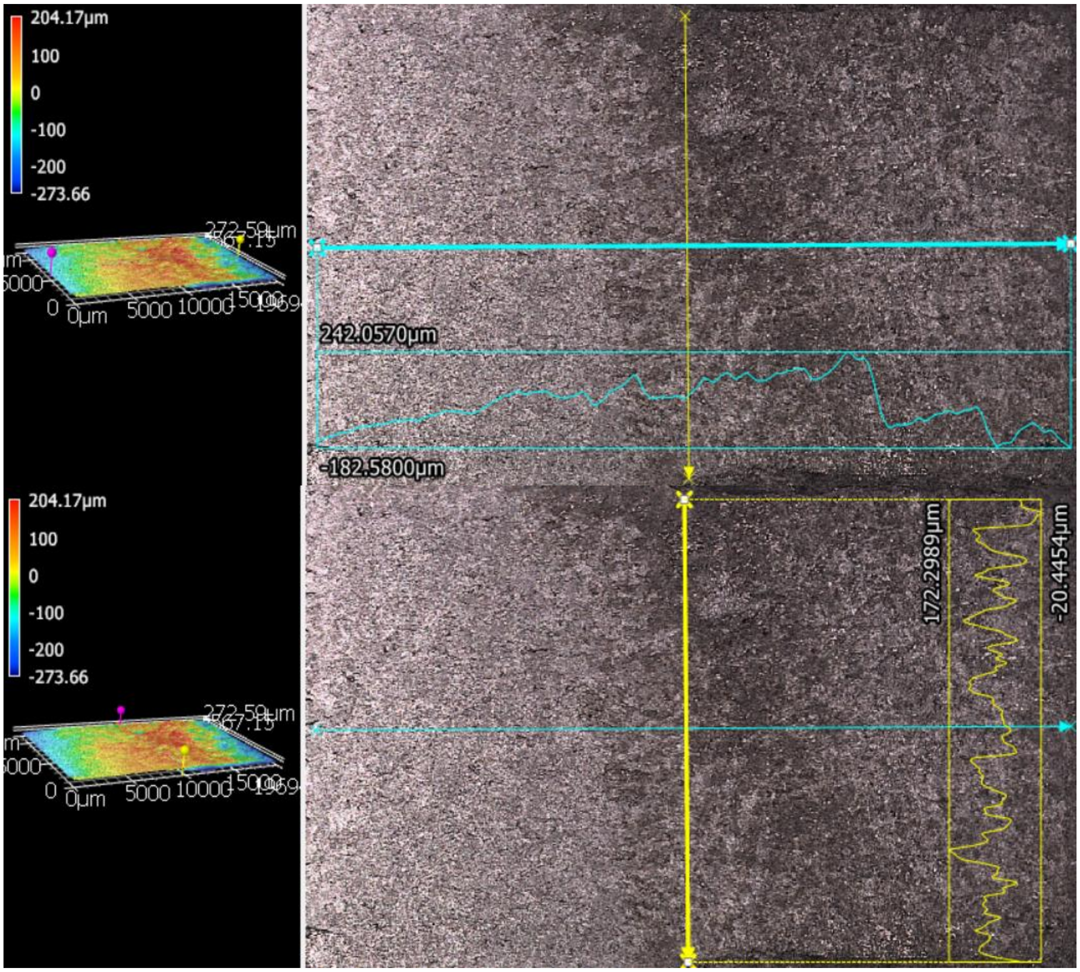

Appendix C: SEM Pictures

C.1 FT (Virgin Powder) Specimen 2 (0 Degrees)

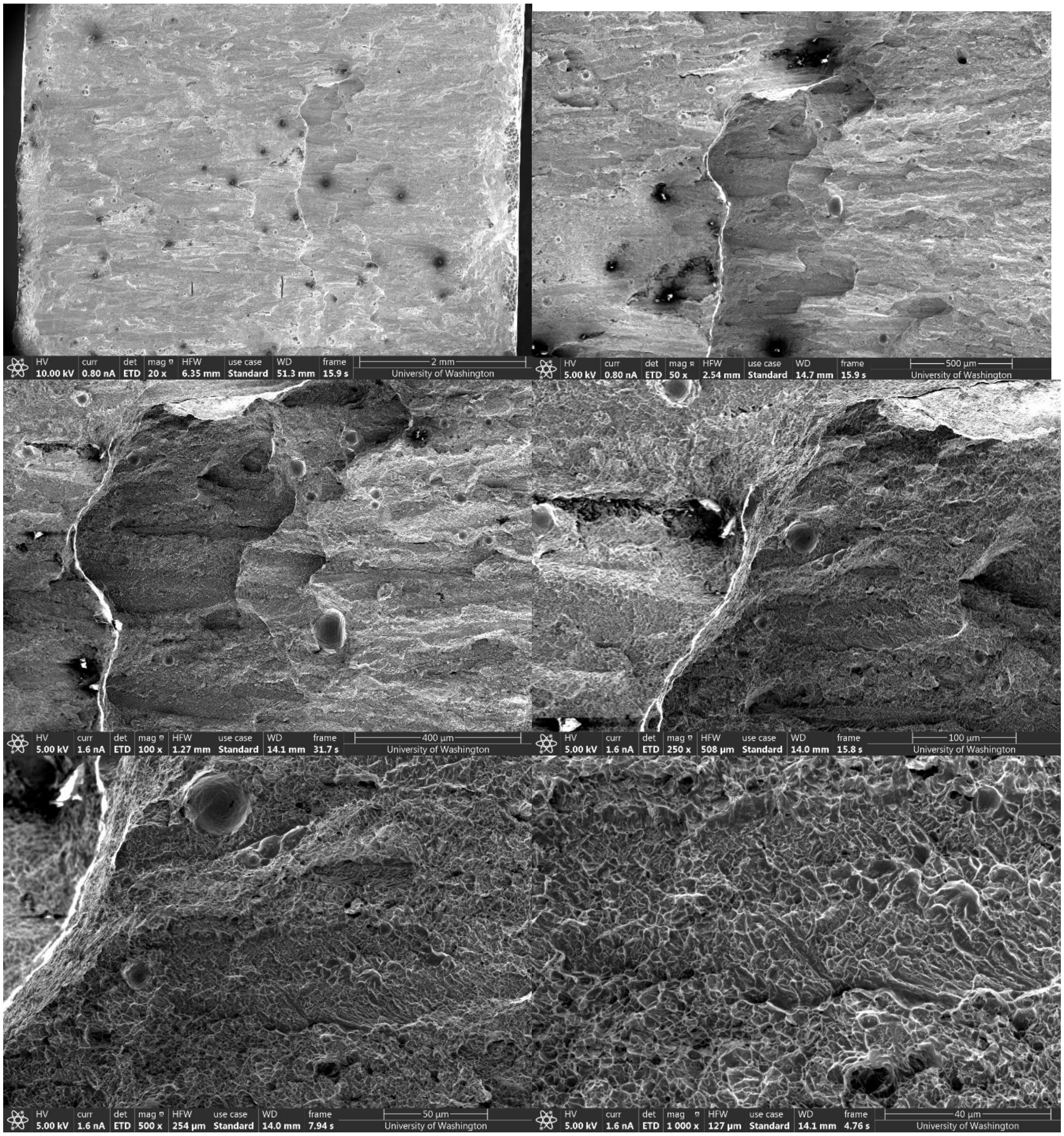

C.1 FT (Virgin Powder) Specimen 2 (0 Degrees) cont.

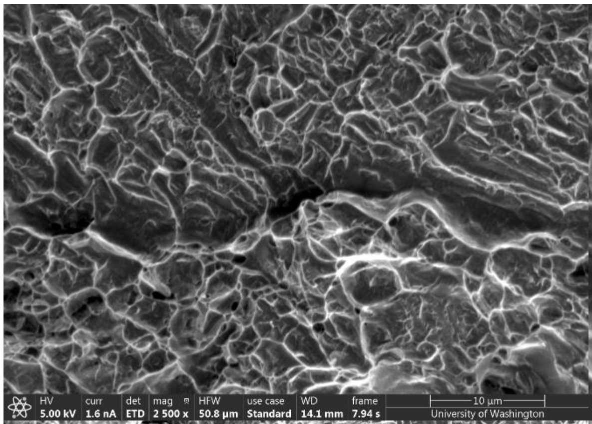

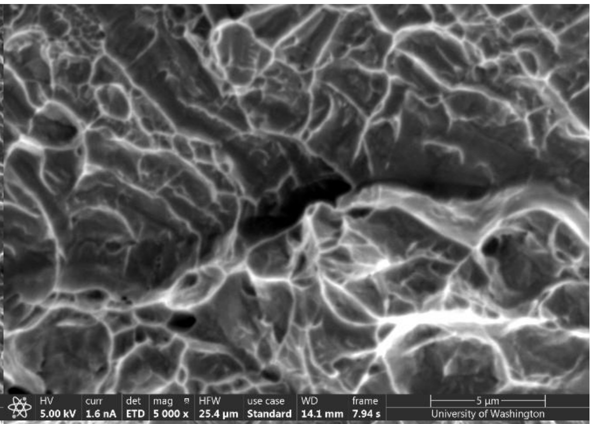

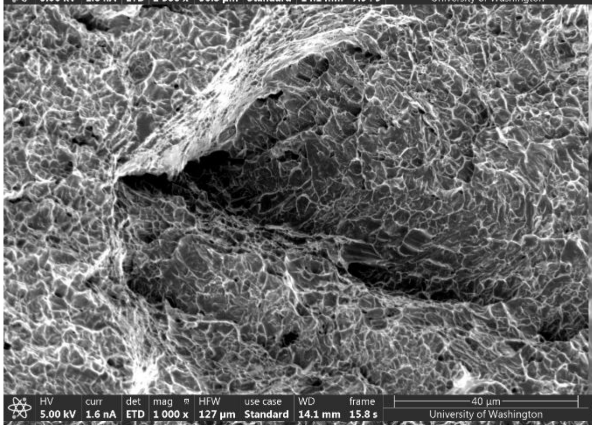

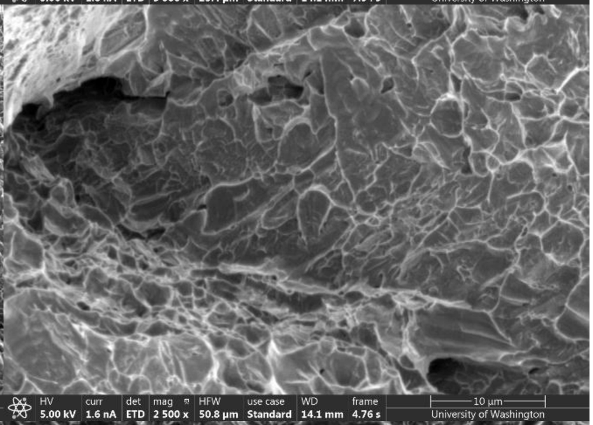

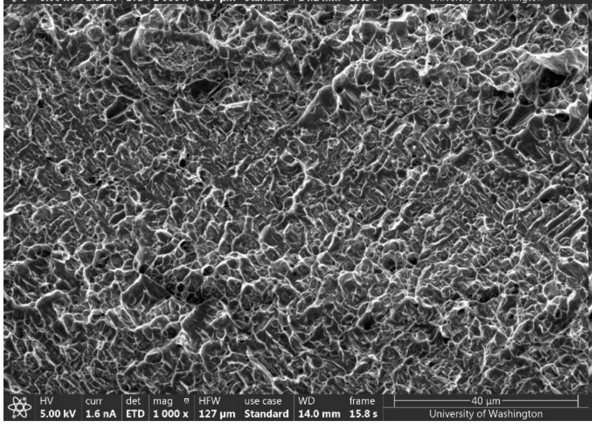

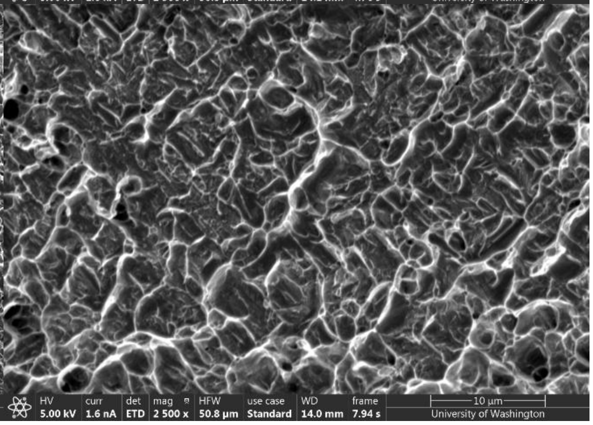

C.1 FT (Virgin Powder) Specimen 2 (0 Degrees) cont.

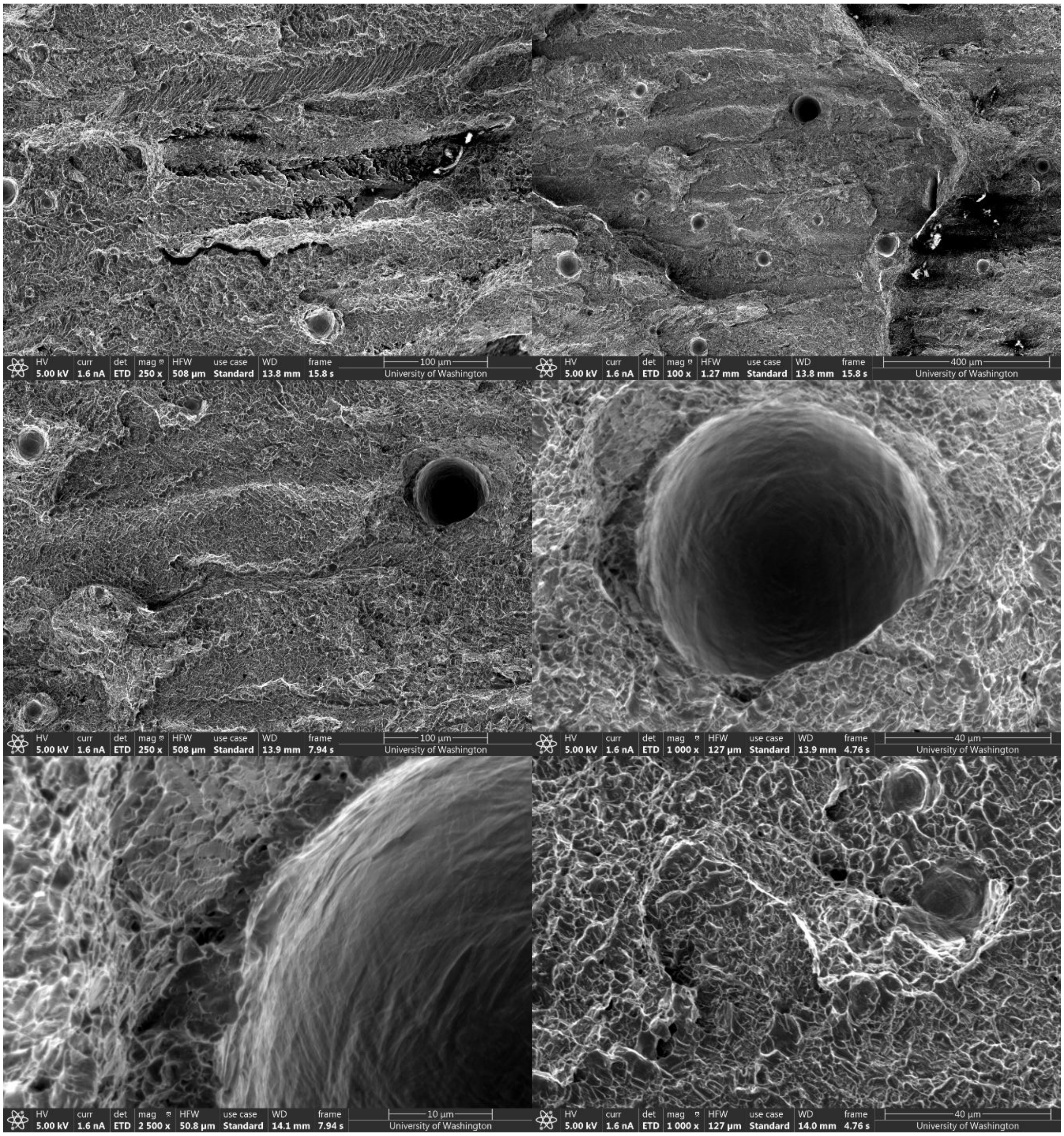

C.1 FT (Virgin Powder) Specimen 2 (0 Degrees) cont.

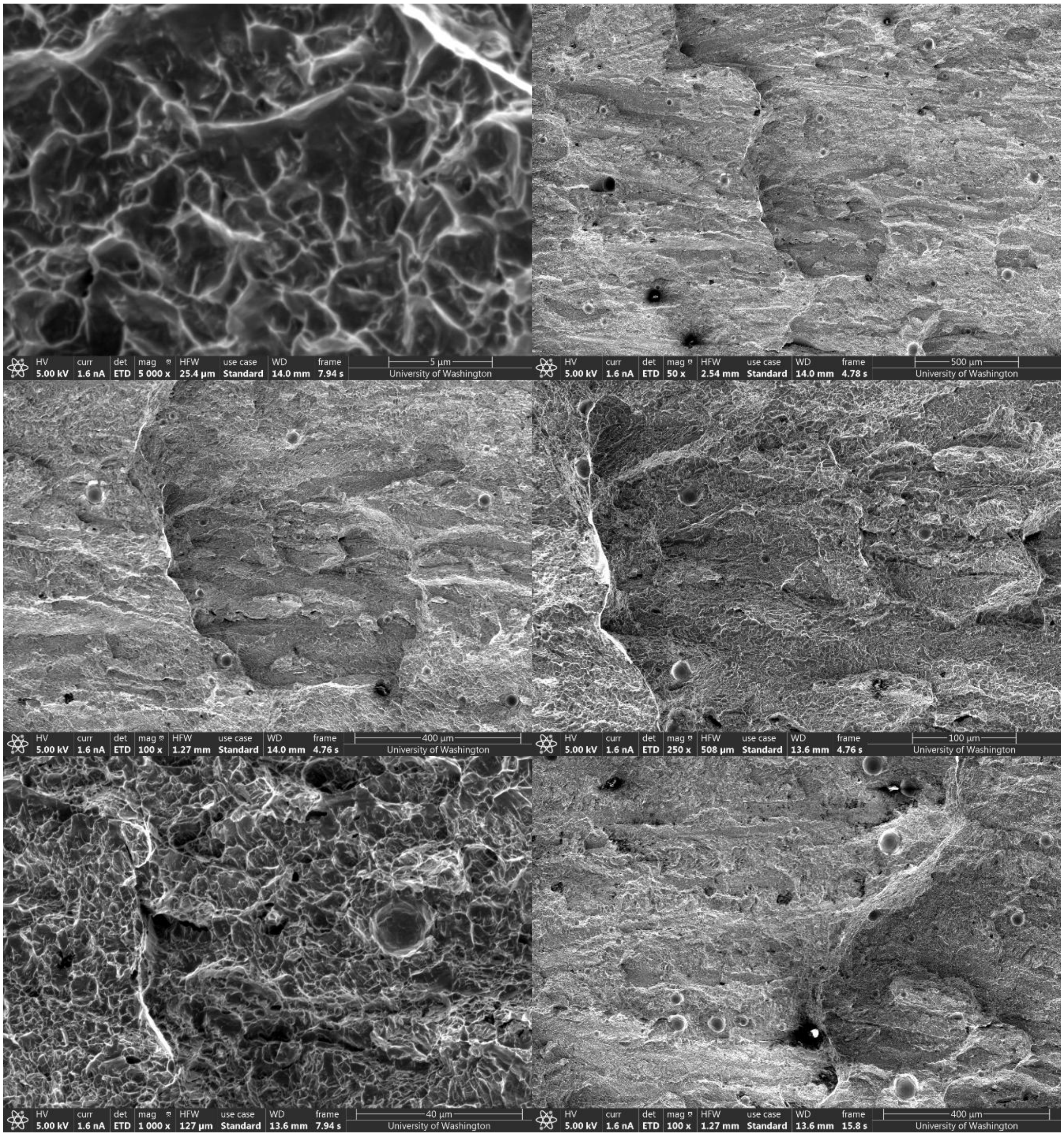

C.1 FT (Virgin Powder) Specimen 2 (0 Degrees) cont.

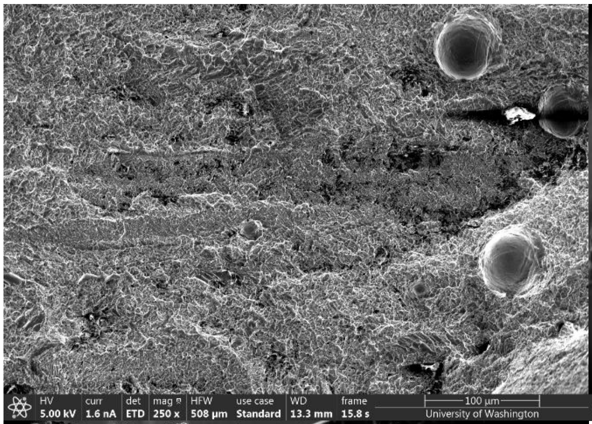

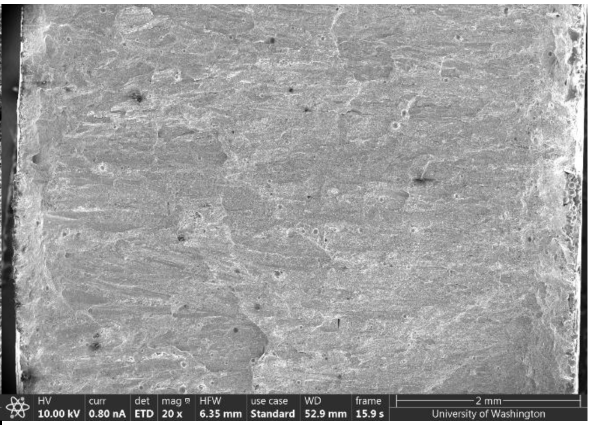

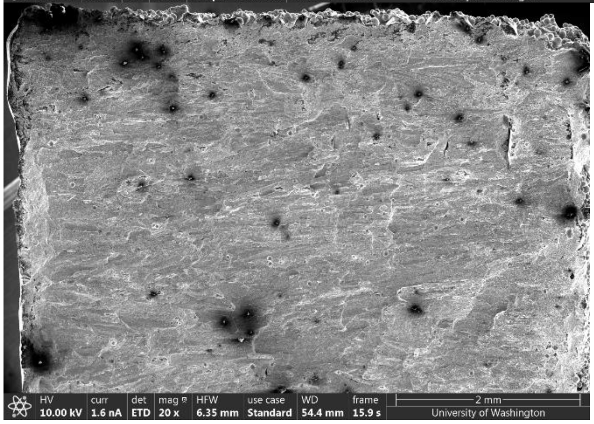

C.2 FT (Virgin Powder) Specimen 6 (30 Degrees)

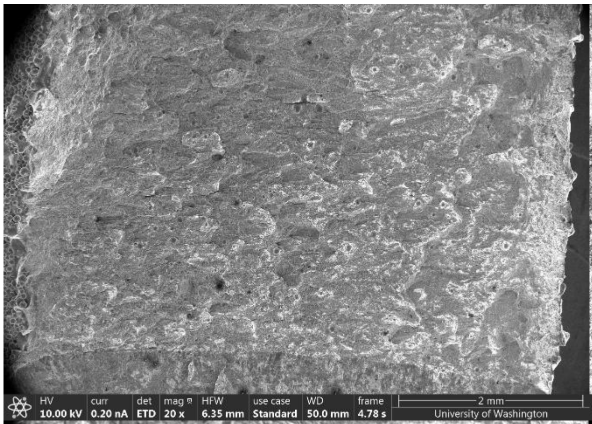

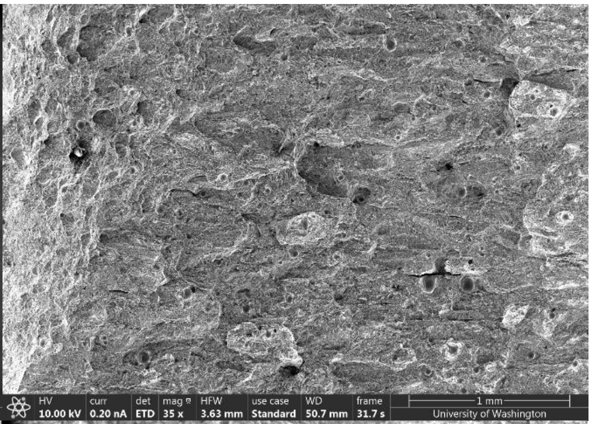

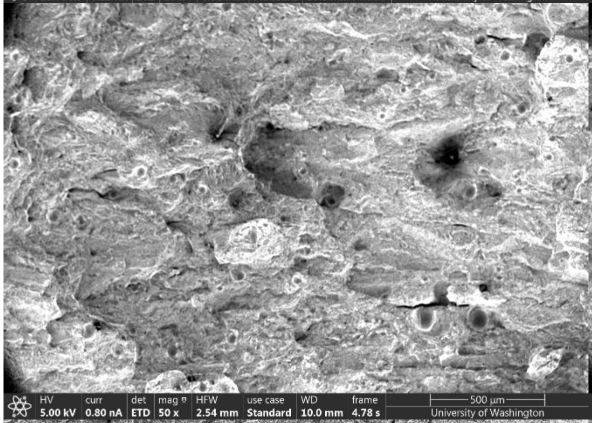

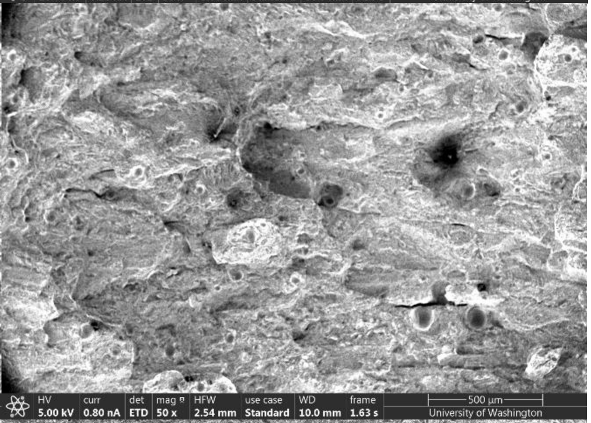

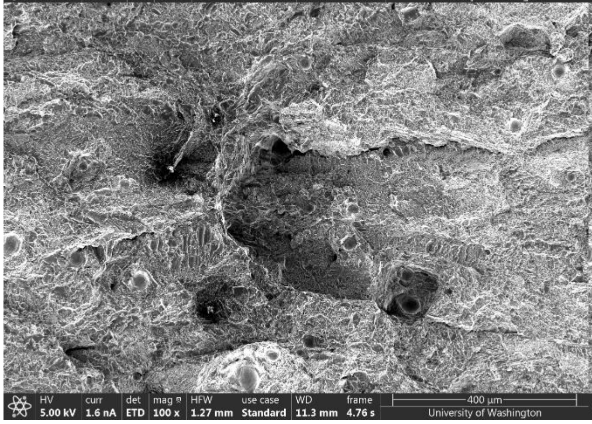

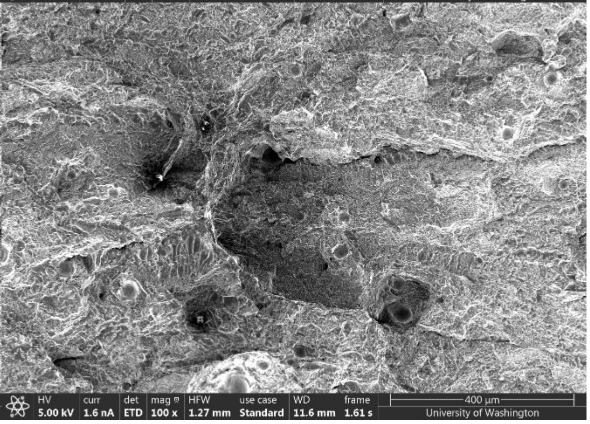

C.2 FT (Virgin Powder) Specimen 6 (30 Degrees) cont.

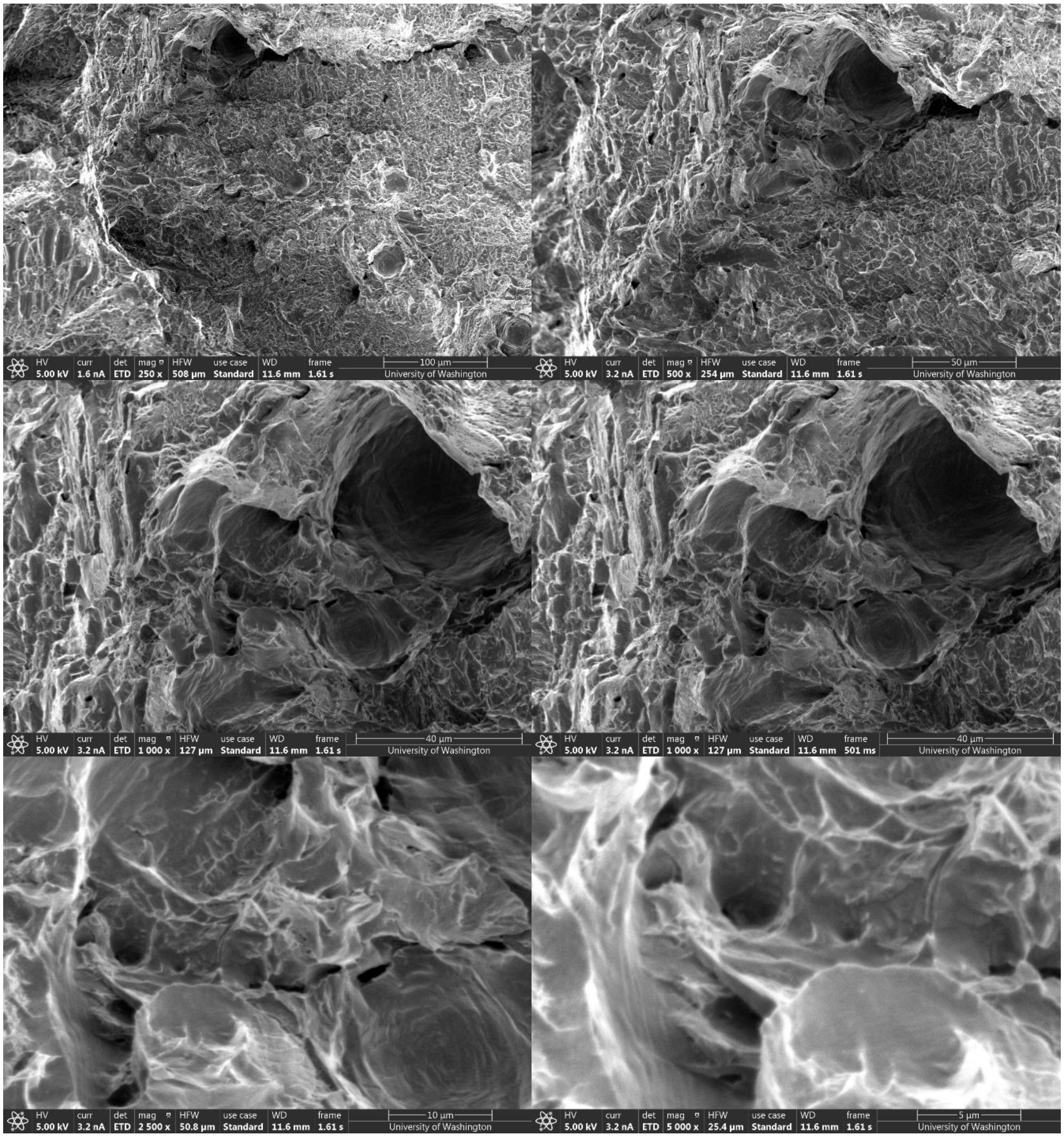

C.2 FT (Virgin Powder) Specimen 6 (30 Degrees) cont.

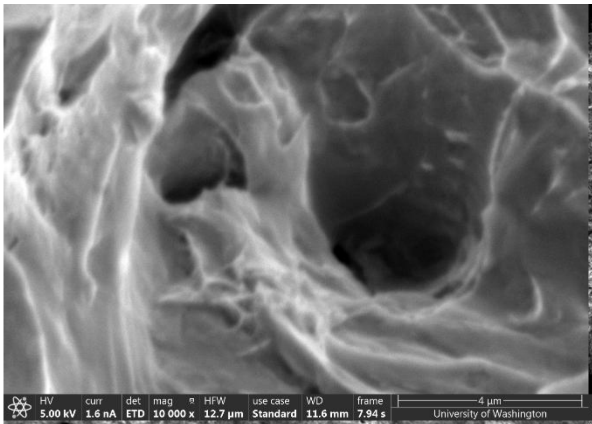

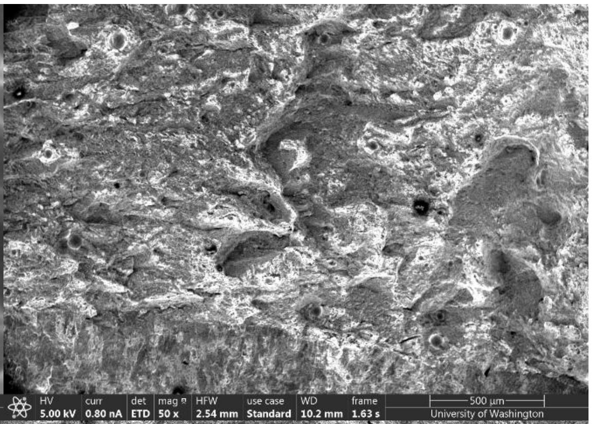

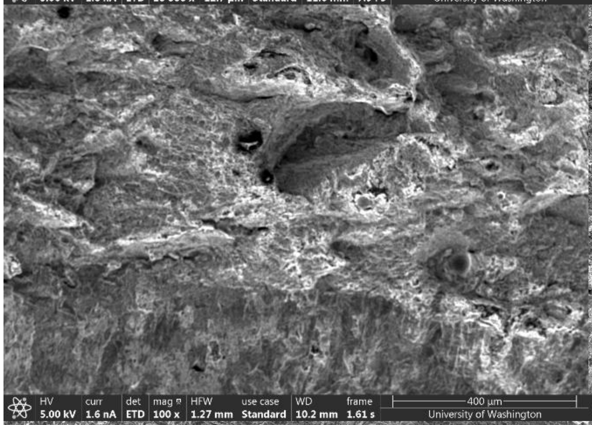

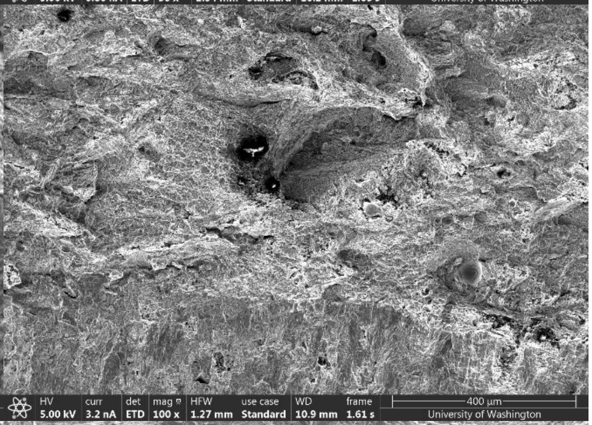

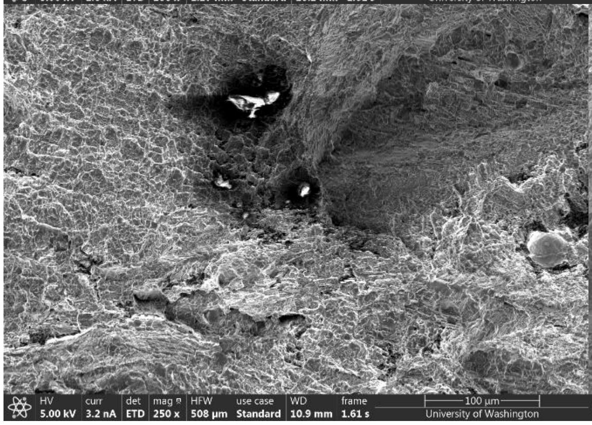

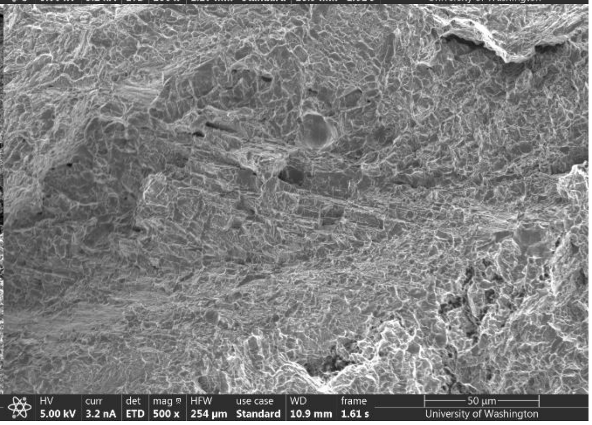

C.2 FT (Virgin Powder) Specimen 6 (30 Degrees) cont.

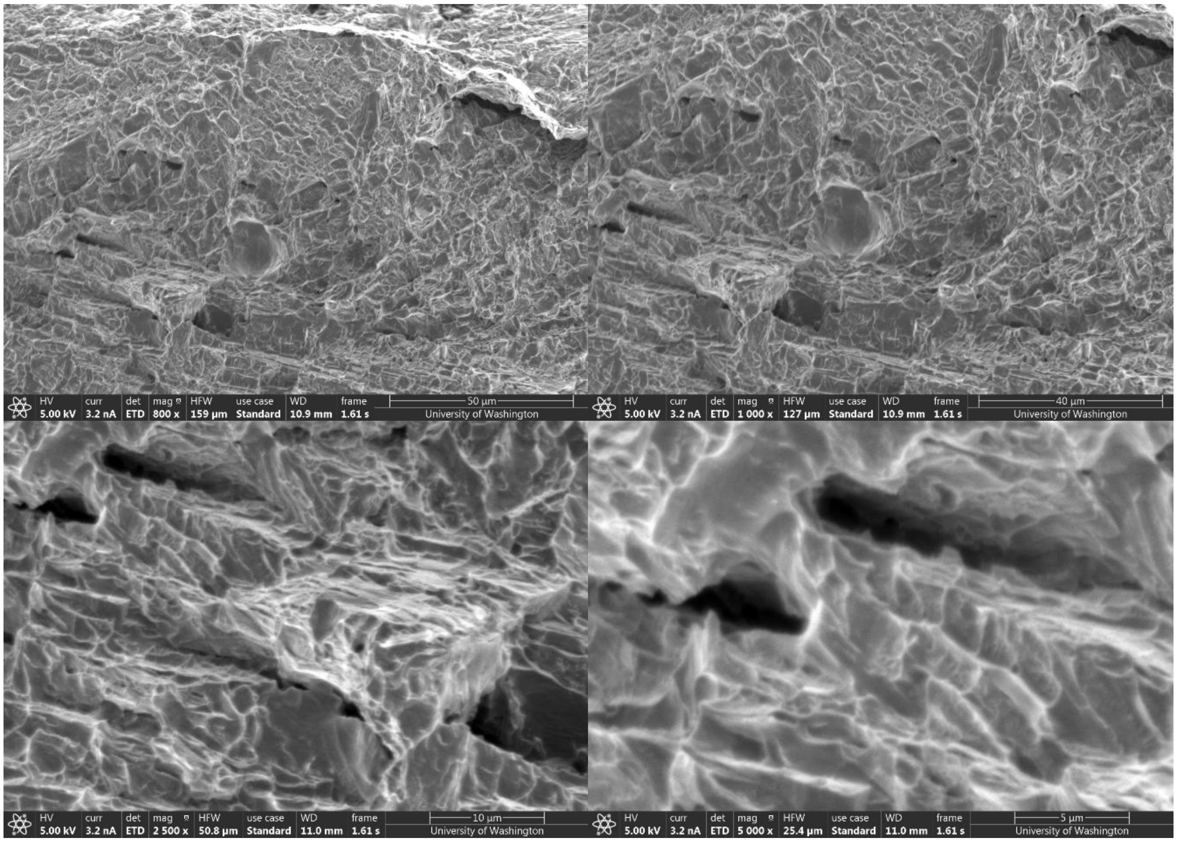

C.2 FT (Virgin Powder) Specimen 6 (30 Degrees) cont.

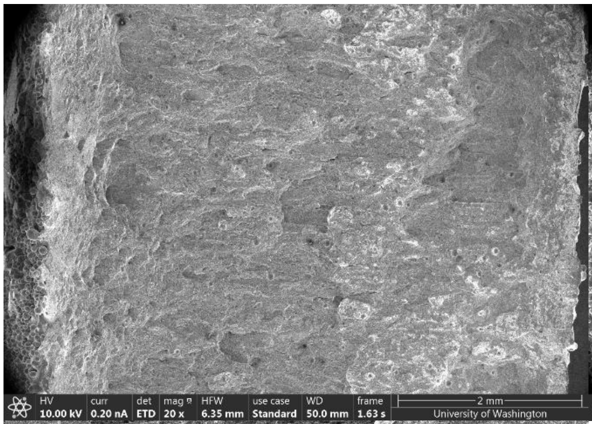

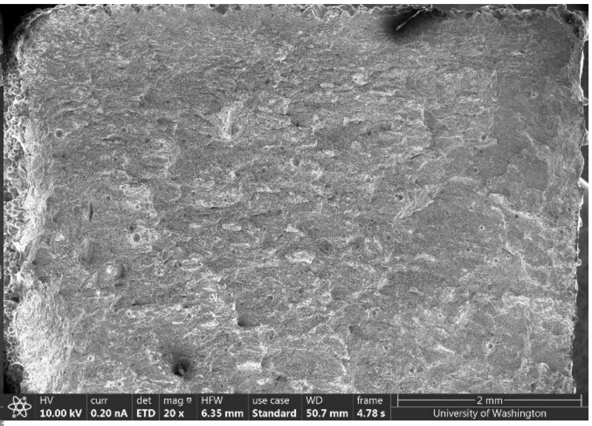

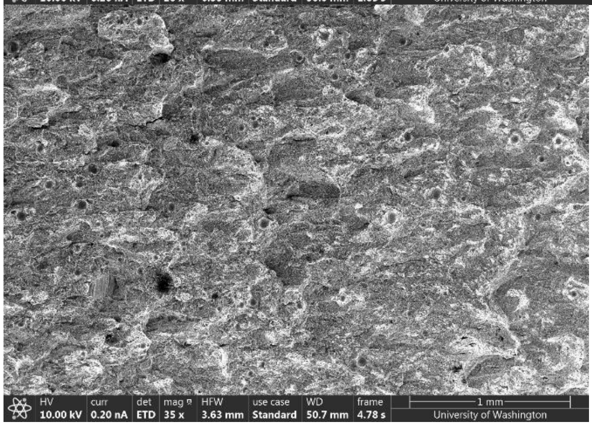

C.3 FT (Virgin Powder) Specimen 7 (60 Degrees)

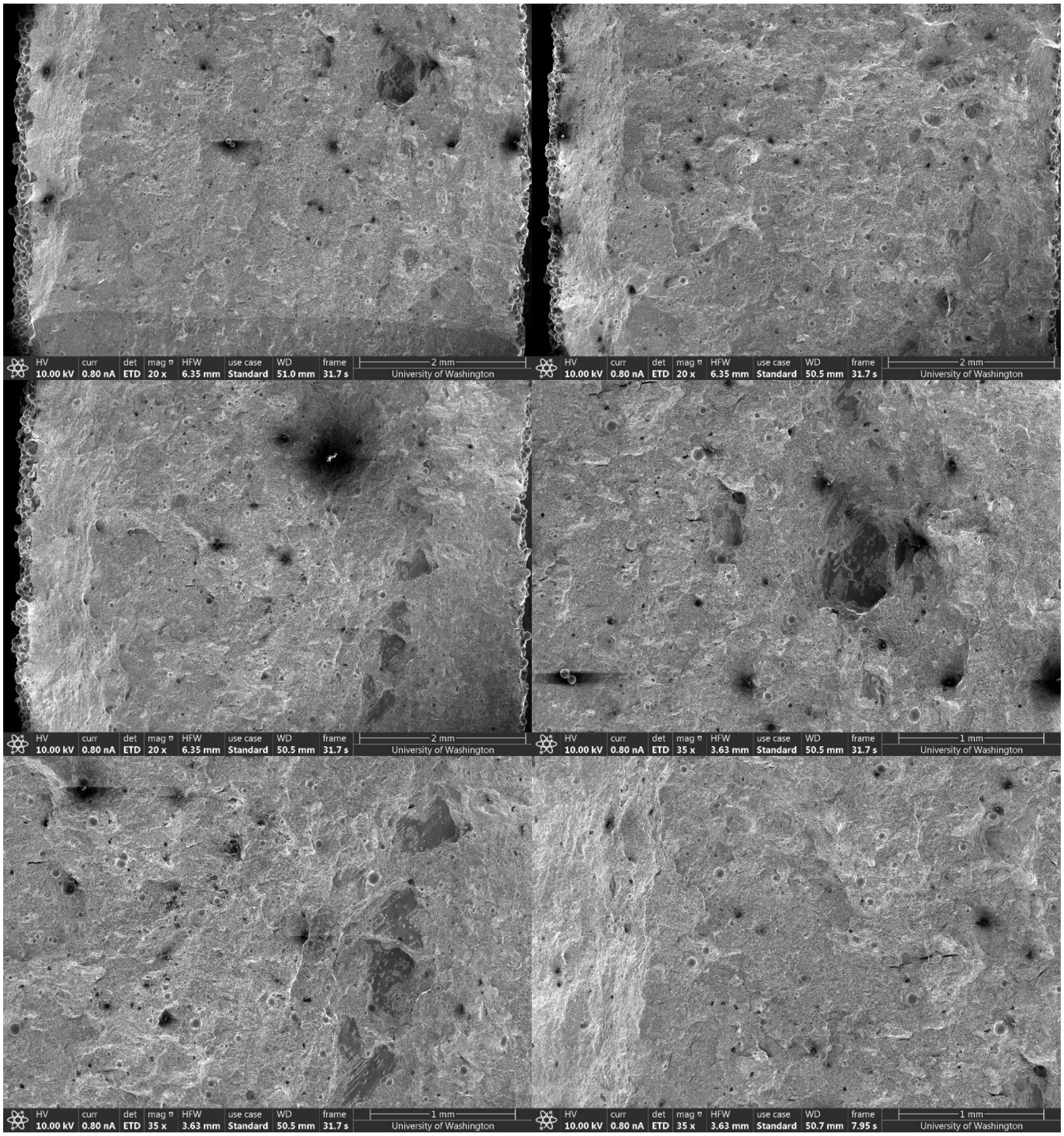

C.3 FT (Virgin Powder) Specimen 7 (60 Degrees) cont.

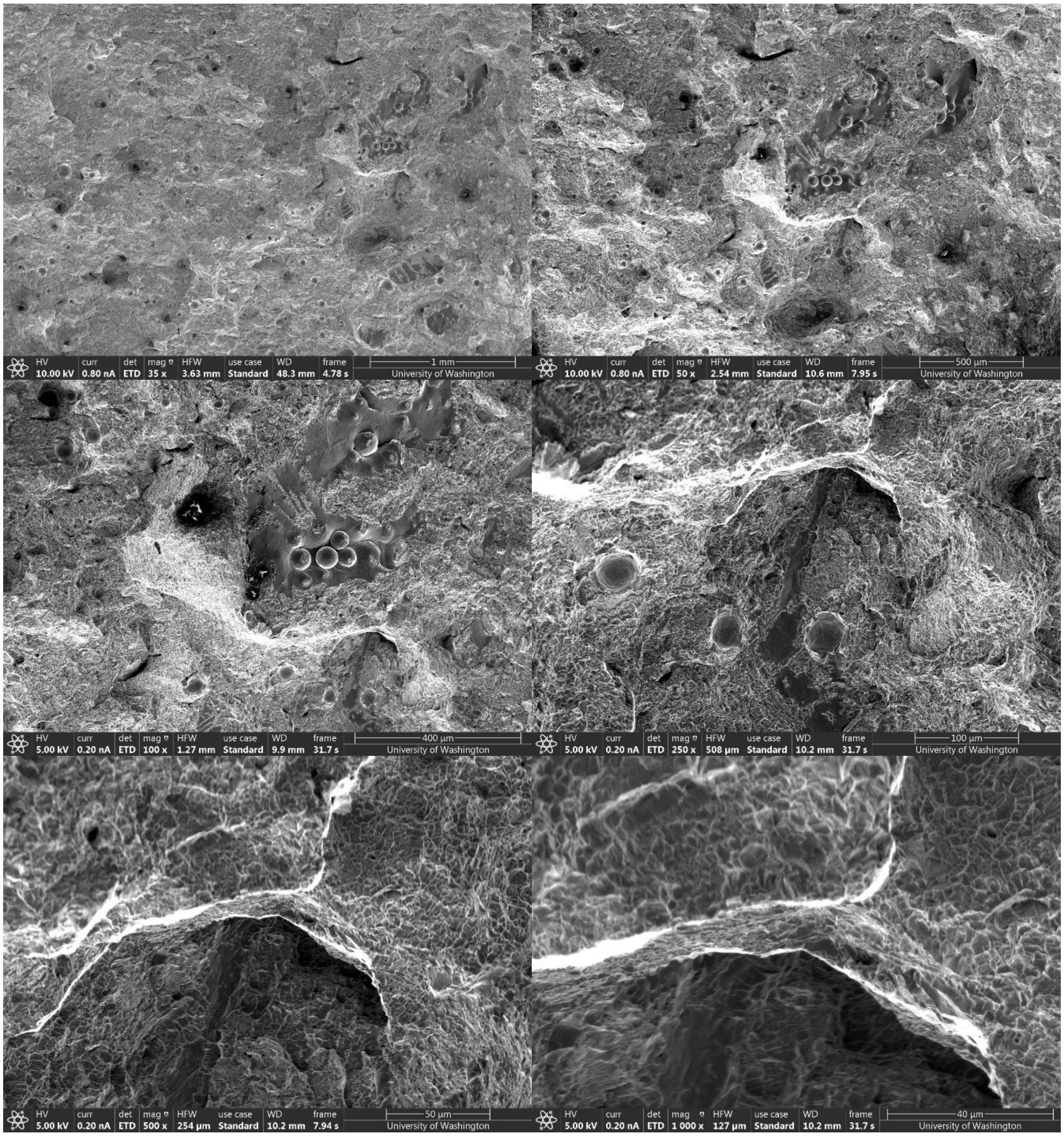

C.3 FT (Virgin Powder) Specimen 7 (60 Degrees) cont.

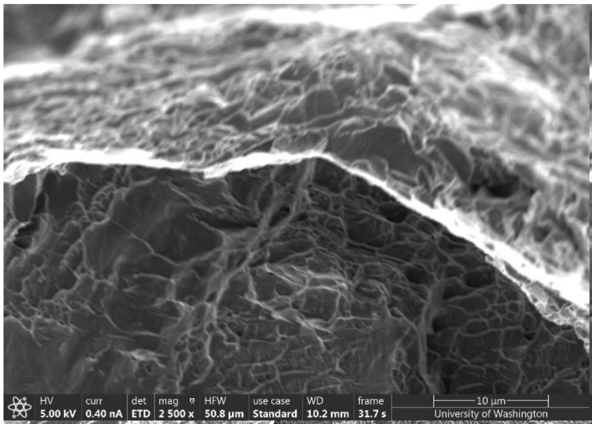

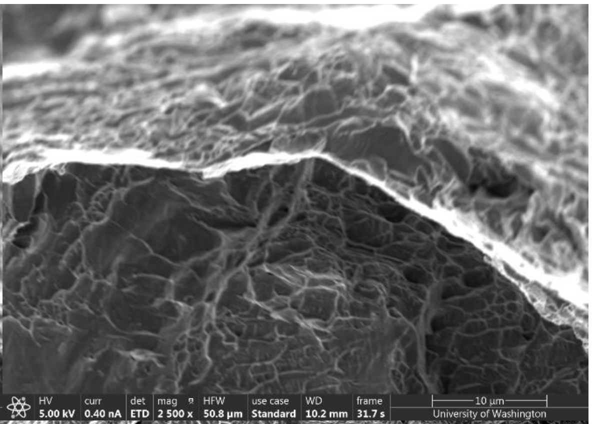

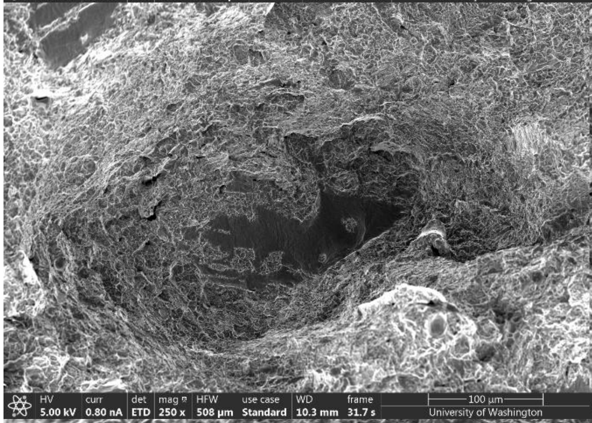

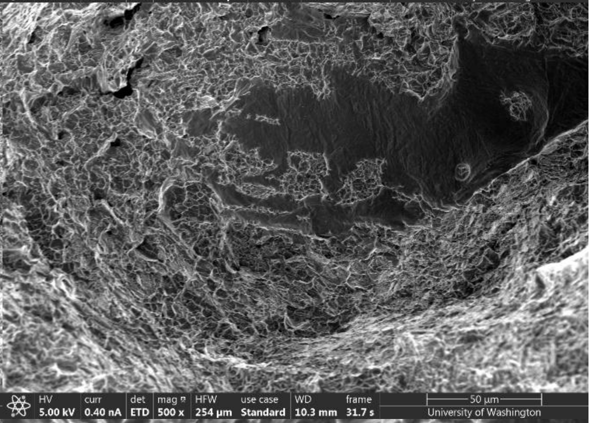

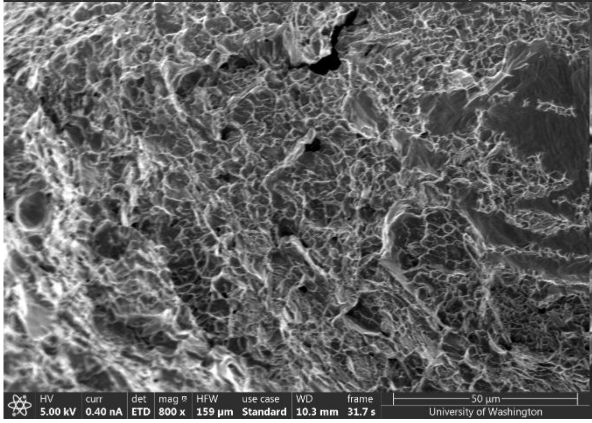

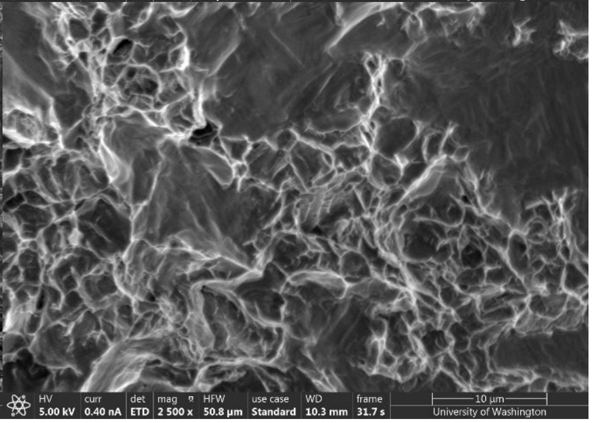

C.3 FT (Virgin Powder) Specimen 7 (60 Degrees) cont.

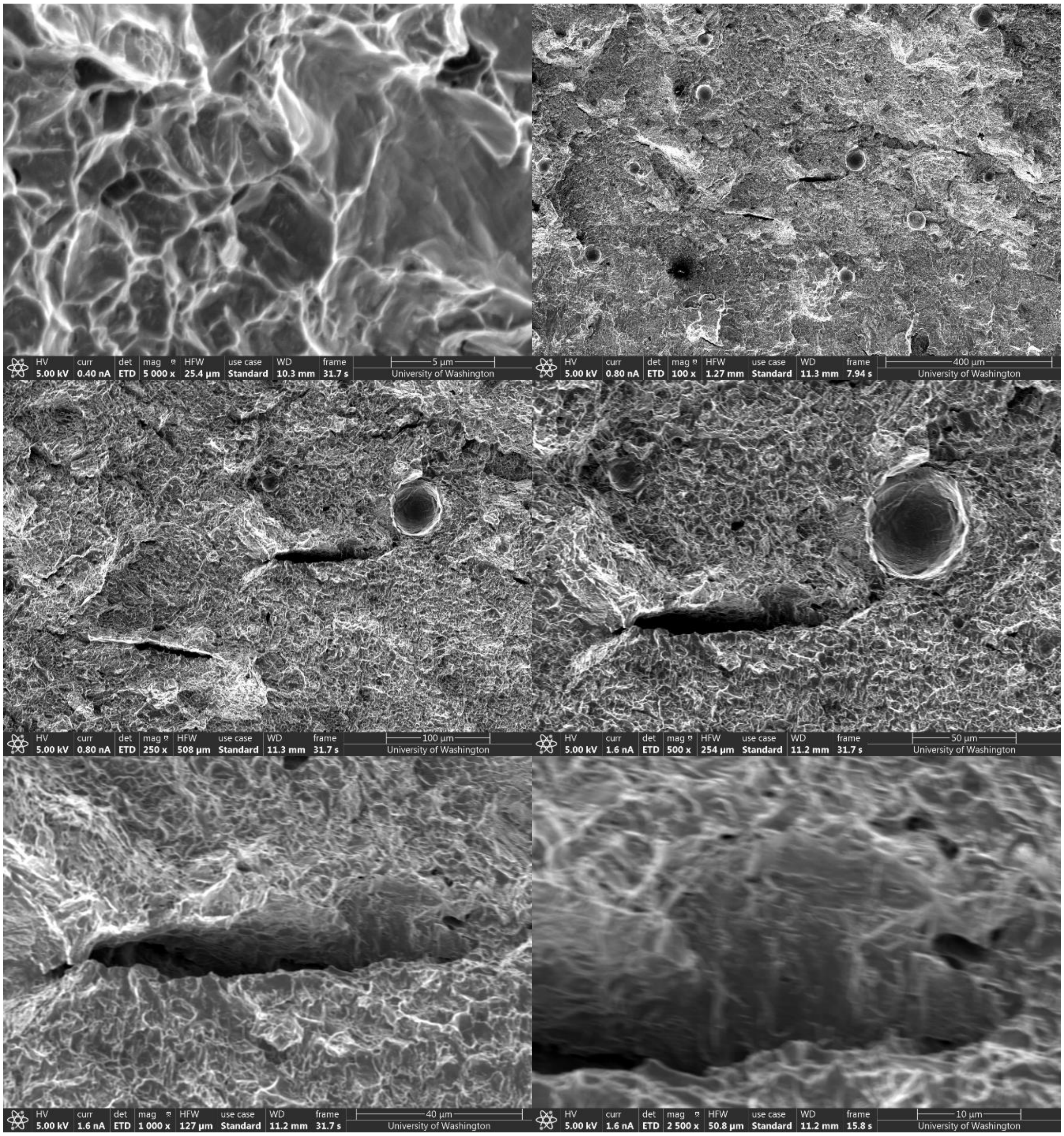

C.3 FT (Virgin Powder) Specimen 7 (60 Degrees) cont.

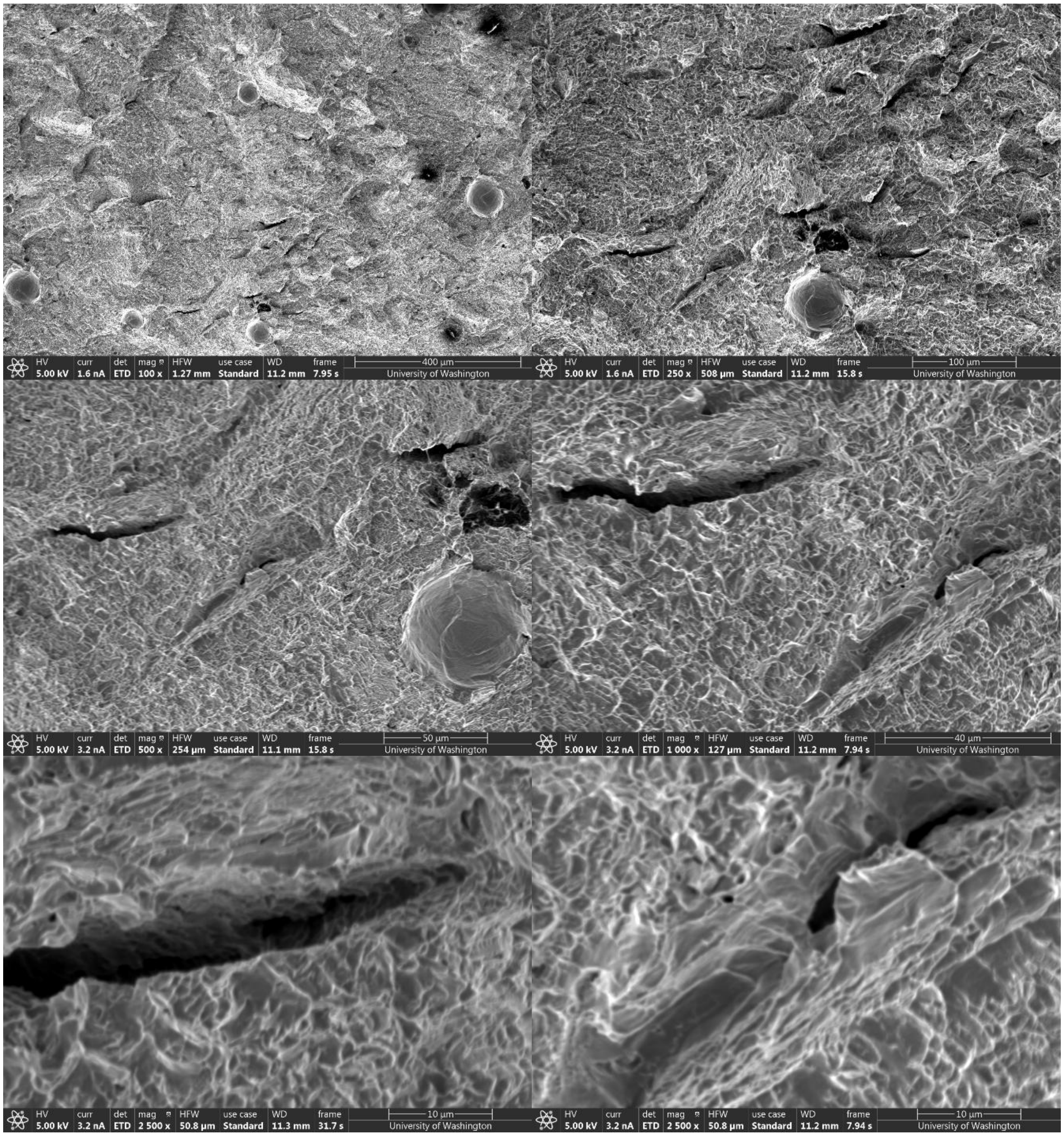

C.3 FT (Virgin Powder) Specimen 7 (60 Degrees) cont.

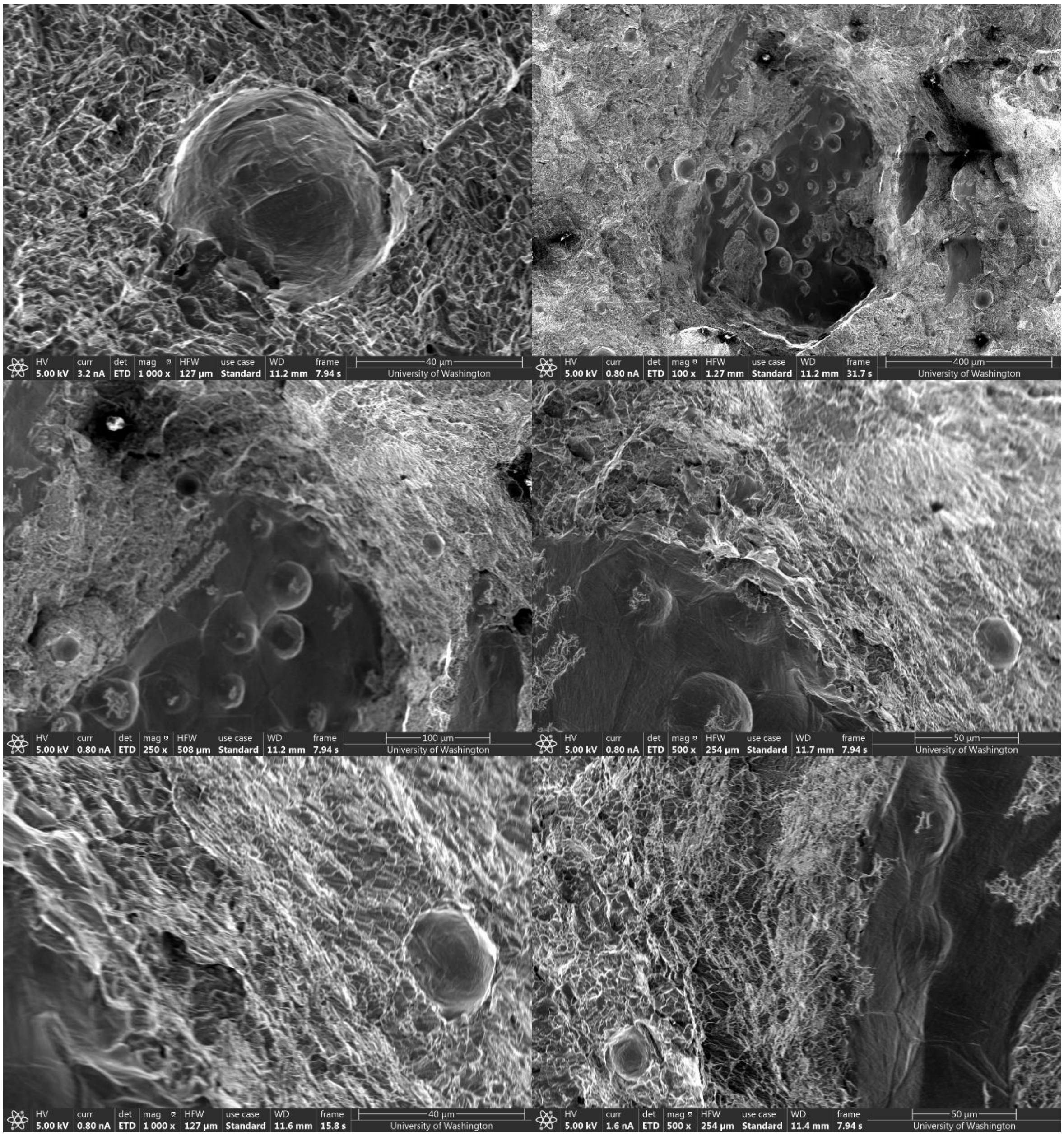

C.3 FT (Virgin Powder) Specimen 7 (60 Degrees) cont.

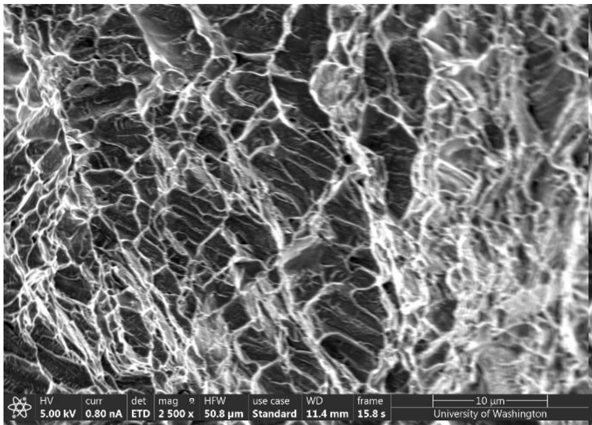

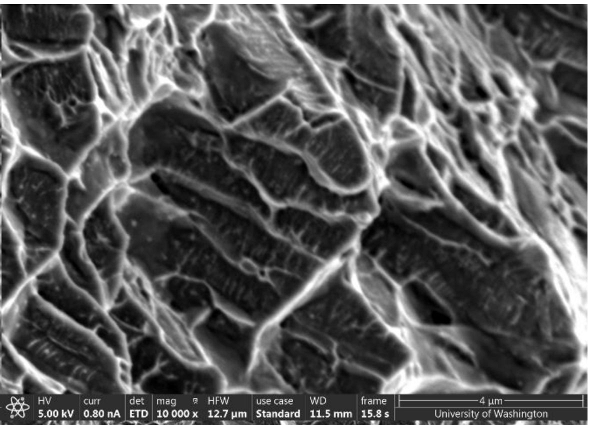

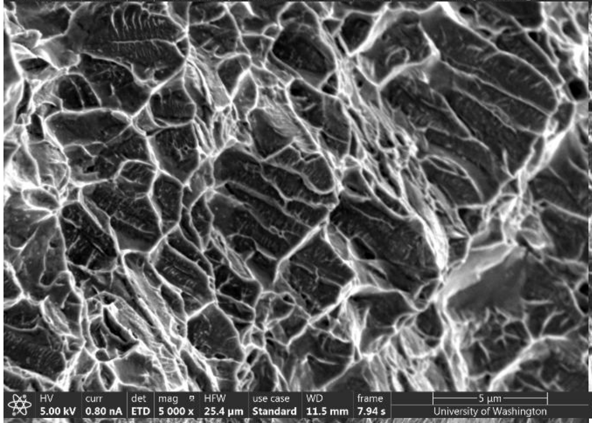

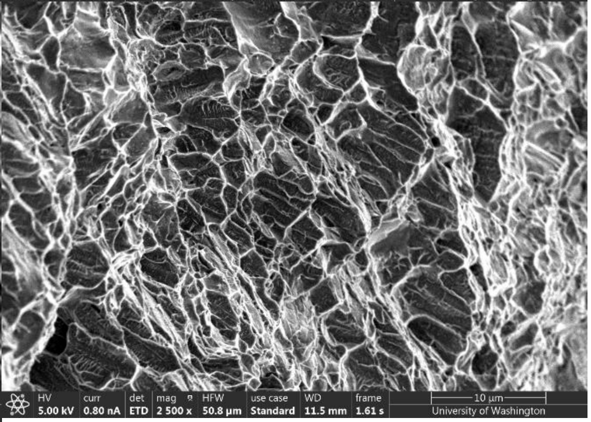

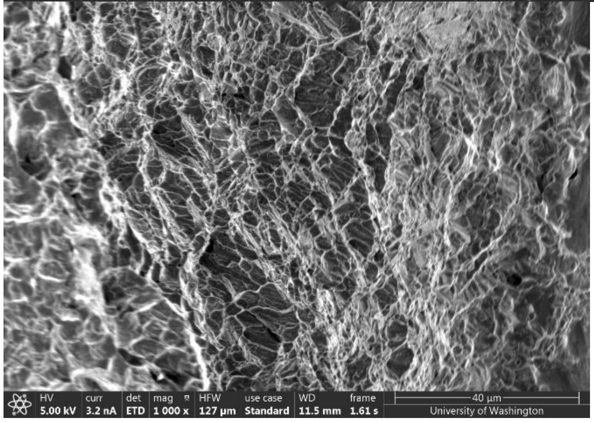

C.4 FT (Virgin Powder) Specimen 10 (90 Degrees)

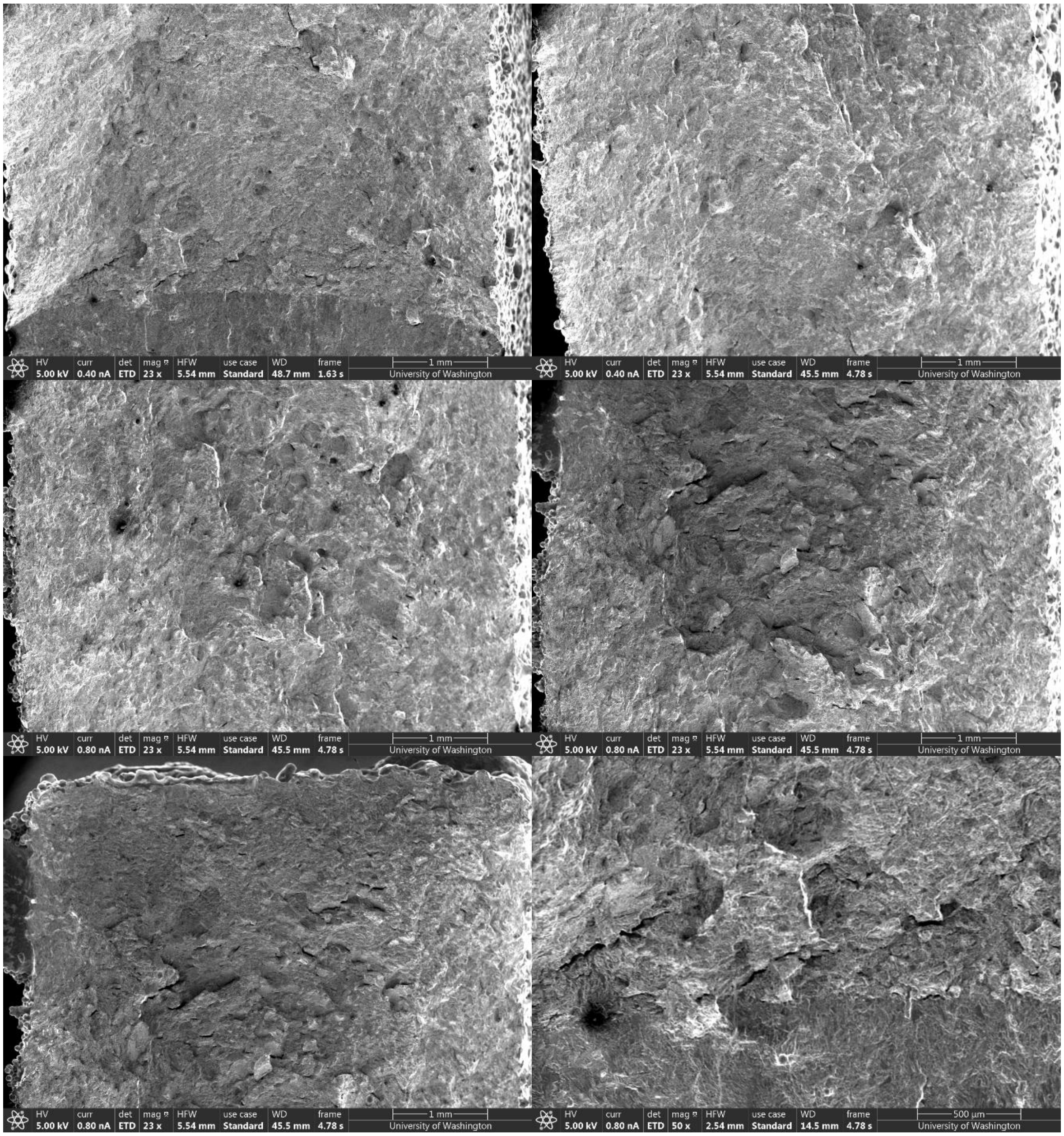

C.4 FT (Virgin Powder) Specimen 10 (90 Degrees) cont.

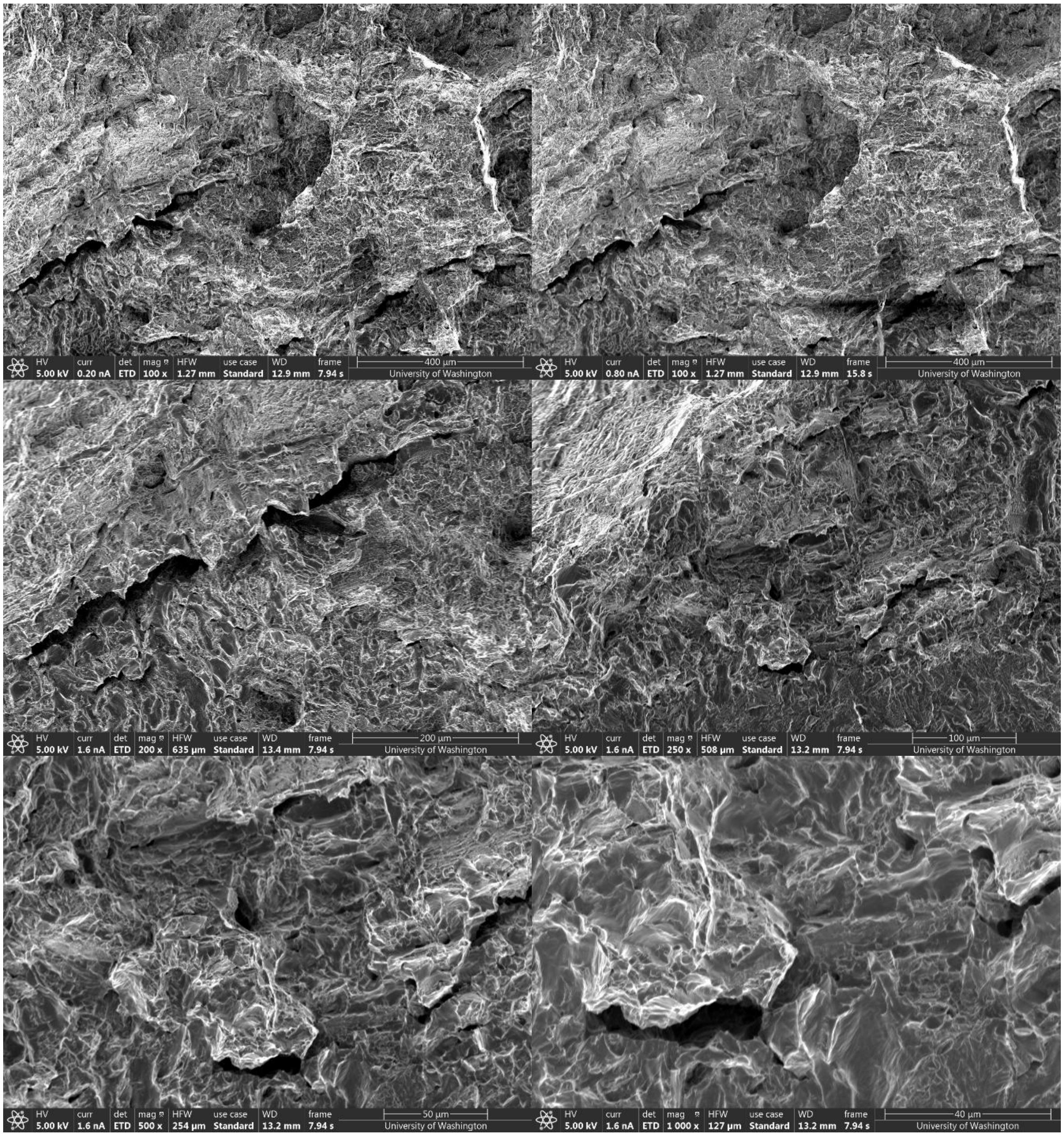

C.4 FT (Virgin Powder) Specimen 10 (90 Degrees) cont.

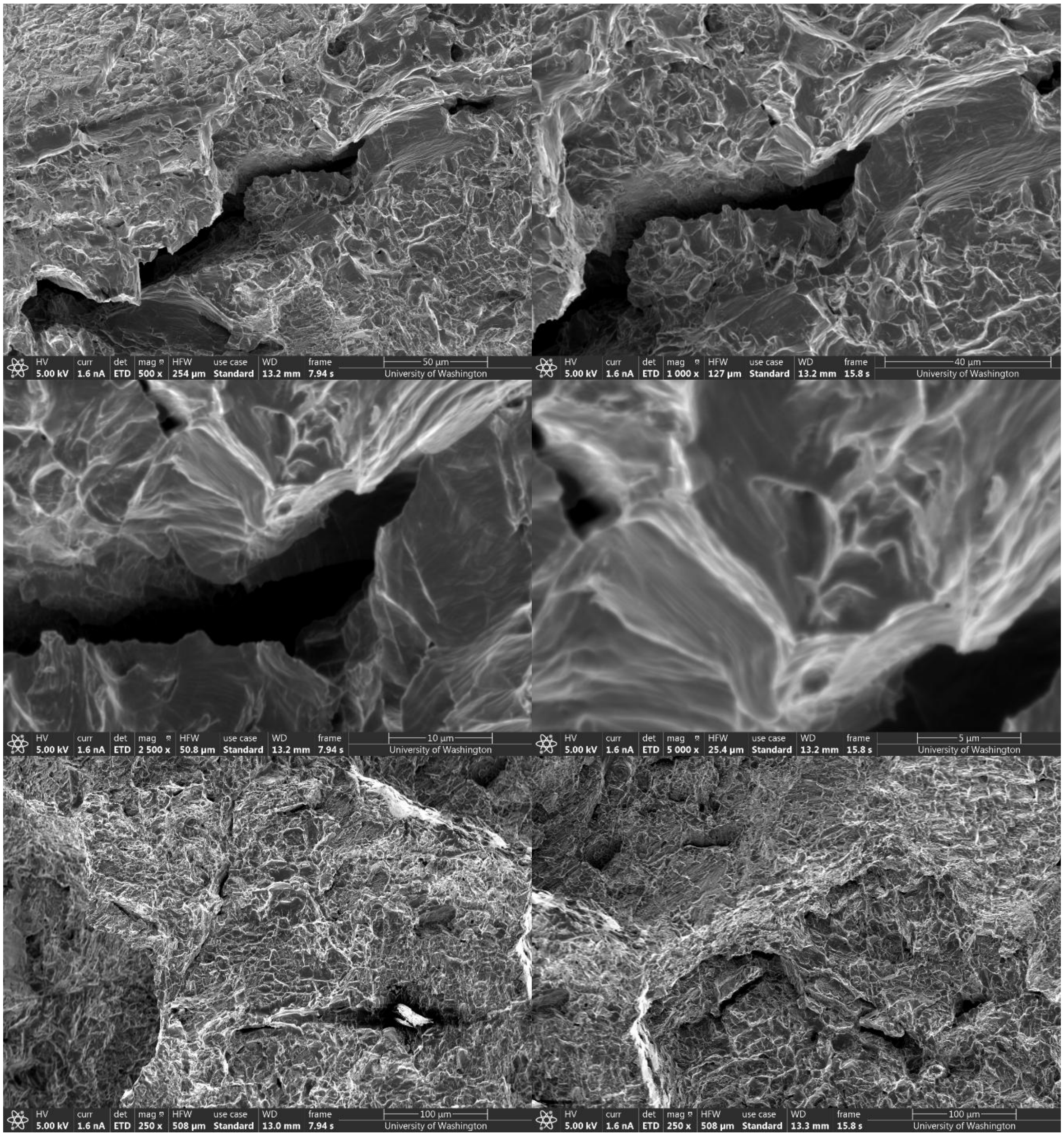

C.4 FT (Virgin Powder) Specimen 10 (90 Degrees) cont.

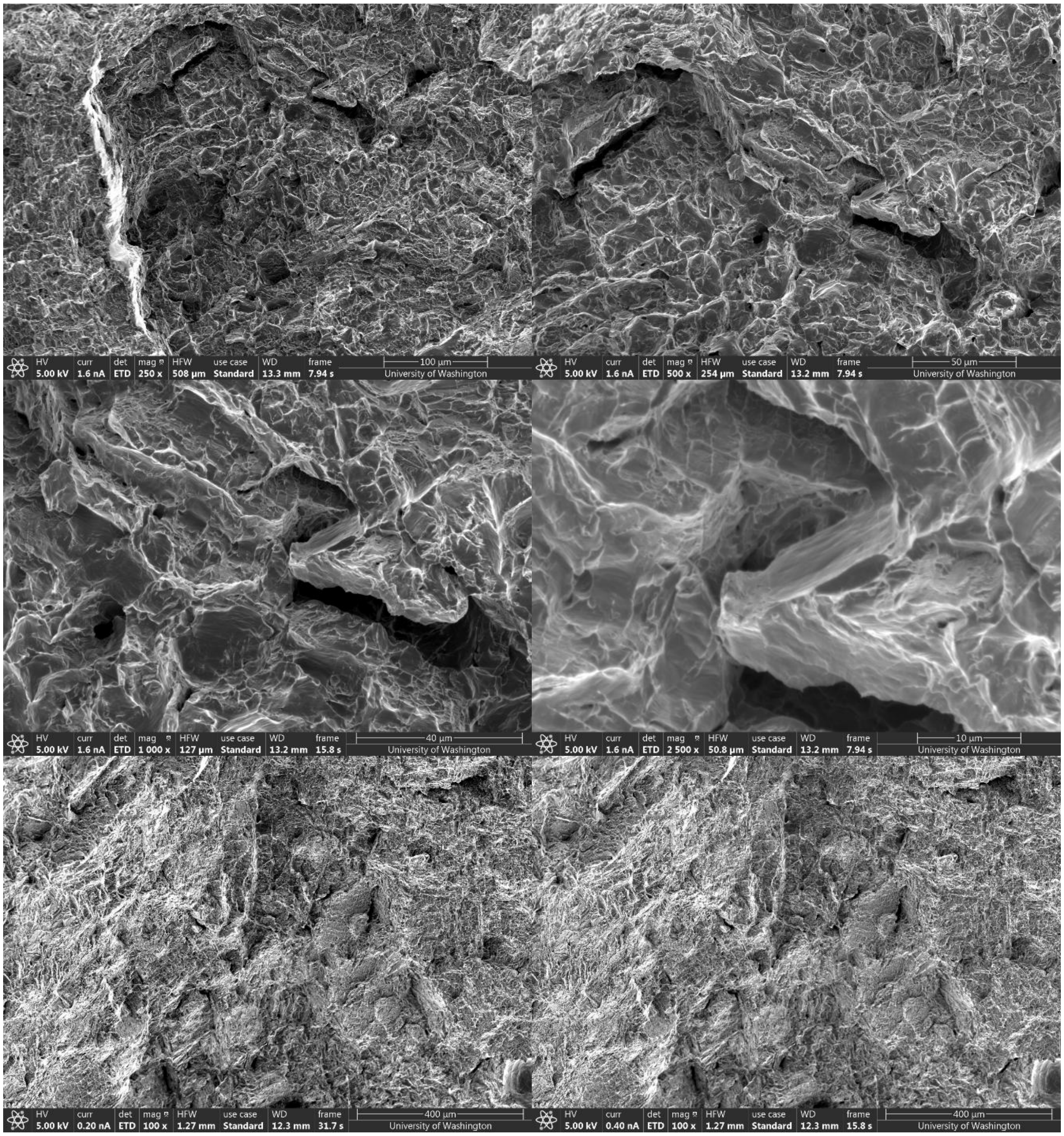

C.4 FT (Virgin Powder) Specimen 10 (90 Degrees) cont.

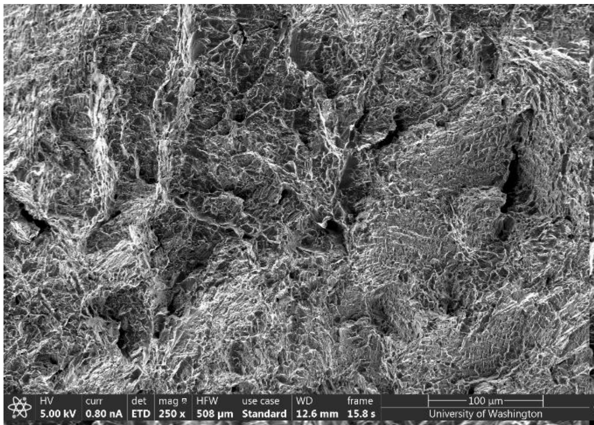

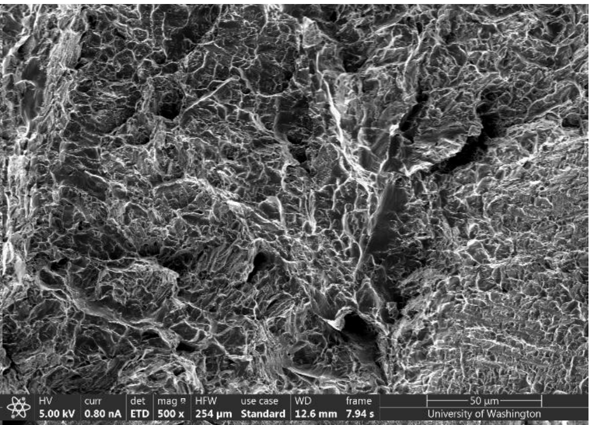

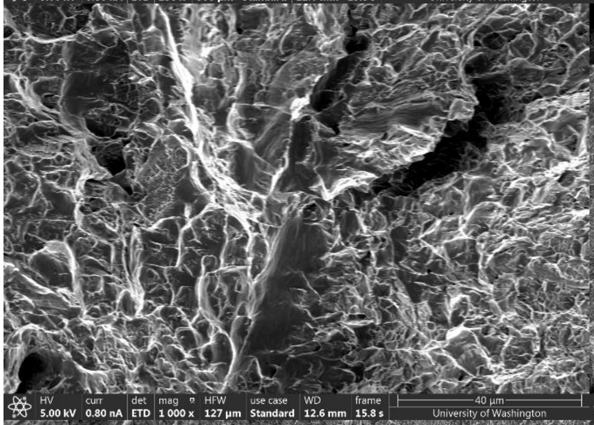

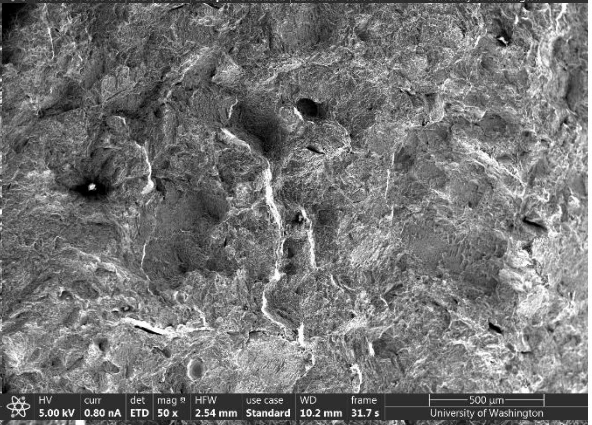

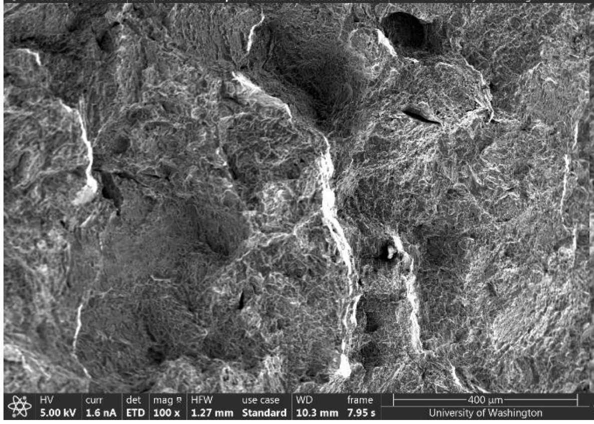

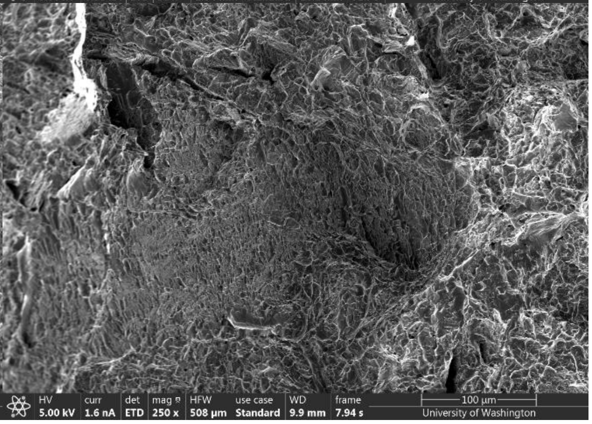

C.4 FT (Virgin Powder) Specimen 10 (90 Degrees) cont.

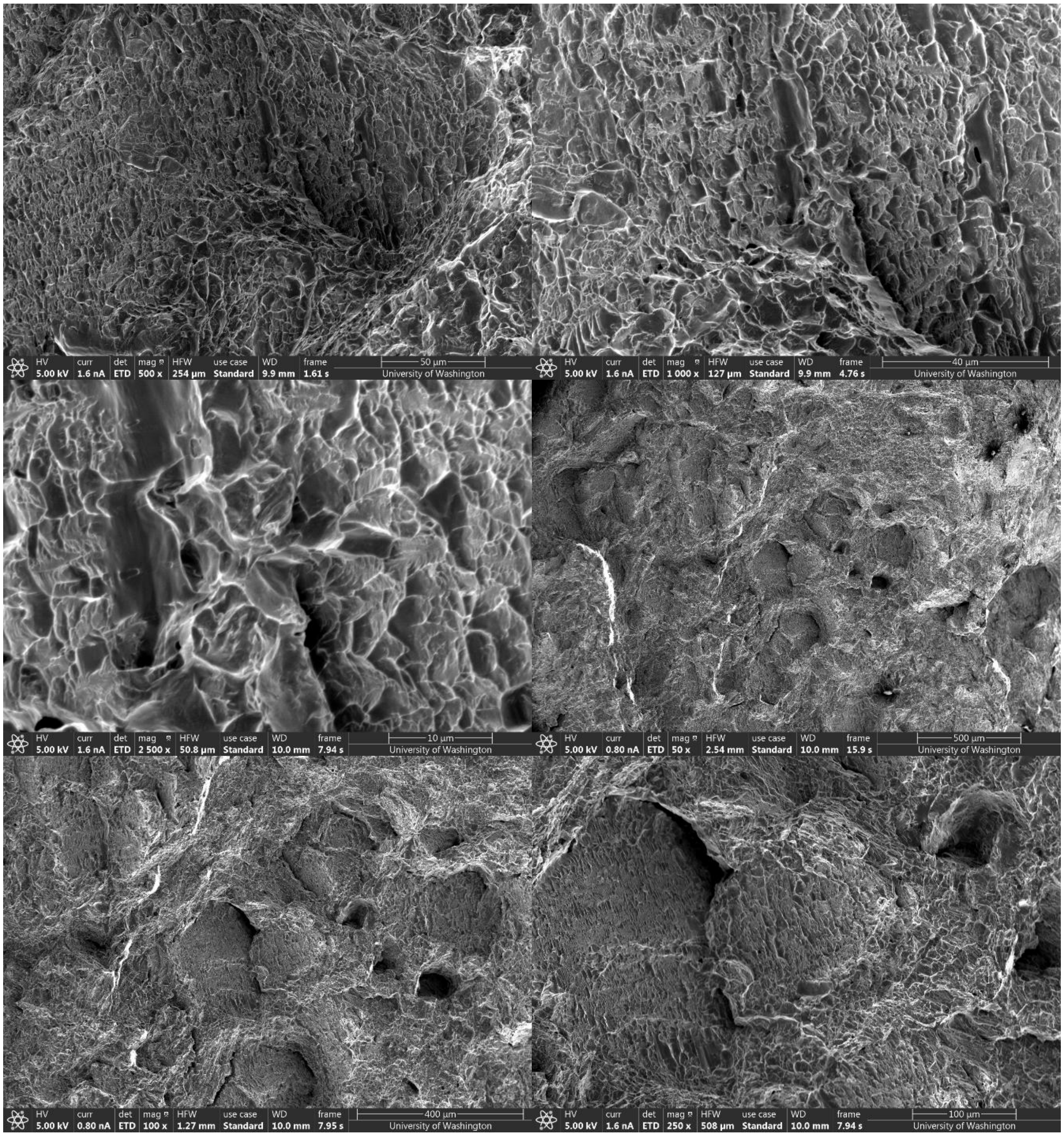

C.4 FT (Virgin Powder) Specimen 10 (90 Degrees) cont.

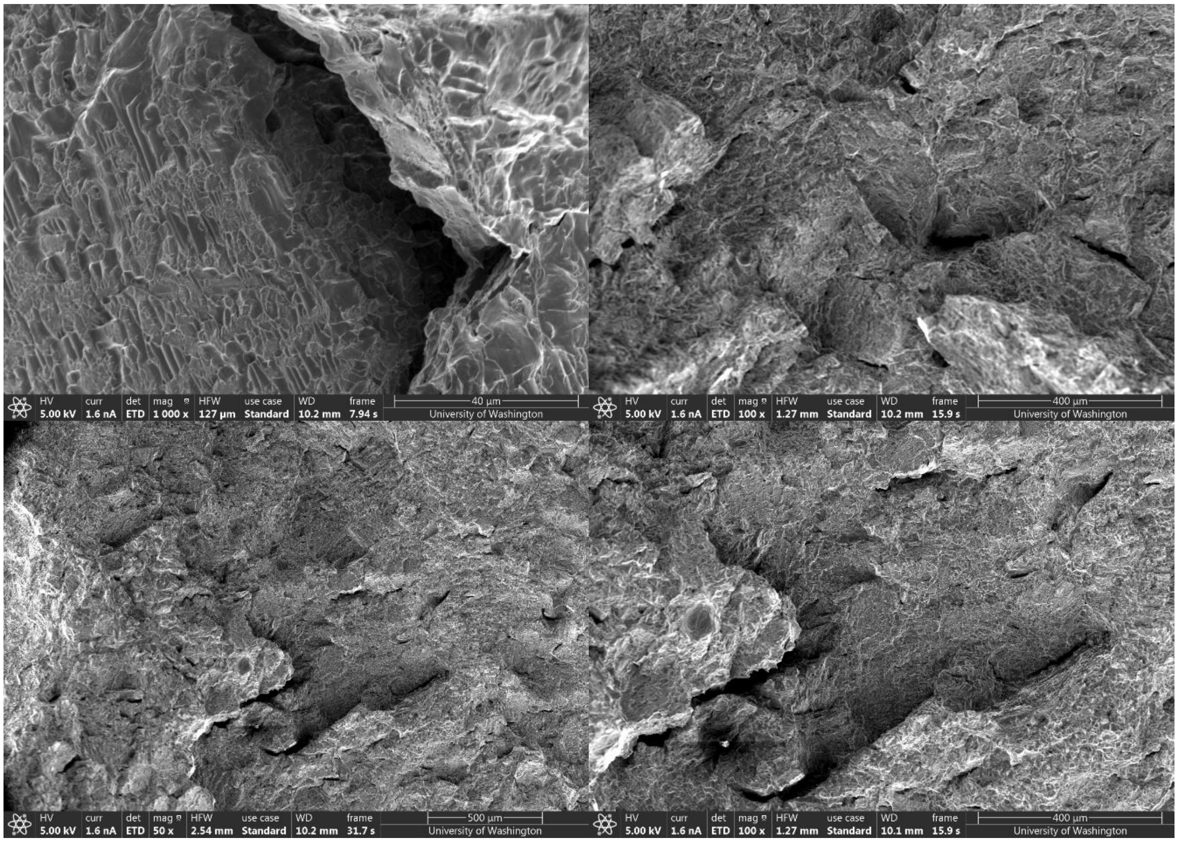

C.5 FCGR (Recycled Powder) Specimen 5 (0 Degrees, B = 6 mm)

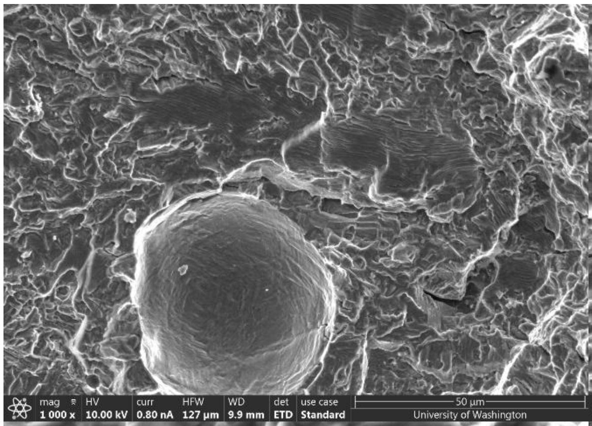

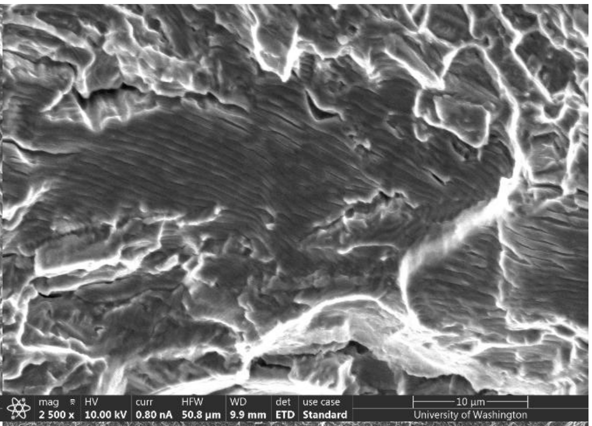

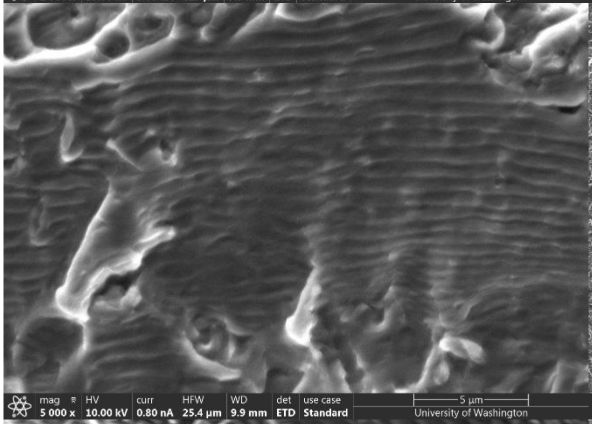

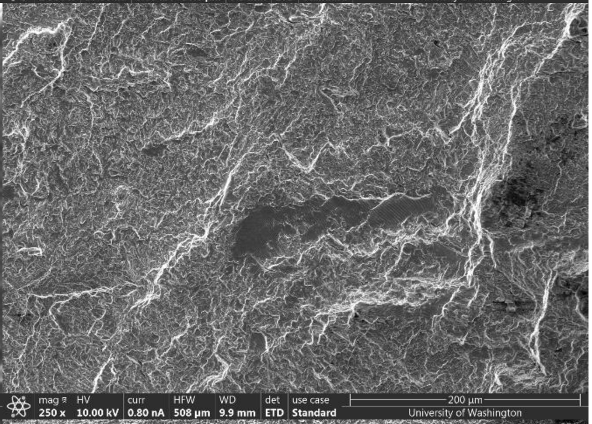

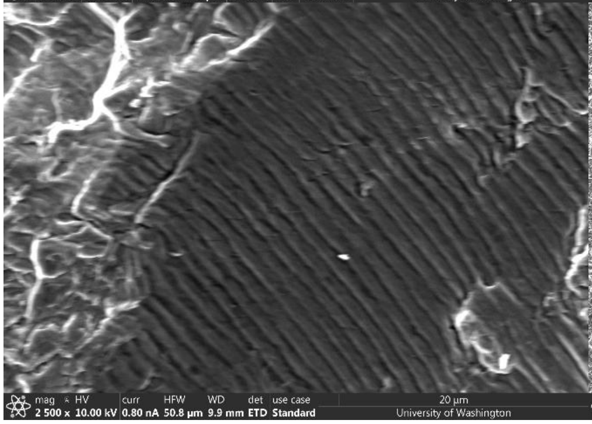

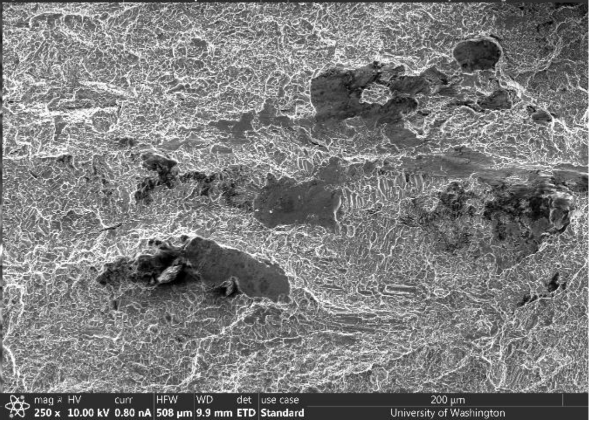

C.5 FCGR (Recycled Powder) Specimen 5 (0 Degrees, B = 6 mm) cont.

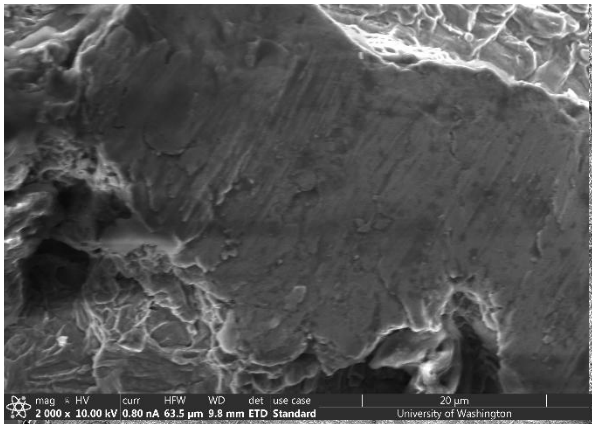

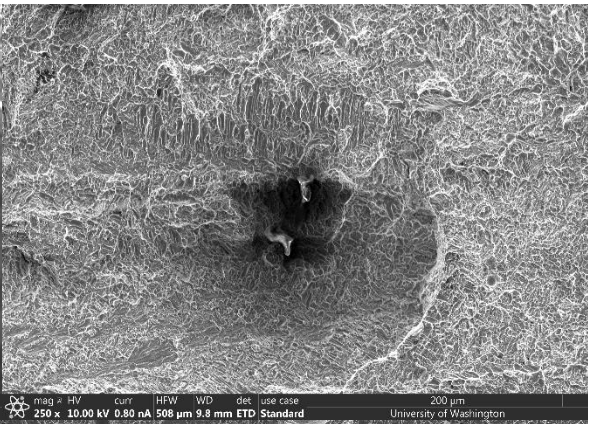

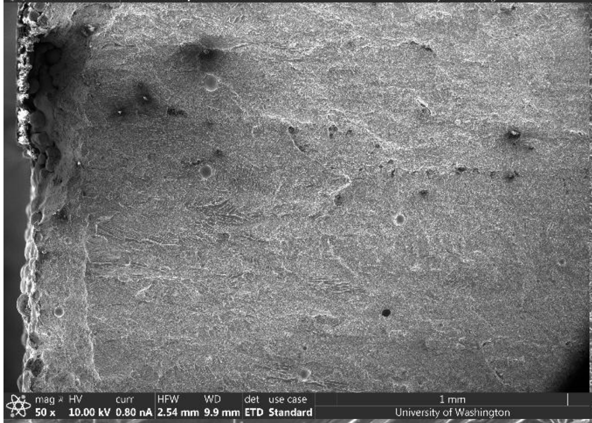

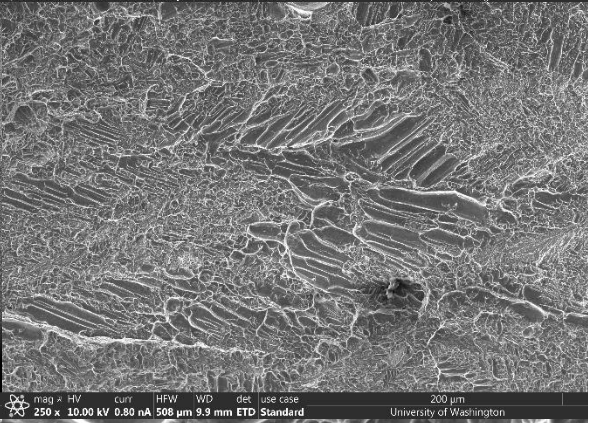

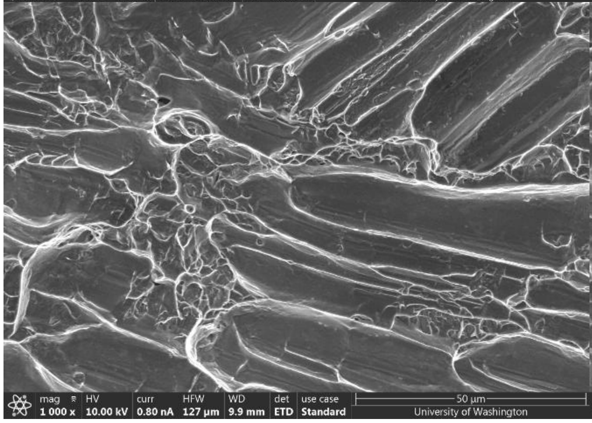

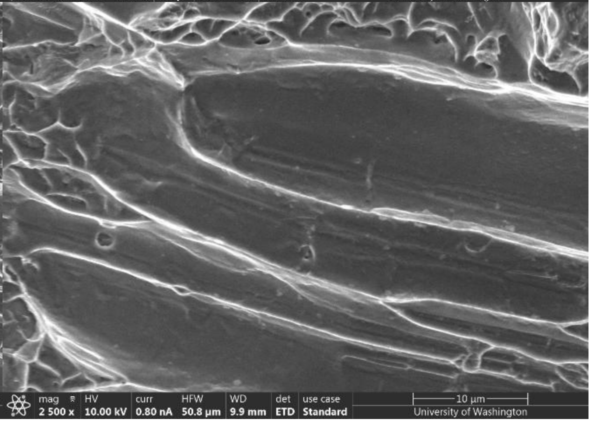

C.5 FCGR (Recycled Powder) Specimen 5 (0 Degrees, B = 6 mm) cont.

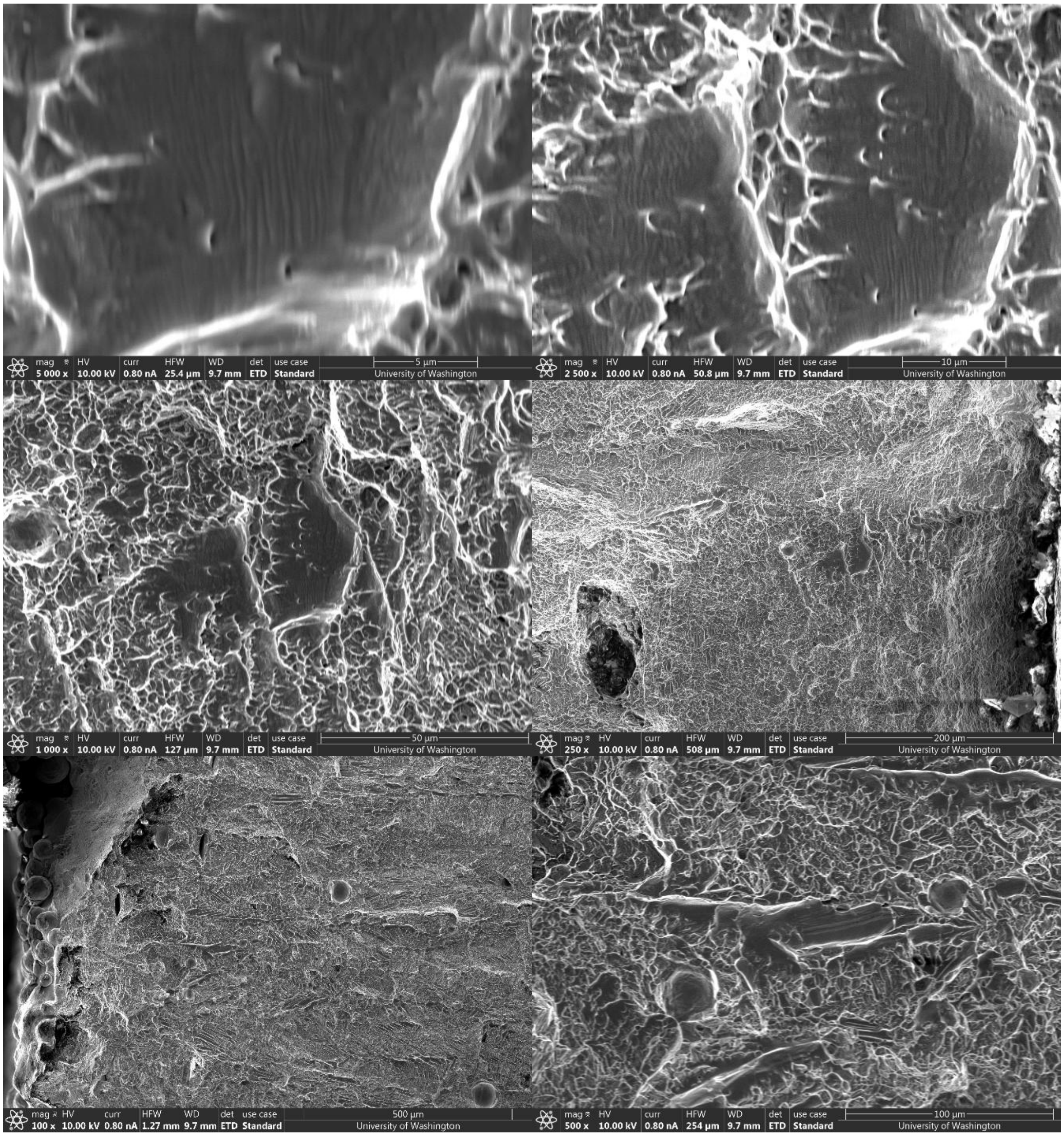

C.5 FCGR (Recycled Powder) Specimen 5 (0 Degrees, B = 6 mm) cont.

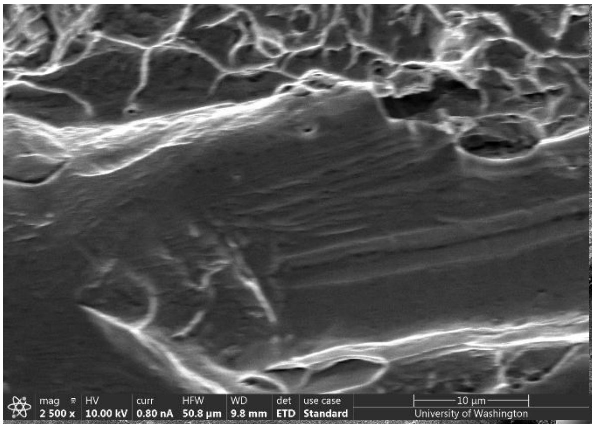

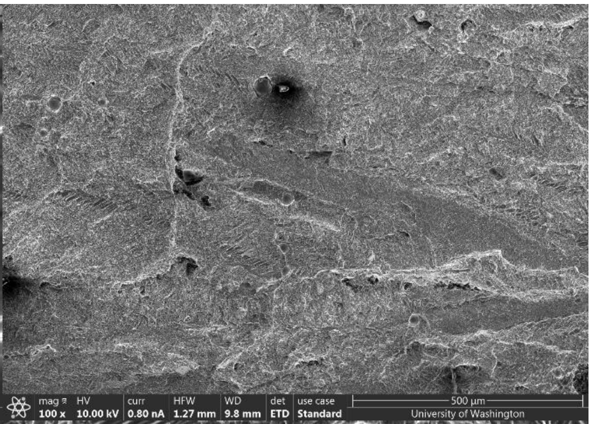

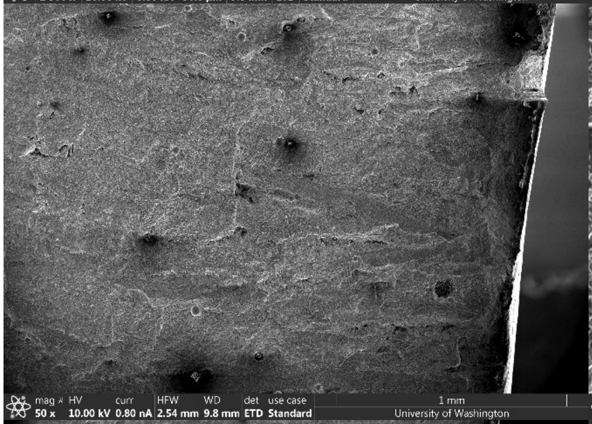

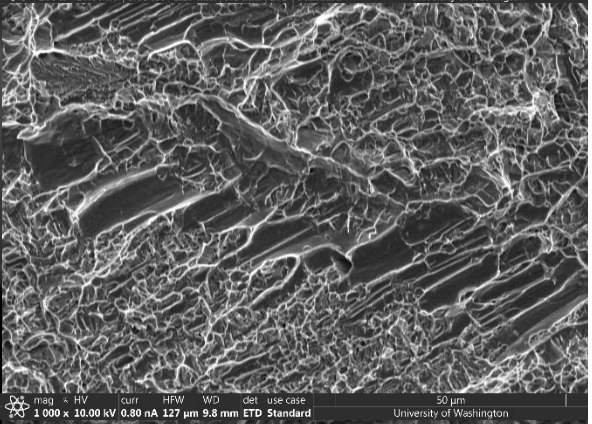

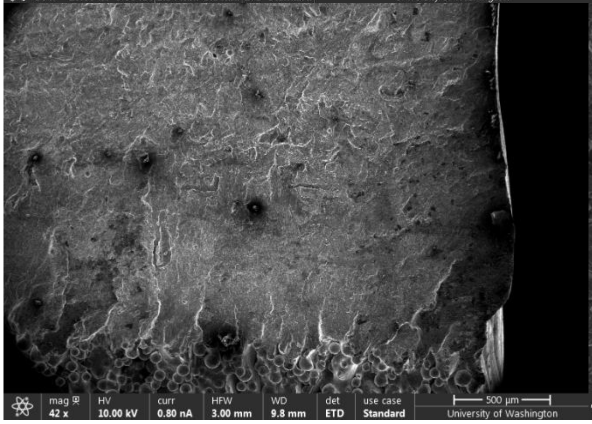

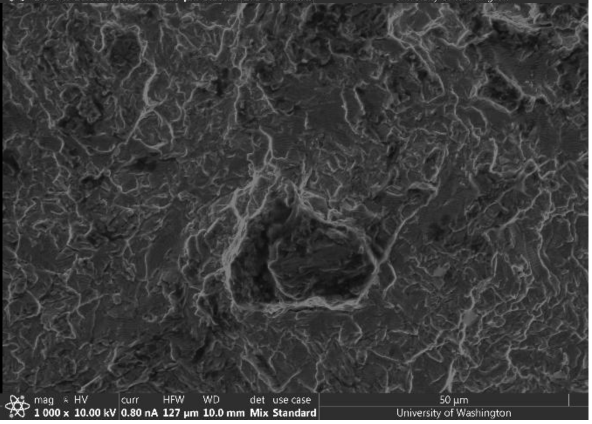

C.6 FCGR (Recycled Powder) Specimen 10 (30 Degrees, B = 6 mm)

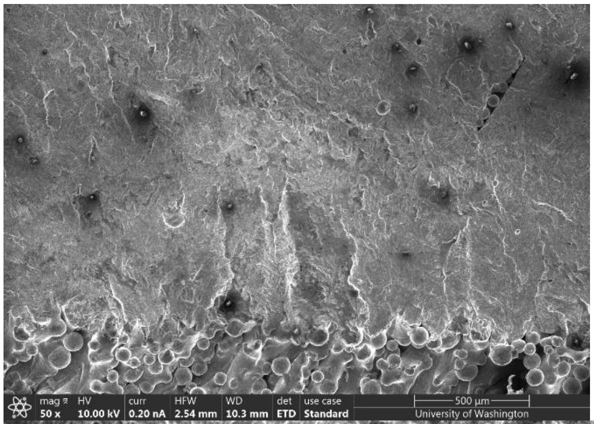

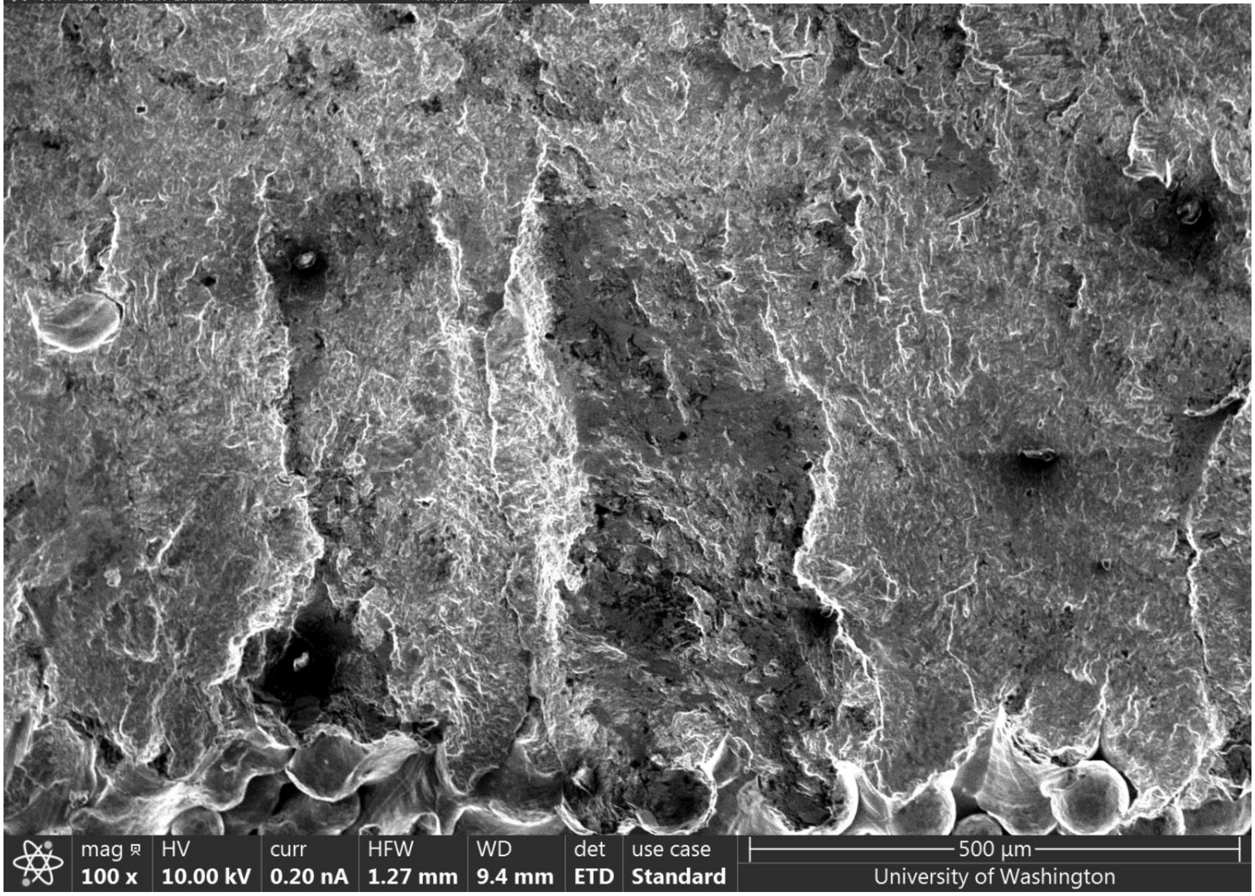

C.6 FCGR (Recycled Powder) Specimen 10 (30 Degrees, B = 6 mm)

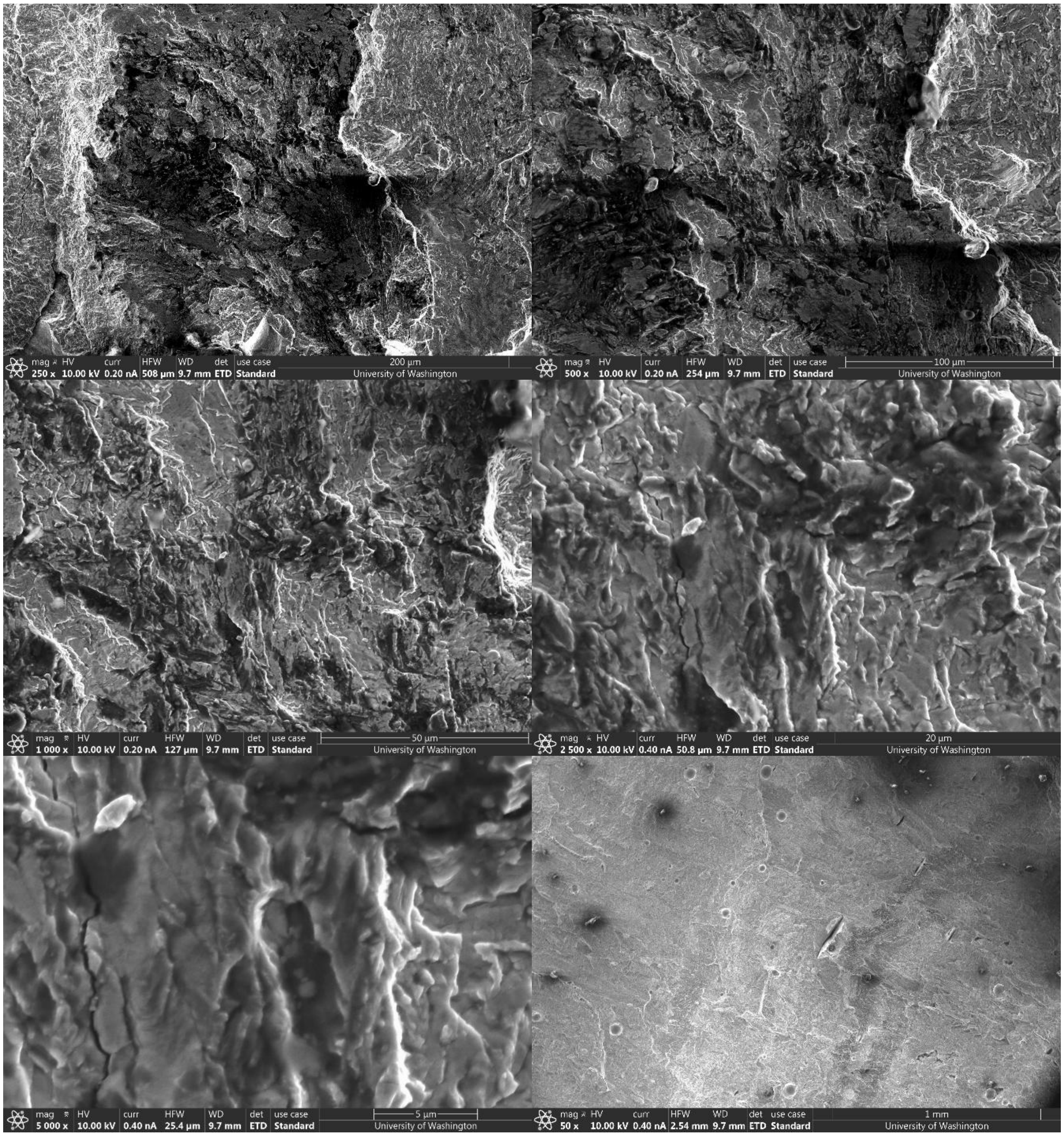

C.6 FCGR (Recycled Powder) Specimen 10 (30 Degrees, B = 6 mm)

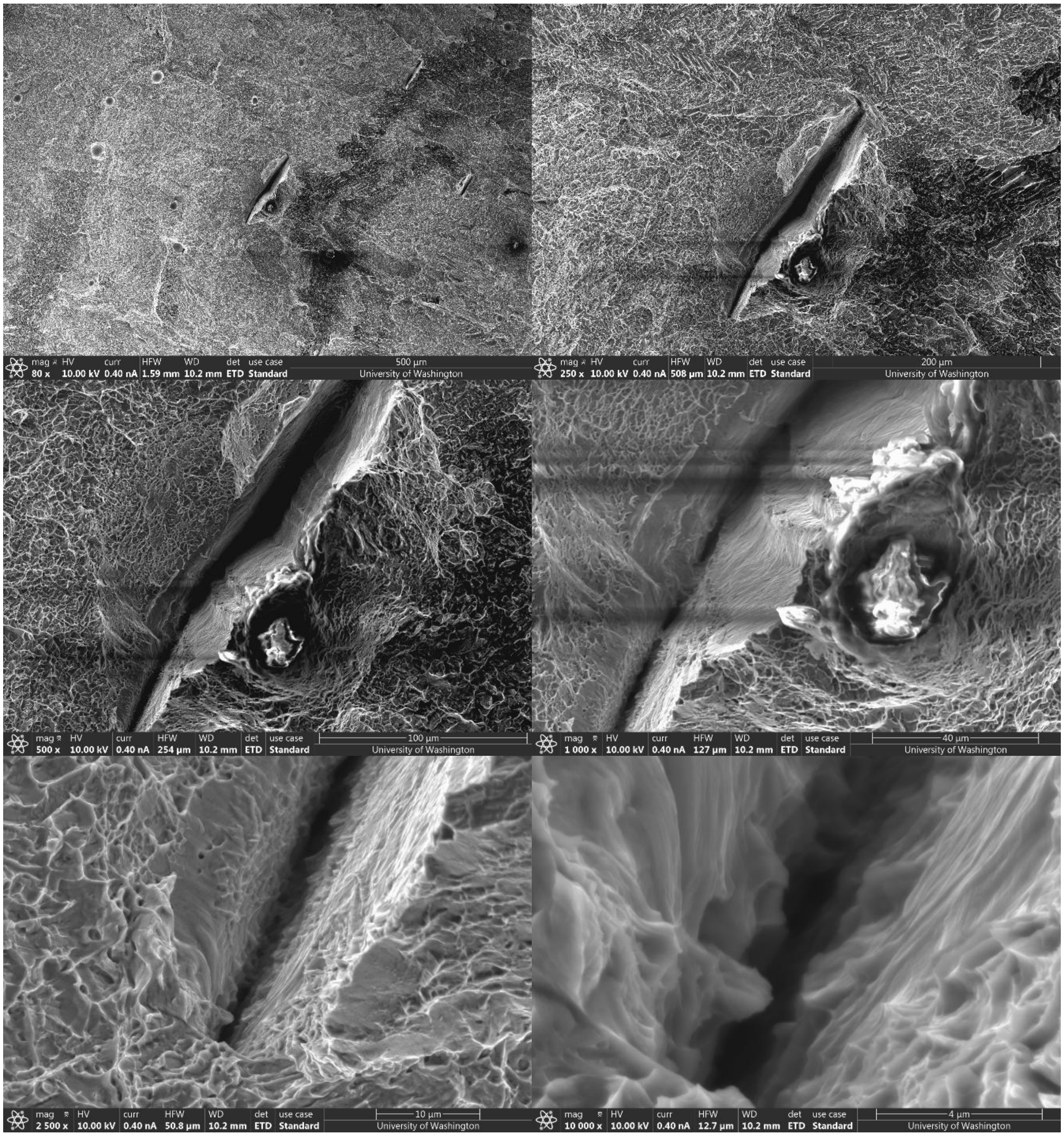

C.6 FCGR (Recycled Powder) Specimen 10 (30 Degrees, B = 6 mm)

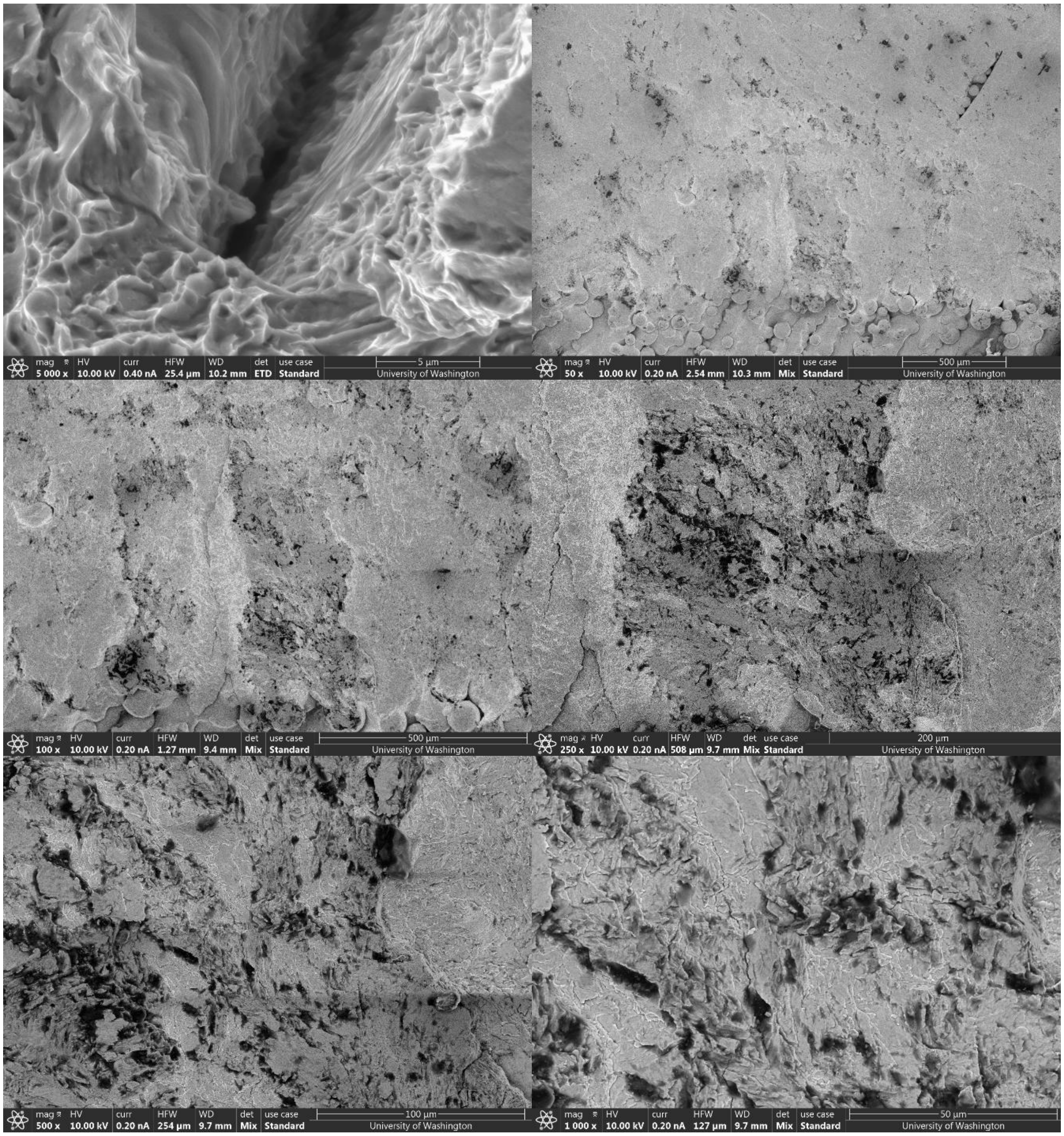

C.6 FCGR (Recycled Powder) Specimen 10 (30 Degrees, B = 6 mm)

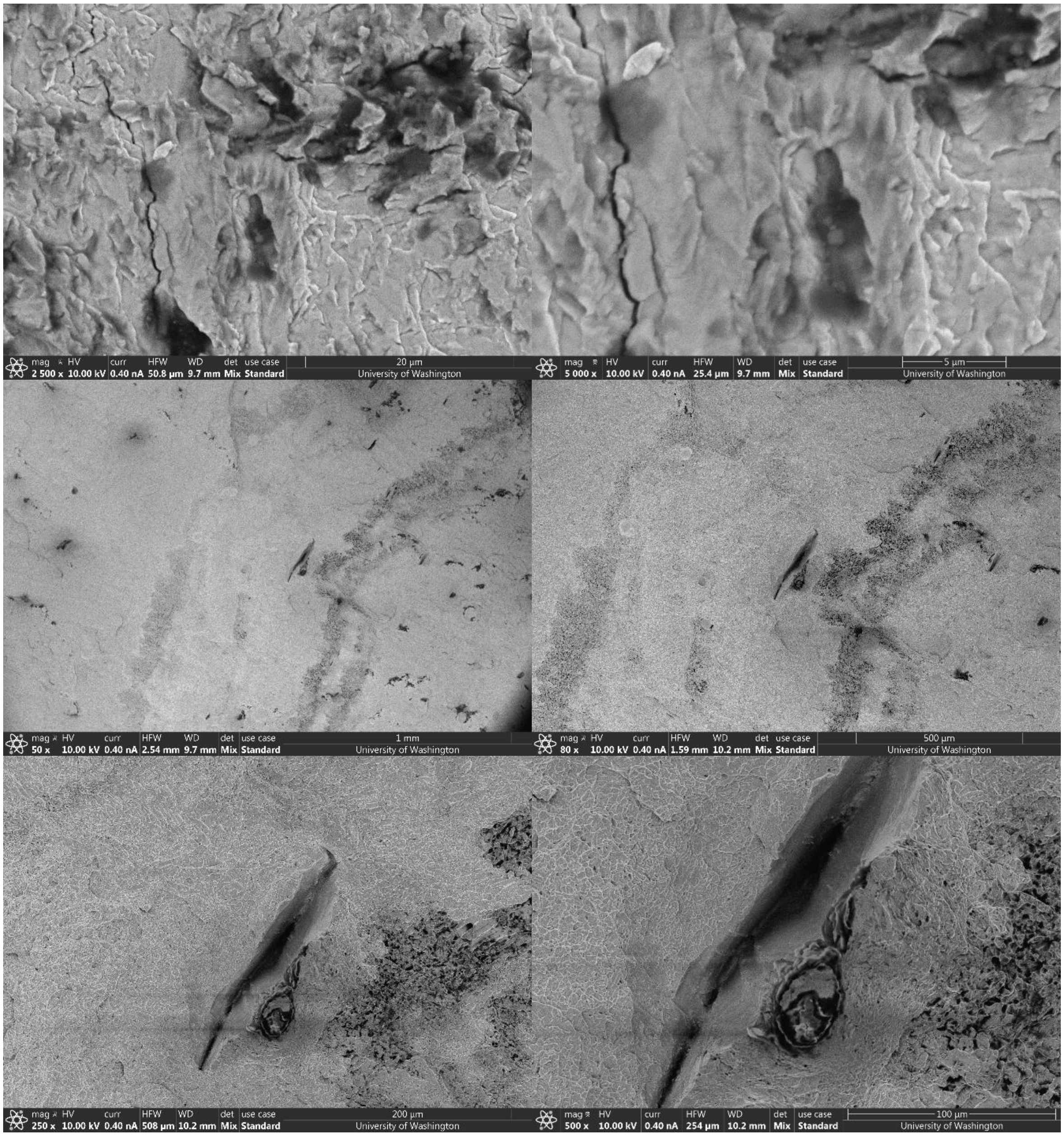

C.6 FCGR (Recycled Powder) Specimen 10 (30 Degrees, B = 6 mm)

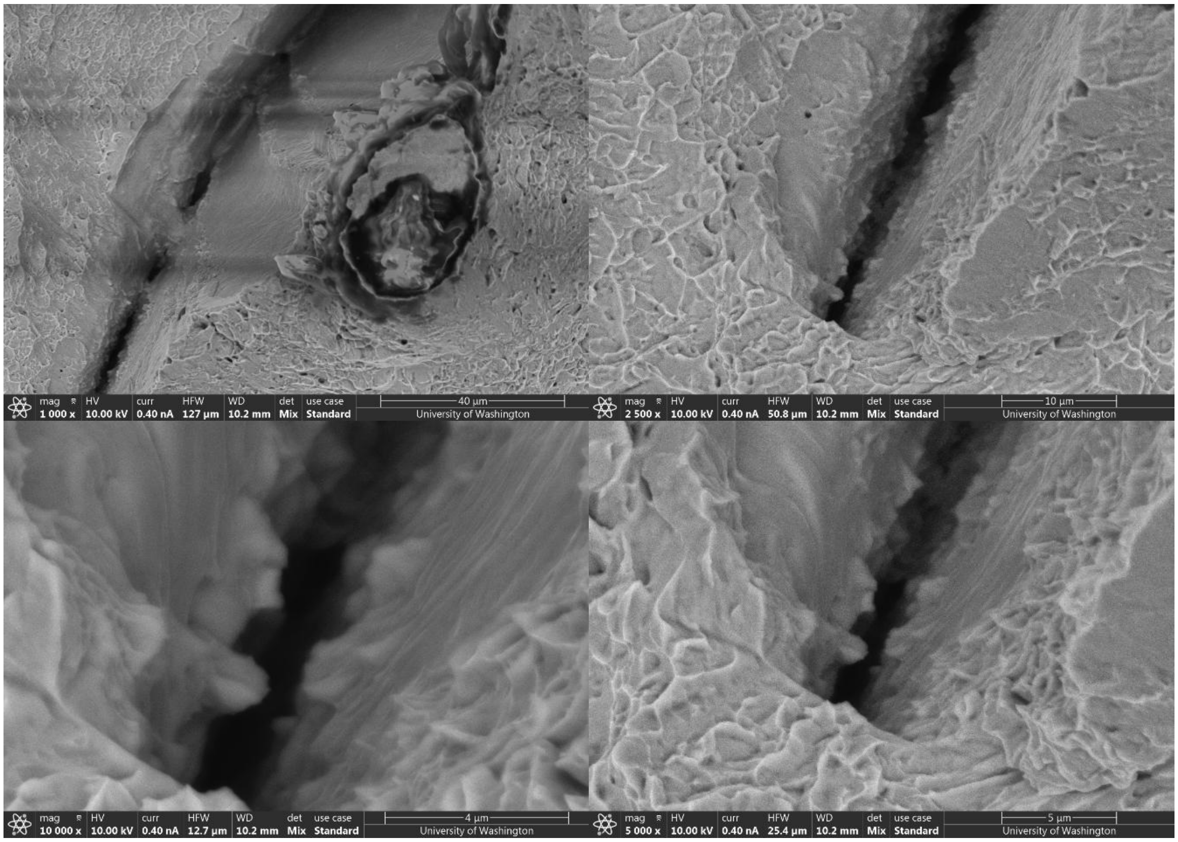

C.7 FCGR (Recycled Powder) Specimen 7 (60 Degrees, B = 6 mm)

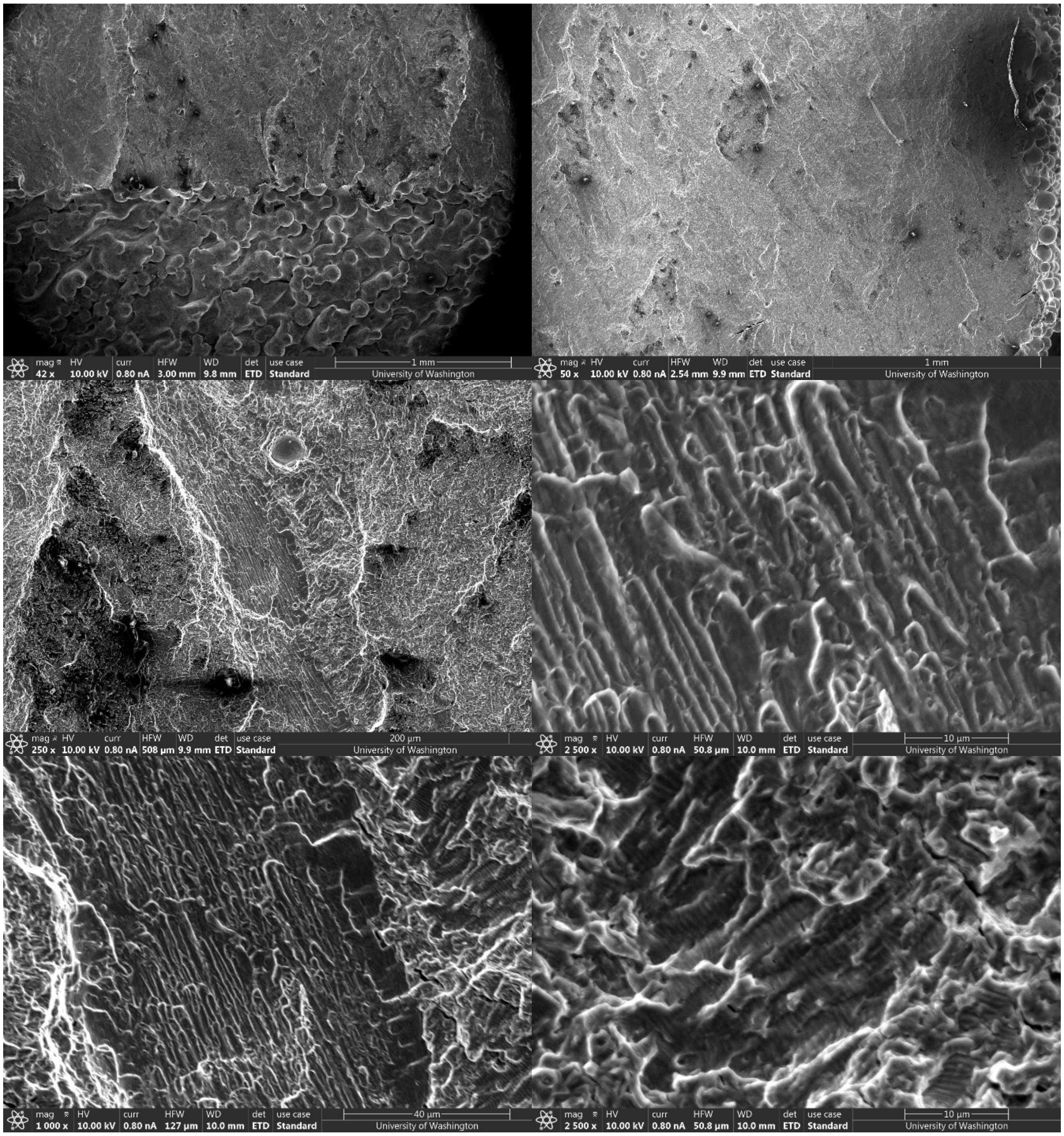

C.7 FCGR (Recycled Powder) Specimen 7 (60 Degrees, B = 6 mm) cont.

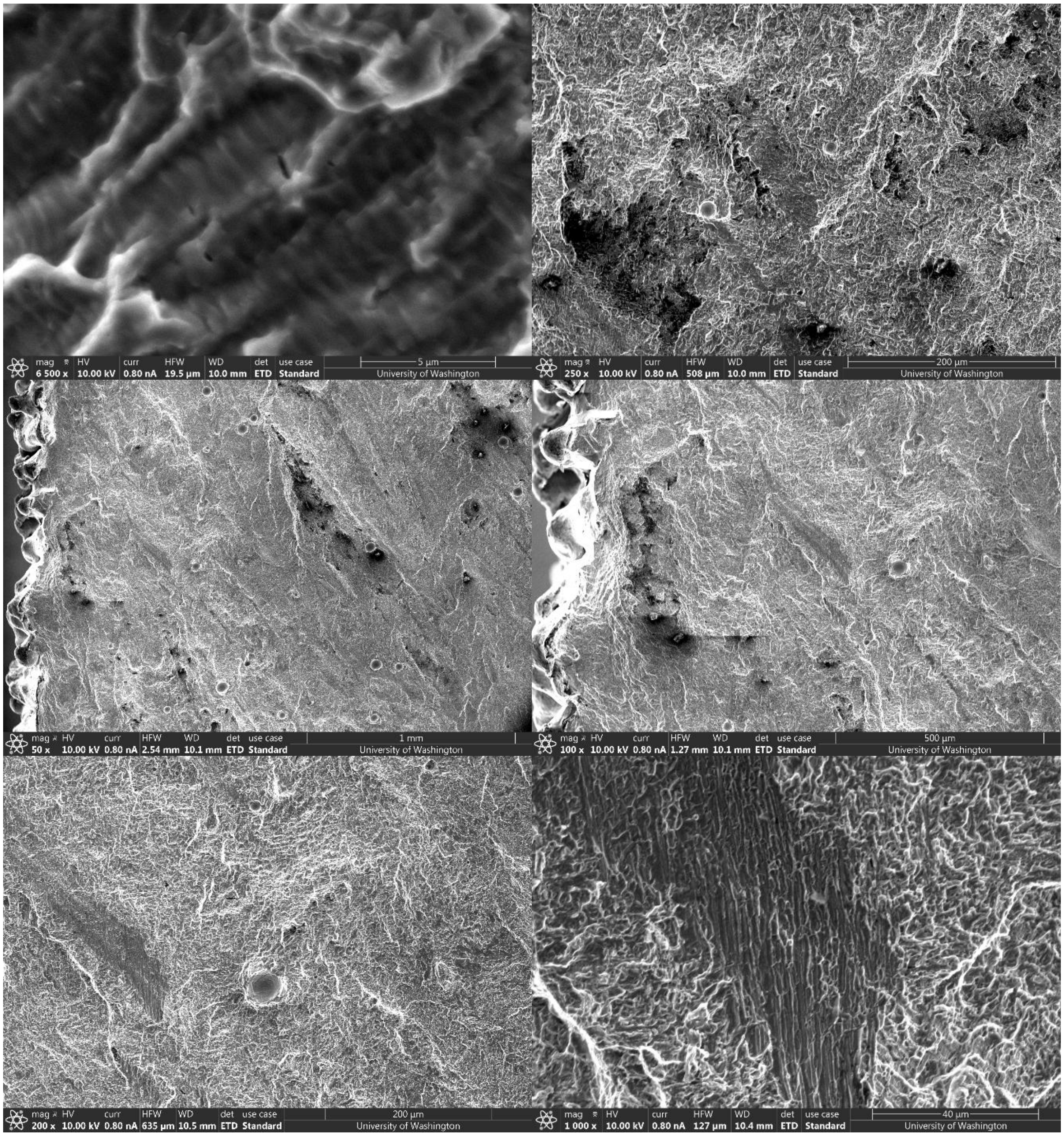

C.7 FCGR (Recycled Powder) Specimen 7 (60 Degrees, B = 6 mm) cont.

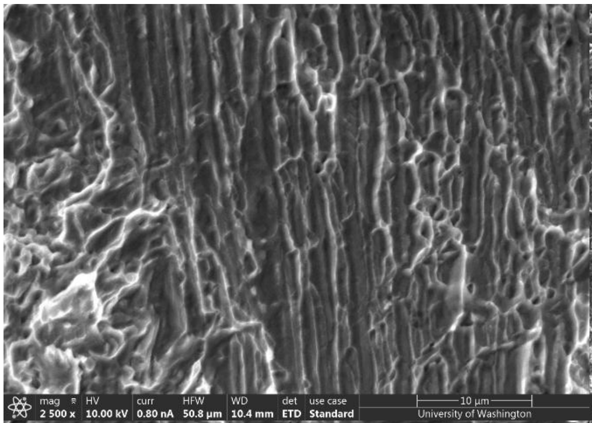

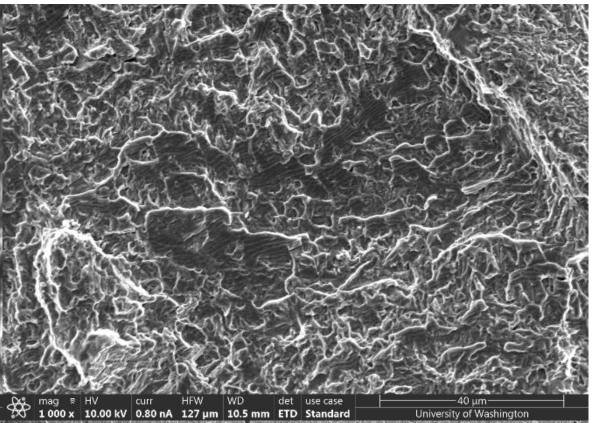

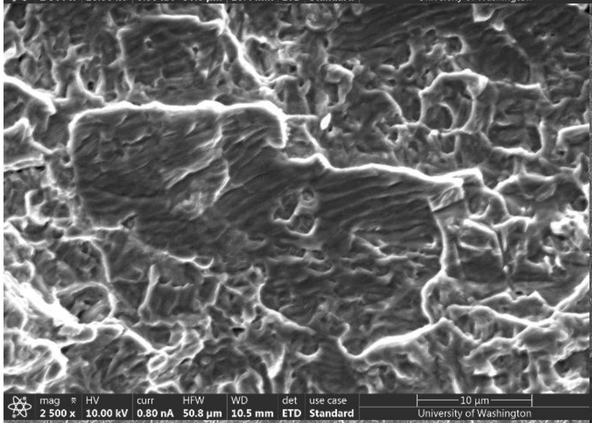

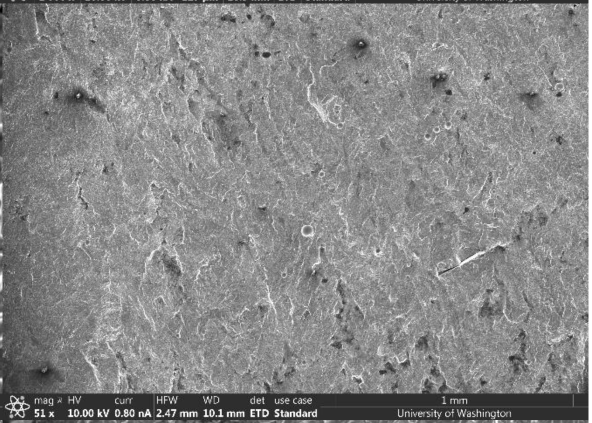

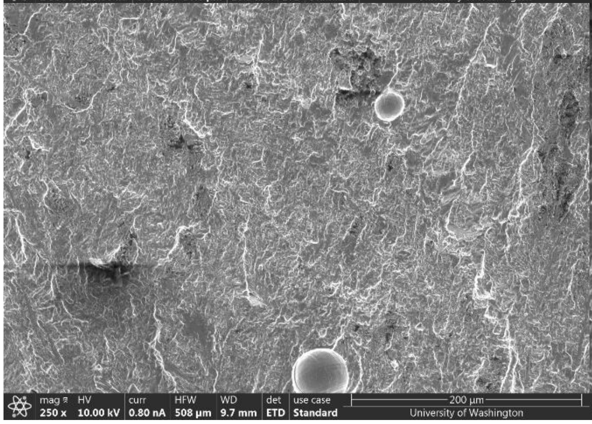

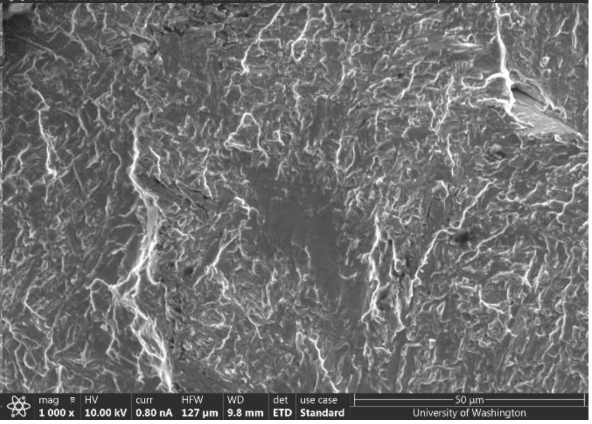

C.7 FCGR (Recycled Powder) Specimen 7 (60 Degrees, B = 6 mm) cont.

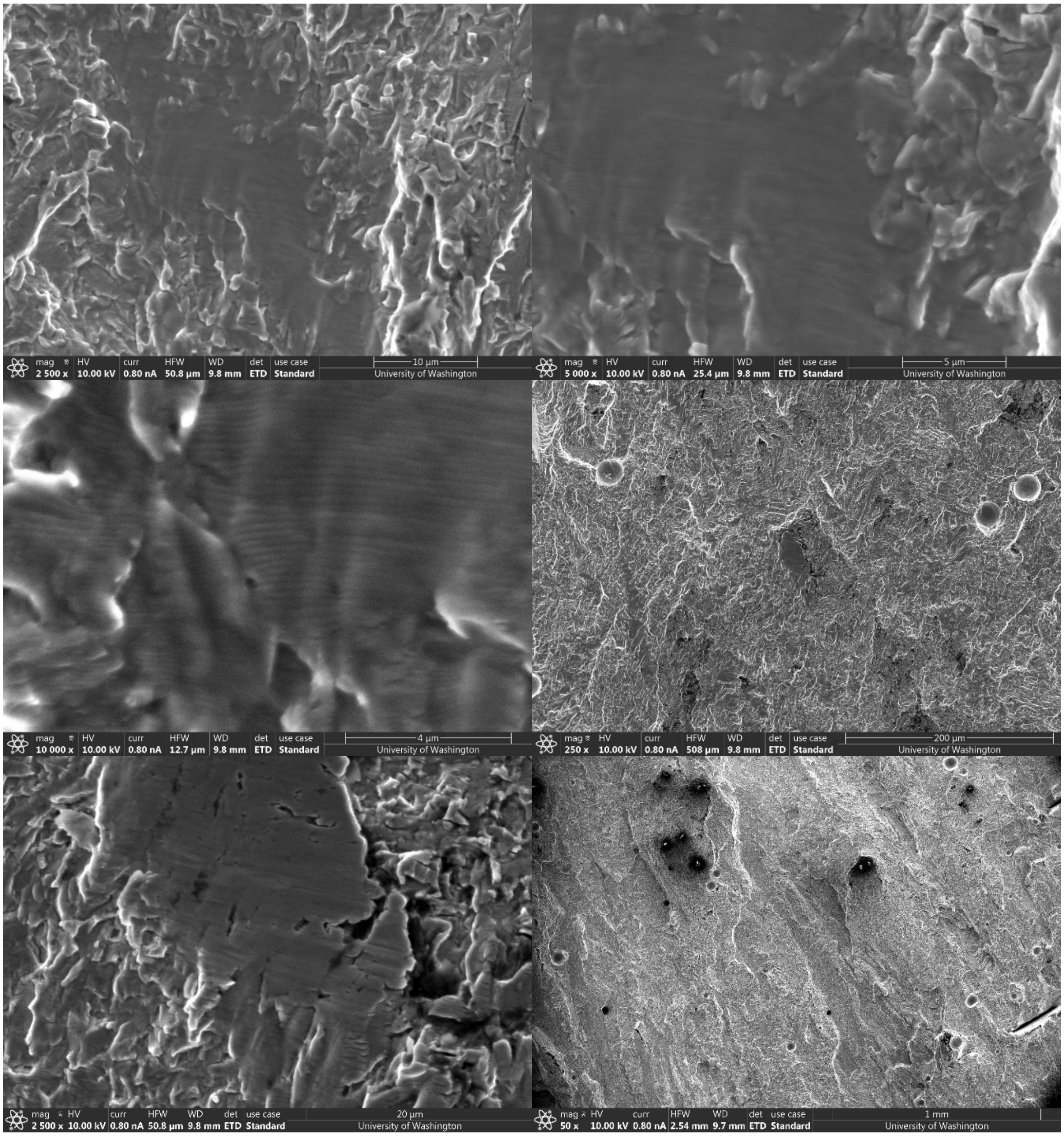

C.7 FCGR (Recycled Powder) Specimen 7 (60 Degrees, B = 6 mm) cont.

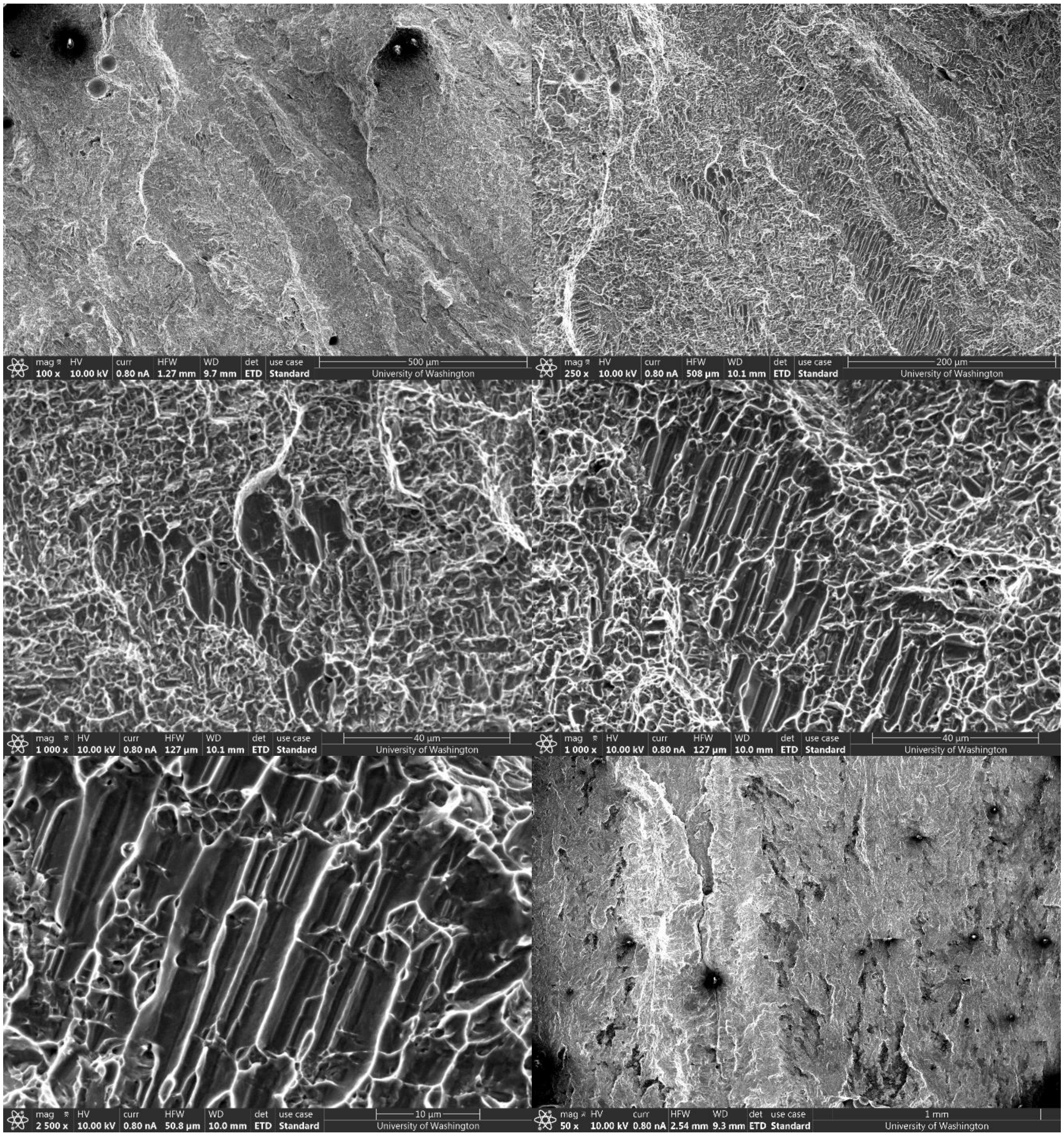

C.7 FCGR (Recycled Powder) Specimen 7 (60 Degrees, B = 6 mm) cont.

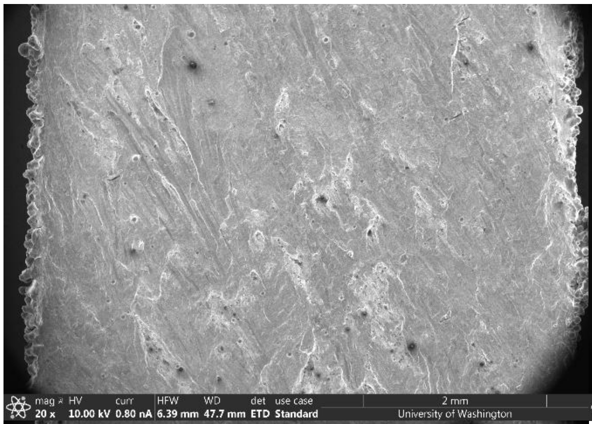

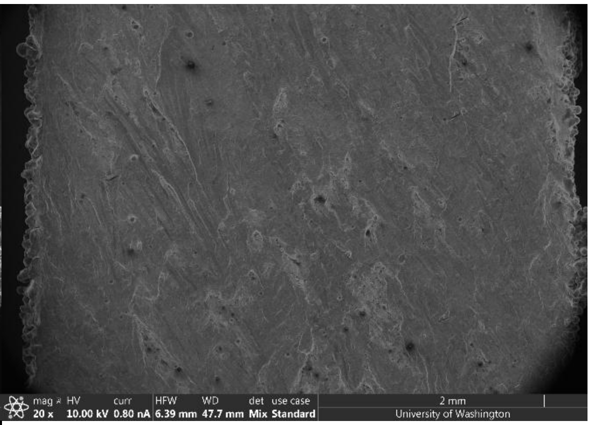

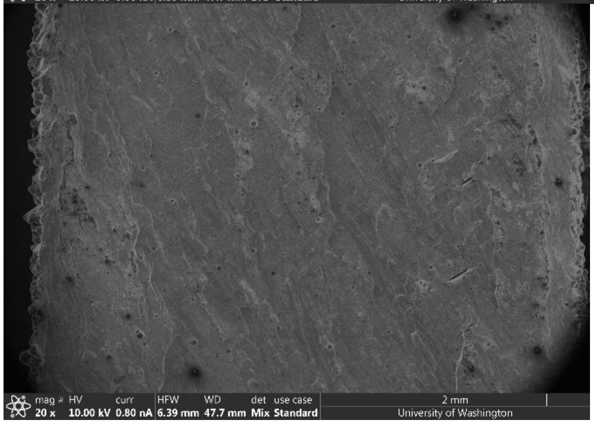

C.8 FCGR (Recycled Powder) Specimen 8 (90 Degrees, B = 6 mm)

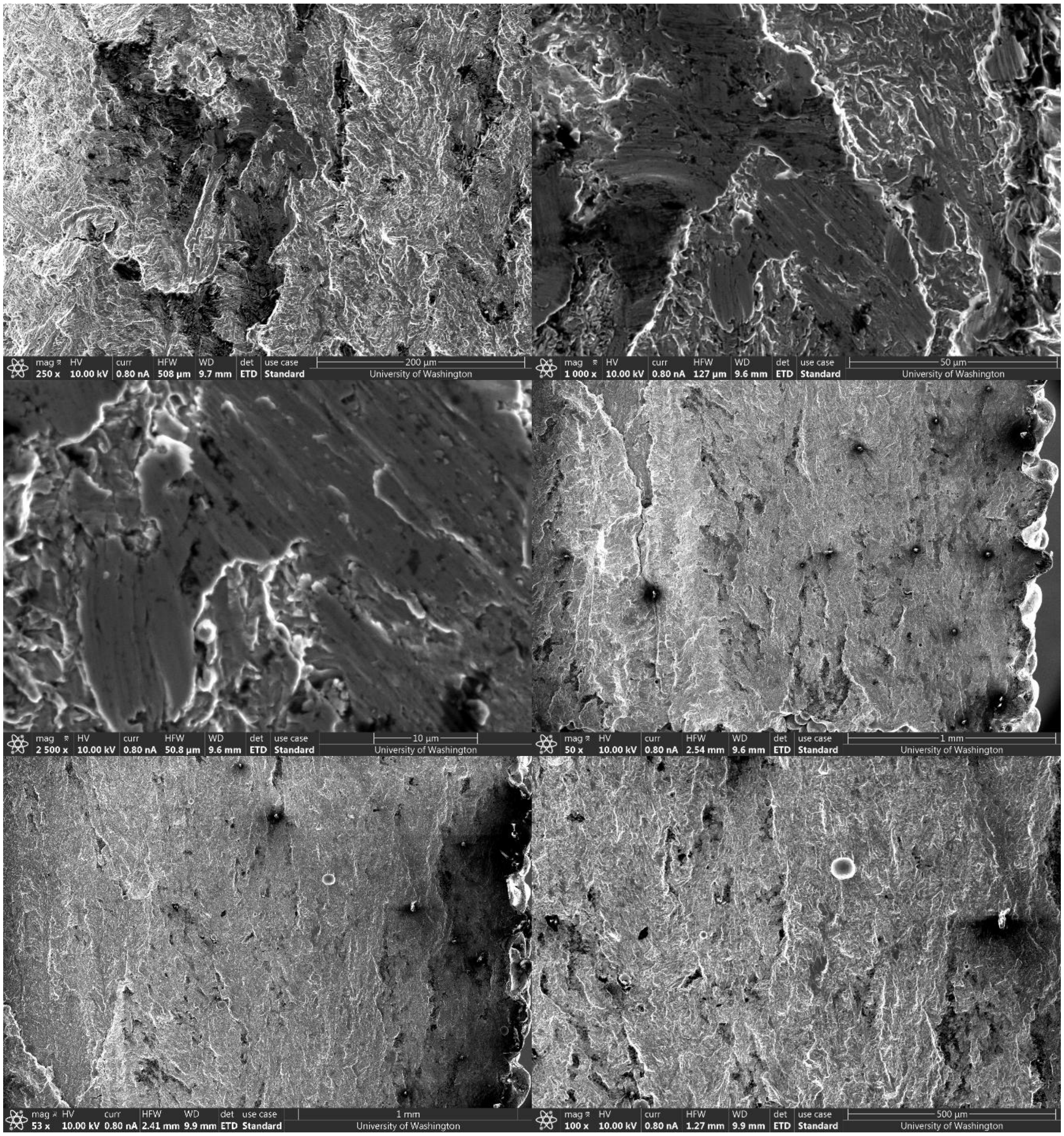

C.8 FCGR (Recycled Powder) Specimen 8 (90 Degrees, B = 6 mm) cont.

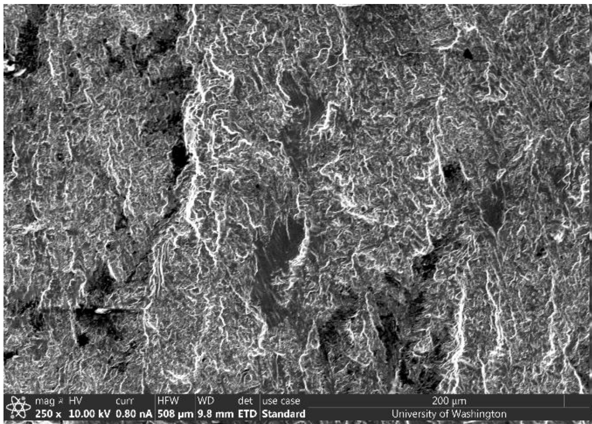

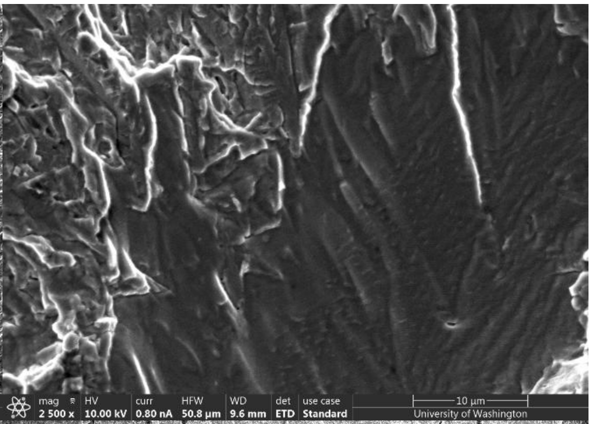

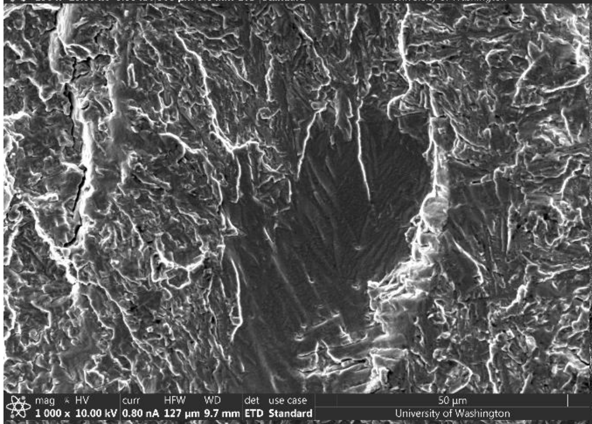

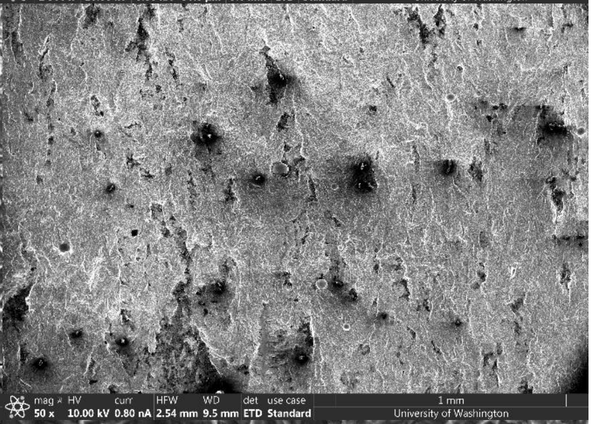

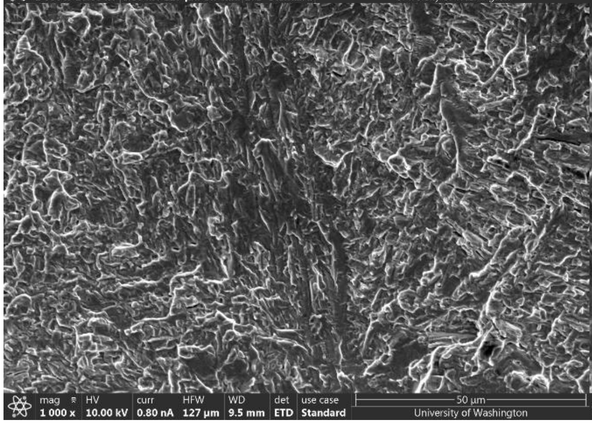

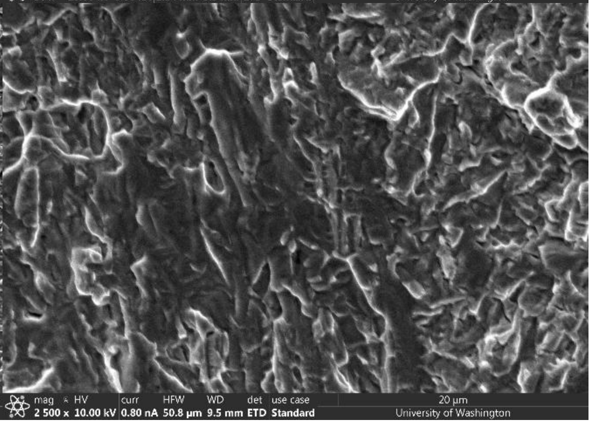

C.8 FCGR (Recycled Powder) Specimen 8 (90 Degrees, B = 6 mm) cont.

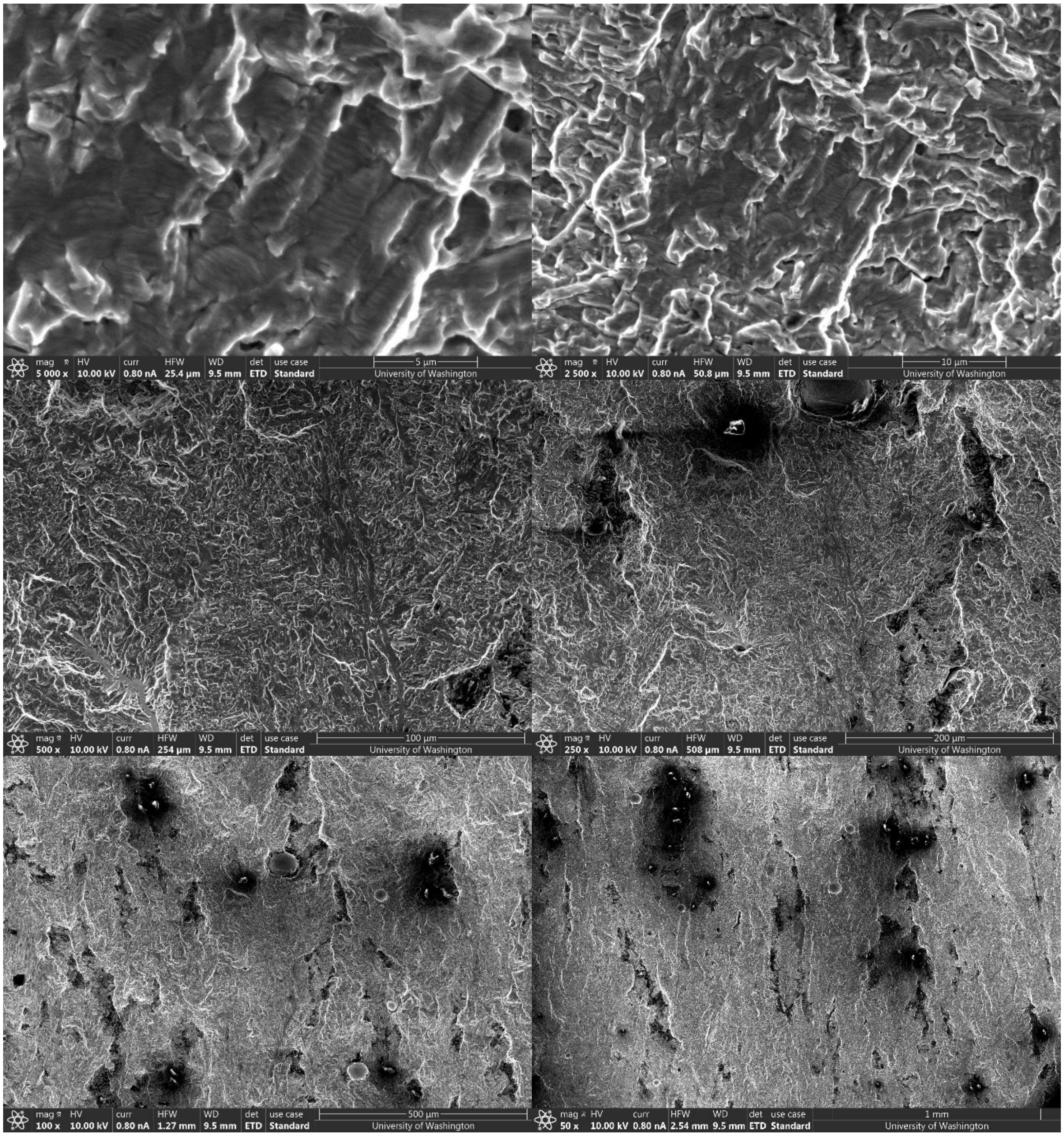

C.8 FCGR (Recycled Powder) Specimen 8 (90 Degrees, B = 6 mm) cont.

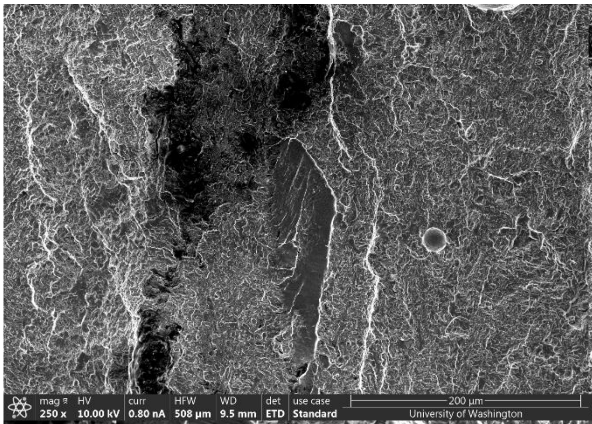

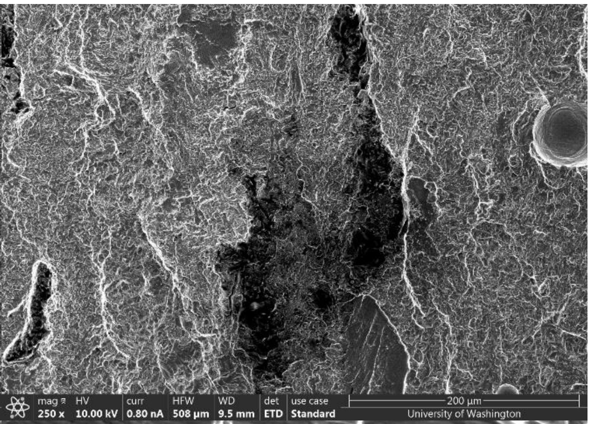

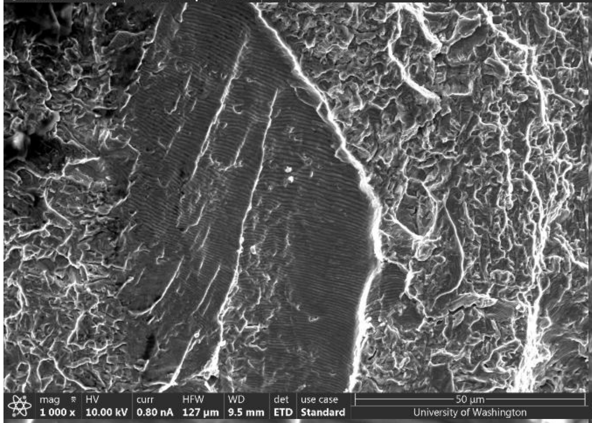

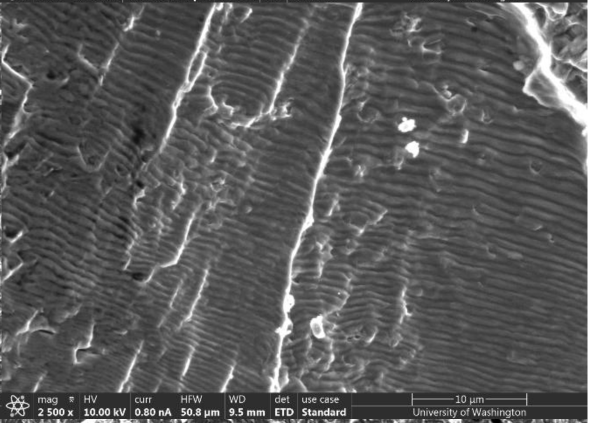

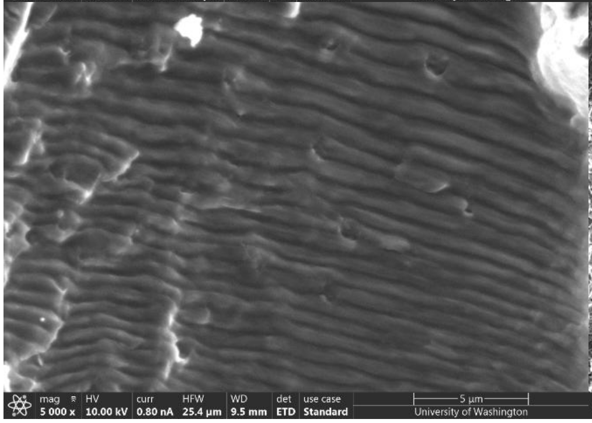

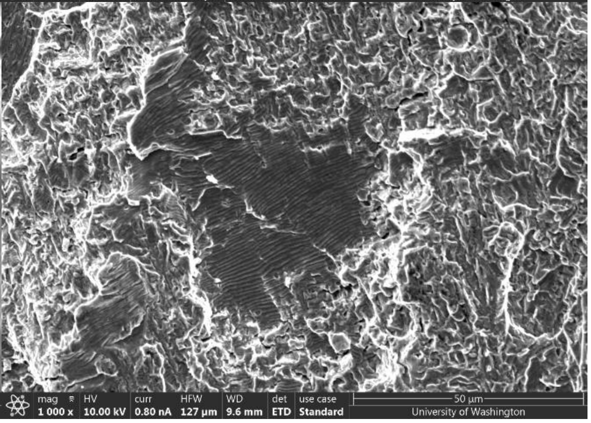

C.8 FCGR (Recycled Powder) Specimen 8 (90 Degrees, B = 6 mm) cont.

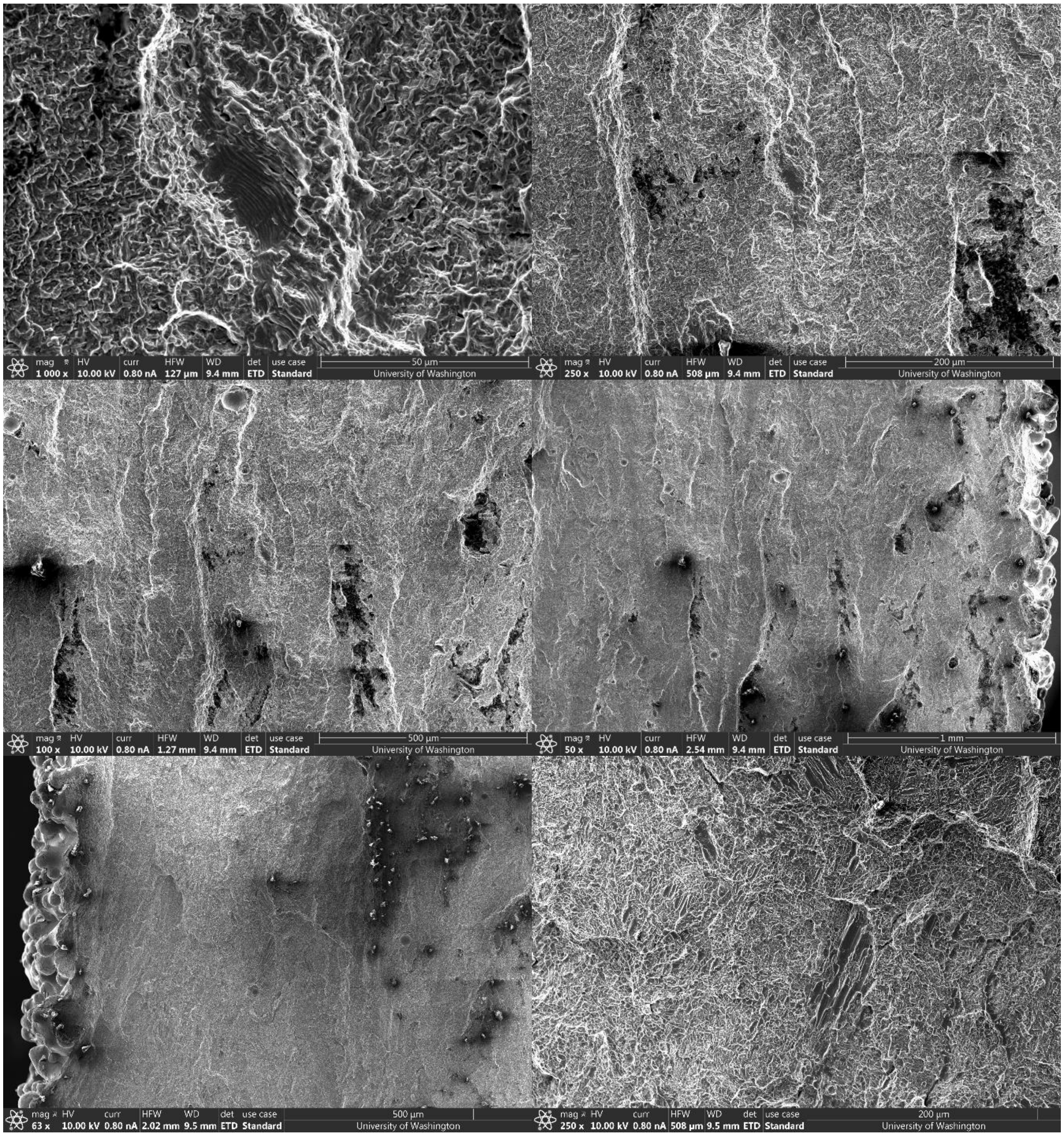

C.8 FCGR (Recycled Powder) Specimen 8 (90 Degrees, B = 6 mm) cont.

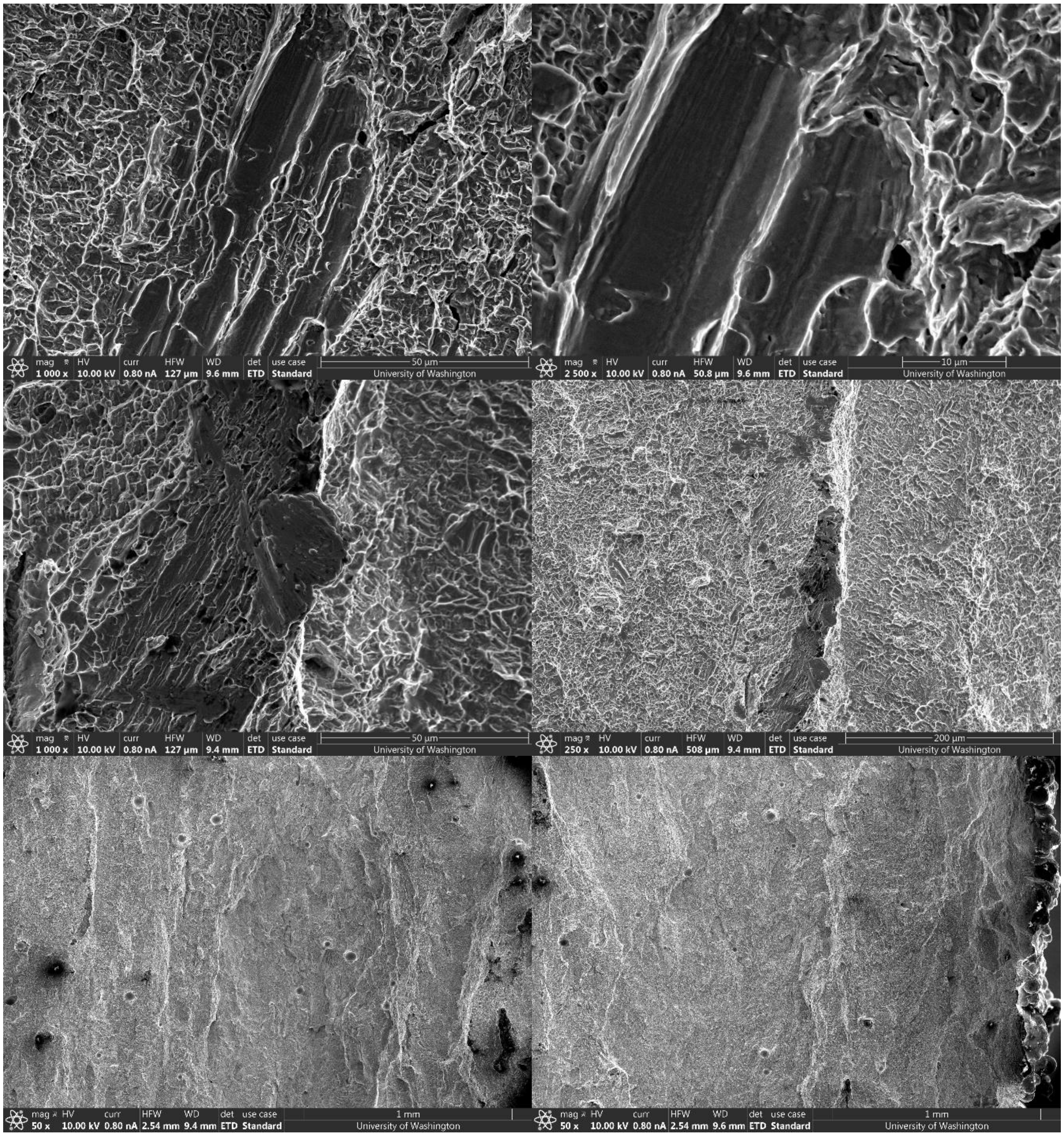

C.8 FCGR (Recycled Powder) Specimen 8 (90 Degrees, B = 6 mm) cont.

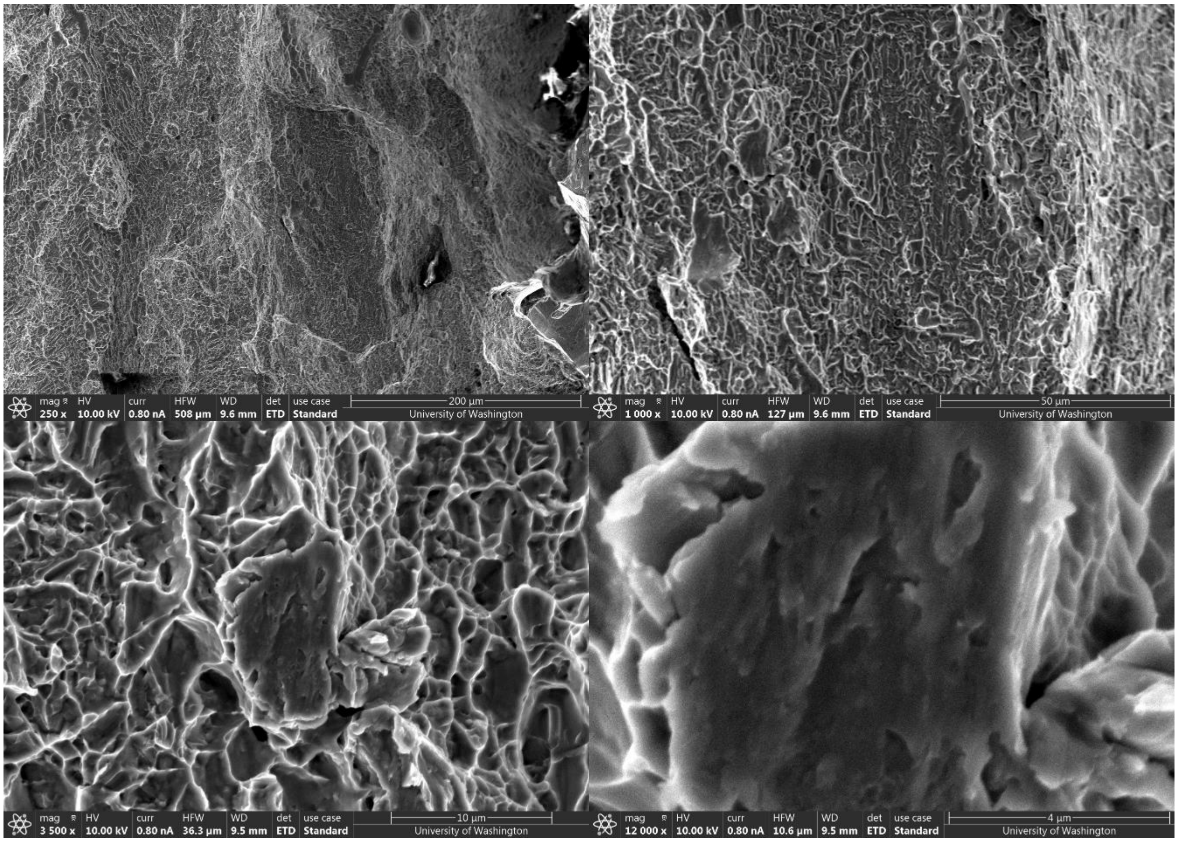

C.9 FCGR (Recycled Powder) Specimen 12 (0 Degrees, B = 12 mm)

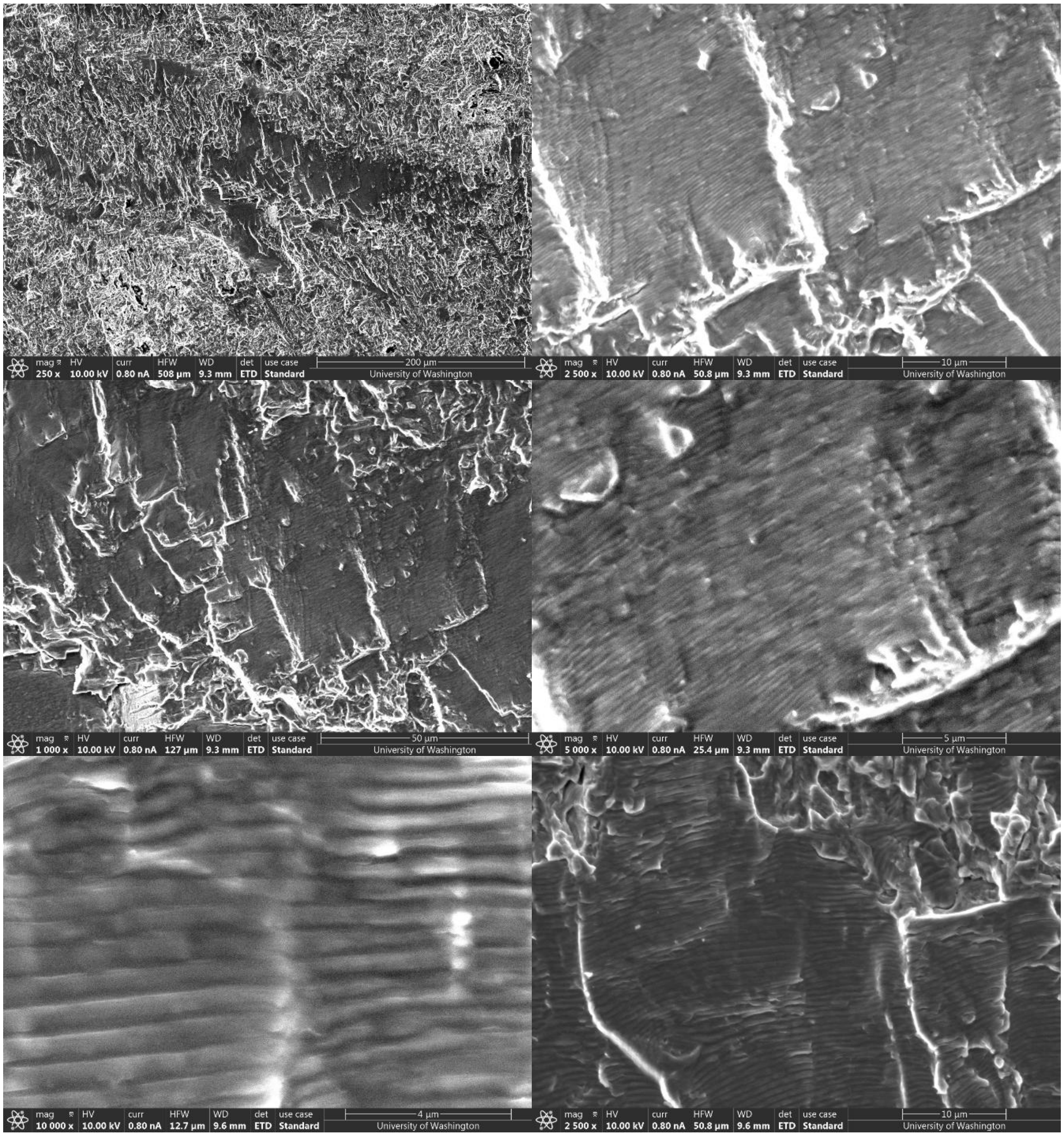

C.9 FCGR (Recycled Powder) Specimen 12 (0 Degrees, B = 12 mm) cont.

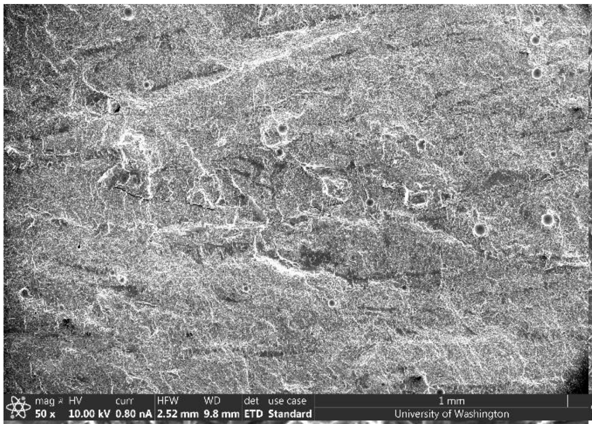

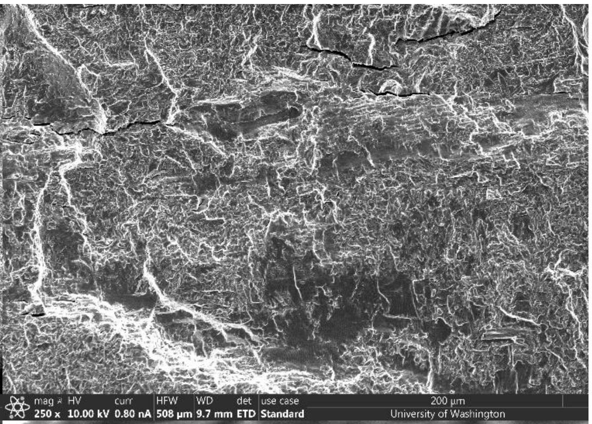

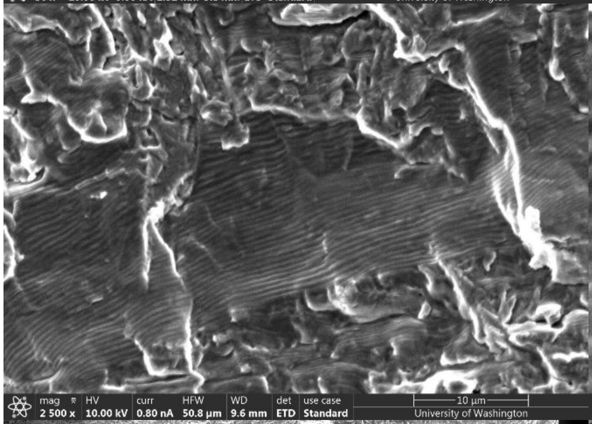

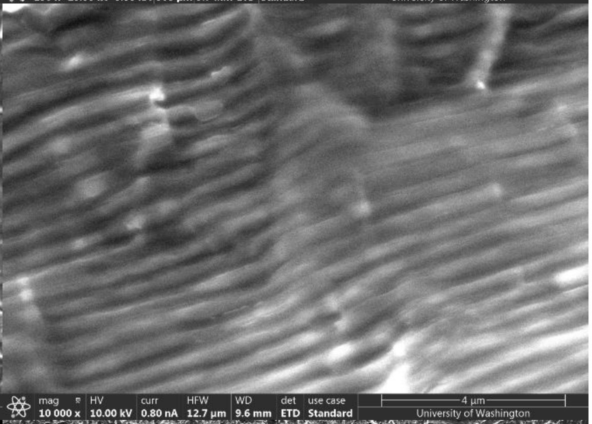

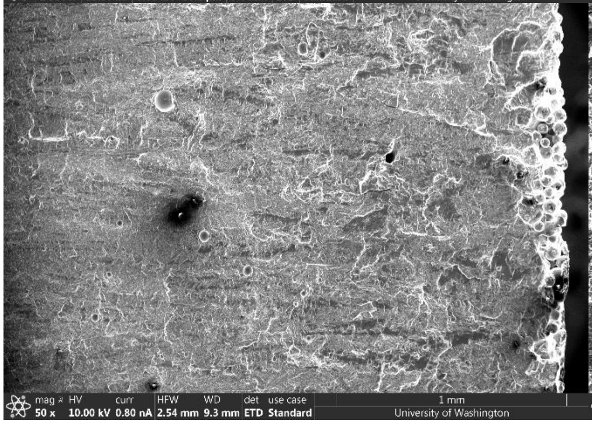

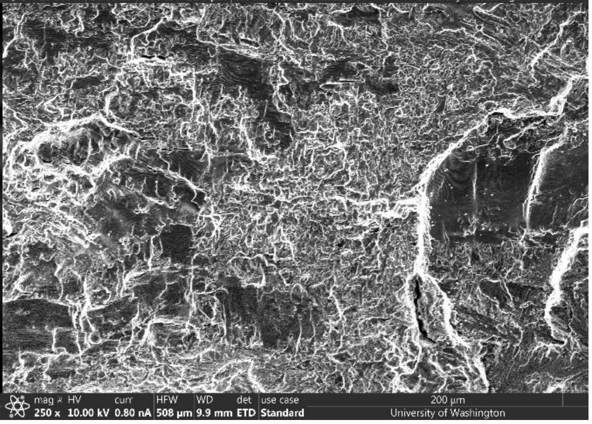

C.9 FCGR (Recycled Powder) Specimen 12 (0 Degrees, B = 12 mm) cont.

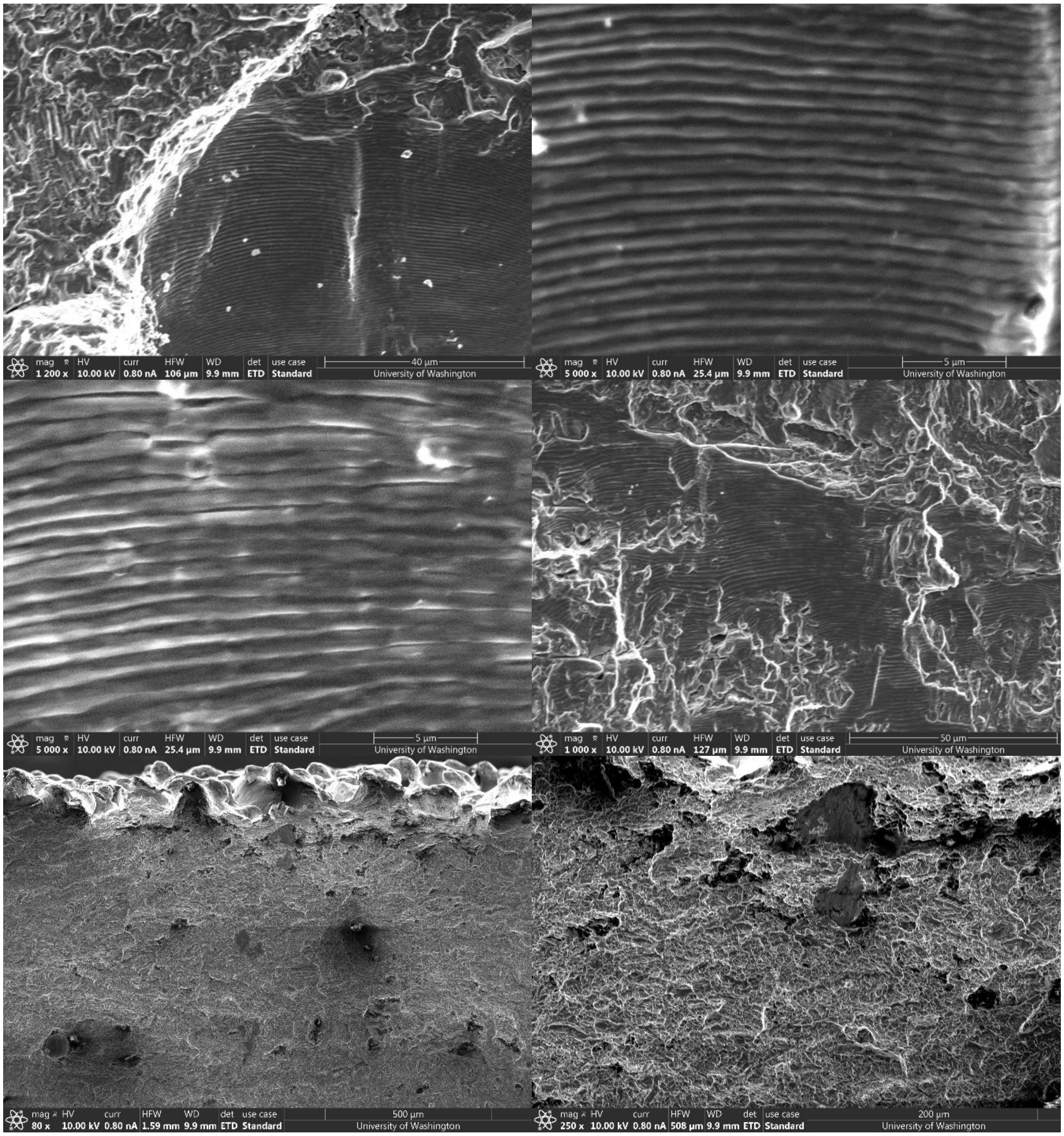

C.9 FCGR (Recycled Powder) Specimen 12 (0 Degrees, B = 12 mm) cont.

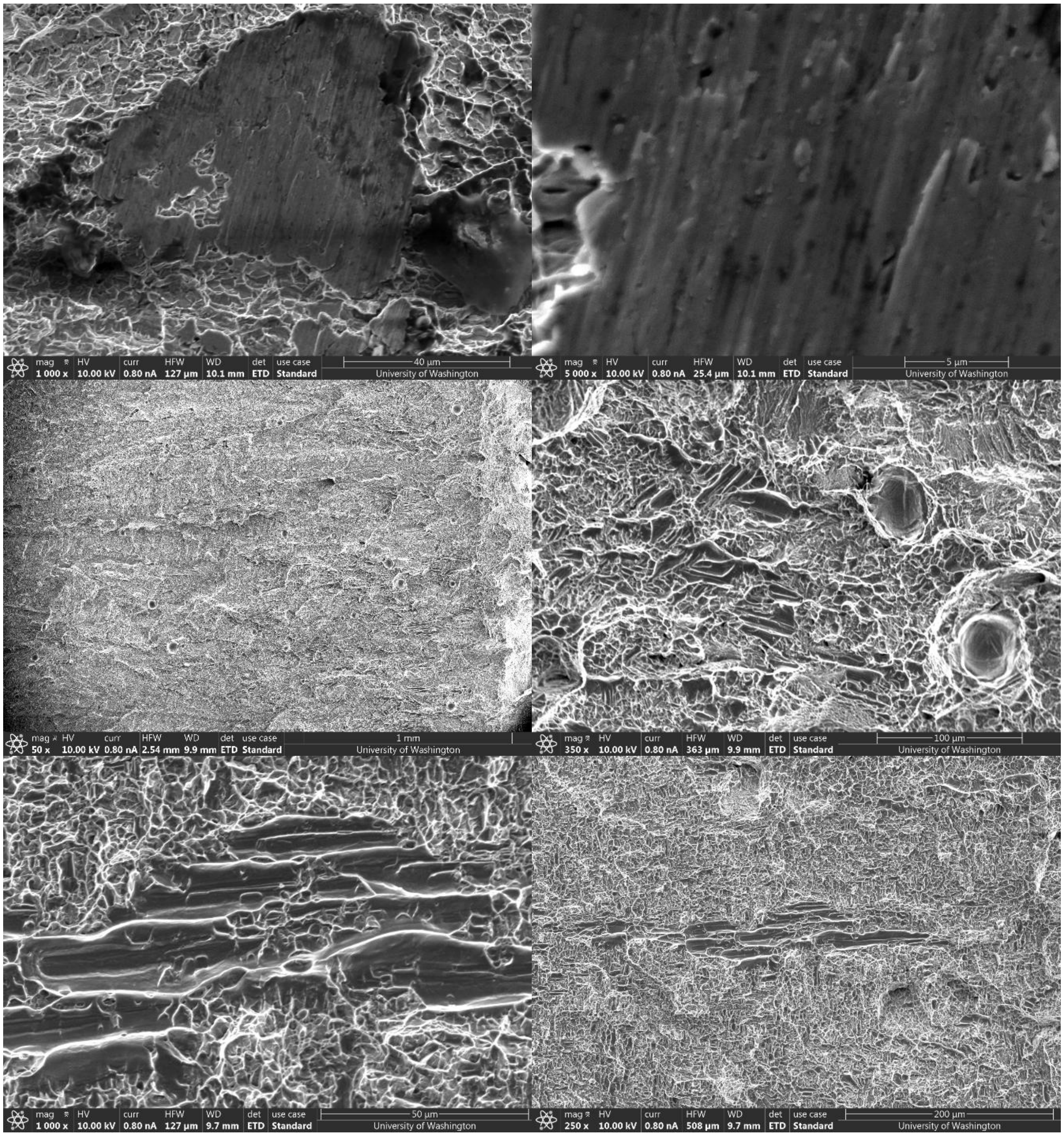

C.9 FCGR (Recycled Powder) Specimen 12 (0 Degrees, B = 12 mm) cont.

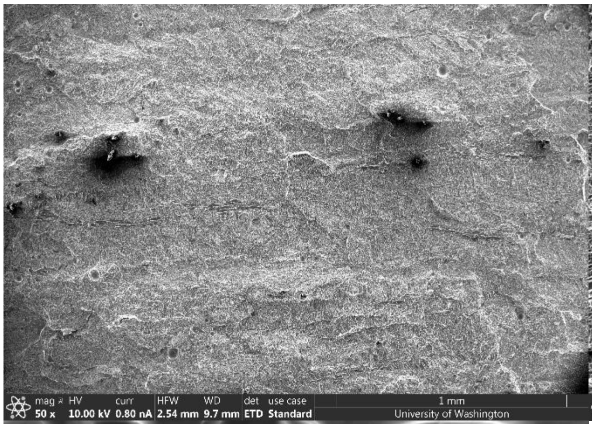

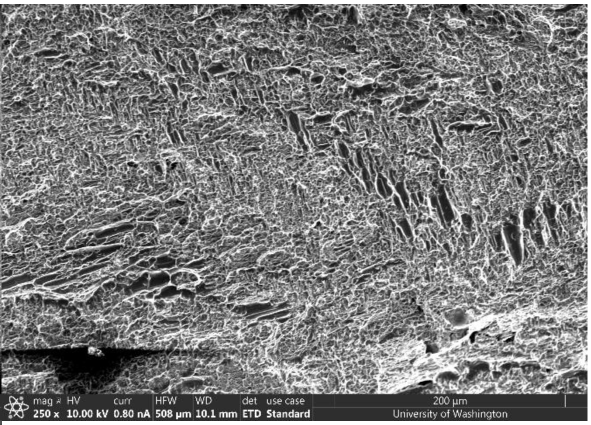

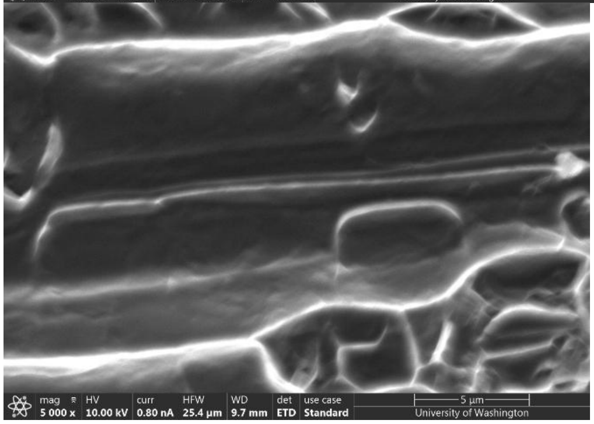

C.10 FCGR (Recycled Powder) Specimen 2 (30 Degrees, B = 12 mm)

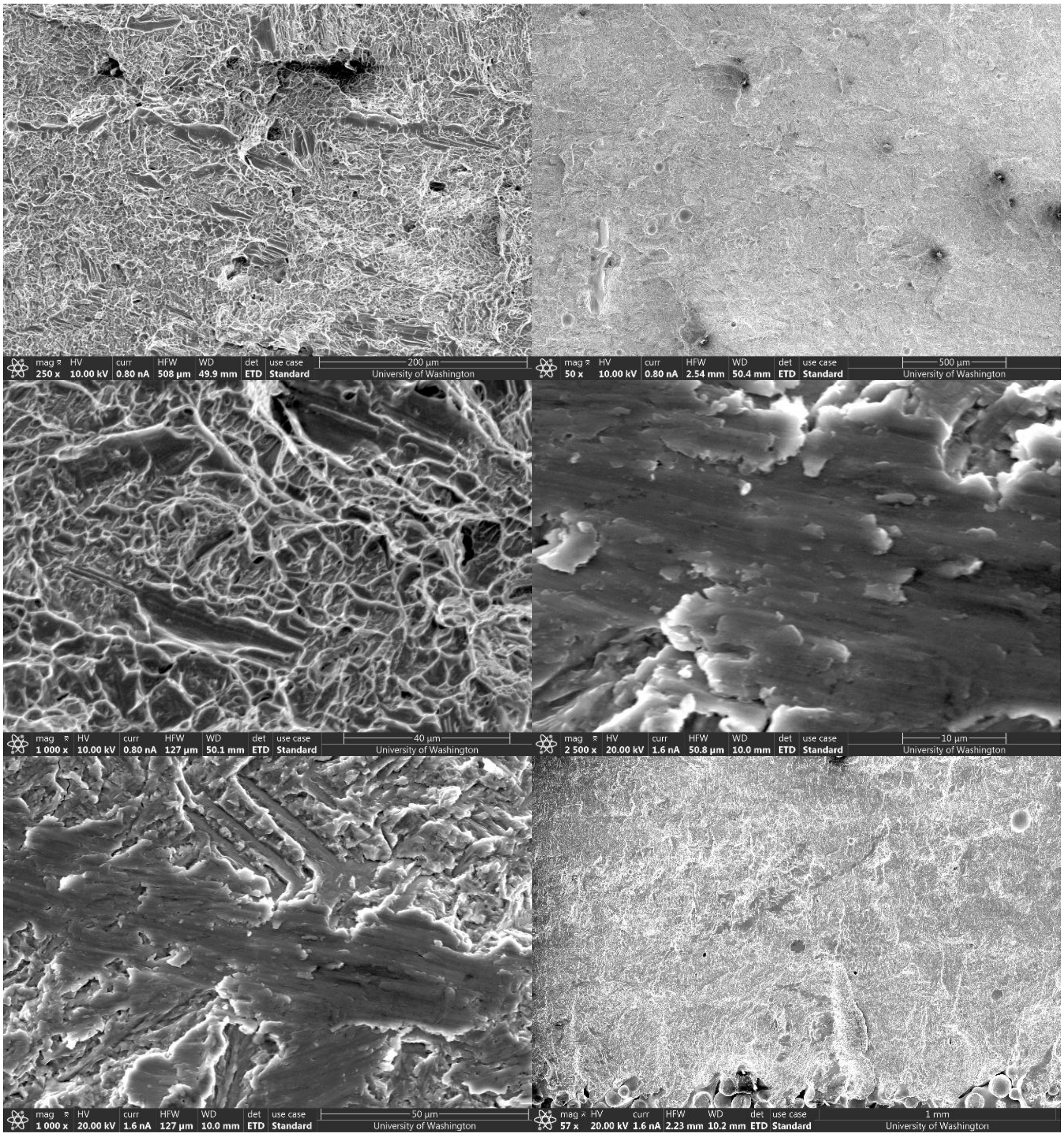

C.10 FCGR (Recycled Powder) Specimen 2 (30 Degrees, B = 12 mm) cont.

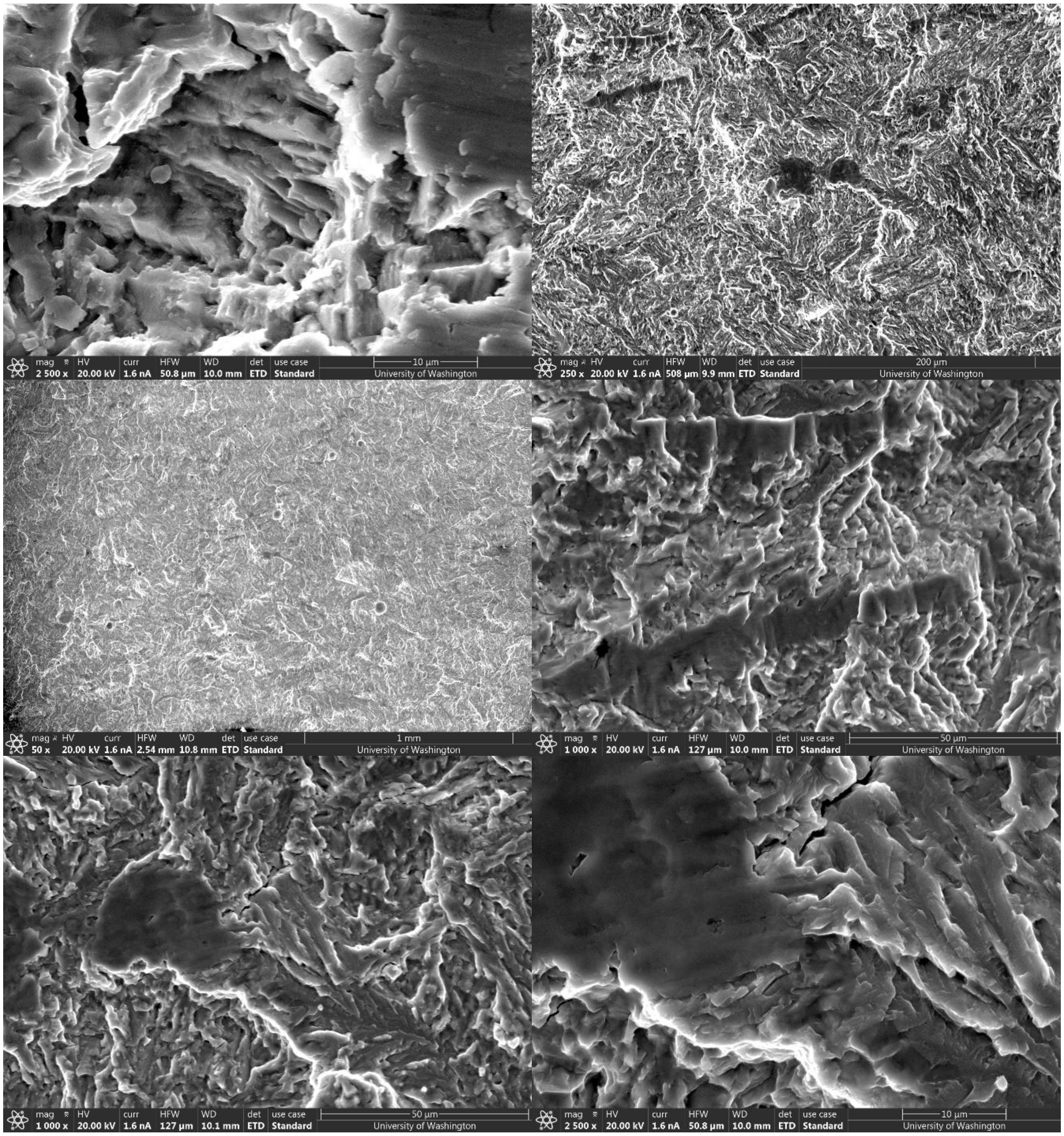

C.10 FCGR (Recycled Powder) Specimen 2 (30 Degrees, B = 12 mm) cont.

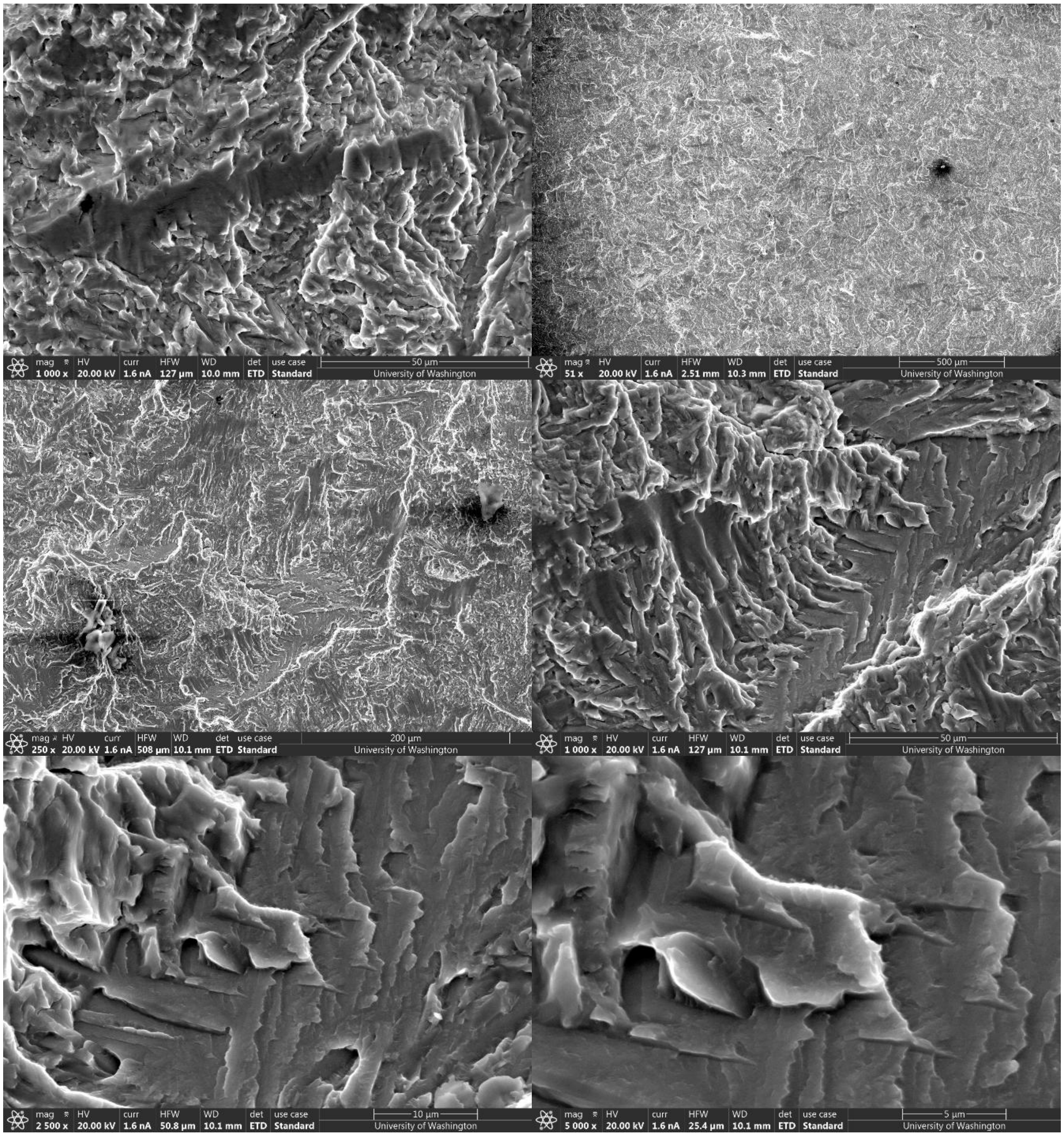

C.10 FCGR (Recycled Powder) Specimen 2 (30 Degrees, B = 12 mm) cont.

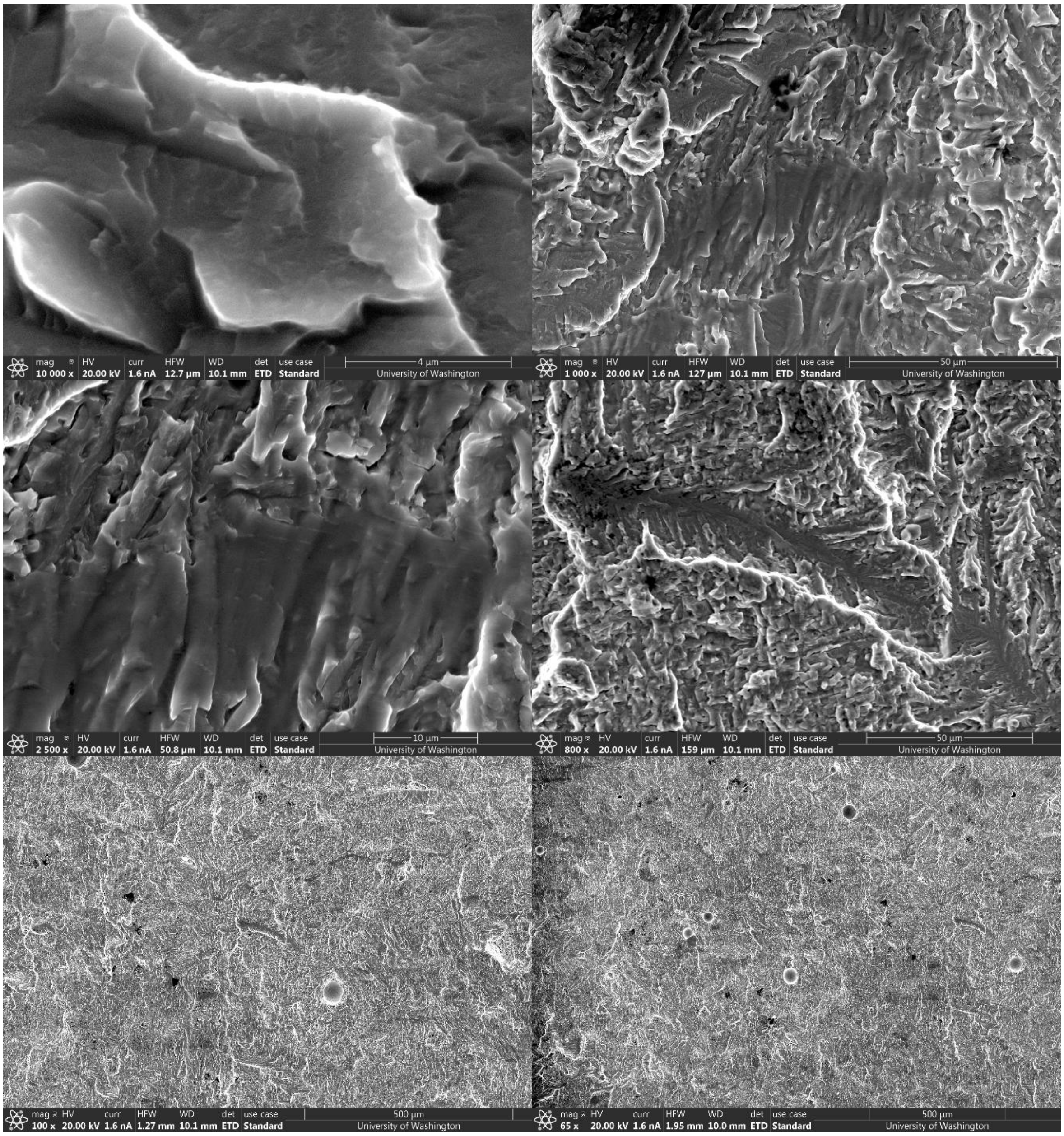

C.10 FCGR (Recycled Powder) Specimen 2 (30 Degrees, B = 12 mm) cont.

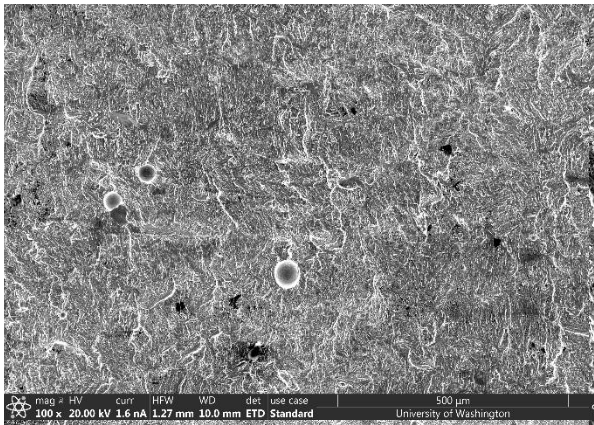

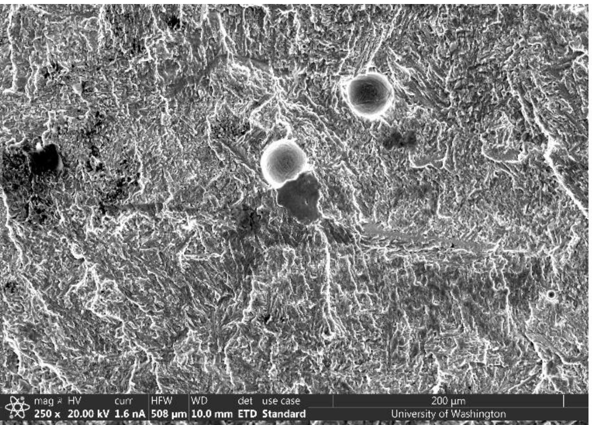

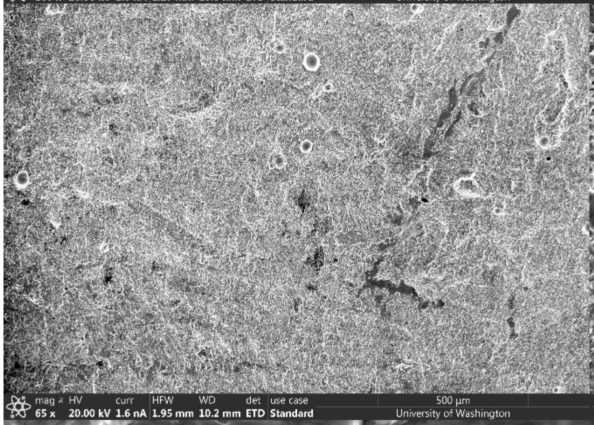

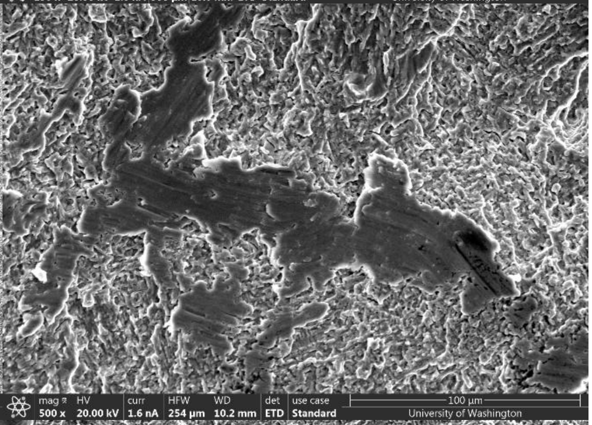

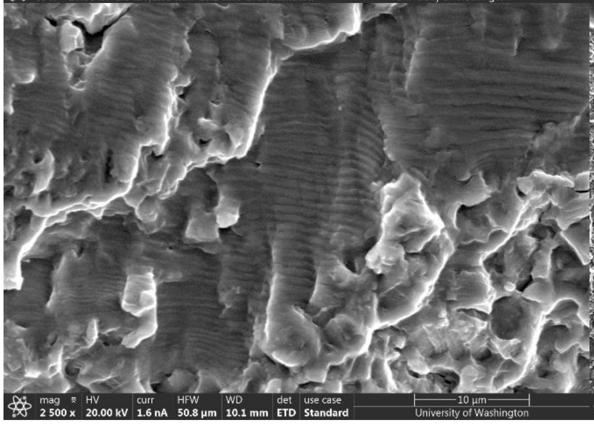

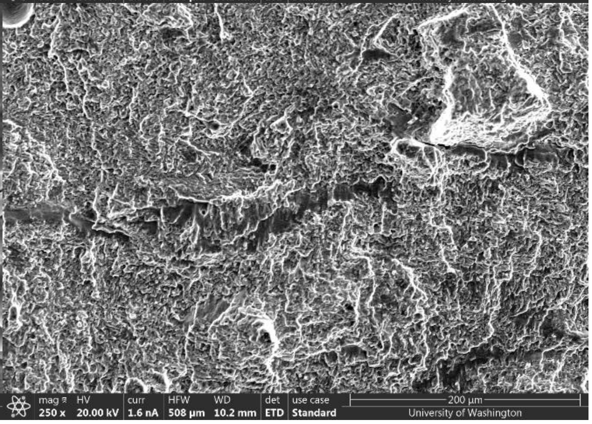

C.10 FCGR (Recycled Powder) Specimen 2 (30 Degrees, B = 12 mm) cont.

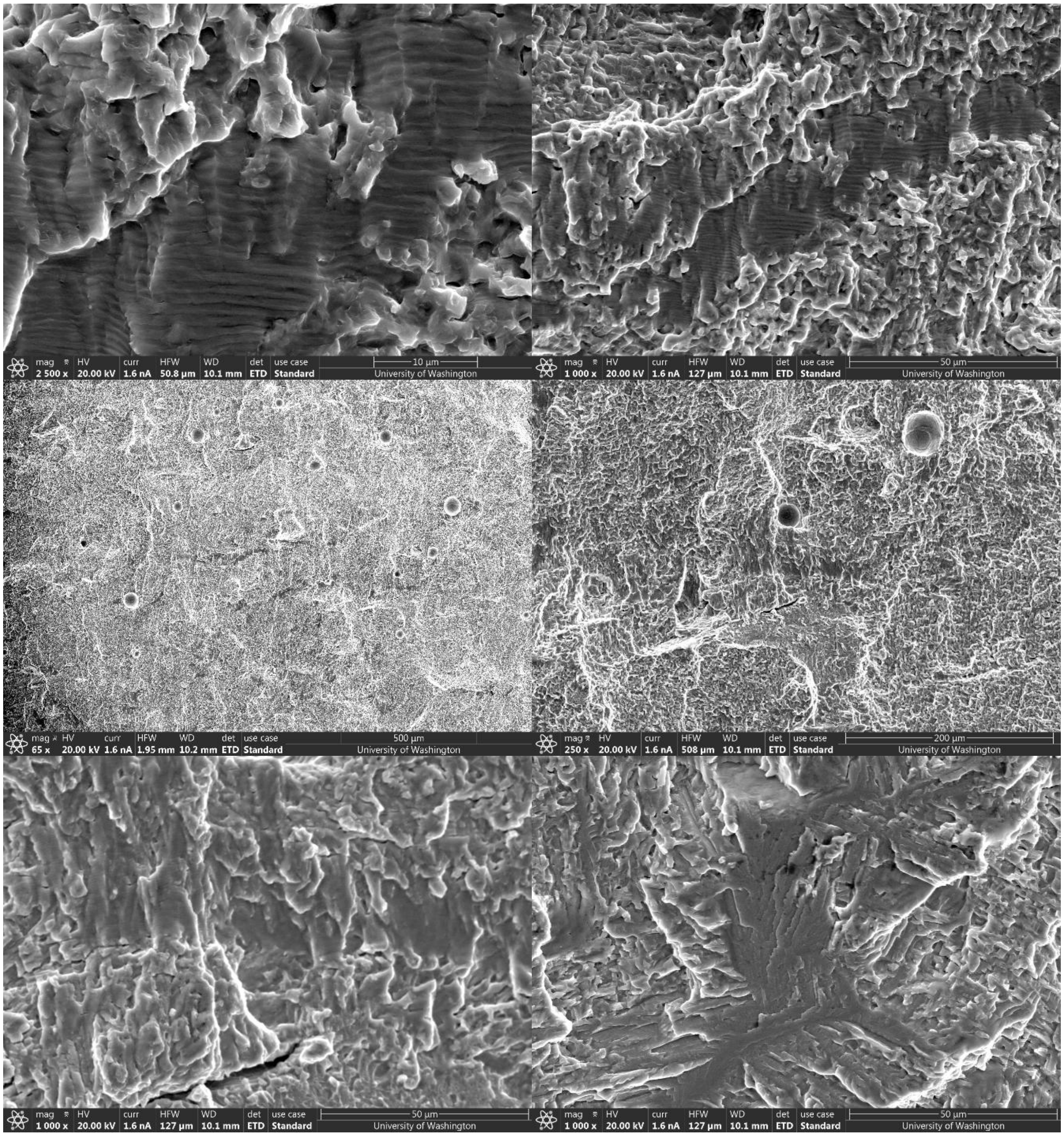

C.10 FCGR (Recycled Powder) Specimen 2 (30 Degrees, B = 12 mm) cont.

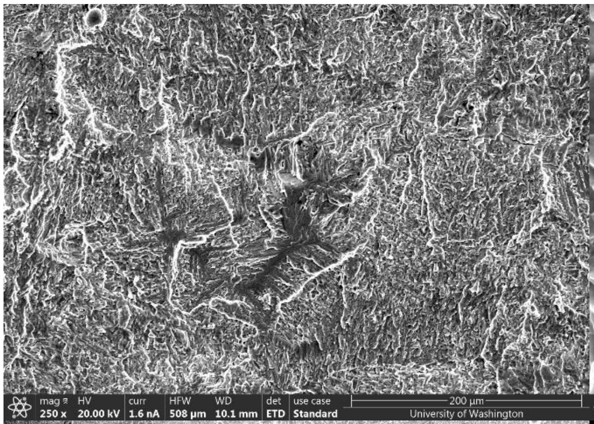

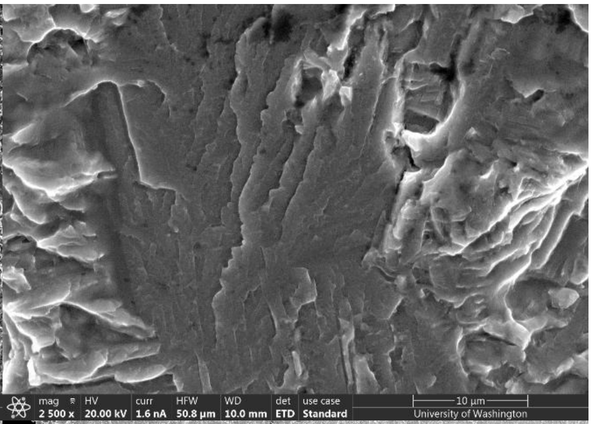

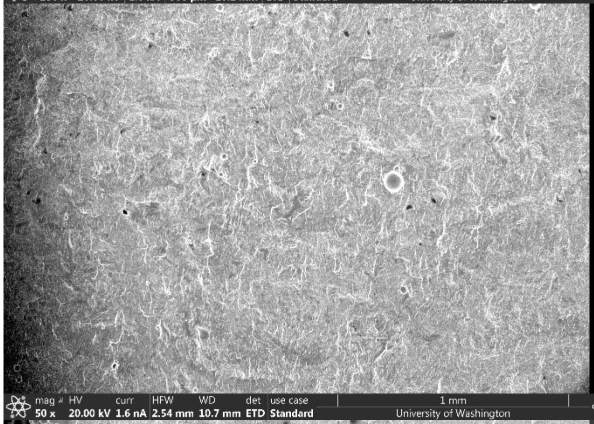

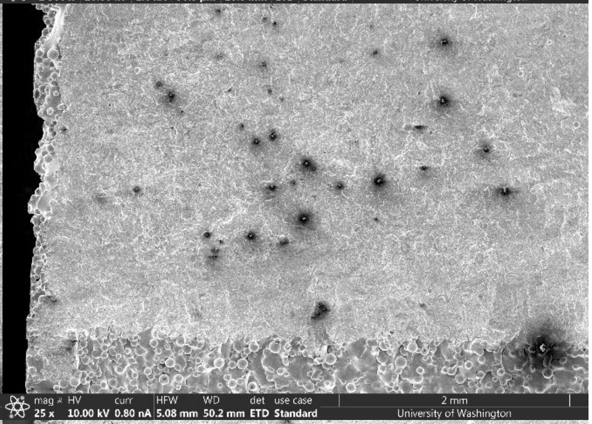

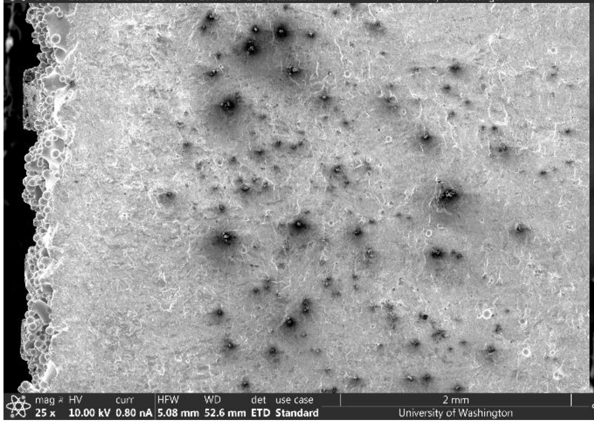

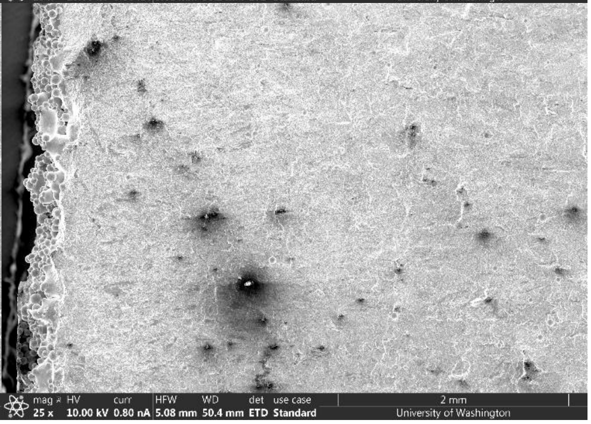

C.10 FCGR (Recycled Powder) Specimen 2 (30 Degrees, B = 12 mm) cont.

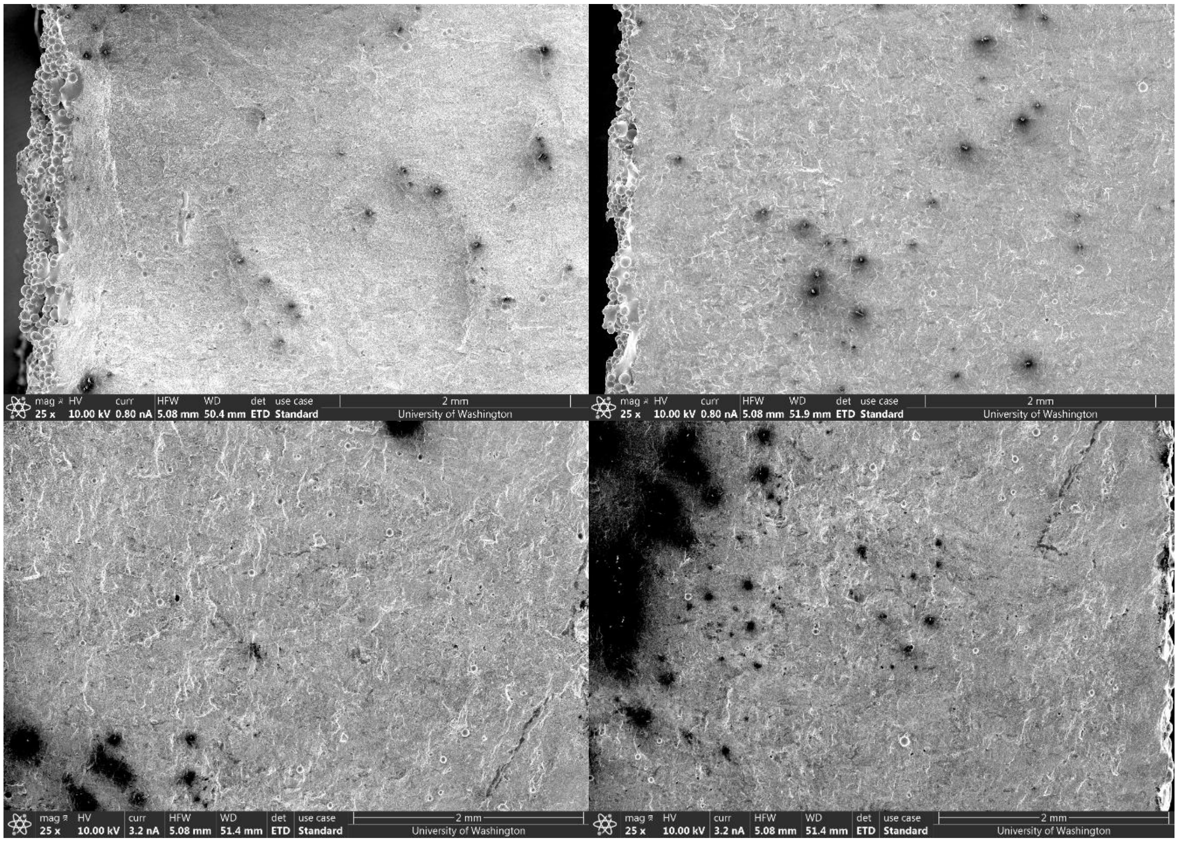

C.10 FCGR (Recycled Powder) Specimen 2 (30 Degrees, B = 12 mm) cont.

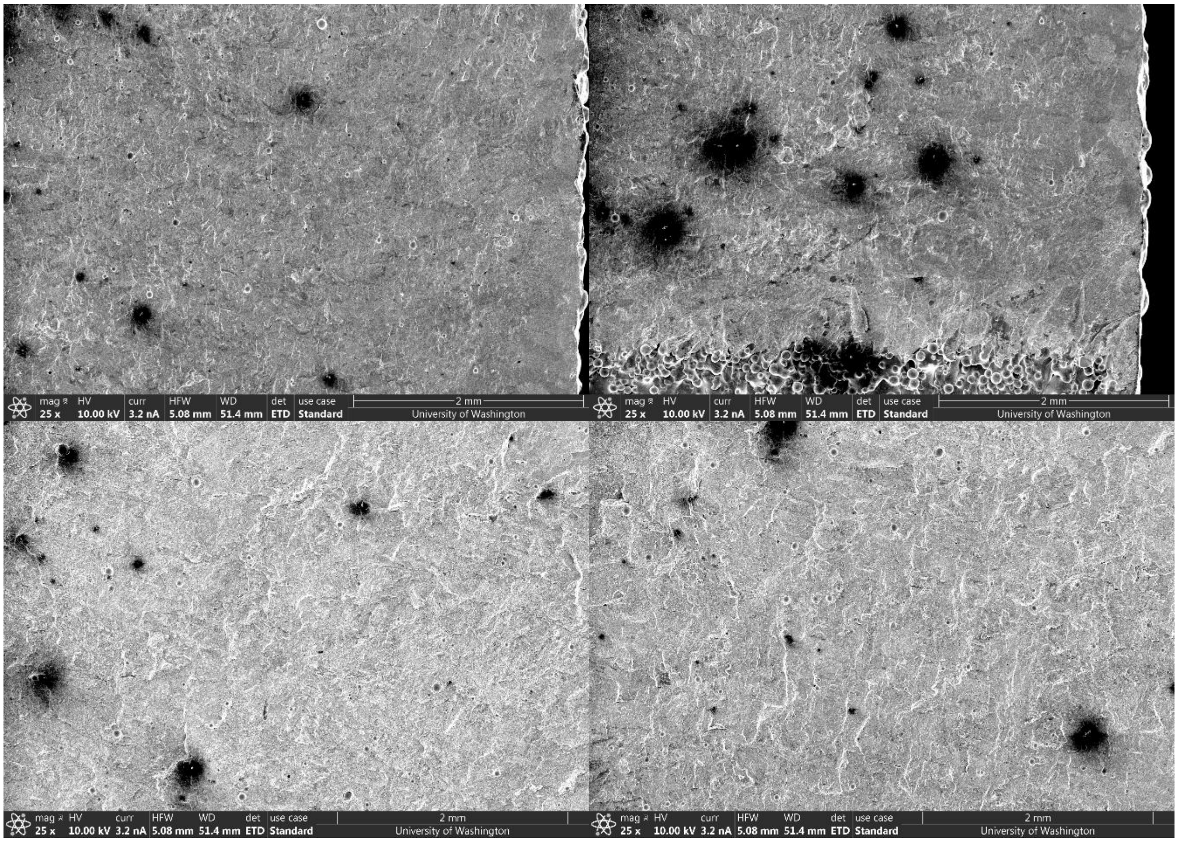

C.11 FCGR (Recycled Powder) Specimen 3 (60 Degrees, B = 12 mm)

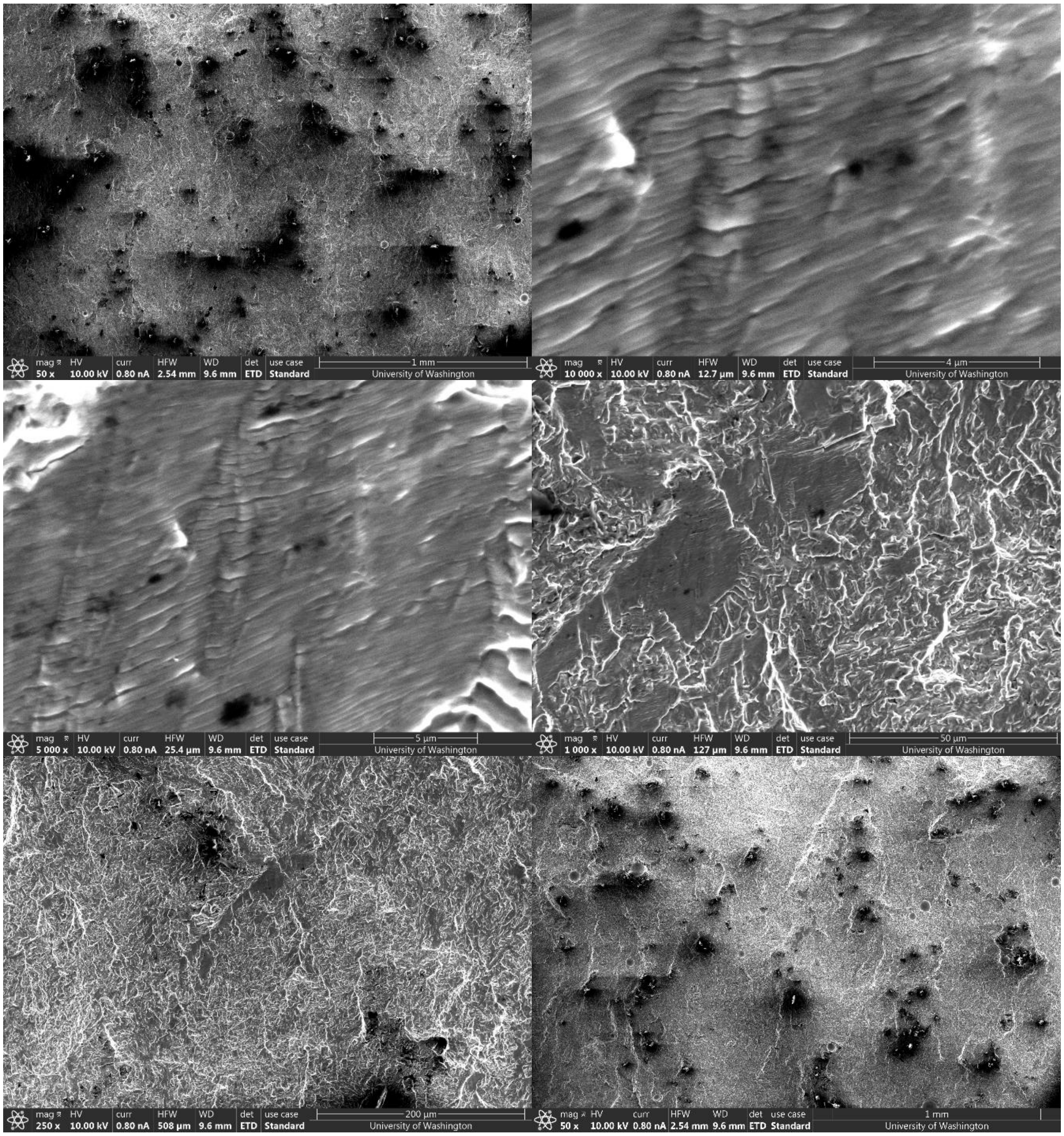

C.11 FCGR (Recycled Powder) Specimen 3 (60 Degrees, B = 12 mm) cont.

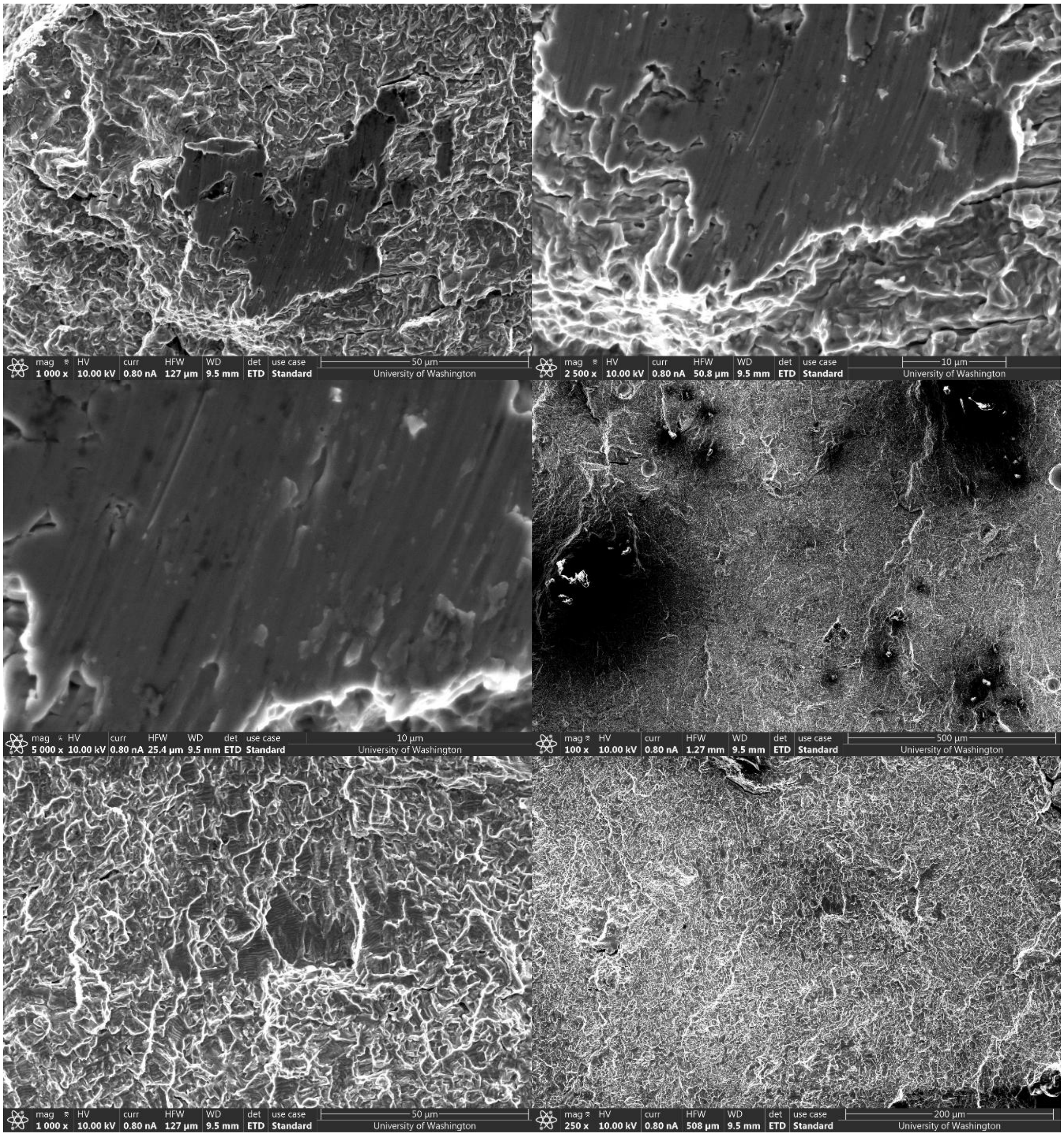

C.11 FCGR (Recycled Powder) Specimen 3 (60 Degrees, B = 12 mm) cont.

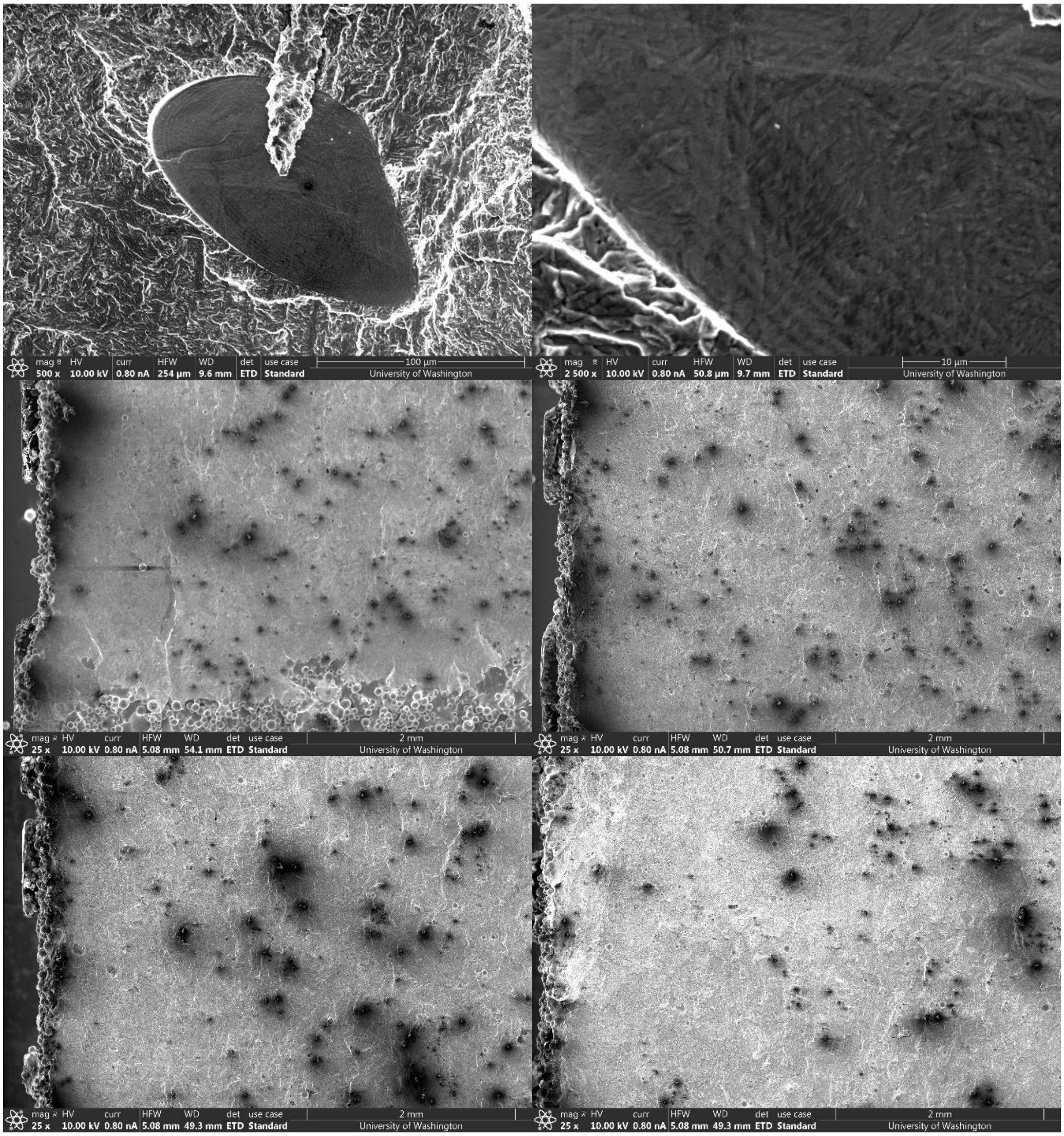

C.11 FCGR (Recycled Powder) Specimen 3 (60 Degrees, B = 12 mm) cont.

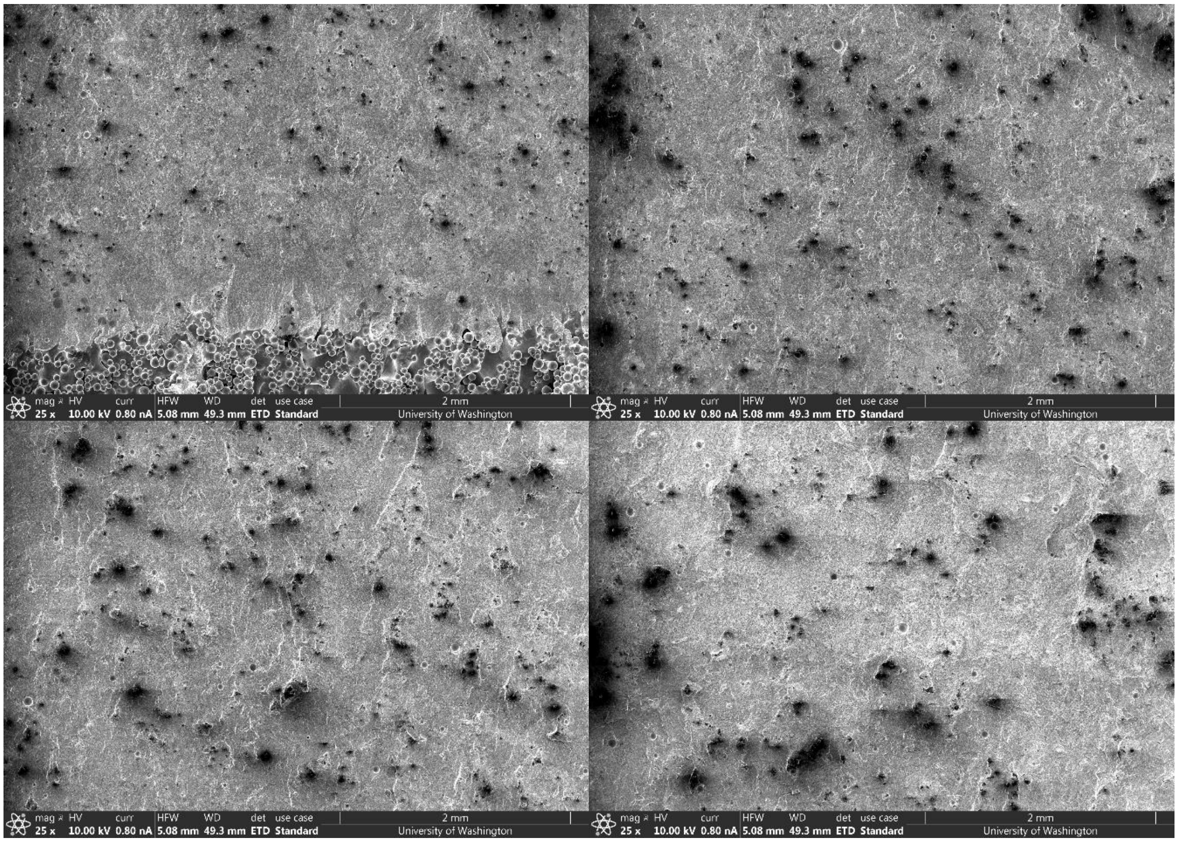

C.12 FCGR (Recycled Powder) Specimen 4 (90 Degrees, B = 12 mm)

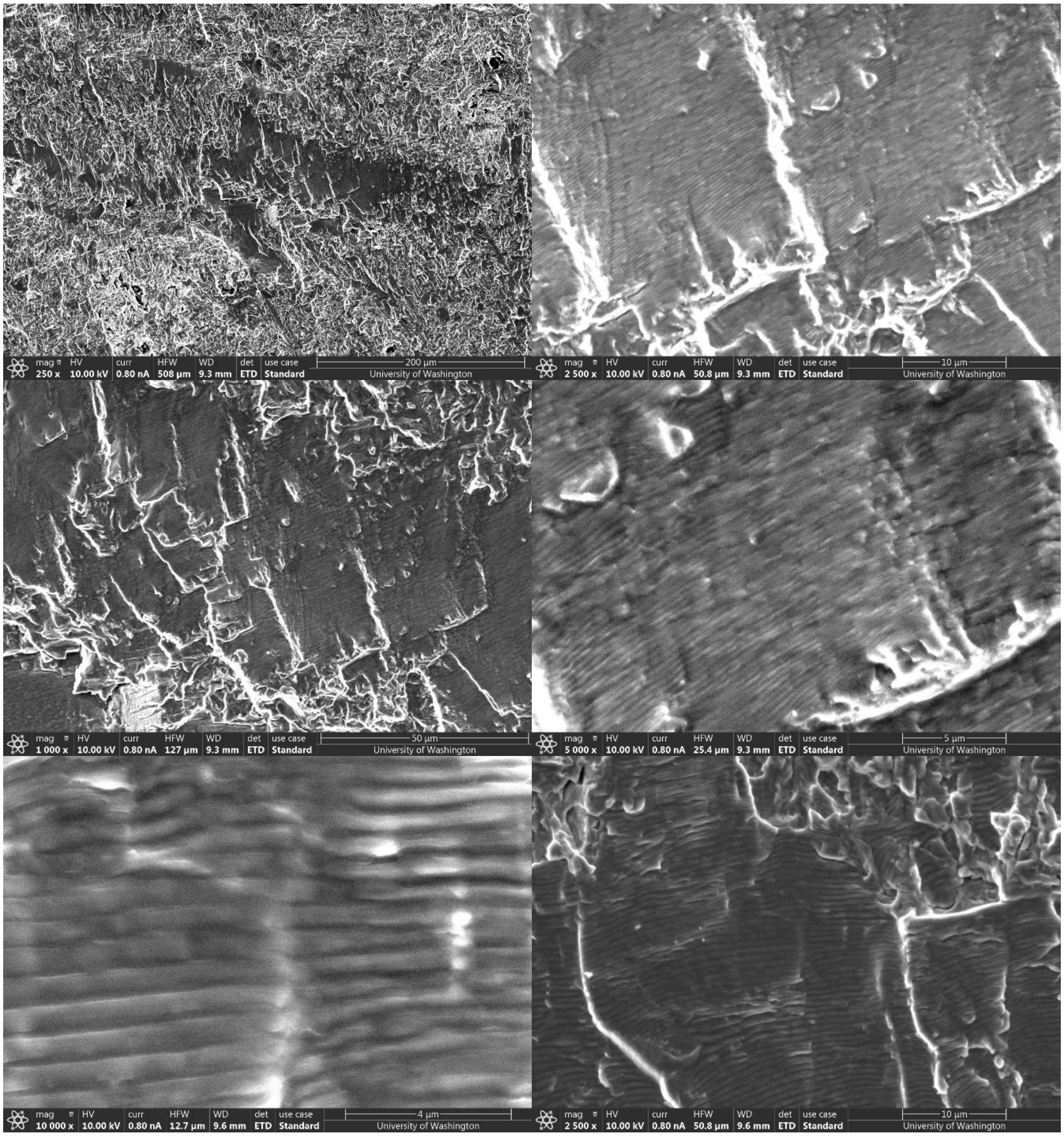

C.12 FCGR (Recycled Powder) Specimen 4 (90 Degrees, B = 12 mm)

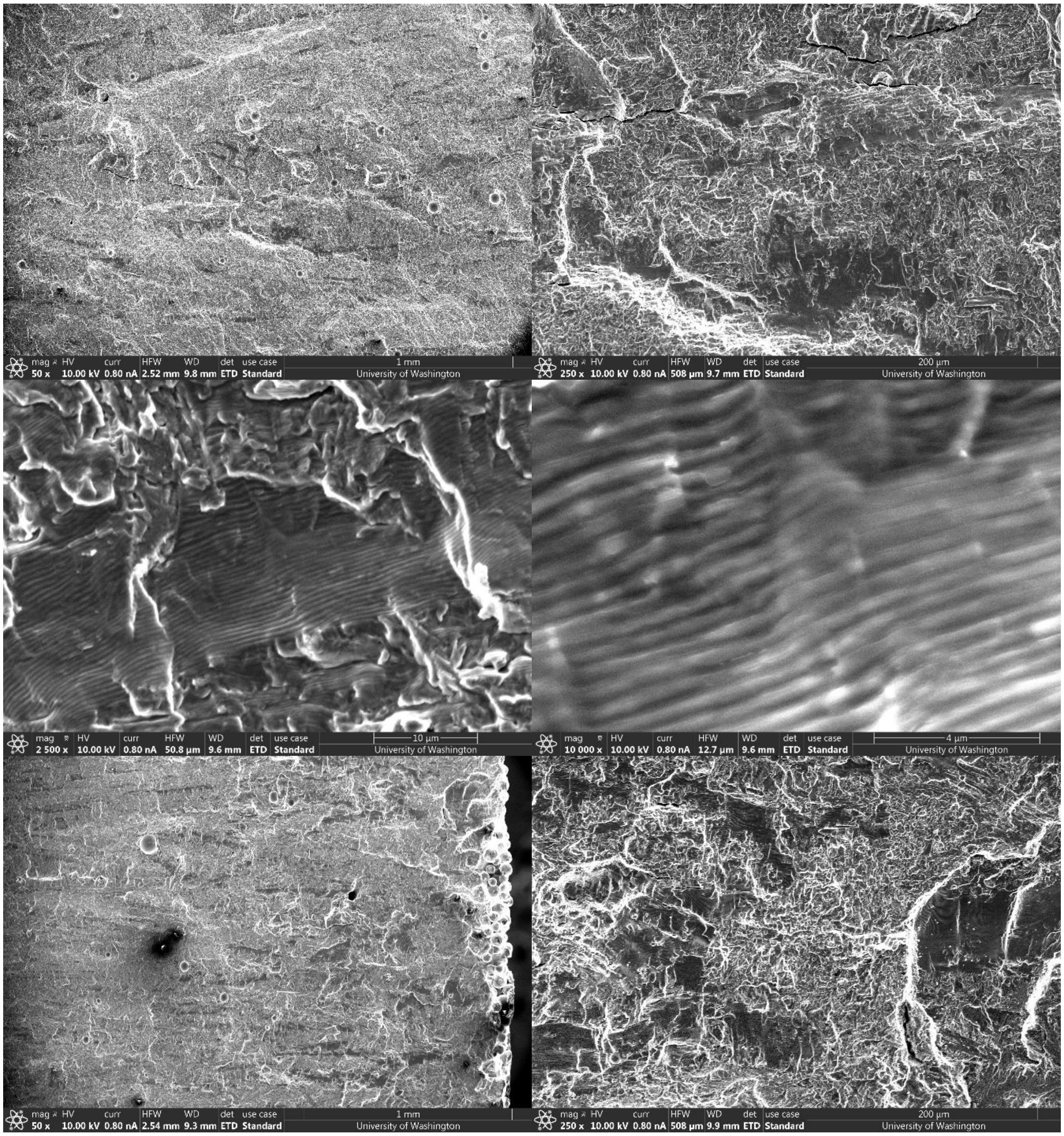

C.12 FCGR (Recycled Powder) Specimen 4 (90 Degrees, B = 12 mm)

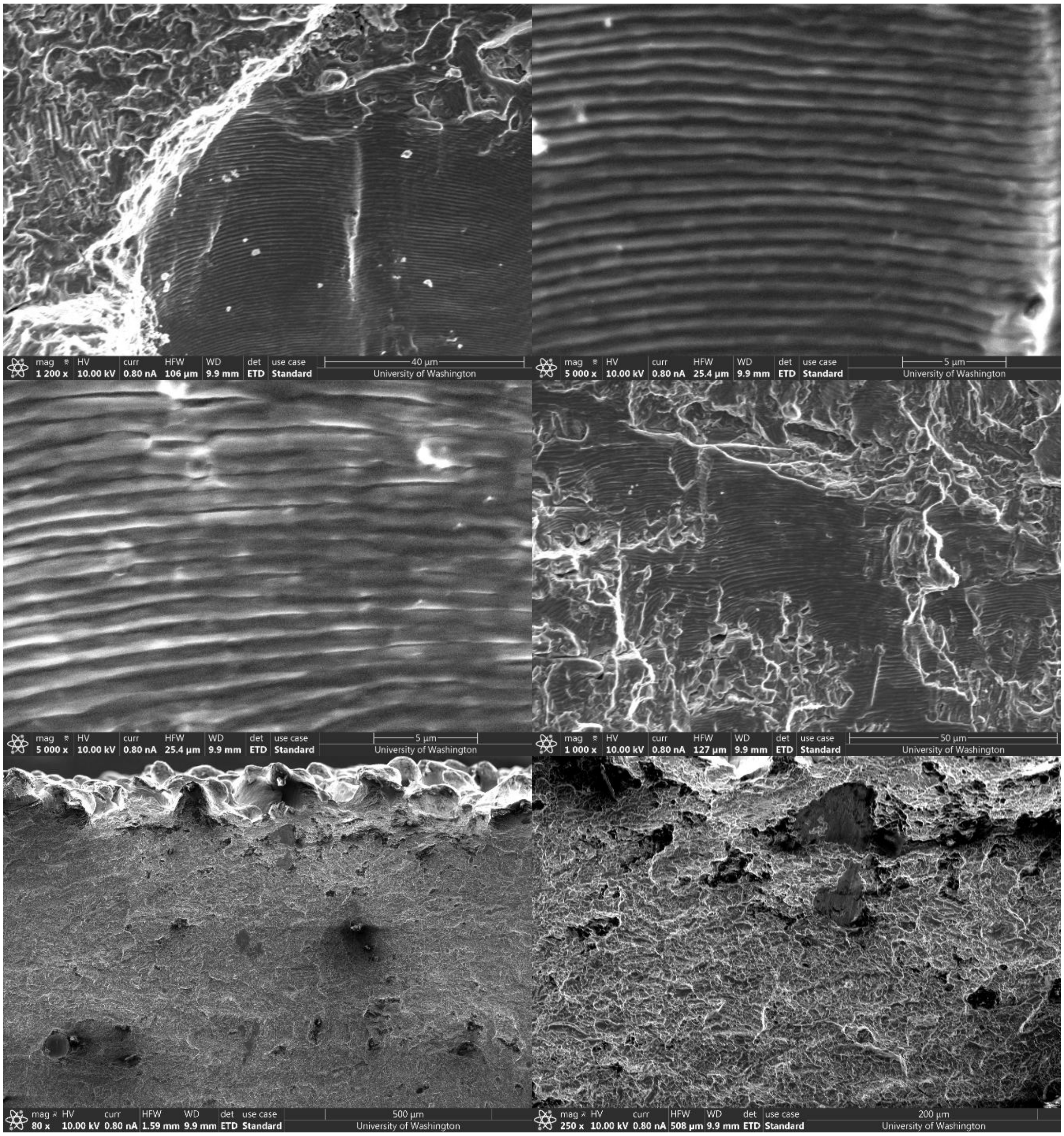

C.12 FCGR (Recycled Powder) Specimen 4 (90 Degrees, B = 12 mm)

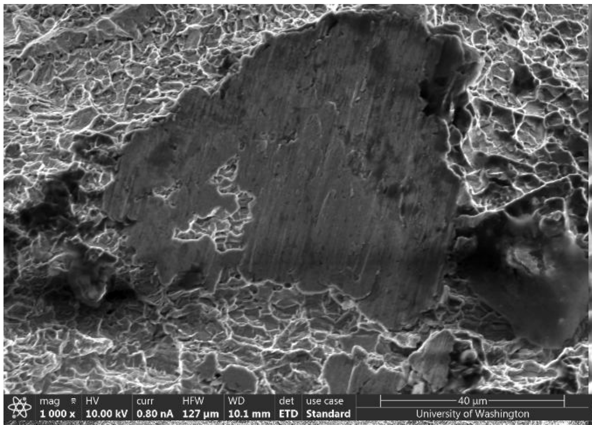

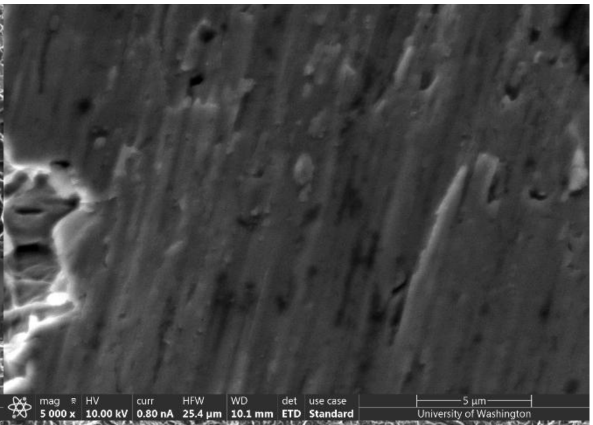

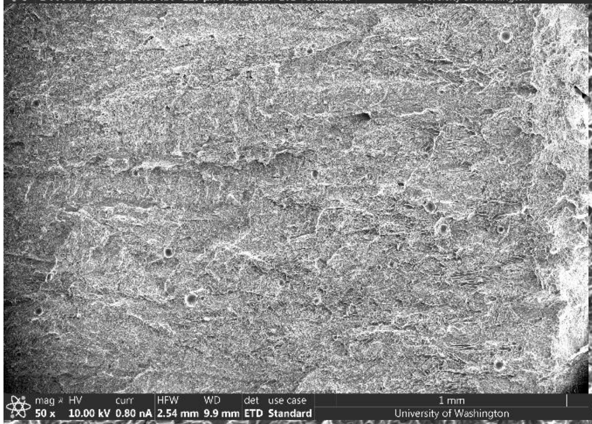

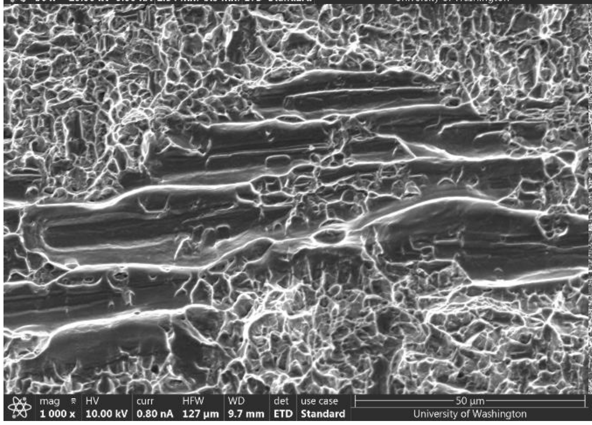

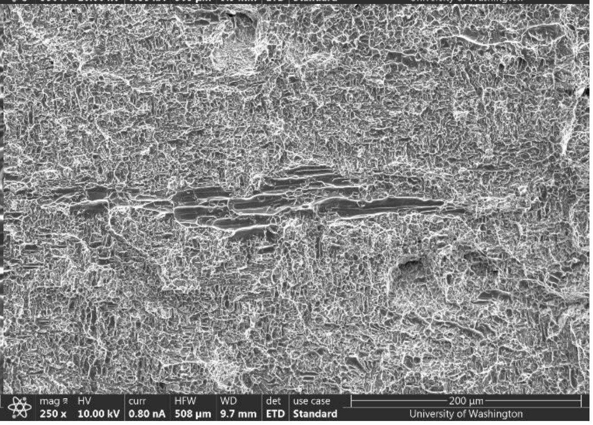

C.12 FCGR (Recycled Powder) Specimen 4 (90 Degrees, B = 12 mm)